

論文 / 著書情報
Article / Book Information

題目(和文)	先端メモリ技術に向けた強誘電体 AlScN 薄膜の高集積化と高信頼性に関する研究
Title(English)	Highly Reliable and Scalable Ferroelectric AlScN Thin Films for Future Advanced Memory Technology
著者(和文)	Chen Si-Meng
Author(English)	Si-Meng Chen
出典(和文)	学位:博士(工学), 学位授与機関:東京科学大学, 報告番号:甲第279号, 授与年月日:2025年3月26日, 学位の種別:課程博士, 審査員:角嶋 邦之,若林 整,渡辺 正裕,大見 俊一郎,飯野 裕明,三谷 祐一郎
Citation(English)	Degree:Doctor (Engineering), Conferring organization: Institute of Science Tokyo, Report number:甲第279号, Conferred date:2025/3/26, Degree Type:Course doctor, Examiner:,,,,,
学位種別(和文)	博士論文
Type(English)	Doctoral Thesis

Institute of Science Tokyo

Department of Electrical and Electronic Engineering

School of Engineering

**Highly Reliable and Scalable Ferroelectric AlScN
Thin Films for Future Advanced Memory Technology**

by

Si-Meng Chen

Academic supervisor: Dr. Kuniyuki Kakushima

A Thesis for the degree of

Doctor of Philosophy

February 2025

Abstract

The increasing computational demands of artificial intelligence (AI) technology are driving advancements in semiconductor research, focusing on developing higher computational efficiency through innovative architectures, novel device operation mechanisms, and new materials exploration. Advanced memory technology with in-memory computing (IMC) unlocks extraneous potential for computational capability and energy efficiency. The integration of non-volatile memory (NVM) technology demonstrates significant promise for realizing IMC and storage class memory (SCM). Within the development of NVM technology, ferroelectric materials have been drawing much attention thanks to their unique charge storage nature. The newly discovered wurtzite III-N ferroelectrics exhibit fascinating properties such as extraordinarily high remanent polarization (P_r) of over $100 \mu\text{C}/\text{cm}^2$, low dielectric constant (ϵ) of 11-20, and good compatibility to CMOS technology. The ferroelectricity of binary III-N compounds is enabled by foreign dopants such as Sc atom, leading to the formation of aluminum scandium nitride (AlScN). The polarization switching mechanism of AlScN is facilitated by Sc content and governed by the translation of N atoms in its wurtzite crystal structure. Despite AlScN thin films feature tunable ferroelectricity by varying Sc doping concentration, less-than-ideal endurance performance ($\sim 10^5$ cycles) and large leakage are urgent issues that should be dealt with. In this research, fabrication, characterization, and analysis are implemented for AlScN films to further improve the endurance performance by two orders and achieve below 5 V operation.

For capacitor fabrication, this research focuses on *in-situ* reactive sputtering of TiN/AlScN/TiN metal-ferroelectric-metal (MFM) capacitors and dedicates to exploring the deposition conditions for better film quality. Herein, the dependence of sputtering conditions such as Sc content of the AlSc alloy target, process pressure, and target-substrate (T/S) distance are examined. It is found that low Sc content film is more favorable over high Sc film due to wider bandgap (E_g), suppressed leakage, lower ϵ , higher P_r , and enhanced breakdown field (E_{BD}). Plus, with the assistance of lower process pressure, the sputtered films demonstrate lower leakage and boosted E_{BD} , along with reduced ϵ_i and increased P_r . Additionally, a suitable T/S distance could also enhance the overall ferroelectricity and E_{BD} . However, a trade-off relationship is found

between the coercive field (E_c) and E_{BD} . These results not only paved the way for improved endurance performance but also created the opportunity for thickness downscaling.

In order to tackle the high E_c characteristics of AlScN, defect engineering via oxygen incorporation is applied, and the role of oxygen-related complex defects is analyzed and understood. Intentionally incorporating O_2 gas flux into the Ar/ N_2 sputtering ambient results in AlScON films with complex defects that allow c -axis shrinkage. Accordingly, E_c decreases along with higher ϵ . Moreover, this technique breaks the aforementioned trade-off as E_{BD} is improved in AlScON films. Note that the incorporated O atoms distributed nonuniformly inside the film, which allows for partial polarization at low bias, resulting in a comparatively linear P_r gain over a wider range of E . Such performance is feasible and can be harnessed as multi-level operation in analog circuits for AI applications. Besides, with defect engineering and TiN serving as electrodes, this research highlights the demonstration of aggressive thickness scaling down to 9 nm of AlScN with under 5 V operation. Nevertheless, severe fatigue effect in endurance is found due to trapping/de-trapping incidents at Sc-O bonds. Decreasing the Sc content in the film could be helpful to mitigate the fatigue effect. Furthermore, oxygen profiling of multi-layer AlSc(O)N ferroelectrics shows that multi-interfaces in the ferroelectric stack could also help inhibit the leakage path and increase the breakdown strength.

In this research, it is identified that considerably high oxygen concentration exists at the ferroelectric/bottom electrode interface, which could greatly affect the endurance performance with non-negligible fatigue effect. Hence, oxygen depletion at the interface is conducted through sputter deposition in reducing ambient, with H_2 gas flux blending into the Ar/ N_2 sputtering ambient to lower the partial pressure of residual oxygen. Though incorporating H_2 gas flow could deteriorate the c -axis crystallinity, AlScN films exhibit excellent robustness against reducing ambient as the ferroelectricity sustained up to over 10% of H_2 flux. The decreasing ϵ serves as a corroborating indicator of the lower oxygen content in the deposited films. It is worth mentioning that with oxygen depletion the leakage is suppressed along with enhanced E_{BD} . This implies a different mechanism that can be explained as E_g broadening. Most importantly, the wake-up and fatigue effects are mitigated by oxygen depletion,

showing the effectiveness of oxygen level lowering at the interface. A record high endurance cycle of 2×10^7 switching cycles is achieved, pushing the endurance limits of AlScN thin films.

The originality of this research is to improve the reliability and scalability features of AlScN films through several consecutive steps: (1) sputtering condition exploration, (2) defect engineering via oxygen incorporation, and (3) interface oxygen depletion by reducing ambient deposition. Based on the results, guidelines which describe exquisite combinations of Sc and O content profiling to multi-layered ferroelectric stack are proposed for future high endurance and low-voltage operation. In summation, this research provides insight into enhancing the reliability and scalability of AlScN thin films and hopefully contributes to the development of ferroelectric AlScN for future advanced NVM technology.

Table of Contents

ABSTRACT	i
TABLE OF CONTENTS	iv
LIST OF FIGURES	viii
LIST OF TABLES	xv
ACKNOWLEDGEMENTS	xvi
ABBREVIATIONS AND SYMBOLS	xviii
CHAPTER 1: INTRODUCTION.....	1
1.1. ADVANCED MEMORY TECHNOLOGY	1
1.2. NEXT GENERATION NON-VOLATILE MEMORY TECHNOLOGY	5
1.3. FERROELECTRIC MATERIALS	7
1.3.1. <i>History and Development of Ferroelectric Materials</i>	7
1.3.2. <i>The Physical Origin of Ferroelectricity</i>	8
1.3.3. <i>Phase Transition in Ferroelectric Materials</i>	11
1.3.4. <i>Perovskite-based Ferroelectrics</i>	13
1.3.5. <i>Fluorite-based Ferroelectrics</i>	14
1.4. FERROELECTRIC MEMORIES	17
1.5. CHAPTER OVERVIEW	19
CHAPTER 2: FERROELECTRICITY IN NITRIDE MATERIALS	21
2.1. THEORETICAL AND EXPERIMENTAL DEMONSTRATION OF FERROELECTRICITY	21
2.2. CRYSTAL GROWTH AND DEPOSITION METHODS.....	23
2.2.1. <i>Wurtzite Crystal Structure</i>	24
2.2.2. <i>Physical Vapor Deposition: Sputtering</i>	28
2.2.3. <i>Epitaxial Growth: MBE and MOCVD</i>	30
2.3. FERROELECTRIC AND DIELECTRIC PROPERTIES OF ALUMINUM SCANDIUM NITRIDE	31
2.3.1. <i>Bandgap and Leakage Current</i>	31
2.3.2. <i>Dielectric Constant</i>	32
2.3.3. <i>Remanent Polarization and Coercive Field</i>	33
2.3.4. <i>Poling-free</i>	35
2.4. THICKNESS DOWNSCALING	36
2.5. RELIABILITY CONCERNS	37

2.6.	AIMS OF THIS RESEARCH	39
CHAPTER 3: FABRICATION PROCESS AND ELECTRICAL CHARACTERIZATION OF ALUMINUM SCANDIUM NITRIDE CAPACITORS		
40		
3.1.	CAPACITOR PREPARATION	40
3.1.1.	<i>Wafer Cleaning</i>	40
3.1.2.	<i>MFM Stack Deposition by in-situ Reactive Sputtering</i>	41
3.1.3.	<i>Capacitor Pattern Formation</i>	43
3.1.4.	<i>Backside Contact Deposition by Evaporation</i>	44
3.2.	ELECTRICAL MEASUREMENT.....	44
3.2.1.	<i>Polarization-Electric Field</i>	44
3.2.2.	<i>Positive-Up Negative-Down</i>	47
3.2.3.	<i>Endurance cycling</i>	49
3.2.4.	<i>Capacitance-Voltage</i>	50
3.2.5.	<i>Time-Zero Dielectric Breakdown</i>	54
CHAPTER 4: EXPLORATION OF REACTIVE SPUTTERING CONDITIONS FOR ALUMINUM SCANDIUM NITRIDE THIN FILMS		
56		
4.1.	INTRODUCTION	56
4.2.	DEPENDENCE OF COMPOSITION OF ALUMINUM SCANDIUM TARGET	56
4.2.1.	<i>Experimental Details</i>	56
4.2.2.	<i>Crystallinity and Composition of Deposited AlScN Thin Films</i>	57
4.2.3.	<i>Dielectric and Ferroelectric Properties</i>	59
4.3.	DEPENDENCE OF PROCESS PRESSURE	61
4.3.1.	<i>Experimental Details</i>	61
4.3.2.	<i>Dielectric and Ferroelectric Properties</i>	62
4.4.	DEPENDENCE OF TAREGET/SUBSTRATE DISTANCE	66
4.4.1.	<i>Experimental Details</i>	66
4.4.2.	<i>Dielectric and Ferroelectric Properties</i>	67
4.5.	SUMMARY OF THIS CHAPTER.....	69
CHAPTER 5: DEFECT ENGINEERING FOR ALUMINUM SCANDIUM NITRIDE THIN FILMS BY OXYGEN INCORPORATED SPUTTERING.....		
72		
5.1.	INTRODUCTION	72
5.2.	EXPERIMENTAL DETAILS.....	73
5.3.	MATERIAL ANALYSIS OF FERROELECTRIC FILMS DEPOSITED WITH OXYGEN FLUX.....	74

5.4.	INFLUENCE ON FERROELECTRIC AND DIELECTRIC PROPERTIES	77
5.4.1.	<i>Dielectric Constant and Imprint Effect</i>	77
5.4.2.	<i>Leakage Current, Breakdown Field and Polarization-Electric Field Hysteresis</i>	78
5.5.	POTENTIAL OF MULTI-LEVEL OPERATION	78
5.6.	ENDURANCE PERFORMANCE AND FATIGUE EFFECT	80
5.7.	POTENTIAL OF AGGRESSIVE SCALING	81
5.7.1.	<i>Experimental Details</i>	81
5.7.2.	<i>Influence on Ferroelectric and Dielectric Properties</i>	82
5.8.	SUMMARY OF THIS CHAPTER.....	84
CHAPTER 6: OXYGEN PROFILING IN MULTI-LAYER ALUMINUM SCANDIUM OXYNITRIDE CAPACITORS.....		86
6.1.	INTRODUCTION	86
6.2.	EXPERIMENTAL DETAILS.....	86
6.3.	DEPENDENCE OF POLARITY AT PRISTINE STATE.....	87
6.3.1.	<i>Control of Polarity</i>	87
6.3.2.	<i>Leakage Current and Breakdown Field</i>	90
6.4.	SUMMARY OF THIS CHAPTER.....	91
CHAPTER 7: INTERFACE OXYGEN DEPLETION BY REDUCING SPUTTERING AMBIENT FOR ENDURANCE ENHANCEMENT		92
7.1.	INTRODUCTION	92
7.2.	EXPERIMENTAL DETAILS.....	93
7.3.	MATERIAL ANALYSIS OF FERROELECTRIC FILMS DEPOSITED WITH HYDROGEN FLUX.....	94
7.4.	INFLUENCE ON FERROELECTRIC AND DIELECTRIC PROPERTIES	95
7.4.1.	<i>Dielectric constant</i>	96
7.4.2.	<i>Leakage Current and Breakdown Field</i>	96
7.4.3.	<i>Remanent Polarization and Coercive Field</i>	97
7.4.4.	<i>Ferroelectric Behavior After Field Cycling</i>	99
7.5.	IMPROVED ENDURANCE PERFORMANCE	100
7.6.	POTENTIAL OF HIGHER HYDROGEN FLUX.....	101
7.6.1.	<i>Experimental Details</i>	101
7.6.2.	<i>Influence on Ferroelectric and Dielectric Properties</i>	102
7.7.	SUMMARY OF THIS CHAPTER.....	104

CHAPTER 8: GUIDELINES FOR ALUMINUM SCANDIUM NITRIDE CAPACITORS FOR HIGH ENDURANCE AND LOW-VOLTAGE OPERATION	107
8.1. INTRODUCTION	107
8.2. CONCEPT OF THE PROPOSED MODEL AND APPLICABLE EXPERIMENTAL APPROACH ...	107
8.3. SUMMARY OF THIS CHAPTER.....	108
CHAPTER 9: CONCLUSIONS AND FUTURE WORK	110
9.1. ORIGINALITY AND KEY OUTCOMES.....	110
9.2. CONCLUSIONS.....	114
9.3. OUTLOOK AND FUTURE WORKS.....	116
REFERENCE	118
APPENDIX	141
CURRICULUM VITAE	142
PUBLICATION LIST	144

List of Figures

Figure 1.1: Worldwide data growth for the past 15 years.	1
Figure 1.2: Capacity for data storage in recent years.	2
Figure 1.3: Process latency versus integration density of volatile and non-volatile memory technologies.....	3
Figure 1.4: Schematics of (a) conventional von Neumann architecture and (b) in-memory computing for computational systems.....	4
Figure 1.5: Schematic architectures of (a) NMC, (b) SRAM-based IMC, and (c) NVM-based IMC.	4
Figure 1.6: Device structure of (a) RRAM, (b) PCRAM, (c) STT-MRAM, and (d) FeRAM for emerging NVM technology. (e) to (h) shows the operation principle of each device.	5
Figure 1.7: (a) Image of a Rochelle salt which is the first ferroelectric material to be discovered. Different domains are visible under polarized light. (b) The first observation of ferroelectricity in Rochelle salt in 1921.	7
Figure 1.8: Publications related to ferroelectric memories over the years.....	8
Figure 1.9: Separated point charges q with a distance d	9
Figure 1.10: (a) When no external bias is applied, dipoles inside the dielectric are randomly distributed. (b) When external bias exists, dipoles can be induced and aligned according to the direction of electric field.	9
Figure 1.11: Classification of crystalline dielectric materials.	10
Figure 1.12: Diagram of piezoelectric, pyroelectric and ferroelectric effects.	11
Figure 1.13: Energy landscape with respect to polarization of ferroelectric, dielectric, and stacked materials.....	12
Figure 1.14: The dependence of energy profile during ferroelectric switching from one polarized state to another.	12
Figure 1.15: Free energy landscape and deduced P-E S curves of ferroelectrics at different temperatures.....	13
Figure 1.16: Two polarization states of perovskite-based ferroelectrics.....	13
Figure 1.17: Crystal structure and corresponding ferroelectric responses. By tuning the process parameters above, ferroelectric orthorhombic phase is achievable. Note that monoclinic and tetragonal phases demonstrate paraelectric and antiferroelectric	

properties, respectively.....	14
Figure 1.18: (a) HYO and (b) HAO films with different doping concentrations.	15
Figure 1.19: P-E hysteresis of HZO films after (a) PDA and (b) PMA process. (c) Comparison of different film thickness.	15
Figure 1.20: P-E hysteresis of HZO films with various thickness.	16
Figure 1.21: The formation of ferroelectric phase for doped HfO₂ during RTA process.	16
Figure 1.22: Development of ferroelectric materials and memory technology.	17
Figure 1.23: Schematics and operation principles of (a) FeRAM, (b) FeFET, and (c) FTJ.	17
Figure 1.24: Schematic flow chart of content in chapters in this thesis.	19
Figure 2.1: Nitride materials showing various properties for various applications.	21
Figure 2.2: Energy landscape of pure AlN and AlScN.	22
Figure 2.3: The first experimental demonstration of P-E hysteresis in wurtzite materials. P_r and E_c are tunable by changing the Sc content in Al_{1-x}Sc_xN.	22
Figure 2.4: Wurtzite crystal is energetically stable only if the Sc content is lower than 32% in Al_{1-x}Sc_xN.	24
Figure 2.5: Wurtzite crystal structure of AlScN. Tetrahedron structures are found among adjacent metal and N atoms.	25
Figure 2.6: (a) Average calculated bond length of first neighbor Al/Sc atoms and N atoms that are orientated either in the basal plane or along c-axis. Average metal-N bond length (b) along c-axis and (c) in the basal plane for AlScN with respect to Sc concentration.	25
Figure 2.7: Calculated geometric dimensions of tetrahedrons in wurtzite crystals of AlScN. h(x) represents the distance between the apex to the basal plane. h_N(x) is the distance of the N atom to the basal plane. b(x) is the bisector of the basal plane.	26
Figure 2.8: Dependence of Sc content with (a) lattice constants a and c, (b) c/a, and (c) u parameter. (d) The average bond ionicity in Al_{1-x}Sc_xN.	27
Figure 2.9: Two polarization states in ferroelectric wurtzite materials.	27
Figure 2.10: (a) XRD profile and (b) FWHM of sputtered Al_{1-x}Sc_xN films.	28
Figure 2.11: (a) XRD profiles of the sputtered films deposited at different temperatures. (b) P_r-E relationship obtained from PUND measurement. (c) Comparison of ferroelectricity.	29

Figure 2.12: P-E hysteresis of sputtered AlScN film using (a) only N ₂ gas and (b) mixed Ar/N ₂ gases during deposition.....	29
Figure 2.13: (a) P-E hysteresis of MBE deposited AlScN films. (b) Comparison of ferroelectricity among sputtered and MBE grown films.....	30
Figure 2.14: (a) Current density in relation to E. (b) STEM image for switched and unswitched areas.	31
Figure 2.15: Calculated E _g by (a) Deng <i>et al.</i> and (b) Baeumler <i>et al.</i>	31
Figure 2.16: (a) Schottky barrier height before and after switching. (b) Band diagram of MFM structure	32
Figure 2.17: ε _r with respect to doping concentration in ternary III-N materials.	33
Figure 2.18: P-E hysteresis of PZT, HZO, and wurtzite ferroelectrics.....	33
Figure 2.19: (a) P _r and (b) E _c with respect to Sc content in Al _{1-x} Sc _x N films.....	34
Figure 2.20: E _c values in relation to temperature and film thickness.	34
Figure 2.21: Initial (a) positive and (b) negative C-V sweeps for pristine films.	35
Figure 2.22: (a) Schematic flow of the confirmation of N-polar state in pristine film. SEM image of the (b) top and (c) oblique view after selective etching.	36
Figure 2.23: (a) P _r and (b) E _c values in relation to film thickness.....	37
Figure 2.24: Endurance tests for AlScN thin films deposited by (a) sputtering and (b) MBE.....	37
Figure 2.25: Model of decreasing Schottky barrier height after field cycling.	38
Figure 2.26: Defect generation in AlScN based on hot atom damage model.	38
Figure 3.1: (a) Schematic figure and (b) process flow of AlScN MFM capacitor.....	40
Figure 3.2: Dependence of sputtering rate and deposited thickness of AlScN. The thickness is measured by ellipsometry.	42
Figure 3.3: P-E measurement of ferroelectric capacitor for ideal and practical cases. The inset shows the input signal. Polarization is calculated by integrating the current density with respect to time.	44
Figure 3.4: Typical P-V hysteresis loops of ferroelectric HfO ₂ -based ferroelectric capacitor under various voltage sweep range.	45
Figure 3.5: Scott <i>et al.</i> elucidated the importance of identifying true ferroelectricity in a humorous way. (a) Banana-shaped hysteresis loops of lossy dielectric, and (b) an actual banana.....	46
Figure 3.6: P-E hysteresis loops from DLCC measurement with two different	

frequencies. Note that a leaky ferroelectric HAO capacitor is used here.46

Figure 3.7: (a) Schematic of PUND measurement. (b) Compensated P-E hysteresis can be derived when triangle pulses are applied in PUND. (c) Current response of PUND with square pulses. Switching current responses are shown in “P” and “N” pulses, whereas non-switching current responses are spotted in “U” and “D” pulses.47

Figure 3.8: P_r with respect to $\pm E$ from a PUND measurement of AlScN capacitor.48

Figure 3.9: Measurement scheme of endurance cycling test in this research.50

Figure 3.10: Illustration of C-V measurement for ferroelectric capacitors.50

Figure 3.11: P-E and C-V curves for HZO capacitor with various Hf/Zr ratios.51

Figure 3.12: An example of C-V measurement for ferroelectric AlScN capacitor. The voltage sweep is indicated by arrows.52

Figure 3.13: C-V measurement for HZO capacitors from 1 kHz to 1 MHz.53

Figure 3.14: (a) Imprint effect indicated by marked difference between $|E_c^+|$ and $|E_c^-|$ values in C-V curve of AlScN capacitor. (b) Imprint effect illustrated by shifting the P-E hysteresis.54

Figure 3.15: TZDB relationships of two as-deposited TiN/AlScN/TiN capacitors underwent positive and negative sweep.55

Figure 4.1: XRD analysis for Al_{1-x}Sc_xN films deposited with high-Sc (Al_{0.53}Sc_{0.47}) and low-Sc (Al_{0.8}Sc_{0.2}) targets. High c-axis crystallinity is shown in both films.57

Figure 4.2: TEM and EDX analysis for chemical compositions of AlScN films deposited using (a) high-Sc (Al_{0.53}Sc_{0.47}) and (b) low-Sc (Al_{0.8}Sc_{0.2}) targets.58

Figure 4.3: Butterfly C-V curves of 50 nm high-Sc and low-Sc content films. The measurement was conducted at 1 MHz. Cross-point of the C-V curves show the information of ϵ_i values.59

Figure 4.4: Results of TZDB measurements for 50 nm high-Sc and low-Sc content films. Different compliance settings were applied due to SMU limitations.60

Figure 4.5: P_r -E relationship of PUND measurements for deposited films. E_c values were extracted via linear extrapolation of the rising P_r before reaching semi-saturation kinks.61

Figure 4.6: Butterfly-shaped C-V curves of 50 nm high-Sc content films. ϵ increases with process pressure.63

Figure 4.7: Leakage current and breakdown properties of high-Sc content films. E_{BD} tends to increase with lower process pressure.64

Figure 4.8: P _r -E relationship of PUND measurements for high-Sc content films.....	64
Figure 4.9: C-V loops of 40 nm low-Sc films. ε increases with process pressure.	65
Figure 4.10: Leakage current and breakdown properties of 40 nm low-Sc content films. Suppressed leakage and boosted E _{BD} can be obtained in the films deposited with lower process pressure.	65
Figure 4.11: Butterfly C-V loops of films deposited with various T/S distance.....	67
Figure 4.12: TZDB results of 50 nm low-Sc content films.	68
Figure 4.13: P _r -E relationship of PUND measurements for low-Sc content films deposited with various T/S distance.....	69
Figure 5.1: AlN wurtzite lattice with complex defect of (V _{Al} -O _N) ²⁻ . The cationic sites (Al/Sc) are only coordinated with anionic sites (O/N) in the wurtzite lattice.....	72
Figure 5.2: XPS spectra and extracted composition of 50 nm AlScON films. The X-ray source is Monochromatic Al Kα (1486.6 eV), and the inspection area is 100 μmψ (7.854 × 10 ³ μm ²). The photoelectron TOA is set to 90°, and the inspection depth is 9 nm. The measurement accuracy is within ±1 at.%.	75
Figure 5.3: (a) Out-of-plane XRD and (b) XRC profiles on 002 plane of 50 nm AlScON films with different oxygen compositions.....	76
Figure 5.4: Shrinkage in lattice constant c is induced by oxygen content.	76
Figure 5.5: (a) Butterfly C-V curves of MFM capacitors with various oxygen contents. (b) E _{imp} and ε _i with respect to the oxygen content.	77
Figure 5.6: (a) TZDB characterization of all the fabricated MFM capacitors. (b) P-V hysteresis loops measured at 10 kHz for the Al _{0.89} Sc _{0.11} O _y N _{1-y} films.	78
Figure 5.7: Results of PUND measurements for Al _{0.89} Sc _{0.11} O _y N _{1-y} MFM capacitors with different oxygen concentrations. The upper-left inset depicts a portion of the applied pulse signal and current response during PUND. The lower-right inset shows the dependence between the linearly extrapolated negative E _c and the oxygen content.	79
Figure 5.8: (a) Endurance measured by field cycling test of all capacitors with various oxygen content. The target P _r is set to be 100 μC/cm ² . (b) A multi-level partial polarization demonstration of Al _{0.89} Sc _{0.11} O _{0.23} N _{0.77} capacitor from 5.2 to 6 MV/cm...80	80
Figure 5.9: C-V curves of 9 nm low-Sc content films. With the incorporation of oxygen, butterfly shape becomes clearer and more symmetrical. The measurement was conducted at 1 MHz.	82

Figure 5.10: TZDB results for 9 nm low-Sc content films. Leakage is suppressed and E_{BD} is improved for AlScON film.....83

Figure 5.11: PUND results for 9 nm AlScON capacitor. Due to the limited film quality at low thickness, the maximum P_r is $4.7 \mu\text{C}/\text{cm}^2$84

Figure 6.1: Various ferroelectric stacks for multi-layer AlSc(O)N capacitors. The total thickness of ferroelectric layers is 50 nm. The TiN BE and TE are 10 nm and 30 nm, respectively. From (a) to (e), the capacitors are denoted as *Full_ASN*, *Top_ASON*, *Bottom_ASON*, *ASN_ASON_ASN*, and *Full_ASON*, respectively.86

Figure 6.2: Left panels [(a)-(e)] and right panels [(f)-(j)] show the initial positive and negative C-V sweeps for pristine films, respectively.88

Figure 6.3: TZDB results of fabricated AlSc(O)N capacitors with various ferroelectric stack structures.90

Figure 7.1: SIMS results of a TiN/AlScN/TiN capacitor stack. The oxygen level is typically higher in AlScN layer. Oxidation from the atmosphere after deposition is effectively blocked by the top TiN layer.92

Figure 7.2: Cross-sectional TEM image of TiN/ $\text{Al}_{1-x}\text{Sc}_x\text{N}$ /TiN MFM capacitor (*low_Sc*). The deposited ferroelectric layer is 60 nm.94

Figure 7.3: (a) Out-of-plane XRD and (b) XRC profiles of deposited 60 nm films sputtered with and without H_2 gas.....95

Figure 7.4: C-V characteristics of all deposited films. Dielectric constant decreases with H_2 gas flow.....96

Figure 7.5: TZDB results of all samples. Leakage is suppressed and E_{BD} is improved with H_2 -included sputtering.97

Figure 7.6: P_r -E relationship from PUND measurements for AlScN MFM capacitors deposited with and without H_2 gas flux.....98

Figure 7.7: C-V measurement sweeping to negative voltage after switching for 10, 10^2 , 10^3 , and 10^4 cycles for (a) *High_Sc* and *Low_Sc* films, and (b) *High_Sc_H2* and *Low_Sc_H2* films.99

Figure 7.8: Endurance field cycling tests for all deposited films. Different E values are used to meet the target P_r of $100 \mu\text{C}/\text{cm}^2$ for fair comparison.....100

Figure 7.9: (a) C-V curves of fabricated $\text{Al}_{0.74}\text{Sc}_{0.26}\text{N}$ MFM capacitors with high H_2 flux. The ferroelectricity sustains up to 11.77% of H_2 flux. (b) E_{imp} and ϵ_i in dependence with the H_2 flux percentage.....103

Figure 7.10: TZDB results of all deposited films. Leakage is suppressed and E_{BD} is improved with H_2 included sputtering up to 11.77% H_2 flux. 103

Figure 7.11: P_r -E relationship of fabricated $Al_{0.74}Sc_{0.26}N$ films in PUND measurements. 104

Figure 7.12: Extracted E_c and E_{BD}/E_c ratio with respect to H_2 flux percentage..... 104

Figure 8.1: Concept of proposed model for AlScN MFM capacitors for high endurance and low-voltage operation. 107

Figure 9.1: Originality of this research illustrated in a flow chart..... 111

List of Tables

Table 1.1: Benchmark of Emerging NVM Technology.....	6
Table 2.1: Comparison of Ferroelectric Materials	23
Table 3.1: Sputtering Conditions for Titanium Nitride.....	41
Table 3.2: Sputtering Conditions for Aluminum Scandium Nitride	42
Table 4.1: Sputtering Conditions for Aluminum Scandium Nitride	57
Table 4.2: Sputtering Conditions for Aluminum Scandium Nitride	62
Table 4.3: Sputtering Conditions for Aluminum Scandium Nitride	67
Table 4.4: Influences of Sputtering Conditions.....	70
Table 5.1: Sputtering Conditions for Aluminum Scandium Oxynitride	74
Table 5.2: Sputtering Conditions for Aluminum Scandium Oxynitride	81
Table 6.1: Sputtering Conditions for Aluminum Scandium (Oxy)Nitride.....	87
Table 7.1: Sputtering Conditions for Aluminum Scandium Nitride	93
Table 7.2: Sputtering Conditions for Aluminum Scandium Nitride	102
Table A1.1: List of Bond Dissociation Energy.....	141

Acknowledgements

First and foremost, I would like to express my deepest gratitude to my supervisor, Prof. Kuniyuki Kakushima, for his sincerity, encouragement, and vital guidance during all the stages of my PhD research. This thesis would never have been accomplished without his dedicated involvement and the extensive discussions we had together after finishing my dual master's degree in Japan and Taiwan. His profound insights and constructive feedback inspired me to refine my thinking, propelling my research to reach greater depths of clarity and excellence.

I am indebted to Prof. Hitoshi Wakabayashi and Prof. Kazuo Tsutsui from our joint research group for their continuous assistance and invaluable advice. My gratitude further extends to Prof. Takuya Hoshii for his numerous times of technical support and comprehensive consultation.

I gratefully recognize the help of my colleague in lab, Mr. An Li, for his kind support and contribution. We have been assisting each other during our journey in PhD research. I wish you the best after graduation.

Moreover, I would like to thank my senior colleague, Mr. Hirofumi Nishida, for his precious encouragement and enthusiasm. Our joint research work has been fabulous and full of excitement.

Special thanks to two visiting researchers from National Sun Yat-sen University, Taiwan, Mr. Jia-Hong Lin and Ms. Ting-Tzu Kuo, for a cherished time spent together in the lab. Your treasured support regarding electrical measurements made up for the deficiencies in my research, improving the quality of my experimental data. Hope you have a smooth graduation back to Taiwan.

I especially want to thank Dr. Sung-Lin Tsai who laid the foundation of this research and supported me with the scholarship application along with Mr. Yu-Wei Lin. Both of you are kind and amiable to me and provided me with lots of heartwarming suggestions.

Additionally, I would like to acknowledge the financial support from the Japan-Taiwan Exchange Association Scholarship (students) and Tokyo Tech Tsubame

Scholarship.

Thank you to all other colleagues in Kakushima lab, past and present, for help and assistance with all things.

Outside of university, I am grateful to my best friend, Mr. Kingjade Yu, for his powerful collecting program that considerably enhances the efficiency of summarizing and curating my experimental data. Wish you the best in your career.

Finally, to my beloved family, I dedicate this PhD thesis in gratitude for your unwavering support and encouragement throughout my academic research. I am particularly grateful to my father, who is my hero, embodying true integrity and honesty. I am also grateful to my mother, who always takes care of the details, as well as motivates me and has given so much for my well-being.

Abbreviations and Symbols

AC alternating current

AI artificial intelligence

Al aluminum

ALD atomic layer deposition

AIBN aluminum boron nitride

AlN aluminum nitride

AlSc aluminum scandium

AlScN aluminum scandium nitride

AlScON aluminum scandium oxynitride

AlYN aluminum yttrium nitride

Al₂O₃ aluminum oxide

ANNs artificial neural networks

APM ammonium hydroxide–hydrogen peroxide mixture

Ar argon

B boron

BE bottom electrode

BEOL back end of line

BTO barium titanate

CiM compute-in-memory

Cl₂ chlorine

CMOS complementary metal-oxide-semiconductor

CPU central processing unit

DC direct current

DI water deionized water

DRAM dynamic random-access memory

DUV deep ultraviolet

E electric field

E_{BD} breakdown field
E_c coercive field
E_{imp} imprint field
E_g bandgap
EDX energy-dispersive X-ray spectroscopy

D electric displacement field
DLCC dynamic leakage current compensation

F² feature size
FET field-effect transistor
FeFET ferroelectric field-effect transistor
FeRAM ferroelectric random-access memory
FFT fast Fourier transform
FTJ ferroelectric tunneling junction
FWHM full-width at half-maximum

GaN gallium nitride
GaScN gallium scandium nitride
Gd gadolinium

H₂ hydrogen
H₂O water
H₂O₂ hydrogen peroxide
H₂SO₄ sulfuric acid
HAO hafnium aluminum oxide
HDD hard disk drive
HEMT high electron mobility transistor
HF hydrogen fluoride
Hf hafnium
HfO₂ hafnium dioxide
HKMG high-κ metal gate
HMDS hexamethyldisilazane

HRS high-resistance state
HYO hafnium yttrium oxide
HZO hafnium zirconium oxide

I current
ICP-RIE inductively coupled plasma - reactive ion etching
I_D drain current
IMC in-memory computing
In₂O₃ indium oxide
IoT internet of things
ITO indium tin oxide
I-V current-voltage

La lanthanum
LED light-emitting diode
LLMs large language models
LRS low-resistance state

MBE molecular beam epitaxy
MFM metal-ferroelectric-metal
Mo molybdenum
MOCVD metal-organic chemical vapor deposition
MRAM magnetic random-access memory

N₂ nitrogen
NH₄OH ammonium hydroxide
NMC near-memory computing
NVM non-volatile memory

O₂ oxygen
O_N substitutional oxygen at nitrogen site

P polarization

Pb lead
PC personal computer
PCRAM phase-change random-access memory
PDA post deposition annealing
PFM piezoresponse force microscopy
PMA post metallization annealing
PRG/ERS program/erase
P_r remanent polarization
P_r-E remanent polarization-electric field
Pt platinum
PUND positive-up negative-down
PVD physical vapor deposition
PZT lead zirconate titanate
P-E polarization-electric field
P-V polarization-voltage

Q charge
Q-E charge-electric field
Q-V charge-voltage

RC resistor-capacitor
RF radio-frequency
RFID radio-frequency identification
RRAM resistive random-access memory
RT room temperature
RTA rapid thermal annealing

SEM scanning electron microscope
Si silicon
SIMS secondary-ion mass spectrometry
Sc scandium
SCM storage-class memory
ScN scandium nitride

SMU source measure unit
SNNs spiking neural networks
SOT-MRAM spin-orbit torque magnetic random-access memory
SPM sulfuric-peroxide mixture
SRAM static random-access memory
STEM scanning transmission electron microscope
STT-MRAM spin-transfer torque magnetic random-access memory

T_c Curie temperature
TE top electrode
TEM transmission electron microscope
Ti titanium
TiN titanium nitride
TiO_x titanium oxide
TiON titanium oxide nitride
TMAH tetramethylammonium hydroxide
TOA take-off angle
TZDB time-zero dielectric breakdown
T/S target/substrate

V voltage
V_{Al} aluminum vacancy
V_c coercive voltage
V_G gate voltage
V_N nitrogen vacancy
V_O oxygen vacancy
V_{th} threshold voltage

XPS X-ray photoelectron spectroscopy
XRC X-ray rocking curve
XRD X-ray diffraction

Y yttrium

Zr zirconium

2DEG two-dimensional electron gas

2D two-dimensional

ϵ permittivity, dielectric constant

ϵ_i static dielectric constant

ϵ_r relative permittivity

ϵ_0 vacuum permittivity

K permittivity, dielectric constant

Chapter 1: Introduction

1.1. Advanced Memory Technology

Since antiquity, people had long been observing electricity from natural phenomenon such as lightning and electrified objects. As civilization thrives, human brilliance and endeavor trigger the attempt to manipulate and utilize electricity to improve our living. Going back a few centuries from now, series of hard work and experiments, that were conducted by pioneers like Sir Isaac Newton and Benjamin Franklin, laid the foundation for electrical and electronic engineering. With Michael Faraday’s electric generator marking the milestone, electricity has become a necessary element in various areas such as infrastructure, scientific research, and technology evolvement. Especially, the invention of transistors not only revolutionized the society, but also enables the opening of digital era [1], [2], [3]. Semiconductor IC technology has been prospering since then [4]. Driven by this force, massive attention and effort have been paid to the development of memory technology.

Human brains are natural and functional storage devices that can retain and recall information, according to neuropsychology. However, as we have already entered the stage of data explosion, it is impossible for human beings to remember everything. Fortunately, thanks to the progress of contemporary memory technology, we no longer need to specifically rely on old-fashioned ways to memorize.

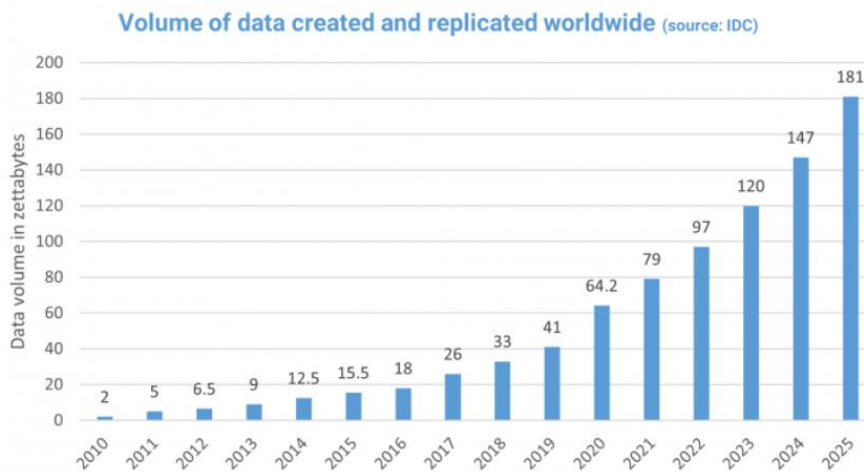


Figure 1.1: Worldwide data growth for the past 15 years [5]. (Source: IDC)

AI technology has been the most powerful engine of flourishing development in data science and engineering, creating hot research in various fields such as LLMs, cloud computing, edge AI gadgets, IoT systems, AI robotics, etc. Figure 1.1 illustrates the data volume created and duplicated in the past 15 years, and an exponential increasing trend can be expected for the near future [5]. With this tendency, it is obvious that data storage and processing are urgent tasks in hand. Figure 1.2 shows that the required data storage gains over time [5], posing challenges to the memory technology.

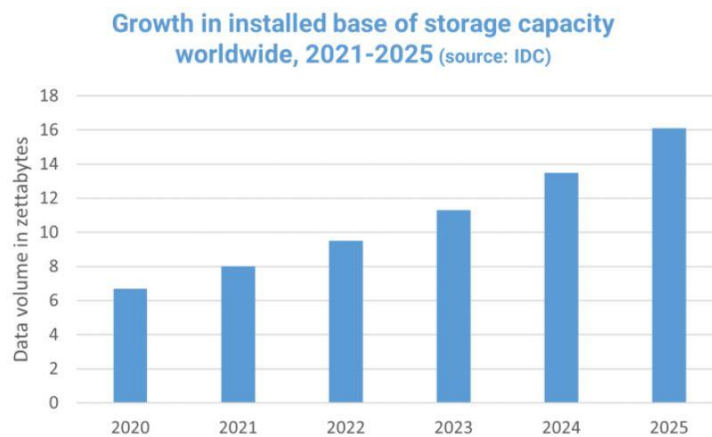


Figure 1.2: Capacity for data storage in recent years [5]. (Source: IDC)

However, addressing the technological challenges for memory requires a comprehensive approach that extends beyond storage capacity, encompassing critical dimensions such as energy efficiency, processing latency, physical size, and cost. An ideal memory should have infinite capacity, zero delay time, and no power consumption. However, realistically, there is no such technology yet, leaving us the opportunity to improve and generate great impact to the current memory technology. In general, the data storage should be distinguished into two types, permanent and temporary, whose requirements of performance are different. For instance, DRAM and SRAM, commonly seen in modern PC systems, are categorized as volatile memory, since they store temporary data solely. Upon removal of the power supply, the retained data of volatile memory is lost. On the other hand, NAND flash, NOR flash and HDD are sorted to be non-volatile memory since the data retention is long and irrelevant to power supply. From the power consumption perspective, non-volatile memory is naturally more desirable than volatile memory, as no standby power is necessary. Nevertheless, the processing latency gap and physical size hinders the

replacement of volatile type to non-volatile type. Figure 1.3 depicts the relationship of access time and integration density of memory technologies [6]. It is obvious that a huge gap exists between volatile and non-volatile types, and SCM technologies are targeted to fill in it. The red box highlighted several contenders such as PCRAM, RRAM, MRAM, FeRAM, etc. These candidates, also called emerging NVM, are in pursuit of faster processing speed close to DRAM, good storage capacity as NAND flash, and non-volatile features for high energy efficiency. Details of emerging NVM technology will be introduced in section 1.2.

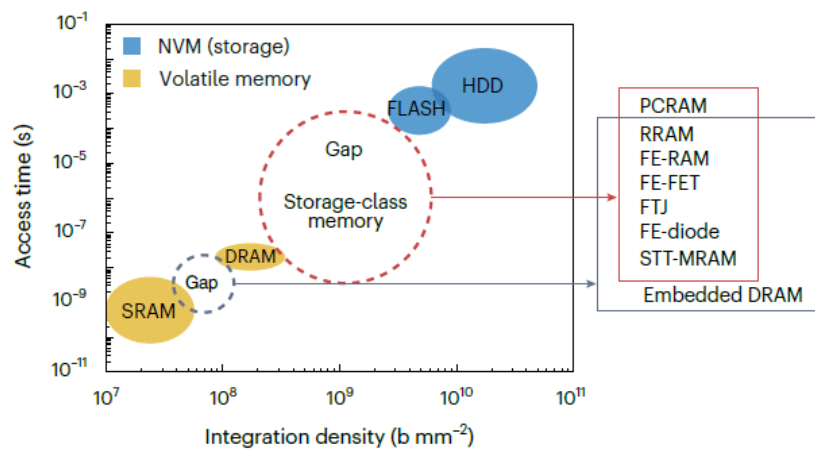


Figure 1.3: Process latency versus integration density of volatile and non-volatile memory technologies [6].

Traditionally, contemporary computational systems utilize the von Neumann architecture in which the CPU and memory blocks are separated [7]. Data transfer back and forth is mandatory to perform computational tasks, as displayed in Figure 1.4(a) [8]. This not only results in high process latency but also large power consumption issues. As AI technology continuously exploits the benefits of big data and intensive computation, the quantities of processing data are increasing unrelentingly, leaving the issues more critical. The performance could hit a “memory wall”, or in other words, the von Neumann bottleneck [9]. Luckily, near-memory computing and in-memory computing are viewed as possible solutions, as they demonstrate potential to alleviate the process latency and enhance the energy efficiency [10]. Schematic in Figure 1.4(b) illustrates the concept of IMC [8]. The amount of transferred data (input/output/instruction) can be reduced since the computation can be done in the memory, giving rise to minimized processing latency and power consumption. Besides,

embedding NVM technology to NMC and IMC unlocks extraneous potential for computational efficiency, and these architectures can be found in Figure 1.5(a), (b), and (c) [11]. Wang *et al.* proposed that SRAM can serve as the cache memory while embedded NVM handles the data storage for NMC [12], as Figure 1.5(a) shows. Mittal *et al.* then further analyzed the method of utilizing SRAM directly as the computing engine for IMC [13], which is displayed in Figure 1.5(b). Eventually, the most advanced architecture should evolve to Figure 1.4(b) or Figure 1.5(c), as embedded NVM technology functions for all purposes.

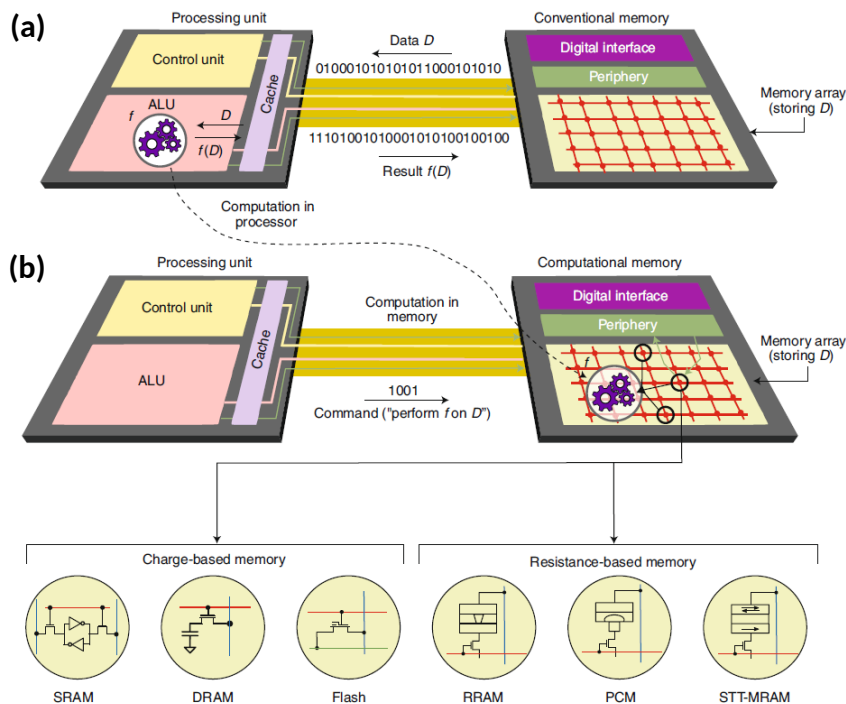


Figure 1.4: Schematics of (a) conventional von Neumann architecture and (b) in-memory computing for computational systems [8].

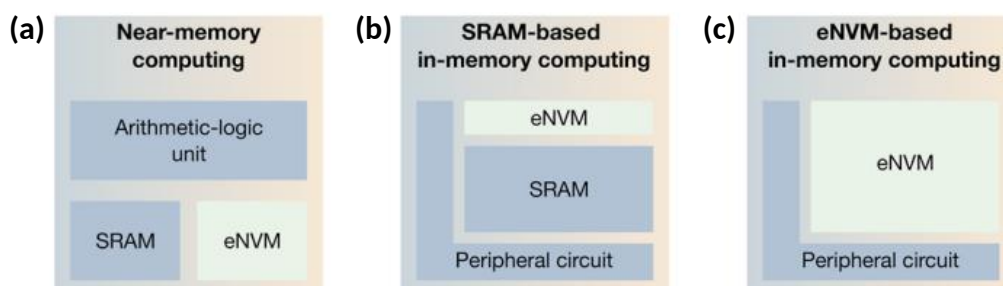


Figure 1.5: Schematic architectures of (a) NMC, (b) SRAM-based IMC, and (c) NVM-based IMC [11].

1.2. Next Generation Non-Volatile Memory Technology

The awareness of adopting innovative architectures and emerging NVM technology for next generation computation has been raised in recent years [8], [14]. Analog IMC with neuromorphic accelerators for ANNs and SNNs has been explored to overcome the von Neumann bottleneck. NVM with a crossbar-based design, featuring high energy efficiency and alleviated processing latency, stands out among the candidates [15]. Figure 1.6(a) to (d) illustrates some of the popular device structure for emerging NVM research currently [16].

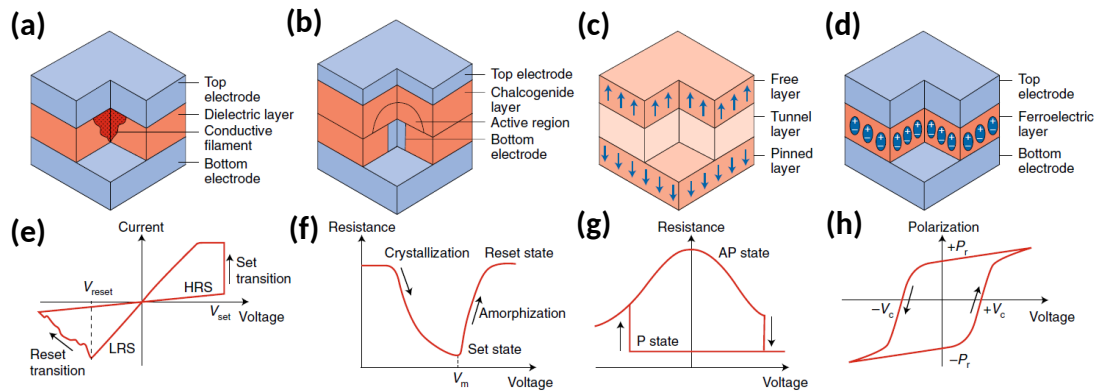


Figure 1.6: Device structure of (a) RRAM, (b) PCRAM, (c) STT-MRAM, and (d) FeRAM for emerging NVM technology. (e) to (h) shows the operation principle of each device [16].

Plenty of research regarding PCRAM has been conducted over the years, as it contains a chalcogenide glass layer for phase transformation, as shown in Figure 1.6(b). Figure 1.6(f) displays that via imposing Joule heating or cooling, the material could change its structure between amorphous and crystalline states, which allows the detection of high and low resistivity possible. Good endurance performance and high on/off ratio are strengths in PCRAM.

RRAM features a dielectric layer with capability of switching between conducting and insulating states, as shown in Figure 1.6(a). Depending on the direction of applied field, thin conducting filament can be formed or dissolved, inducing LRS and HRS conditions, as Figure 1.6(e) depicts. RRAM demonstrates feasible traits such as low

PRG/ERS energy and high switching speed, which are attractive to NVM technology. Current research mainly focus on the formation of filament as the alignment of metallic ions or V_O is the origin of filamentary resistive switching. However, the stochastic nature makes universal variation among RRAM devices unavoidable, limiting the endurance to 10^6 – 10^9 cycles.

MRAM is another attractive option for emerging NVM devices, since they are able to achieve excellent endurance cycle over 10^{15} and low latency. In Figure 1.6(c), the magnetic tunnel junction consists of a tunnel oxide and two ferromagnetic layers. The polarization direction in two ferromagnetic layers can be either parallel or antiparallel, which generates HRS and LRS in the junction owing to tunnel magnetoresistive effect, as demonstrated in Figure 1.6(g). STT-MRAM and SOT-MRAM are improved versions of MRAM, as they show better scalability and lower power consumption.

FeRAM is a strong and promising candidate for future NVM devices. As illustrated in Figure 1.6(d), a ferroelectric material is sandwiched between two electrodes, forming the MFM capacitor structure. Figure 1.6(h) reveals that the ferroelectric polarization can be reversed by electric field application, yielding two stable P_r states in the capacitor. Commonly, perovskite-based $Pb(Zr,Ti)O_3$ (PZT) is used as the ferroelectric material, which features nice endurance performance over 10^{14} cycles, high switching speed, and high energy efficiency. HfO_2 -based ferroelectrics are hot topics in the field since they could offer greater scalability, better PRG/ERS latency, and even lower power consumption [17]. It is noteworthy that the emerging NVM counterparts of FeRAM are FeFET and FTJ, which will be introduced in section 1.4.

TABLE 1.1
BENCHMARK OF EMERGING NVM TECHNOLOGY [11]

Technology	NOR flash	NAND flash	RRAM	PCM	STT-MRAM	FeRAM	FeFET	SOT-MRAM	Li-ion
On/off ratio	10^4	10^4	10 – 10^2	10^2 – 10^4	1.5–2	10^2 – 10^3	5–50	1.5–2	40 – 10^3
Multilevel operation	2 bit	4 bit	2 bit	2 bit	1 bit	1 bit	5 bit	1 bit	10 bit
Write voltage (V)	<10	10	<3	<3	<1.5	<3	<5	<1.5	<1
Write time	1–10 μ s	0.1–1 ms	<10 ns	~50 ns	<10 ns	~30 ns	~10 ns	<10 ns	<10 ns
Read time	~50 ns	~10 μ s	<10 ns	<10 ns	<10 ns	<10 ns	~10 ns	<10 ns	<10 ns
Stand-by power	Low	Low	Low	Low	Low	Low	Low	Low	Low
Write energy [J/bit]	~100 pJ	~10 fJ	0.1–1 pJ	10 pJ	~100 fJ	~100 fJ	<1 fJ	<100 fJ	~100 fJ
Linearity	Low	Low	Low	Low	None	None	Low	None	High
Drift	No	No	Weak	Yes	No	No	No	No	No
Integration density	High	Very high	High	High	High	Low	High	High	Low
Retention	Long	Long	Medium	Long	Medium	Long	Long	Medium	...
Endurance	10^5	10^4	10^5 – 10^8	10^6 – 10^9	10^{15}	10^{10}	> 10^5	> 10^{15}	> 10^5
Suitability for DNN training	No	No	No	No	No	No	Moderate	No	Yes
Suitability for DNN inference	Yes	Yes	Moderate	Yes	No	No	Yes	No	Yes
Suitability for SNN applications	Yes	No	Yes	Yes	Moderate	Yes	Yes	Moderate	Moderate

Table 1.1 presents the benchmark of various emerging NVM technology [11].

1.3. Ferroelectric Materials

In Figure 1.3, it is shown that various emerging NVM technologies are suitable for SCM. Interestingly, ferroelectric-related devices, e.g., FeRAM, FeFET take several places among all. This fact implies that ferroelectric materials possess great potential for realizing NVM technology because of their charge storage nature [18]. In fact, numerous research has been conducted to better understand the material property and the mechanism of polarization reversal. Therefore, it is especially crucial to take a look into the basics and development of ferroelectric materials before integrating them into advanced memory technology.

1.3.1. History and Development of Ferroelectric Materials

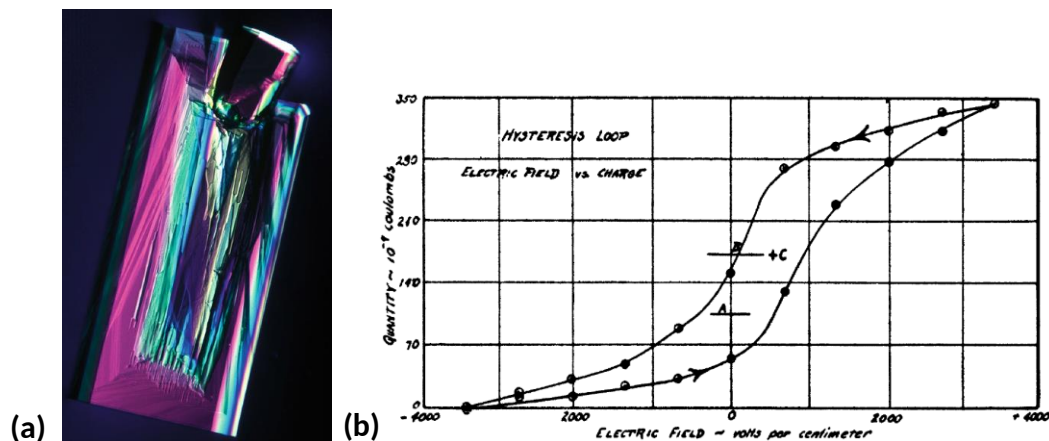


Figure 1.7: (a) Image of a Rochelle salt which is the first ferroelectric material to be discovered [19]. Different domains are visible under polarized light. (b) The first observation of ferroelectricity in Rochelle salt in 1921 [20].

History of ferroelectrics can be traced back to 1921 when Joseph Valasek discovered remanent polarization and hysteretic switching behavior in potassium sodium tartrate tetrahydrate, which is also named as Rochelle salt [20]. Since then, the interests for ferroelectric research have extended to other materials such as potassium dihydrogen phosphate and BaTiO₃ (BTO) [21], [22]. In 1952, Shirane *et al.* published several papers about PZT, the most commonly used ferroelectric material now, which open the gate

for intensive research on ferroelectrics [23], [24]. Details of perovskite ferroelectrics will be discussed in section 1.3.4. Despite the concept of FeFET had been proposed in 1957 [25], the commercialization of ferroelectric memory did not occur until 1990s [26], owing to non-ideal factors such as short retention time and leakage [27]. Thankfully, with the efforts dedicated by scientists and engineers for decades, the current society enjoys the conveniences brought by perovskite-based FeRAM technology [28]. For example, Sony Corp. developed the FeliCa technology using the embedded FeRAM technology for RFID applications. Other than memory technology, ferroelectric materials can also be utilized in various fields, e.g., energy harvesting and ultrasonic [29].

Recently, the discovery of ferroelectricity in HfO₂-based and III-N materials has encouraged more and more researches about ferroelectric memory, as plotted in Figure 1.8 [30]. In 2011, Böschke *et al.* demonstrated the ferroelectric properties by doping Si into HfO₂ crystal [31]. Besides, Fichtner *et al.* experimentally presented ferroelectricity in Sc-doped wurtzite AlN in 2019 [32]. These astonishing discoveries have paved the way for the investigation for novel ferroelectrics [33], [34]. Details of fluorite and wurtzite ferroelectrics will be discussed in section 1.3.5 and chapter 2, respectively.

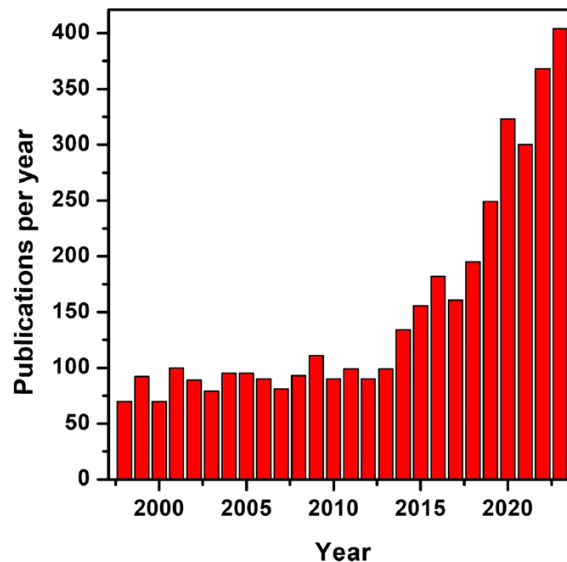


Figure 1.8: Publications related to ferroelectric memories over the years [30].

1.3.2. The Physical Origin of Ferroelectricity

In general, the origin of ferroelectricity is the net dipole moment inside the material.

Simply speaking, in a molecule, dipoles could exist if positive and negative charges are separated due to different electronegativity among various atoms. Therefore, the quantity of dipole moment can be described by the multiplication of charge q and separated distance d . Plus, the direction of dipole moment is defined as negative charge pointing toward positive charge. Considering the simplest case, Figure 1.9 displays a diagram for a set of separated point charges, where dipole moment μ can be calculated as the following equation shows.

$$\mu = q \cdot d$$

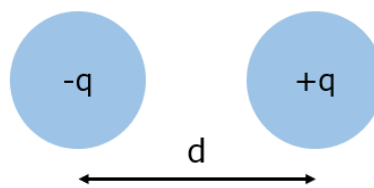


Figure 1.9: Separated point charges q with a distance d .

As materials are composed of dozens of molecules, dipole moment can be summed or compensated to zero, according to the vector of dipoles. Accumulation of dipoles at a certain volume gives the electric polarization P , as described in the following equation, where N is the total number of dipoles per unit volume.

$$P = N \cdot \mu$$

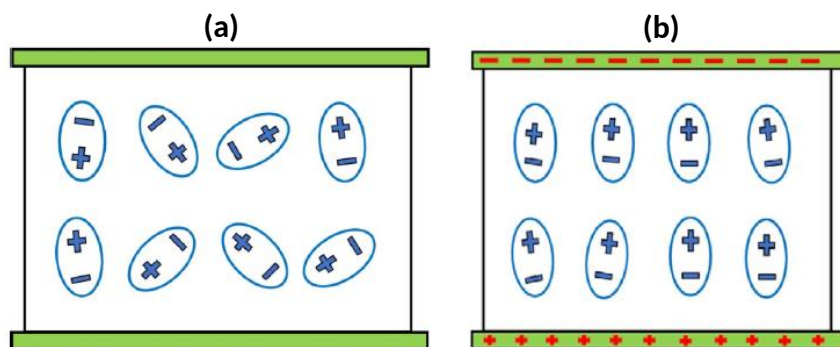


Figure 1.10: (a) When no external bias is applied, dipoles inside the dielectric are randomly distributed. (b) When external bias exists, dipoles can be induced and aligned according to the direction of electric field [35].

It is easy to observe the presence of dipoles in dielectric materials since they are typically insulating. Let us consider a simple capacitor with a dielectric material

sandwiched between electrodes. If there is no external voltage bias applied to the capacitor, dipoles tend to randomly distribute inside the dielectric layer, as Figure 1.10(a) shows [35]. On the other hand, when an external voltage bias is applied, polarization is induced and the dipoles align parallelly to the direction of the E, as depicted in Figure 1.10(b) [35]. In other words, polarization can be understood as the total charge induced per unit volume inside the dielectric under E. In some materials, net polarization could exist and pointing toward a specific direction without any external field, and it is named as spontaneous polarization. Once the direction of spontaneous polarization of a dielectric can be switched by external field, the dielectric is perceived as a ferroelectric material. Note that P_r refers to remanent polarization after ferroelectric switching, and E_c represents the coercive field required for polarization inversion.

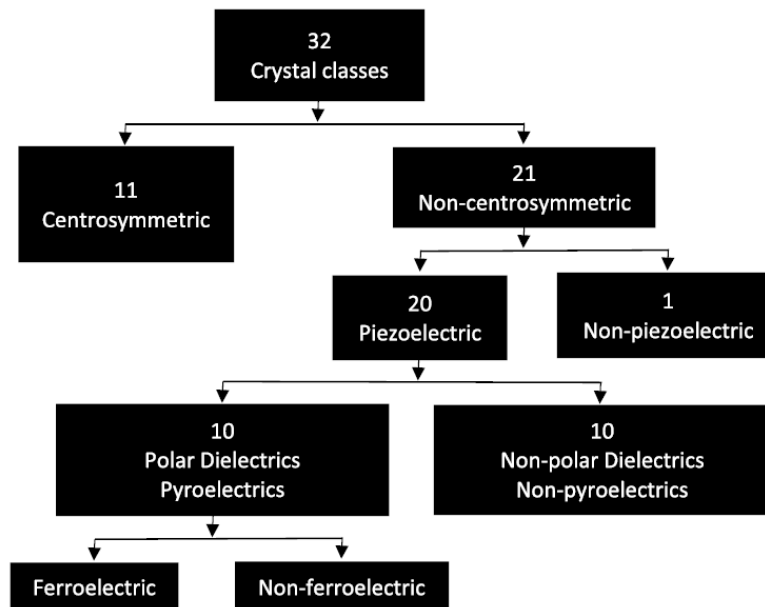


Figure 1.11: Classification of crystalline dielectric materials [35].

In fact, as Figure 1.11 displays, all crystalline materials are divided into 32 crystal classes and can be categorized as centrosymmetric and non-centrosymmetric materials. For centrosymmetric materials, the net dipole moment is naturally compensated to zero due to the crystal structure. Among all 21 non-centrosymmetric materials classes, since net dipole moment could be non-zero, 20 of them can exhibit piezoelectric effect. Furthermore, only 10 classes with piezoelectric characteristics can possess pyroelectric effect, and ferroelectric materials lay under these classes. Note

that the schematic pie chart in Figure 1.12 illustrates the effect of piezoelectric, pyroelectric, and ferroelectric [36]. For piezoelectric materials, the polarization quantity could be altered by external mechanical force, either compressive or tensile stress. The polarization change can be monitored by the induced electrical signals from the dielectric. For pyroelectric materials, temperature variation serves as the stimulating force to change the polarization quantity. Naturally, ferroelectric materials could exhibit piezoelectric and pyroelectric effects, which makes them fascinating for research and suitable for various practical applications.

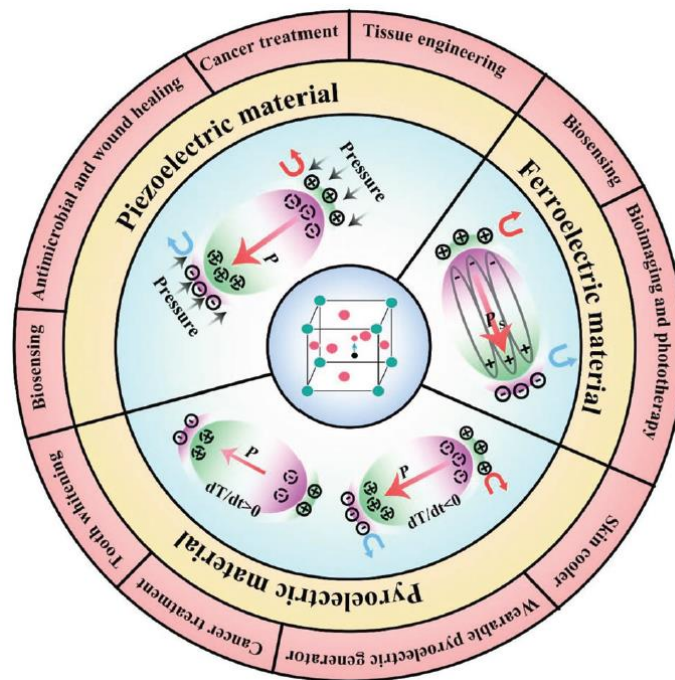


Figure 1.12: Diagram of piezoelectric, pyroelectric and ferroelectric effects [36].

1.3.3. Phase Transition in Ferroelectric Materials

In previous sections, it is stated that polarization state of ferroelectric materials can be switched by external field. Figure 1.13 shows the energy landscape of normal dielectric and ferroelectric materials [37]. For dielectrics without spontaneous polarization, since the lowest energy is favorable, the polarization state should be zero when no voltage is applied. To induce polarization in the dielectric, application of E is required. However, removing E sets the polarization back to zero. As for dielectrics with spontaneous polarization, the polarization state can be non-zero at steady-state. If the applied E overcomes the energy barrier between two states, polarization reversal is

realized as revealed in Figure 1.14 [38]. Therefore, ferroelectric materials generally possess energy barriers that are low enough to overcome to achieve polarization reversal. In addition, during transient switching between two steady-states, negative-capacitance effect could happen. Nevertheless, this is out of the scope of this research.

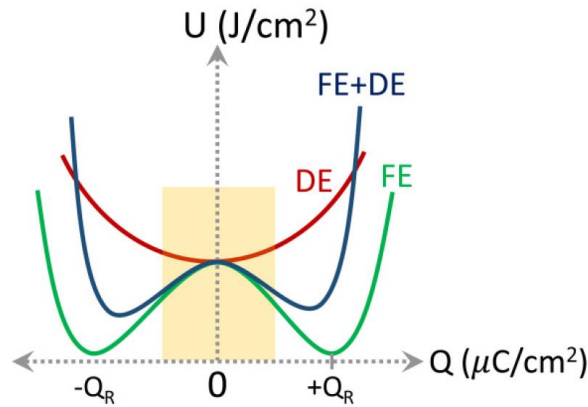


Figure 1.13: Energy landscape with respect to polarization of ferroelectric, dielectric, and stacked materials [37].

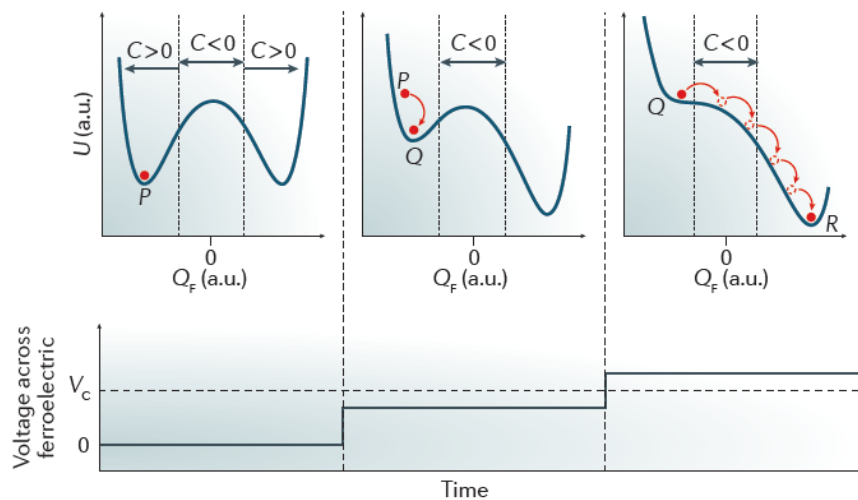


Figure 1.14: The dependence of energy profile during ferroelectric switching from one polarized state to another [38].

In thermodynamics, potential barrier could be temperature-dependent. Consequently, it is important to discuss the influence of temperature for ferroelectric switching. Figure 1.15 demonstrates the change of energy profile and the stable/metastable states at different temperature conditions [39]. At temperature below T_0 , two stable polarized states are energetically stable and switching is

manipulated by external E . When $T_0 < T < T_c$, a metastable non-polarized state could form, and the distance between two stable polarized states is shortened. When $T_c < T < T_1$, the stable state becomes non-polarized, and polarized states are metastable. When $T_1 < T < T_2$, the polarized states are still achievable by high E application. When $T_2 < T$, the material completely loses the ability to switch.

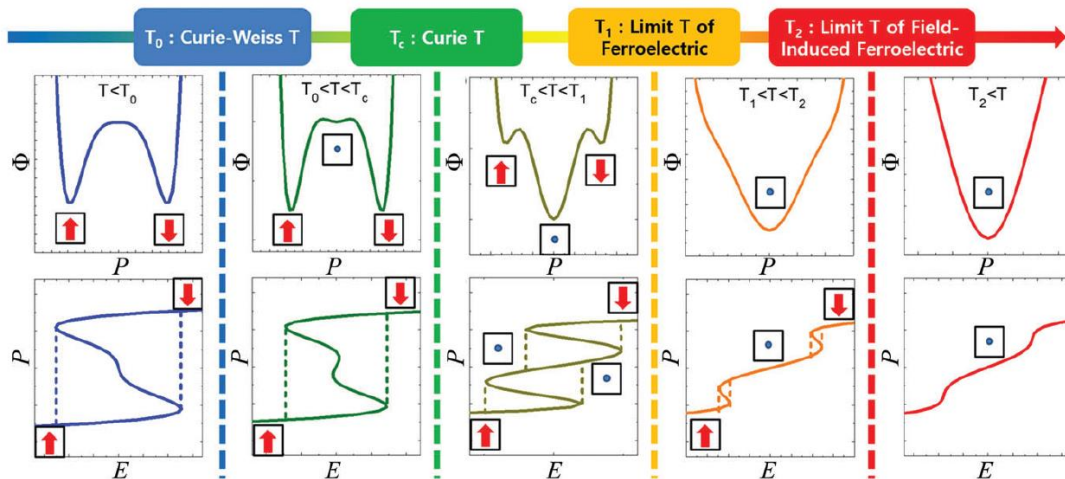


Figure 1.15: Free energy landscape and deduced P-E S curves of ferroelectrics at different temperatures [39].

1.3.4. Perovskite-based Ferroelectrics

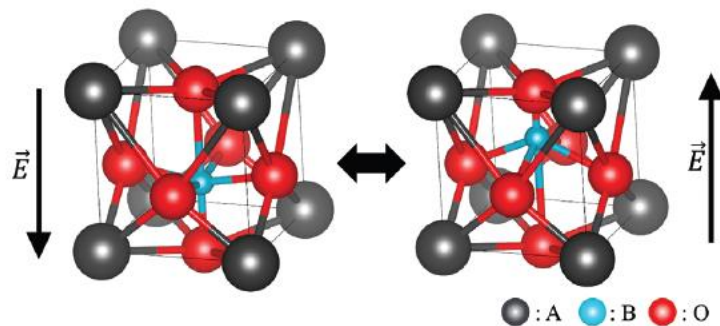


Figure 1.16: Two polarization states of perovskite-based ferroelectrics [40].

The perovskite-based materials have been dominating the ferroelectric research for a long time. The most commonly seen are PZT, BTO, BiFeO₃ (BFO), SrBi₂Ta₂O₉ (SBT), KNbO₃, etc. These materials typically feature perovskite ABO₃ structure, as illustrated in Figure 1.16 [40]. With atom A occupying the corner sites and O atoms residing at the face-centered sites, the polarization reversal is determined by the movement of

the center atom B. Early research has resolved the fatigue issue in PZT by utilizing IrO₂ as electrodes [41]. However, the incompatibility to CMOS process along with restricted scalability of PZT is the limiting factor for advanced memory technology [42].

1.3.5. Fluorite-based Ferroelectrics

HfO₂, a crucial dielectric material since 45 nm CMOS HKMG technology [43], is discovered to possess ferroelectricity by incorporating dopants such as Si, Zr, Y, Al, La, Gd, etc. [31], [33], [44], [45], [46], [47]. For bulk HfO₂, the stable phase after synthesis is typically monoclinic up to 2000K, which contains no ferroelectricity nor antiferroelectricity. Increasing the temperature beyond could transform the crystal structure to tetragonal or cubic phases. As these three phases are centrosymmetric, ferroelectricity is impossible to present. Fortunately, through specialized process and growth conditions, ferroelectric orthorhombic phase HfO₂ is achievable. Figure 1.17 discloses the crystal and corresponding ferroelectricity of HfO₂ at different phases [48].

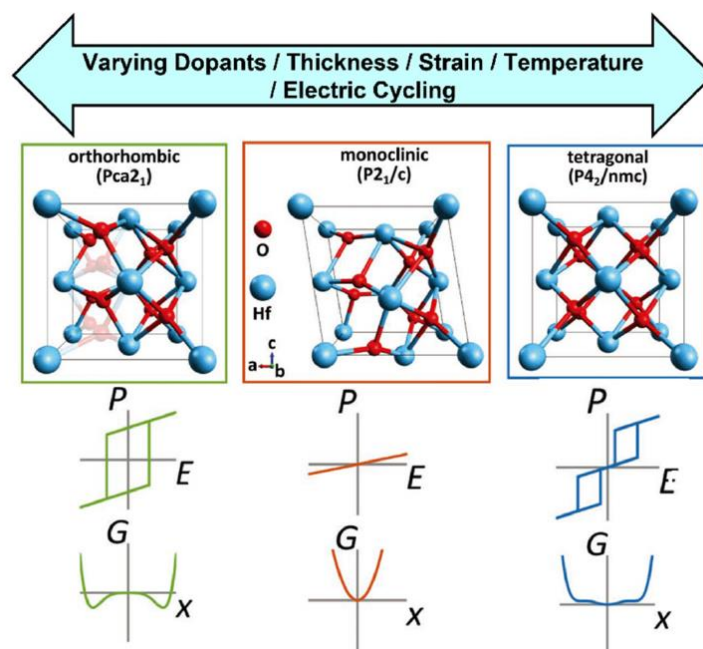


Figure 1.17: Crystal structure and corresponding ferroelectric responses [48].

By tuning the process parameters above, ferroelectric orthorhombic phase is achievable. Note that monoclinic and tetragonal phases demonstrate paraelectric and antiferroelectric properties, respectively.

The role of dopant is important as they help stabilize the formation of ferroelectric phase [49]. Müller *et al.* demonstrated the effect of Zr doping, which then

became the most popular dopant for HfO_2 [33]. Figure 1.18(a) and (b) demonstrate the effectiveness of Y and Al doping with different concentrations, respectively [44], [45]. Besides, the mechanical stress provided from capping electrode is also decisive for the ferroelectricity since it can help suppress non-ferroelectric phase [31], [44]. Figure 1.19(a) and (b) compares the ferroelectricity of films that underwent PDA and PMA, respectively [50]. It is apparent that the latter shows better results, indicating the effectiveness of capping electrode. Therefore, a PMA process is generally more feasible than PDA. Moreover, in Figure 1.19(c) and Figure 1.20, HZO films usually present inferior P_r at larger thickness due to insufficient ferroelectric grains [50], [51].

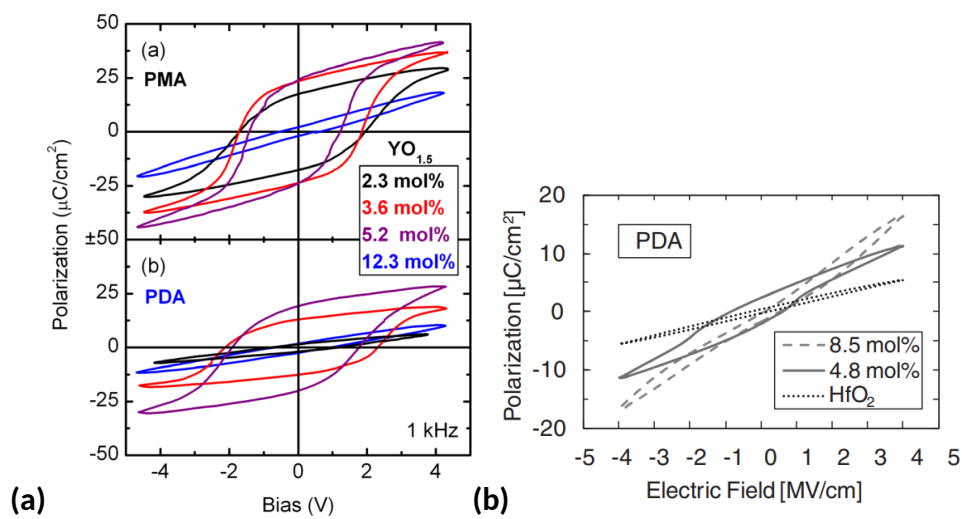


Figure 1.18: (a) HYO and (b) HAO films with different doping concentrations [44], [45].

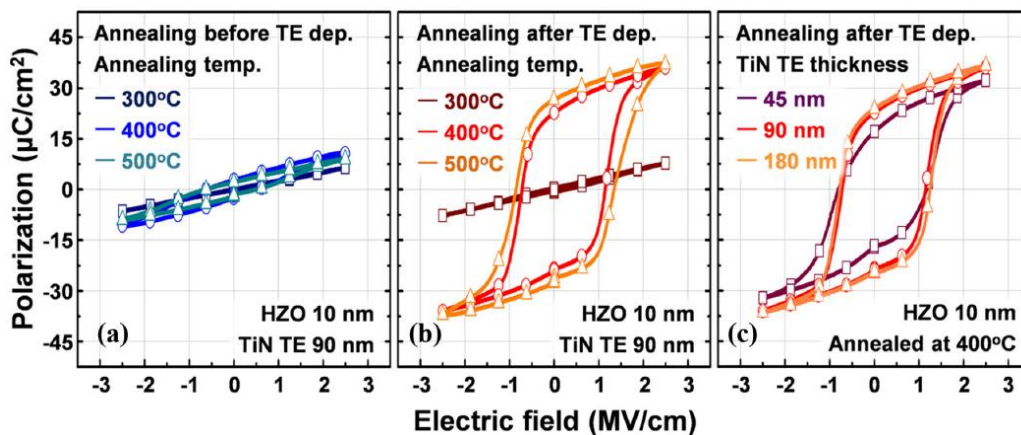


Figure 1.19: P-E hysteresis of HZO films after (a) PDA and (b) PMA process. (c) Comparison of different film thickness [50].

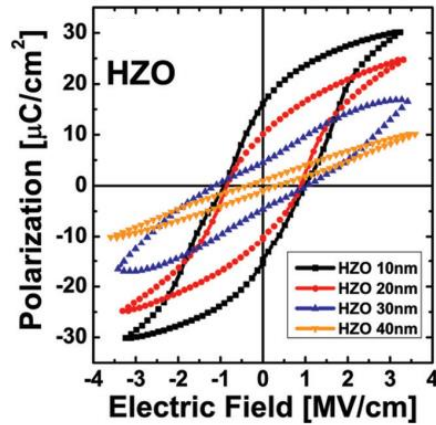


Figure 1.20: P-E hysteresis of HZO films with various thickness [51].

As briefly mentioned above, RTA process is required to obtain the ferroelectric orthorhombic phase in doped HfO_2 thin films. The phase transition during RTA is illustrated in Figure 1.21 [52]. At the heating stage, tetragonal phase begins to nucleate and completely crystallize the film. When cooling or quenching initiates, monoclinic and orthorhombic phases could start forming. However, monoclinic is naturally more stable than orthorhombic phase. Thankfully, with the assistance from electrode-induced stress, the amount of orthorhombic phase could be increased, generating better ferroelectricity in the film.

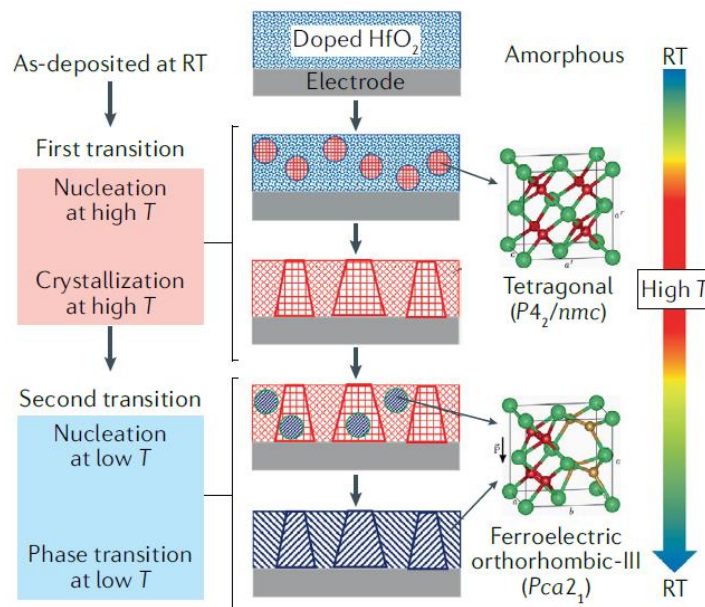


Figure 1.21: The formation of ferroelectric phase for doped HfO_2 during RTA process [52].

1.4. Ferroelectric Memories

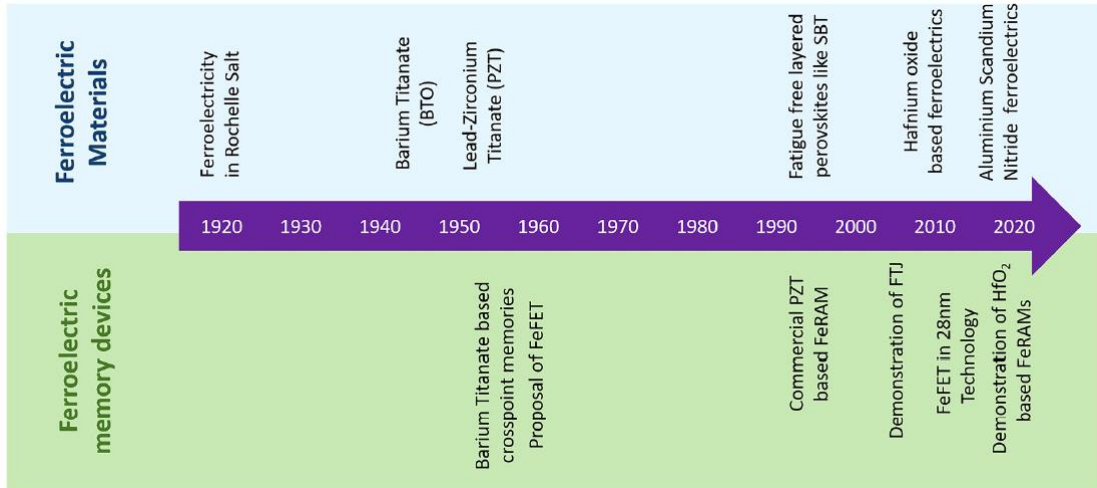


Figure 1.22: Development of ferroelectric materials and memory technology [53].

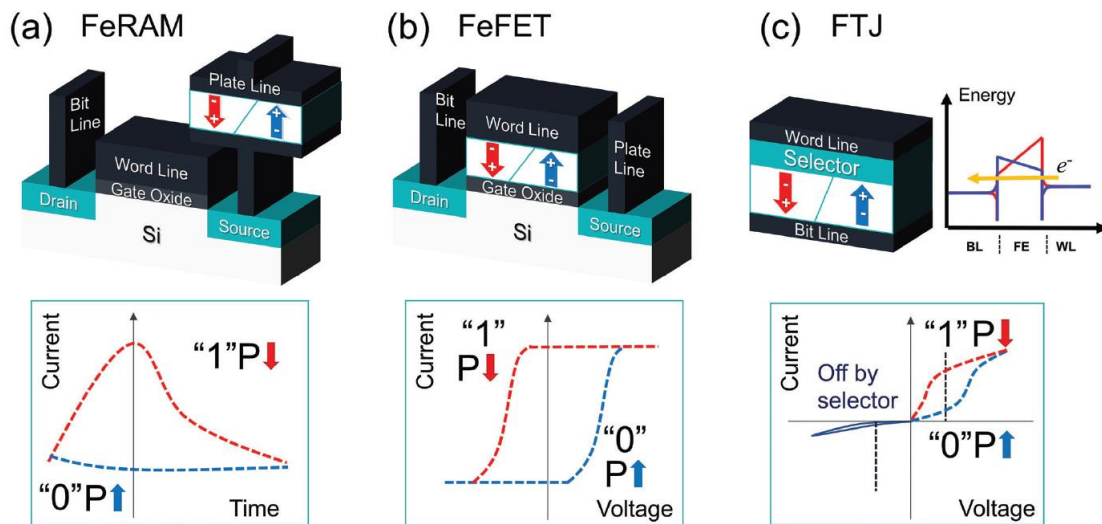


Figure 1.23: Schematics and operation principles of (a) FeRAM, (b) FeFET, and (c) FTJ [39].

As introduced previously, ferroelectric memories show great potential for emerging NVM technology. Figure 1.22 shows the timeline of the development of ferroelectric materials and memory technology [53]. For the past two decades, with new discoveries of novel ferroelectrics, the research on memory applications have been thriving. In this journey, FeRAM, FeFET, and FTJ are devices that have drawn massive

attention, and their structures are depicted in Figure 1.23 [39]. FeRAM and FeFET are three terminal devices that the operation is controlled by word, bit, and plate lines, whereas FTJ only features two terminals.

FeRAM features combinations of MFM capacitors and transistors. Data could be stored in the capacitors, whereas the transistors execute read/write operations. The advantages of FeRAM were described in section 1.2. Current researches mainly focus on 1T1C architecture since it provides the best scalability and simple operation [54]. One of the drawbacks of FeRAM is the destructive read-out which could be influential to power consumption and endurance performance [55]. Regarding the read operation, sense amplifier in the peripheral circuit detects the bit line voltage level which depends on “0” or “1” polarization states in the capacitor. According to IRDS roadmap for More Moore applications in 2023, current PZT-based FeRAMs utilize 65 nm CMOS technology with 1T1C cell structure and $20F^2$ ($0.22 \mu\text{m}^2$) of cell size [56]. The operation voltage is 1 V and the minimum required switching polarization is $18.1 \mu\text{C}/\text{cm}^2$. Additionally, the endurance and retention performance are excellent with the over 10^{14} - 10^{15} cycles and over 10 years, respectively [57].

FeFET is a promising device that directly integrates ferroelectric material as the gate dielectric in a FET. Electrical charges induced by the polarization can influence the I_D - V_G characteristics. Once V_{th} difference between forward and reverse sweeps is presented, memory window can be defined. Different from FeRAM, read operation of FeFET is non-destructive, and as HfO_2 -based ferroelectrics feature high downscaling capability, plenty of researches have been conducted [58]. Compared to FeRAM, FeFET could benefit from its 1T cell structure with $4F^2$ size [56]. Nevertheless, since high- κ materials generally have intrinsic defects and non-ideal interfaces to Si, Ge, or III-V channels [59], [60], [61], it is unavoidable to insert an additional dielectric interlayer [62], [63], as shown in Figure 1.23(b). Due to the degradation of ferroelectric/channel interface, HfO_2 -based FeFETs typically show 10^5 - 10^9 cycles of endurance [64]. Tan *et al.* proposed a HZO FeFET featuring record high endurance over 10^{10} cycles by improving the interface quality [65].

FTJ possess a natural advantage for crossbar-based design circuits owing to its two terminals. The structure of FTJ devices could be MFM, MFIM, or MFIS, as long as the tunneling electroresistance can be induced. Write operation is conducted by

applying E that is larger than E_c , switching the polarization state in the ferroelectric layer. Read operation can be done by an external E smaller than E_c , and the current level responses according to its HRS or LRS states which are depending on the polarization states. One issue of FTJ devices is that low read current requires amplification to obtain fast sensing. The endurance usually exhibits about 10^7 - 10^9 cycles [66], [67].

1.5. Chapter Overview

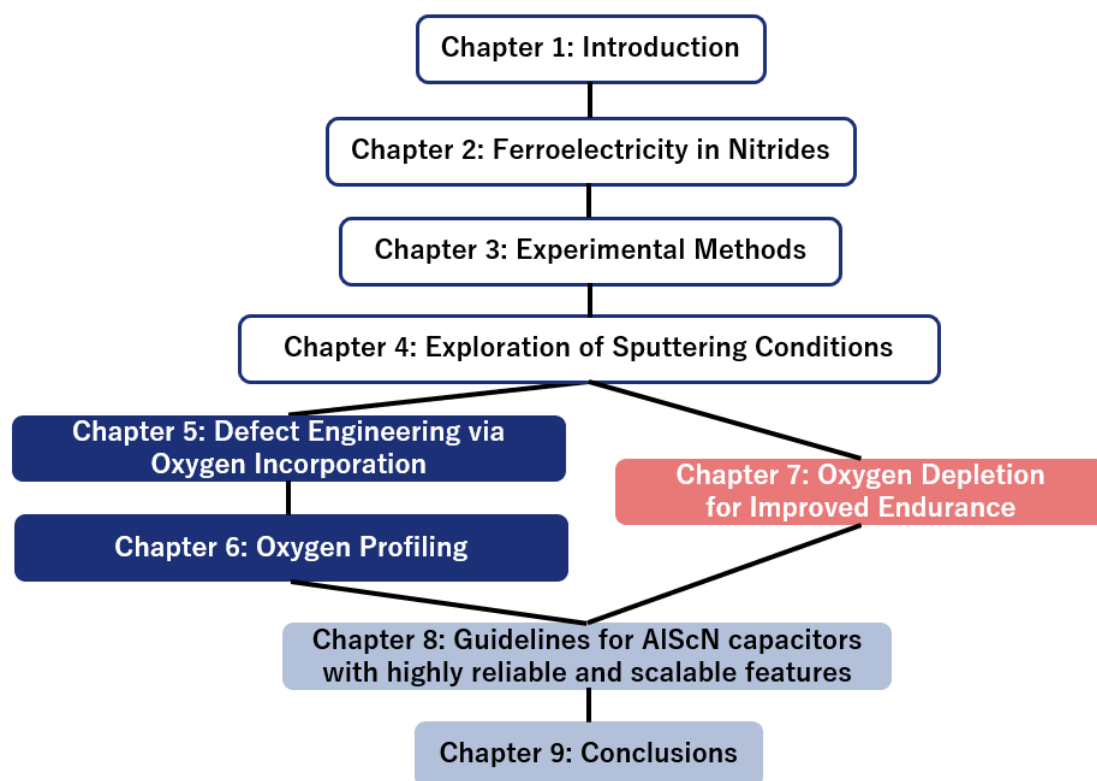


Figure 1.24: Schematic flow chart of content in chapters in this thesis.

In this thesis, the content is arranged as Figure 1.24 shows. Chapter 1 introduces and reviews the advanced technology for future memory applications. Ferroelectricity, ferroelectric materials and memories are discussed in detail. Chapter 2 specifically elucidates the ferroelectricity in novel III-N materials, as it is the key material of this work. The purpose of this research is emphasized at the end of chapter 2. After that, information regarding the fabrication process and the electrical characterizations of AlScN ferroelectric thin films are given in chapter 3. Then, chapter 4 describes the

exploration of deposition conditions to realize scalable and reliable AlScN films. Subsequently, chapter 5 demonstrates the influence of defect engineering in AlScN thin films by doping oxygen to tune the ferroelectricity. Additionally, chapter 6 covers the concept of oxygen profiling for multi-layered AlScN films. Chapter 7 shows the effectiveness of interface oxygen depletion by H₂ flux involved reactive sputtering for significant endurance improvement. Chapter 8 summarizes all the acquired results and proposed guidelines for reliable and scalable AlScN MFM capacitors. Finally, chapter 9 concludes the contribution of this research and provides future perspectives.

Chapter 2: Ferroelectricity in Nitride Materials

2.1. Theoretical and Experimental Demonstration of Ferroelectricity

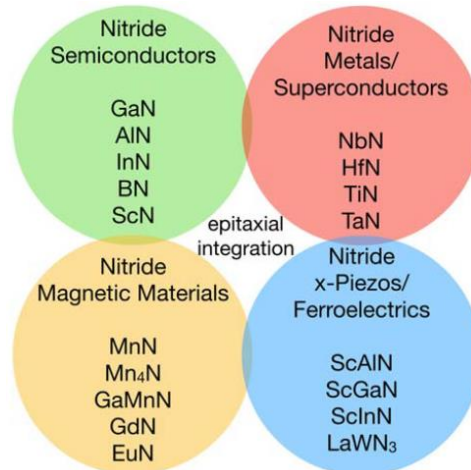


Figure 2.1: Nitride materials showing various properties for various applications [68].

Nitride materials have been demonstrating potential in various fields, as displayed in Figure 2.1 [68]. Conventional III-N materials such as AlN, GaN, and InN possess wurtzite crystal structure along with spontaneous polarization. Binary or ternary III-N materials also possess direct bandgaps, allowing themselves to be applied in various fields like blue light LED [69], [70], [71], DUV LED [72], photodetectors [73], lasers [74], etc. Moreover, 2DEG has been discovered in III-V-based heterostructures [75], leading to prosperity in HEMTs for high power and high frequency applications [76], [77], [78], [79], [80], [81], [82].

AlN has been receiving attention with regards to piezoelectric applications [83], [84]. Predictions of ferroelectricity were also proposed in the early 2010s [85], [86]. However, not until 2019, the ferroelectricity in III-N materials has been experimentally demonstrated [32]. The wurtzite-type ferroelectrics are capable of retaining high P_r and have garnered interest in the semiconductor society since then. For conventional III-N compounds, though spontaneous polarization exists in the forms of metal-polar or N-polar [87], switching event is difficult to realize due to high potential barrier between two polar states. Applying excessive E to the dielectric could lead to electrical breakdown before the polarization reversal. Fortunately, by including dopants such as

Sc, B, and Y atoms that reduces polarization switching barrier in binary AlN or GaN [88], [89], ferroelectricity can be achieved in AlScN, AIBN, AIYN, GaScN, and AlScGaN [32], [34], [90], [91], [92]. Figure 2.2 unveiled the energy landscape of pure AlN and Sc-doped AlN [53]. Obviously, N-atom displacement along the *c*-axis, corresponding to metal-polar or N-polar in wurtzite crystals, enables polarization reversal [93], [94], [95]. Therefore, the polarization magnitude and switching barrier are highly related to the structural factors in AlN. Basically, with Sc atoms joining the wurtzite lattice, the basal plane receives tensile stress, which decreases E_c and realizes the polarization switching. The details about wurtzite structure will be discussed in section 2.2.1.

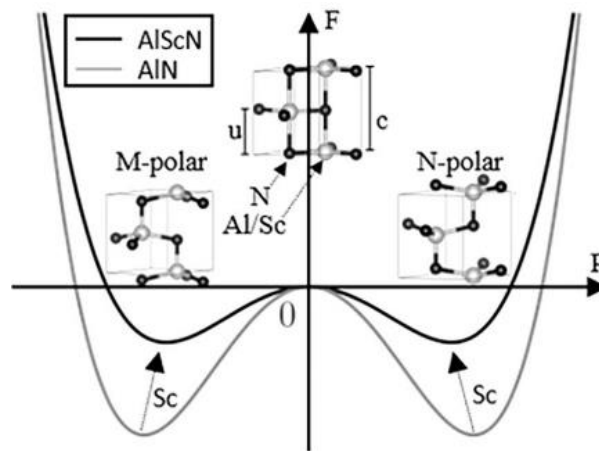


Figure 2.2: Energy landscape of pure AlN and AlScN [53].

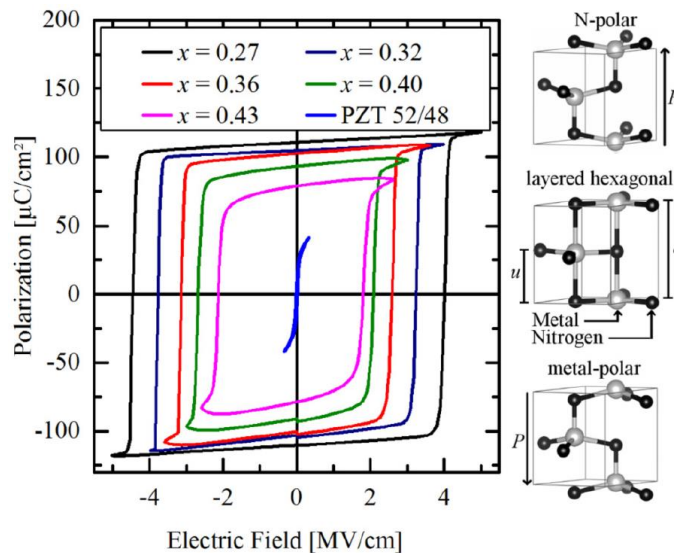


Figure 2.3: The first experimental demonstration of P-E hysteresis in wurtzite materials. P_r and E_c are tunable by changing the Sc content in $Al_{1-x}Sc_xN$ [32].

Figure 2.3 reveals the ferroelectric P-E hysteresis in $\text{Al}_{1-x}\text{Sc}_x\text{N}$ films [32]. The box-like ferroelectricity draws massive attention, and P_r and E_c are shown to be tunable by changing the Sc content. With more Sc atoms involved, the polarization magnitude and the potential barrier decreases. Dielectric and ferroelectric properties will be elucidated in section 2.3.

Table 2.1 compares the properties of ferroelectrics, including PZT, SBT, BFO, HZO, and AlScN [53]. It is shown AlScN demonstrates extraordinarily high P_r and E_c values. Low ϵ is another advantage for mitigating the RC delay in electrical circuits. High T_c implies good retention and thermal stability in critical environments [96]. In addition, AlScN are free of heavy metal atoms like Pb and the process temperature are lower than 400°C , or even at RT [97], [98], which benefits itself for CMOS BEOL integration.

TABLE 2.1
COMPARISON OF FERROELECTRIC MATERIALS [53]

Ferroelectrics	$\text{Pb}(\text{Zr,Ti})\text{O}_3$ ^{99,100}	$\text{SrBi}_2\text{Ta}_2\text{O}_9$ ²⁵	BiFeO_3 ^{46,47}	Doped HfO_2 $\text{Hf}_x\text{Zr}_{1-x}\text{O}_2$ ^{101,102}	$\text{Al}_x\text{Sc}_{1-x}\text{N}$ ⁸
P_r ($\mu\text{C}/\text{cm}^2$)	10–40	5–10	90–95 (along [111])	10–40	80–110
E_c (kV/cm)	50–70	30–50	100–1500	800–2000	2000–5000
ϵ_0	~400	~200	~50	~30	~25
Endurance (cycles)	$>1 \times 10^{15}$ on oxide electrode	Good on Pt electrode	Good on oxide electrode	$>1 \times 10^{11}$ on TiN	$>1 \times 10^{5a}$
Min. physical thickness (nm)	50			<5	<50 ^a
Crystallization temperature ($^\circ\text{C}$)	Low	High	Low	400–800	300–400
Curie temperature ($^\circ\text{C}$)	~400	~400	~700	0–500	>600

^aEarly results, improvements expected.

However, two primary challenges in the development of $\text{Al}_{1-x}\text{Sc}_x\text{N}$ ferroelectrics must be addressed: (1) the large E_c approaching the E_{BD} , compromises endurance performance [53]; and (2) high leakage through the film impairs the ferroelectric properties [99]. Thickness scaling for the sub-50-nm region is also constrained because of further increases in E_c and leakage [100], [101]. Consequently, minimizing E_c and suppressing leakage in $\text{Al}_{1-x}\text{Sc}_x\text{N}$ films are crucial for enhancing their compatibility with future nanoelectronics.

2.2. Crystal Growth and Deposition Methods

This section discusses the crystal growth and deposition methods of AlScN thin films. Section 2.2.1. will show the crystal structure of AlScN and its relationship with Sc

concentration. The growth of $\text{Al}_{1-x}\text{Sc}_x\text{N}$ ferroelectric films has mainly been accomplished by sputtering and MBE [32], [102]. Even MOCVD grown AlScN showed ferroelectricity recently [103]. Section 2.2.2. will focus on sputtered AlScN films, and epitaxial growth will be described in section 2.2.3.

2.2.1. Wurtzite Crystal Structure

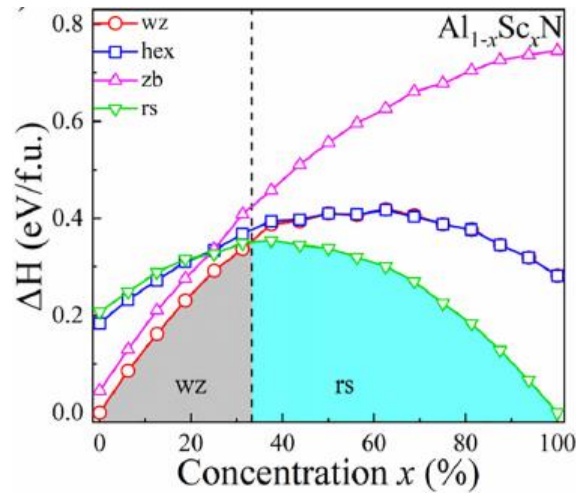


Figure 2.4: Wurtzite crystal is energetically stable only if the Sc content is lower than 32% in $\text{Al}_{1-x}\text{Sc}_x\text{N}$ [104].

Before introducing the wurtzite crystal structure for ferroelectric AlScN, the influence of Sc doping to the crystal structures should be understood. Figure 2.4 reveals that at Sc concentration below 32%, the wurtzite structure is stable in $\text{Al}_{1-x}\text{Sc}_x\text{N}$ [104]. However, when more Sc atoms are incorporated, the crystal structure change to rocksalt is more favorable, which could lose the ferroelectricity [105]. With different calculation methods, the border between wurtzite and rocksalt generally falls into the region of 30-50% [104], [106], [107].

Figure 2.5 depicts the wurtzite crystal structure of AlScN [108]. Wurtzite is a structure based on hexagonal in which the lattice constants a and c are used. Note that spontaneous polarization does not exist in layered hexagonal structures, as the dipole moments are compensated. Plus, u is another parameter to show the deviation status of wurtzite comparing to layered hexagonal. The calculation of u is shown in the following equation.

$$u = \frac{a^2}{3c^2} + \frac{1}{4}$$

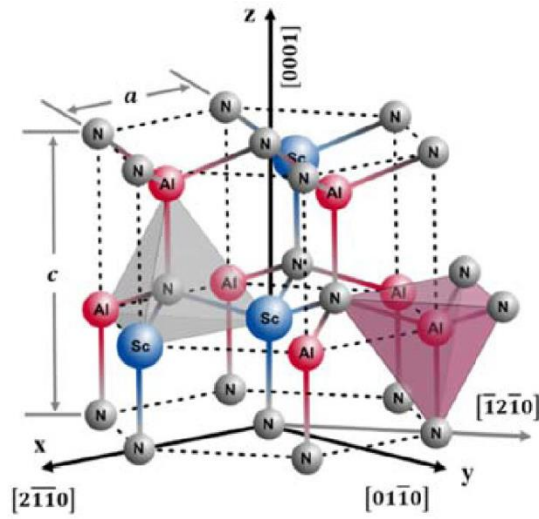


Figure 2.5: Wurtzite crystal structure of AlScN [108]. Tetrahedron structures are found among adjacent metal and N atoms.

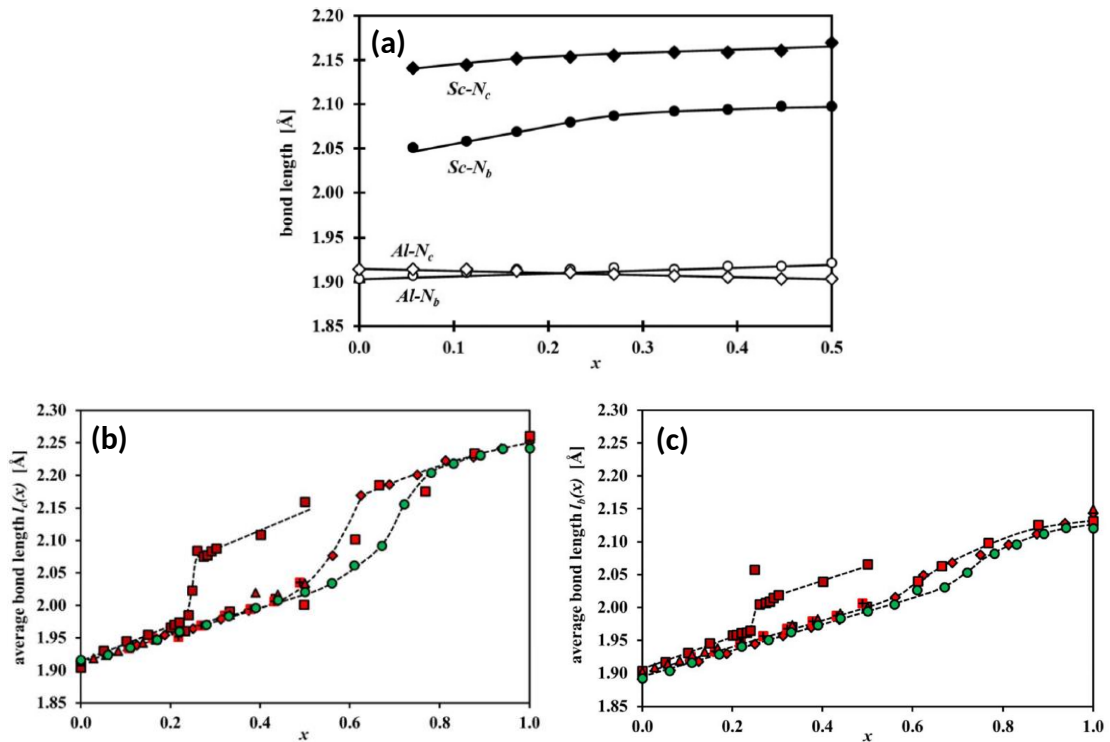


Figure 2.6: (a) Average calculated bond length of first neighbor Al/Sc atoms and N atoms that are orientated either in the basal plane or along c-axis [109]. Average metal-N bond length (b) along c-axis and (c) in the basal plane for AlScN with respect to Sc concentration [108].

To understand the origin of polarization reversal in AlScN, it is worth investigating the wurtzite crystal structure change with Sc doping. Figure 2.6(a) delineates the calculated bond length of first neighbor Al-N and Sc-N bonds along the c -axis and in the basal plane for AlScN [109]. Apparently, Sc-N bonds have larger length than Al-N bonds. When more Sc atoms are incorporated into the wurtzite lattice, average metal-N bond length increases accordingly, as Figure 2.6(b) and (c) show [108]. Since tetrahedrons are formed by metal and N atoms, as depicted in Figure 2.5, it is also necessary to consider the bond angles. In other words, the variation of geometric dimensions in tetrahedrons is the key factor to the ferroelectricity of AlScN. Figure 2.7 illustrates the relationship between geometric dimensions of tetrahedrons and Sc doping content [108]. When Sc concentration increases, the basal plane is relaxed by tensile strain and the distance of N atom to the basal plane ($h_N(x)$) declines. This indicates that the translation of N atoms through tetrahedron basal planes becomes easier with external field application and thereby achieving polarization inversion.

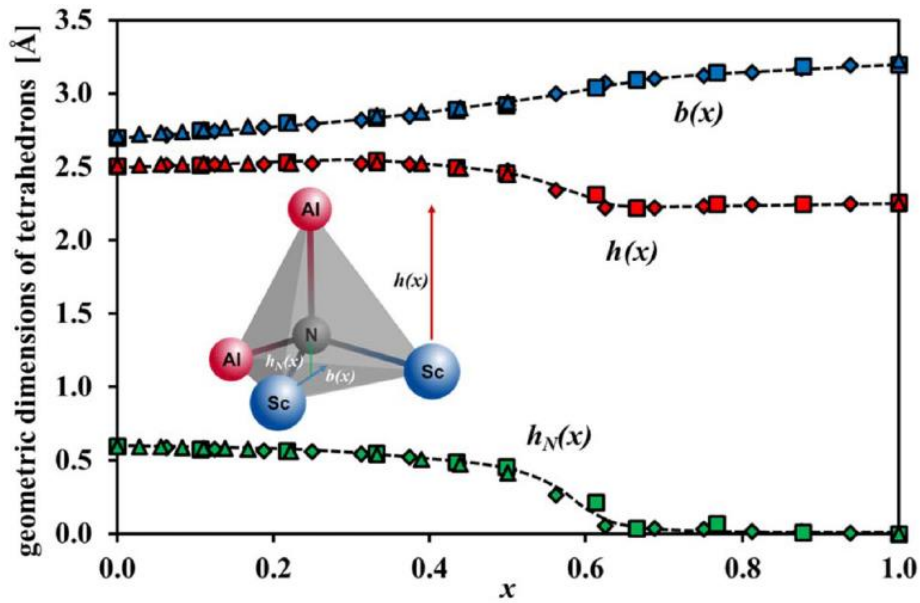


Figure 2.7: Calculated geometric dimensions of tetrahedrons in wurtzite crystals of AlScN [108]. $h(x)$ represents the distance between the apex to the basal plane. $h_N(x)$ is the distance of the N atom to the basal plane. $b(x)$ is the bisector of the basal plane.

Naturally, the change of Sc content would vary the lattice constants and parameters in wurtzite crystals. Figure 2.8(a), (b), and (c) delineate the relationship of

Sc concentration with lattice constants, c/a , and u parameters, respectively [110]. When Sc is included below 40%, lattice constant c shows a very slightly declining trend whereas lattice constant a gains linearly. This results in a linear decline of c/a ratio, which reduces the energy barrier for ferroelectric switching. Moreover, a gradual increasing trend is spotted in the dependence of u at low Sc content region. In addition, due to the increasing amount of Sc-N bonds in the crystal, the average bond ionicity is increasing monotonically with Sc content, as depicted in Figure 2.8(d) [110].

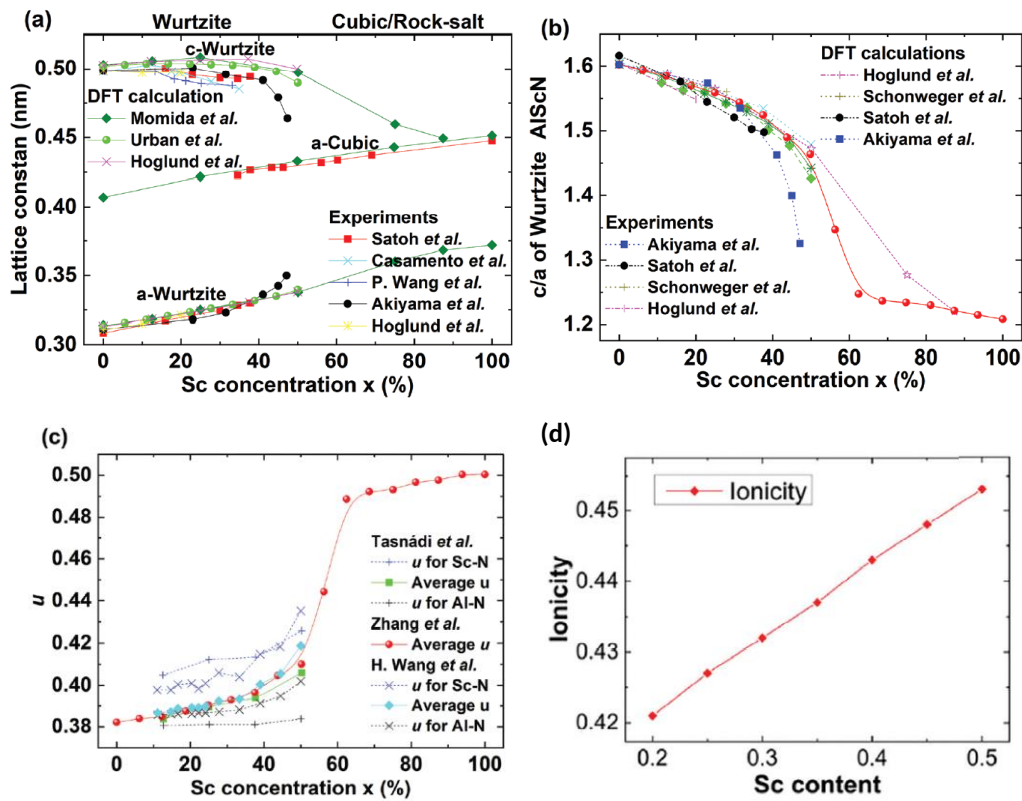


Figure 2.8: Dependence of Sc content with (a) lattice constants a and c , (b) c/a , and (c) u parameter [110]. (d) The average bond ionicity in $Al_{1-x}Sc_xN$ [110].

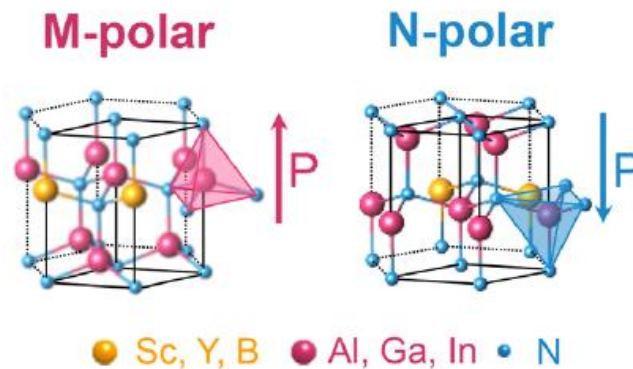


Figure 2.9: Two polarization states in ferroelectric wurtzite materials [111].

As briefly mentioned in the previous section 2.1., wurtzite crystals have two polar states, metal-polar and N-polar which are illustrated in Figure 2.9 [111]. The confusion of polarization direction in wurtzite crystals was clarified by literature [112]. In this research, metal-polar is assigned with upward polarization direction, and N-polar is assigned to negative.

2.2.2. Physical Vapor Deposition: Sputtering

Sputtering is one of the most common ways to deposit AlN films [113], [114]. As the deposition techniques of AlN have been researched for a long time, wide choices are available for AlScN films. Including pure N₂ or mixed Ar/N₂ gas ambient, DC or RF power supply, single or dual targets, etc. Akiyama *et al.* presented the influence of Sc content on crystallinity for piezoelectric applications [115], [116]. As displayed in Figure 2.10(a), the XRD peak for AlScN 002 phase is the most prominent at Sc content of 40%. Note that the peak positions are shifted due to lattice parameter changes. The c-axis crystallinity is also enhanced at 40% of Sc, as Figure 2.10(b) shows.

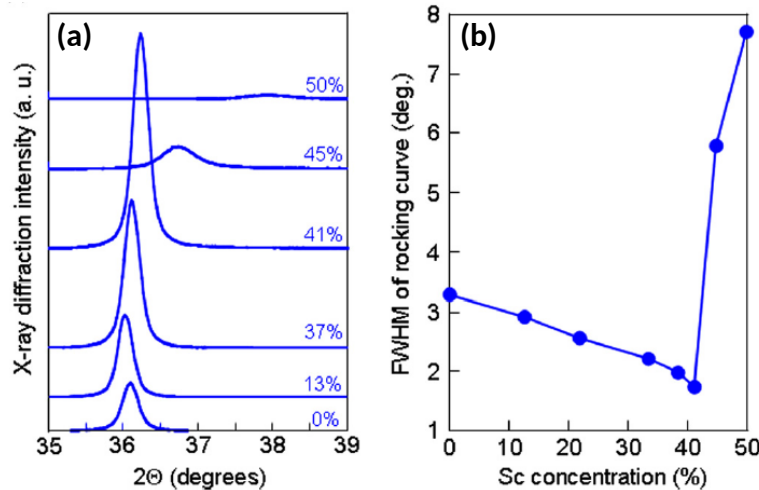


Figure 2.10: (a) XRD profile and (b) FWHM of sputtered Al_{1-x}Sc_xN films [116].

Yasuoka *et al.* investigated the impact of deposition temperature for ferroelectric AlScN films [98]. In Figure 2.11(a), films deposited at temperatures above 300°C show distinct 002 peaks, indicating the presence of c-axis oriented grains. Results of PUND measurement are plotted in Figure 2.11(b) which shows that 400°C is the most suitable

deposition temperature for sharp P_r - E slope and highest P_r values. Deposition below 200°C leads to low P_r and unsaturated performance. Moreover, E_c tends to exhibit an increasing trend when temperature increases, as shown in Figure 2.11(c). It can be concluded that 400°C is the most optimal temperature for the best ferroelectricity in AlScN. Additionally, another work from Yasuoka *et al.* demonstrated that both pure N_2 or mixed Ar/N_2 gas ambient can be used during sputter deposition, as depicted in Figure 2.12(a) and (b) [117].

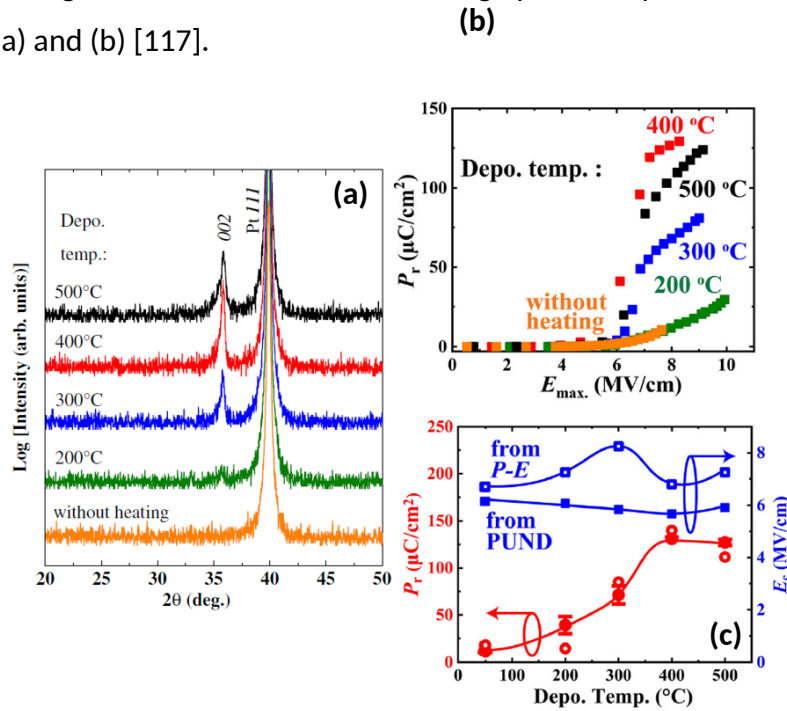


Figure 2.11: (a) XRD profiles of the sputtered films deposited at different temperatures. (b) P_r - E relationship obtained from PUND measurement. (c) Comparison of ferroelectricity [98].

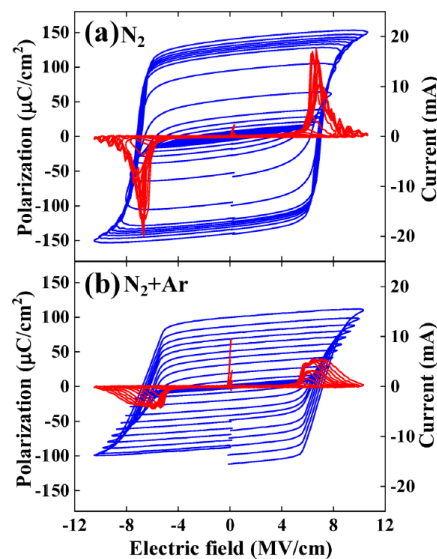


Figure 2.12: P-E hysteresis of sputtered AlScN film using (a) only N_2 gas and (b)

mixed Ar/N₂ gases during deposition [117].

Although low-temperature deposition below 400°C could be achieved by sputtering, contaminants such as oxygen coming from the vacuum chamber were found inside the prepared AlN film [118], [119]. Both sputtered AlN and ScN films have reported resistivity degradation on account of oxygen contamination [118], [120]. The source of oxygen is found to be the residual O₂ and H₂O inside the chamber and the oxidized targets [121], [122]. Since Ti, Al, and Sc atoms possess strong affinity toward oxygen than nitrogen [123], residual oxygen deteriorates the purity of nitride films, posing threats to mechanical, electrical, optical properties. In addition, as listed in Table A1.1, the dissociation energy of cation-O bonds is typically higher than cation-N bonds. Long-time pumping to high vacuum level could help to decrease the residual O₂, but residual H₂O attached to the chamber wall is hardly removed. This can be solved by chamber baking, which vaporizes the water, making it easy to be evacuated by the pumping system. High temperature or high power plasma deposition offers another way to decrease the incorporated oxygen in the sputtered films [124], [125].

2.2.3. Epitaxial Growth: MBE and MOCVD

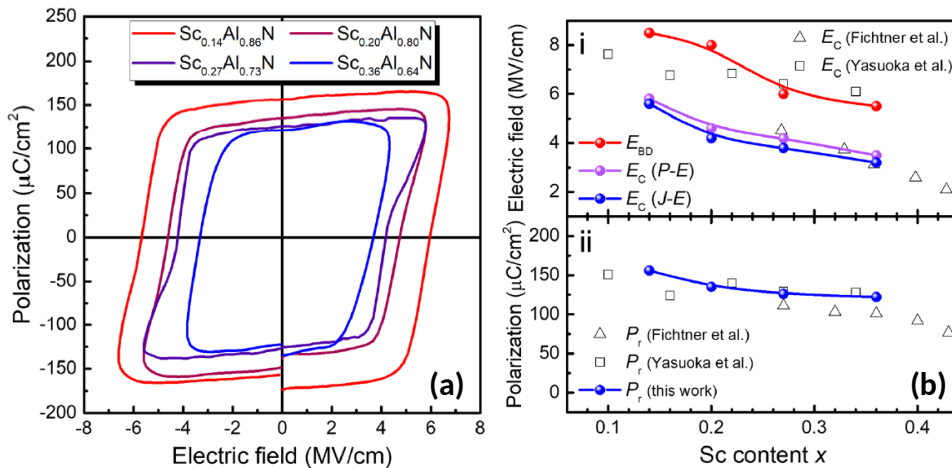


Figure 2.13: (a) P-E hysteresis of MBE deposited AlScN films. (b) Comparison of ferroelectricity among sputtered and MBE grown films [102].

The epitaxial growth of AlScN films are mainly conducted on GaN templates as they also possess wurtzite crystal structure. Wang *et al.* demonstrated MBE growth of ferroelectric AlScN with various Sc concentrations, as depicted in Figure 2.13(a) [102]. Figure 2.13(b) shows that the ferroelectricity of MBE films is close to the results of

sputter cases. However, the origin of leakage current in both cases might be different, which will be detailed in section 2.3.1. Wolff *et al.* presented ferroelectric AlScN using MOCVD growth [103]. In Figure 2.14(a), ferroelectric switching is demonstrated by current response. Figure 2.14(b) additionally provides the STEM image for switched and unswitched areas. After switching, the film shows cone-like domains.

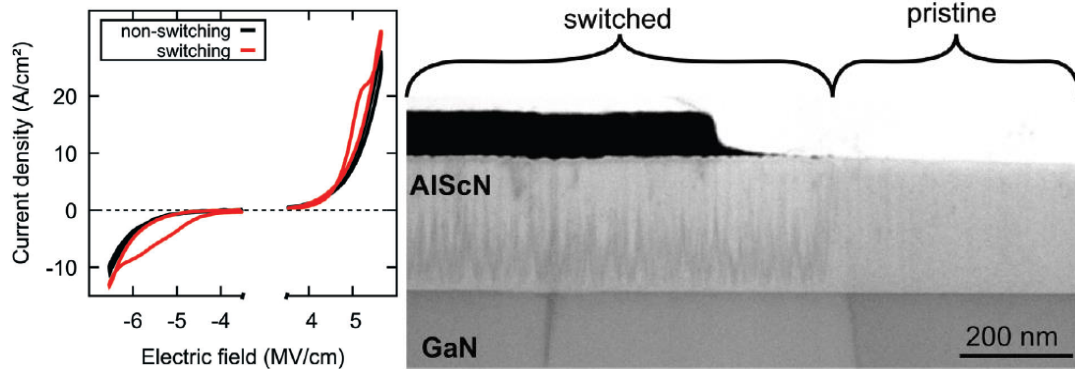


Figure 2.14: (a) Current density in relation to E. (b) STEM image for switched and unswitched areas [103].

2.3. Ferroelectric and Dielectric Properties of Aluminum Scandium Nitride

The ferroelectric properties of III-N materials such as Al_{1-x}Sc_xN, Ga_{1-x}Sc_xN, and Al_{1-x}B_xN can be tuned by changing the chemical composition [32], [34], [90], [117], [126], [127]. This section discusses the influence of Sc content on material properties of Al_{1-x}Sc_xN.

2.3.1. Bandgap and Leakage Current

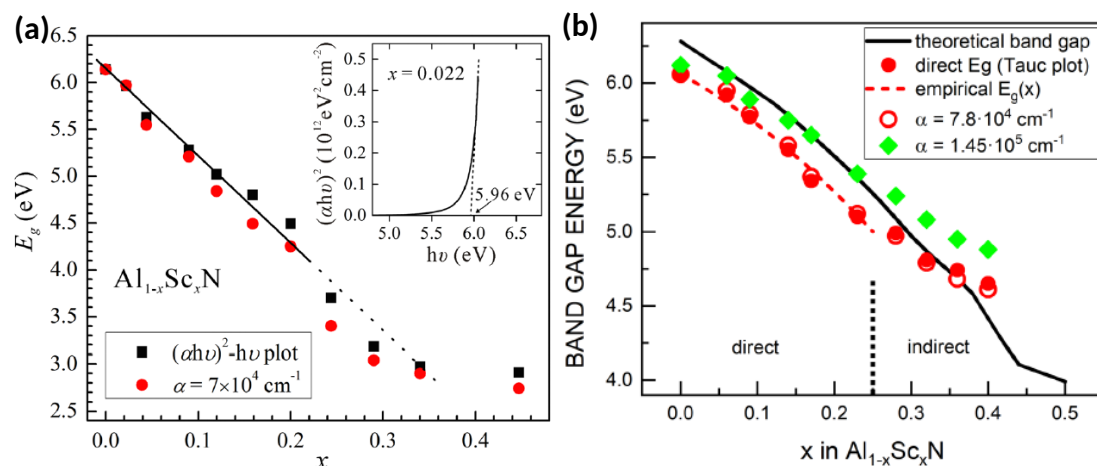


Figure 2.15: Calculated E_g by (a) Deng *et al.* [128] and (b) Baeumler *et al.* [129].

Figure 2.15(a) and (b) demonstrate the relationship of E_g and Sc content in AlScN, and the results are derived by Deng *et al.* and Baeumler *et al.*, respectively [128], [129]. The difference can be attributed to different methods used. Generally, as Sc content increases, the E_g values show decreasing trend, which is related to the bond angles, bond lengths and c/a ratio in wurtzite structure. Besides, the bandgap changed from direct to indirect at approximately 25% of Sc content.

The decreasing trend of E_g with higher Sc content raises the concern about leakage current. Though the E_g values at low Sc content condition, unexpected high leakage is found in AlScN films, comparing to HZO films with good insulating property. Indeed, in section 4.2.3., the leakage current will be shown depending on the Sc content. In addition, it has been demonstrated that leakage in ferroelectric materials could increase after field cycling [130], [131], [132], [133]. Kataoka *et al.* suggests that Schottky emission could be the dominating mechanism for leakage current in sputtered AlScN films [134]. As displayed in Figure 2.16(a) and (b), the Schottky barrier height at ferroelectric/electrode interfaces decreases after switching, and the formation V_N is attributed to this effect [134], [135]. For epitaxial AlScN films, Wang *et al.* proposed that the leakage current is related to the dislocation density [136].

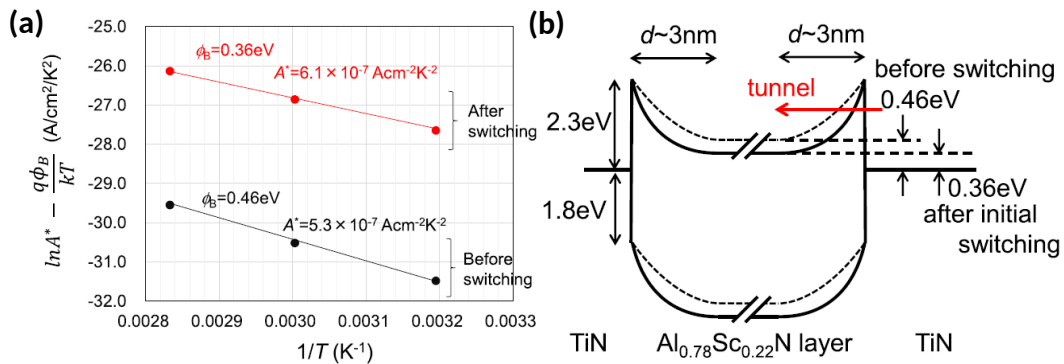


Figure 2.16: (a) Schottky barrier height before and after switching. (b) Band diagram of MFM structure [134].

2.3.2. Dielectric Constant

Ambacher *et al.* theoretically calculated the ϵ_r of Al_{1-x}Sc_xN, as illustrated in Figure 2.17

[109]. Yagitani *et al.* published similar results with practical experiments [137]. For pure AlN, the ϵ_r value is around 10. Considering ferroelectricity only stays up to 30-40% of Sc content, the ϵ_r range of ferroelectric AlScN is between 10-25. This value is typically lower than HfO₂-based ferroelectrics, and significantly lower than PZT, which is advantageous for future memory technology.

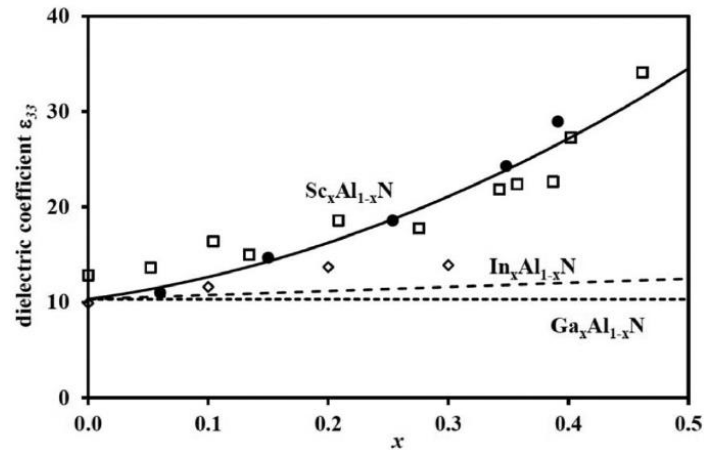


Figure 2.17: ϵ_r with respect to doping concentration in ternary III-N materials [109].

2.3.3. Remanent Polarization and Coercive Field

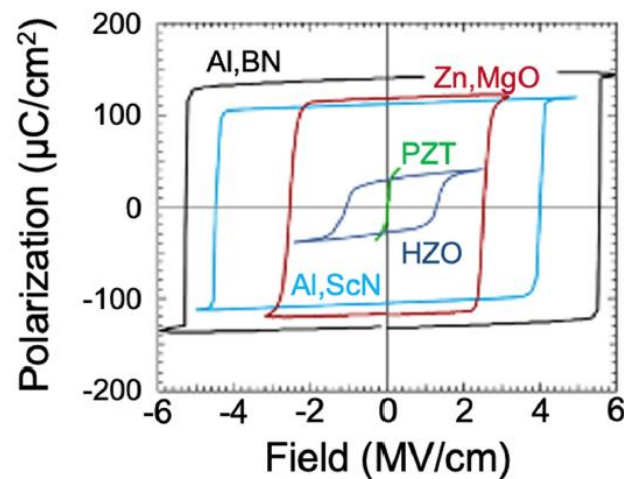


Figure 2.18: P-E hysteresis of PZT, HZO, and wurtzite ferroelectrics [138].

Prior to elaborate the influence of Sc content for ferroelectric properties, it is interesting to take a look at the P-E curves in popular ferroelectrics first. Figure 2.18 reveals the ferroelectricity in perovskite, fluorite, and wurtzite materials [138].

Apparently, higher P_r and E_c values are demonstrated in wurtzite materials. The P-E hysteresis for wurtzite cases is more box-like, indicating the switching mechanism among domains could be different from the fluorite case.

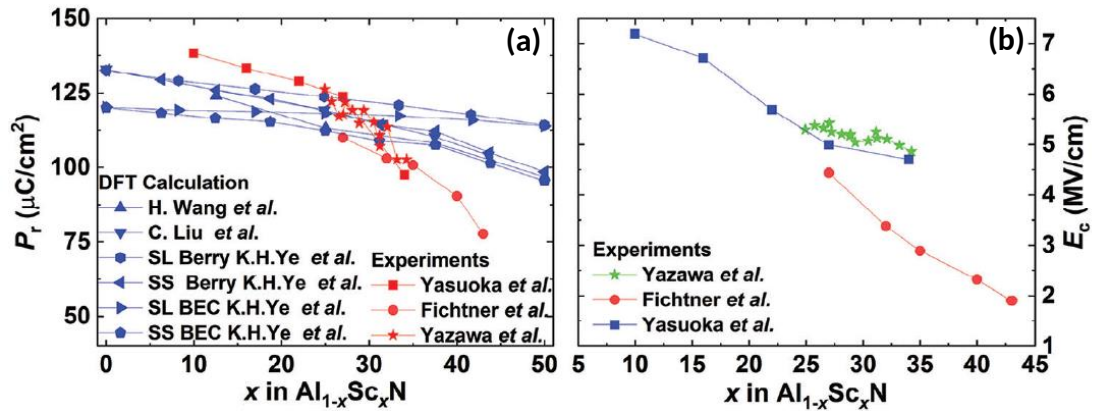


Figure 2.19: (a) P_r and (b) E_c with respect to Sc content in $Al_{1-x}Sc_xN$ films [110].

Figure 2.19(a) and (b) demonstrate the dependence of P_r and E_c with Sc content, respectively [110]. Both ferroelectric parameters show decreasing tendency with higher Sc concentration. For experimental P_r , a high value over $130 \mu C/cm^2$ can be achieved [117]. The decreasing trend of P_r is related to the structural change in the lattice, as the u parameter increases from the ideal value of 0.375 [139], according to Figure 2.8(c). Therefore, the lattice generates less P_r at higher Sc content. In the case of experimental E_c , it is shown that the variation falls into the range of 2-7 MV/cm. The reason of the decreasing trend in E_c is described previously in section 2.1.

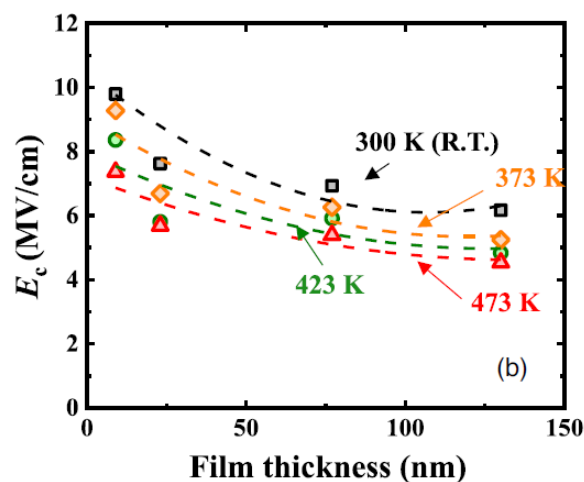


Figure 2.20: E_c values in relation to temperature and film thickness [100].

Additionally, from the thermodynamics point of view, the potential barrier of

switching can be overcome in an easier approach such as applying higher excitation energy. Therefore, the E_c value can be tuned by changing the temperature [100], [140]. Mizutani *et al.* presented lower E_c values of AlScN at higher temperature than RT, as shown in Figure 2.20 [100].

2.3.4. Poling-free

For HZO, it is generally necessary to apply a set of field cycling to “wake-up” the ferroelectricity and mitigate the antiferroelectricity. However, this is not the case of AlScN. It has been considered that AlScN is wake-up free, as the P_r values of the first few cycles are very close to the maximum [141]. Therefore, it is reasonable to consider that P_r already exists after deposition. Tsai *et al.* discovered the poling-free characteristics in 2021 [97]. Figure 2.21(a) and (b) show the C-V sweeps of two pristine AlScN capacitors. In Figure 2.21(a), a positive sweep is conducted initially, and no peaks are found. Subsequent sweeps exhibit ferroelectric switching due to the presence of peaks. On the other hand, in Figure 2.21(b), a negative sweep is conducted initially, and ferroelectric switching occurred. Naturally, peaks in the subsequent sweeps are present. Moreover, the magnitude of drastic capacitance variation, i.e., peak heights in sweep #1 and #3 are quite the same. The observed phenomenon indicates that AlScN is already polarized to N-polar after deposition.

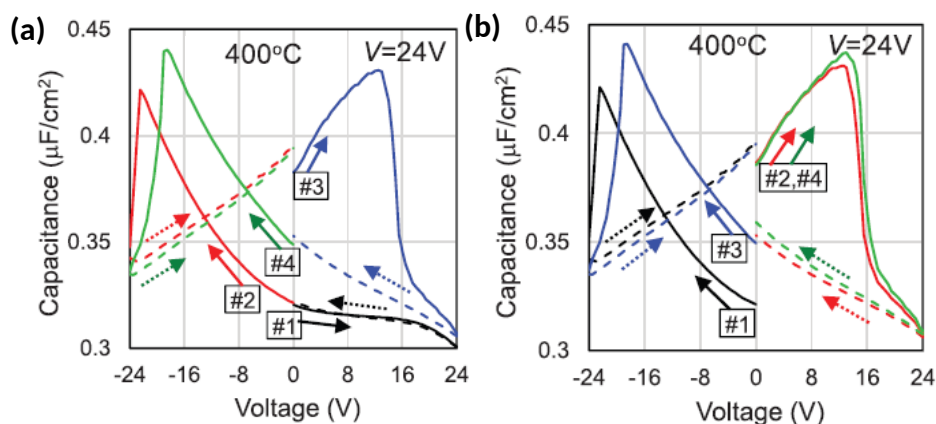


Figure 2.21: Initial (a) positive and (b) negative C-V sweeps for pristine films [97].

Wolff *et al.* demonstrated the poling-free characteristics by experimental methods, as shown in Figure 2.22(a), (b), and (c) [94]. In Figure 2.22(a), the ferroelectric film is partially covered by TE and underwent switching operation. Then,

the TE is removed to expose the switched area. Since the switched and unswitched areas have different polar states, selective wet etching is conducted to etch away N-polar area, which is unswitched. Figure 2.22(b) and (c) provide SEM evidence after selective etching.

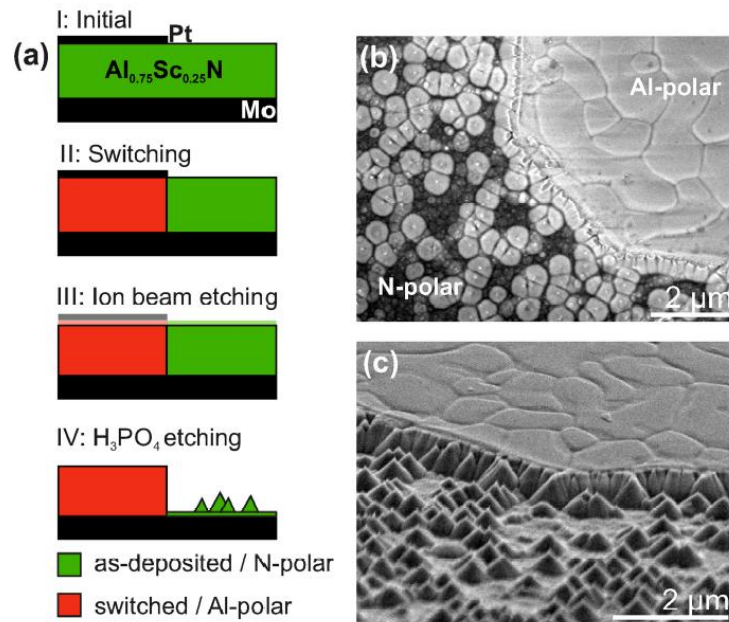


Figure 2.22: (a) Schematic flow of the confirmation of N-polar state in pristine film. SEM image of the (b) top and (c) oblique view after selective etching [94].

2.4. Thickness Downscaling

In order to achieve high energy efficiency for advanced memory technology, it is crucial to downscale the operation voltage. Therefore, minimizing the thickness of ferroelectric films is an urgent task to be tackled. PZT has its struggle when the thickness is reduced under 50 nm. One reason for P_r distinction at scaled PZT films is the existence of dead-layer. HZO films, on the other hand, have already demonstrated good scalability under 5 nm [142], [143]. Though some efforts have been dedicated to scaled AlScN films, more effort to realize low-voltage operation is desirable, since still limited publications have been published with below 10 nm AlScN film [101], [144]. Section 2.1. briefly mentioned that several challenges could be encountered during the progress of downscaling. One major obstacle is leakage current. This could be

resolved by fine tuning the deposition conditions and E_g engineering in the film. Chapter 4 will focus on this aspect. The other obstacle is the deteriorated ferroelectricity in ultra-thin films. Figure 2.23(a) and (b) illustrate the trend of E_c and P_r values during thickness downscaling, respectively [110]. As the thickness decreases, E_c tends to increase. It is explained that at thinner thickness, the ferroelectric layer suffers more compressive strain due to lattice mismatch with electrodes [145]. Therefore, lattice parameter a variation due to the influenced lattices could contribute to this effect. Moreover, the gradually inferior P_r values in scaled films indicates worse c -axis crystallinity. This could be possibly solved by fine tuning the deposition conditions.

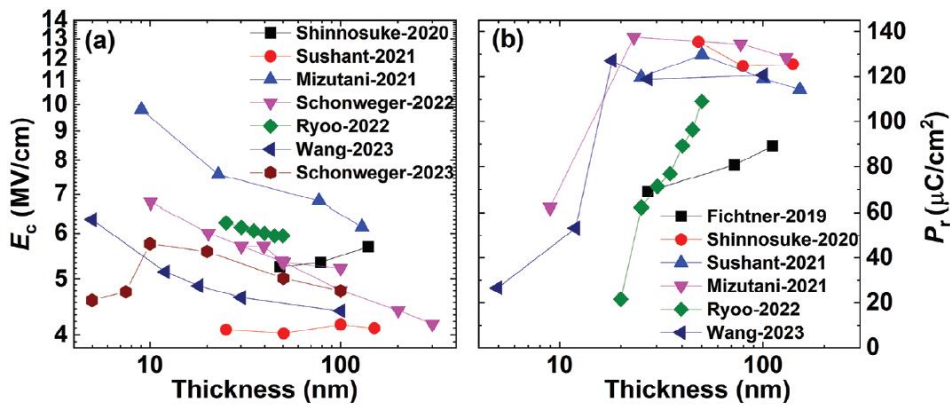


Figure 2.23: (a) P_r and (b) E_c values in relation to film thickness [110].

2.5. Reliability Concerns

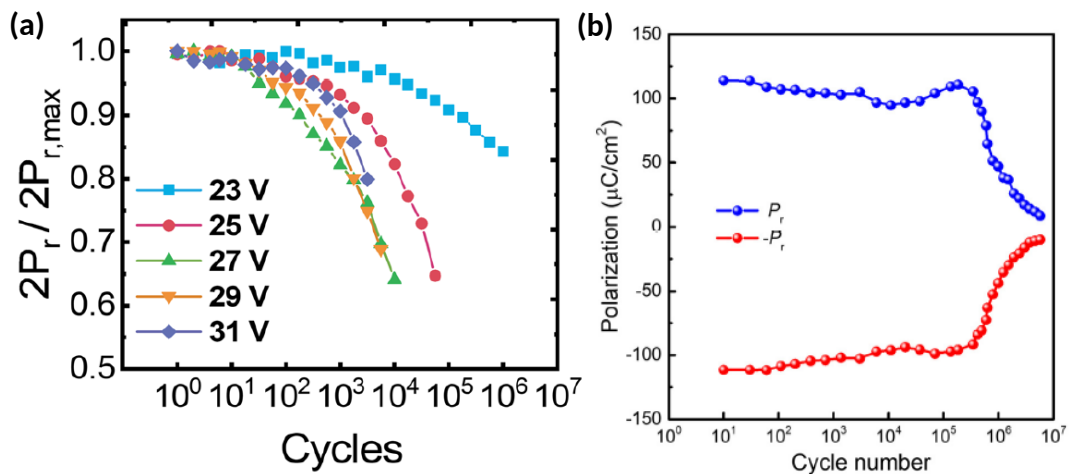


Figure 2.24: Endurance tests for AlScN thin films deposited by (a) sputtering [146] and (b) MBE [102].

Other than the aforementioned issue about thickness downscaling, AlScN suffers from reliability issues including limited endurance strength about 10^5 - 10^6 cycles and deteriorated breakdown field due to the presence of high leakage and high E_c/E_{BD} ratios [53], [99], [124], [133], [136]. Figure 2.24(a) and (b) give examples of endurance measurements for sputtered and MBE deposited films [102], [146].

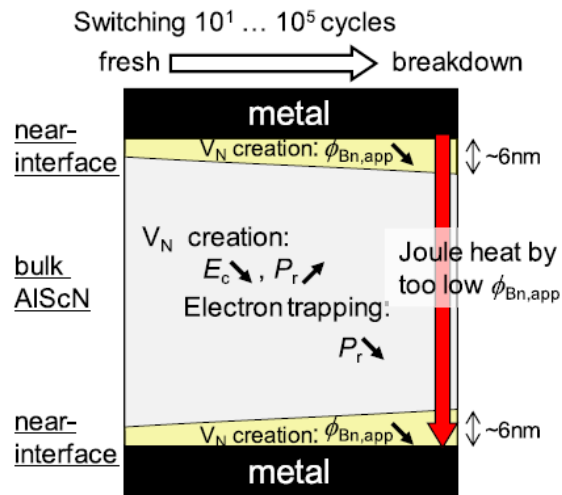


Figure 2.25: Model of decreasing Schottky barrier height after field cycling [133].

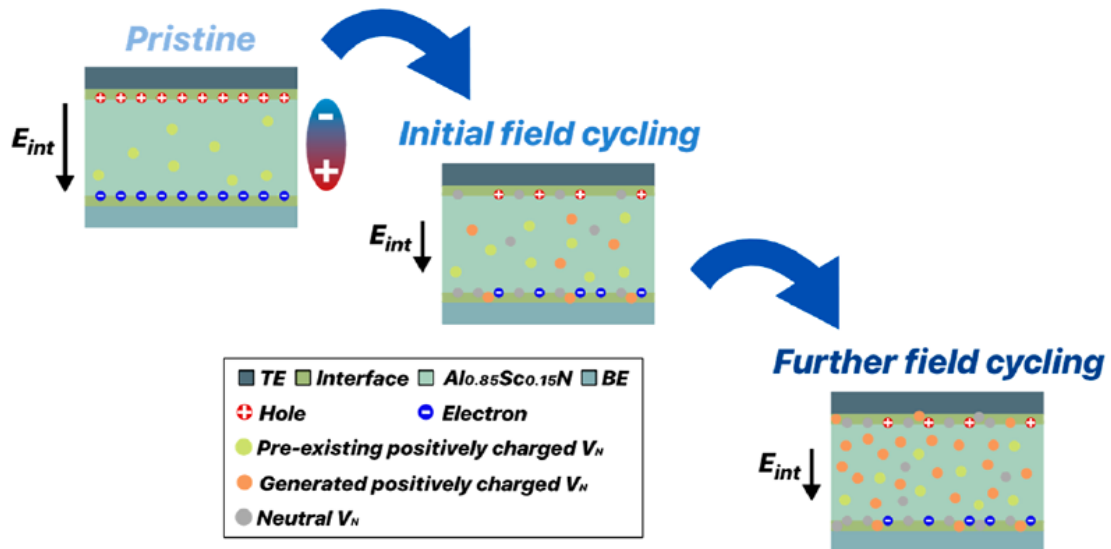


Figure 2.26: Defect generation in AlScN based on hot atom damage model [147].

As stated in section 2.3.1., the high leakage current could originate from the V_N inside the sputtered film [134], [135], and the amount of V_N increases even more after cycling [133]. This phenomenon is suggested by Tsai *et al.* and attribute the breakdown event to reduced Schottky barrier height and excessive Joule heating in the film, as illustrated in Figure 2.25 [133]. Moreover, Guido *et al.* attributes the high leakage current to the formation of conductive filaments, which is highly related to charged V_N generation [147]. Figure 2.26 depicts the schematic illustration of defect generation based on hot atom damage which is explained as follows [147]. During ferroelectric switching, transient overshoot of N atom displacement can result in defect generation due to domain wall motion. The produced defect would accumulate by field cycling and form filaments to breakdown. It is worth mentioning that when the leakage current is inhibited, the generation of defects and filament can be suppressed, giving rise to high E_{BD} , as will be shown in chapter 4.

2.6. Aims of This Research

Addressing the issues of AlScN thin films in section 2.4. and section 2.5., the aims of this research are clear, which is to propose highly scalable and reliable AlScN thin films. Herein, fabrication, characterization, and analysis are conducted for AlScN films. Since most publications to date demonstrate 10^5 cycles of endurance, this research aims to elongate the endurance cycle by two orders of magnitude. Plus, as only limited amounts of work are able to achieve low voltage operation, this research targets below 5 V operation with enhanced ferroelectricity. Though there are some trade-offs among some ferroelectric and dielectric properties, this research intends to contribute to the development of ferroelectric AlScN thin films for future NVM technology applications.

Chapter 3: Fabrication Process and Electrical Characterization of Aluminum Scandium Nitride Capacitors

In this chapter, experimental details of this research will be described. The fabrication process of ferroelectric AlScN capacitors is shown in section 3.1. Note that section 3.1. only expounds the general process, and some key parameters might be changed to fulfill certain purposes. These key changes will be specified in the subsequent chapters. Section 3.2. demonstrates the methods of measurement for electrical characterization.

3.1. Capacitor Preparation

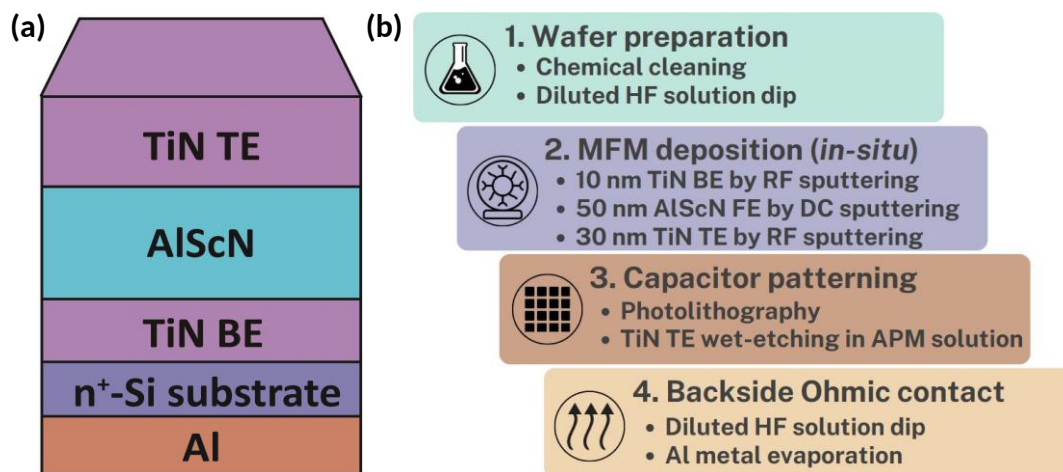


Figure 3.1: (a) Schematic figure and (b) process flow of AlScN MFM capacitor.

The schematic view and the flow chart of MFM capacitor fabrication process are illustrated in Figure 3.1(a) and (b), respectively. Details are provided in the following sections.

3.1.1. Wafer Cleaning

In this research, n⁺-Si wafers with the following features are used as substrates: (100) orientation, 625 ± 25 μm of thickness, and resistivity below 0.005 Ω·cm. These 6-inch wafers are diced into 2 cm × 2 cm samples. The process starts with removing the particles on n⁺-Si substrates by ultrasonic cleaner in DI water for 3 minutes at RT. The chemical cleaning on the surface is implemented using SPM solution, which contains

the mixture of H₂O₂/H₂SO₄ = 1:2, for 10 minutes at 180°C. Then, a 5-minute rinse in DI water takes the residual solution and reactant away. In order to remove the native oxide, the n⁺-Si substrates are dipped into 1% HF solution for 1 minute and followed by 1 minute DI water rinse.

3.1.2. MFM Stack Deposition by *in-situ* Reactive Sputtering

To avoid surface re-oxidation in atmosphere, the samples are brought to the loadlock of the sputtering machine as soon as possible (5~10 minutes). It is worth mentioning that confirmation of chamber base pressure is required before transferring samples from loadlock to chamber. The base pressure should be at the range of 10⁻⁶ Pa or lower, otherwise the sputtered films are likely to contain high amount of oxygen contaminants which deteriorate the films' quality [118], [119], [120], [121]. After sample transfer, the substrate temperature is increased and sustained at 400°C for 1 hour. This long waiting time not only prevents the temperature fluctuation at the substrate but also ensures that the chamber pressure is maintained at the range of 10⁻⁵ Pa or lower. Here, due to heated conditions, the tolerance value of chamber pressure is slightly higher.

TABLE 3.1
SPUTTERING CONDITIONS FOR TITANIUM NITRIDE

Deposition parameters	
Sputtering target	Ti (80 mm dia.)
Process temperature (°C)	400
RF power supply (W)	300 (13.56 MHz)
T/S distance (mm)	100
Process pressure (Pa)	0.16
Ar/N ₂ gas flow (sccm)	4/6

The MFM stack is *in-situ* deposited on n⁺-Si substrates by single source reactive sputtering to refrain from surface oxidation of the ferroelectric AlScN layer [148], [149]. First, 10 nm TiN BE layer is deposited by sputtering a Ti target in Ar (4 sccm)/N₂ (6 sccm) gas ambient with the power of RF 300 W and the chamber pressure of 0.16 Pa. Note that for TiN sputtering, the T/S distance is fixed at 100 mm. Detailed

sputtering conditions for TiN films are summarized in Table 3.1.

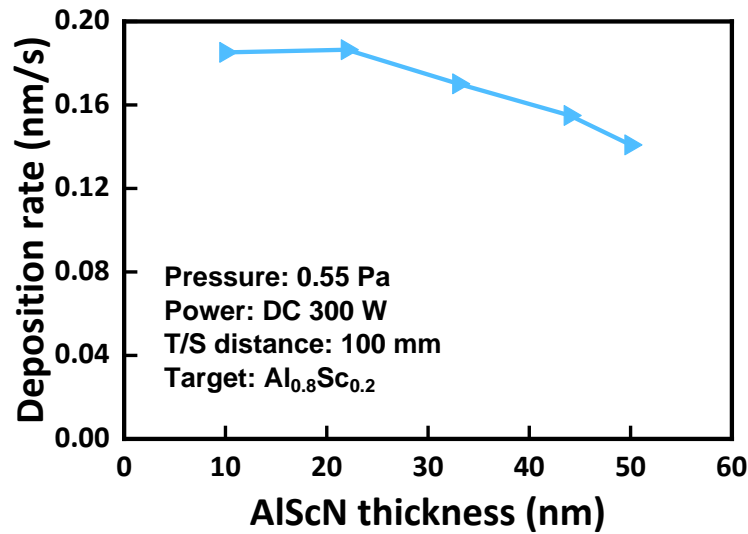


Figure 3.2: Dependence of sputtering rate and deposited thickness of AlScN. The thickness is measured by ellipsometry.

TABLE 3.2
SPUTTERING CONDITIONS FOR ALUMINUM SCANDIUM NITRIDE

Deposition parameters		
Sputtering target	Al _{0.53} Sc _{0.47} (80 mm dia.)	Al _{0.8} Sc _{0.2} (80 mm dia.)
Process temperature (°C)	400	
DC power supply (W)	300	
T/S distance (mm)	100	
Process pressure (Pa)	0.65-0.7	0.55-0.6
Ar/N ₂ gas flow (sccm)	5/10	

Second, by sputtering the 80 mm diameter AlSc alloy target, the AlScN layer is deposited in Ar (5 sccm)/N₂ (10 sccm) gas ambient with the power of DC 300 W. Herein, the chamber pressure is the lowest reachable value for plasma ignition, and it is related to the composition of AlSc alloy target. This value is around 0.65-0.7 Pa and 0.55-0.6 Pa for Al_{0.53}Sc_{0.47} and Al_{0.8}Sc_{0.2} targets, respectively. In addition, the T/S distance is set to 100 mm. Moreover, the AlScN film thickness could be controlled by varying the sputtering time. It is observed that the cathode current, monitored by the

DC power supply, shows decreasing tendency as the deposition time increases, indicating less ions are generated over time. Figure 3.2 confirms that the sputtering rate gradually decreases as the AlScN layer becomes thicker. This could be the influence of decreasing sputter yield. If not specified particularly, the deposited film is 50 nm. Chapter 4 will focus on the dependence of target composition, chamber pressure and T/S distance for AlScN ferroelectric and dielectric properties. Detailed sputtering conditions for AlScN are summarized in Table 3.2.

Finally, 30 nm TiN TE layer is grown using the same condition as the BE layer, and the MFM deposition process is completed. The samples are transferred back to the loadlock for 1 hour cool-down.

3.1.3. Capacitor Pattern Formation

Contact lithography is conducted to create the capacitor patterns. Prior to S1818 photoresist (MICROPOSIT S1800 series) coating, the samples were exposed to evaporated HMDS for 2 minutes on a 115°C hot-plate to improve the photoresist adhesion. Subsequently, 115°C pre-bake for 5 minutes is applied to remove the solvent of coated photoresist. Exposure to 365 nm DUV light continues the process, and the patterns are developed by NMD-3 solution (TMAH 2.38%) for 1 minutes 30 seconds. Thereafter, in order to solidify the photoresist for the following etching process, the samples undergo 130°C post-bake for 10 minutes.

For TiN TE etching process, both wet and dry etching are available. In the case of wet etching, APM solution, a mixture of $\text{NH}_4\text{OH}/\text{H}_2\text{O}_2/\text{H}_2\text{O} = 1:5:5$, is used as etchant. 8 minutes etching time at RT is sufficient to etch away 30 nm TiN. For the case of dry etching, Cl_2/Ar gas mixture is utilized as etchant in the ICP-RIE system. This research mainly adopts the wet etching method to define TE patterns.

After TiN TE etching process, the sample surface is again coated with another photoresist layer, and followed by 5 minutes baking at 115°C. Native oxide on the sample backside is then removed by floating the sample on 1% HF solution for 1 minute. The purpose of additional photoresist layer is to prevent direct contact between HF solution and exposed area on the sample surface. The photoresist removal is carried out using ultrasonic cleaner, acetone, ethanol and DI water. Note that the created TE patterns have a common size of $2.5 \times 10^{-5} \text{ cm}^2$ in square shape.

3.1.4. Backside Contact Deposition by Evaporation

Subsequent to capacitor patterning, the samples are transferred to the evaporator machine as soon as possible (5~10 minutes) to prevent surface re-oxidation. 100 nm Al layer is evaporated to the sample backside to create Ohmic contact to the TiN BE layer. This ends the capacitor fabrication process, and the capacitors are ready for electrical characterization.

3.2. Electrical Measurement

This section describes the measurement methods that are used to characterize the fabricated ferroelectric AlScN capacitors.

3.2.1. Polarization-Electric Field

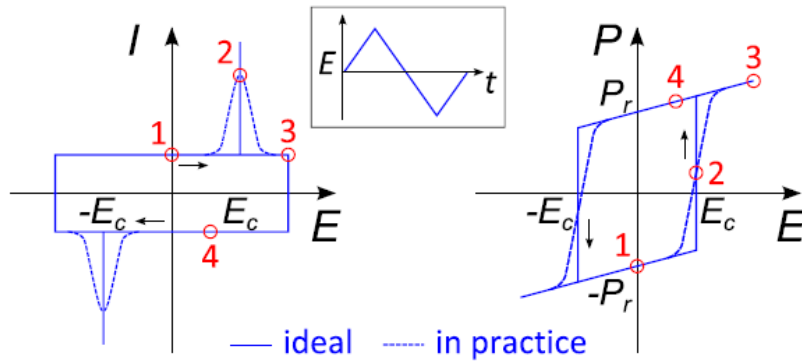


Figure 3.3: P-E measurement of ferroelectric capacitor for ideal and practical cases [150]. The inset shows the input signal. Polarization is calculated by integrating the current density with respect to time.

The polarization of ferroelectric film can be directly read out by monitoring the current response upon polarization reversal. In other words, ferroelectric domains are reoriented toward the most favorable direction when the film is subjected to voltage bias, and thereby generating switching current. Therefore, it is convenient to measure the ferroelectric properties by simple I-V measurement. Additionally, according to Gauss's law of Maxwell's equations, the polarization P can be calculated as

$$D = \varepsilon_0 \cdot \varepsilon_r \cdot E = D_0 + P = \varepsilon_0 \cdot E + P = \frac{Q}{A} = \frac{\int I(t)dt}{A}$$

, where vacuum contribution D_0 is neglectable in most cases. Figure 3.3 illustrates simple I-V measurement for both ideal and practical circumstances [150]. The x-intercepts of the P-E loop are defined to be E_c values as the polarization is considerably inversed at the electric field. P_r values are determined at the y-intercepts which corresponds to remanent polarization at zero electric field. Owing to the hysteresis loop in P-E relationship, simple I-V measurement of ferroelectric capacitors is also called P-E measurement. Some research may adopt Q-V, P-V, or Q-E hysteresis loop instead, but the physical meaning remains the same. Examples of typical ferroelectric hysteresis loops are shown in Figure 3.4 [151].

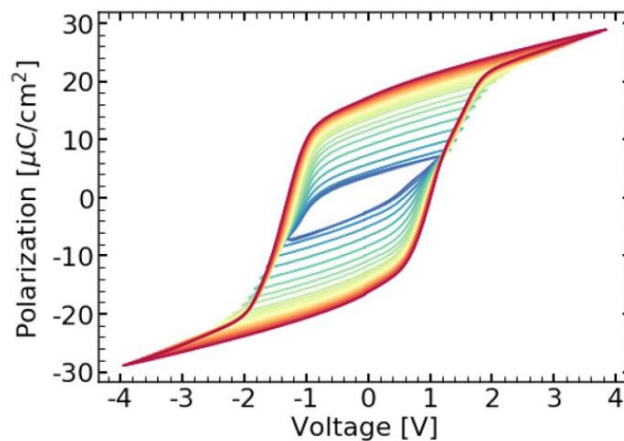


Figure 3.4: Typical P-V hysteresis loops of ferroelectric HfO_2 -based ferroelectric capacitor under various voltage sweep range [151].

Although the P-E measurement is intuitive to examine the ferroelectricity inside the film, i.e., a hysteresis loop represents ferroelectricity, there are some drawbacks in this method. First, the measured current not only consists of ferroelectric switching contribution, but also contain non-ideal contributions from paraelectric switching and resistive leakage. Second, the ferroelectric and paraelectric switching is dependent to the measurement frequency, whereas the resistive leakage current is mainly related to the applied electric field. Thus, eliminating the impact of non-ideal contributions is crucial when dealing with leaky films.

P-E hysteresis loops generated by films with high leakage may be misleading. Figure 3.5(a) shows a hysteresis loop of a lossy dielectric, which is similar to the shape of banana in Figure 3.5(b) [152]. The extraction of P_r and E_c in Figure 3.5(a) is

meaningless since the hysteresis is not dominated by ferroelectric switching but high leakage current. True ferroelectric films should present ferroelectric traits such as abrupt polarization change at E_c , as shown in Figure 3.4. Consequently, films presenting banana-shaped hysteresis loops should be measured with the methods introduced below.

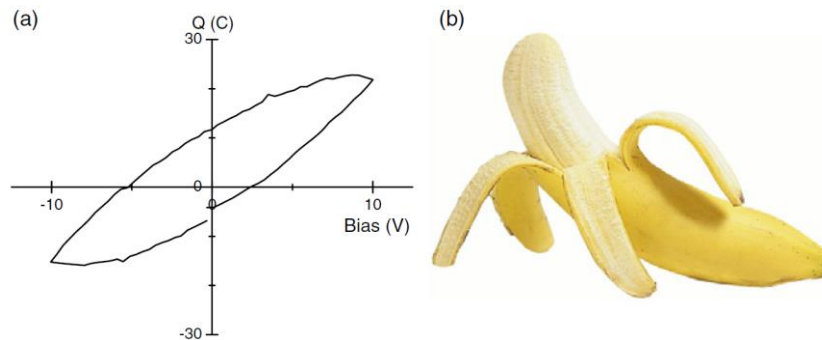


Figure 3.5: Scott *et al.* elucidated the importance of identifying true ferroelectricity in a humorous way. (a) Banana-shaped hysteresis loops of lossy dielectric, and (b) an actual banana [152].

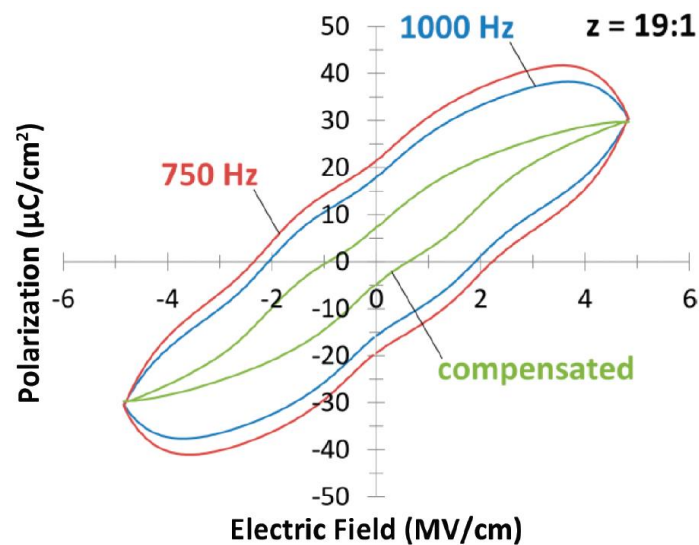


Figure 3.6: P-E hysteresis loops from DLCC measurement with two different frequencies. Note that a leaky ferroelectric HAO capacitor is used here [153].

Fortunately, dynamic leakage current compensation (DLCC) proposed by Meyer *et al.* and further elaborated by Schenk *et al.* can tackle the above issue [153], [154]. The main concept of this method is to conduct two sets of P-E measurements with different cycle frequencies, and thereby subtracting the non-ideal contributions.

Figure 3.6 shows the P-E hysteresis loops of DLCC measurement, and ferroelectric traits of a leaky HAO capacitor is successfully unveiled [153]. However, limitations to this method (e.g., frequency-dependent E_c shift, material-related frequency selection, and the leakage should not be significantly larger than switching current) should be taken into consideration. Detailed calculation of DLCC can be found in literature [153].

Other than DLCC method, positive-up negative-down (PUND), which was demonstrated by Scott *et al.*, is another effective method to isolate the ferroelectric contribution from the overall current response [155]. This method is explained in the following section.

3.2.2. Positive-Up Negative-Down

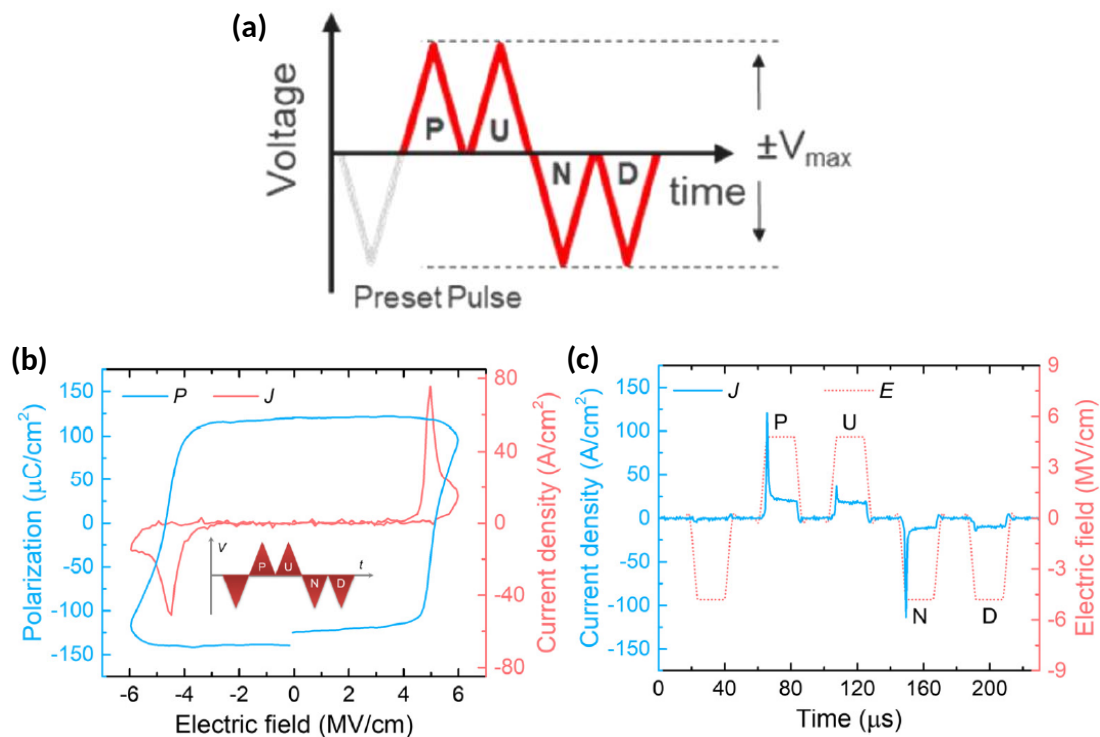


Figure 3.7: (a) Schematic of PUND measurement [156]. (b) Compensated P-E hysteresis can be derived when triangle pulses are applied in PUND [157]. (c) Current response of PUND with square pulses [157]. Switching current responses are shown in “P” and “N” pulses, whereas non-switching current responses are spotted in “U” and “D” pulses.

PUND measurement might be by far the most powerful weapon in the arsenal to mitigate the influence of leakage current. The PUND scheme consists of one preset,

two consecutive positive, and two consecutive negative excitation signals, as illustrated in Figure 3.7(a) [156]. The input could be triangle or square waveform [157], [158], [159], [160]. The current response with respect to “P” and “N” signals includes ferroelectric and non-ideal contributions. If the polarization is completely reversed, current response of “U” and “D” signals includes only non-ideal contributions. Thus, subtracting the latter from the former signals gives the ferroelectric switching current, to which the equation in section 3.2.1. can be applied. Note that when triangle waveform is used, compensated current and P-E hysteresis are extracted accordingly, as depicted in Figure 3.7(b) [157]. In the case of square waveform, current response are plotted in Figure 3.7(c) [157]. Here, the P_r values are directly calculated corresponding to each applied voltage. Though there are still some limitations to PUND [161], it is still the most effective measurement scheme to reveal the true P_r values, as AlScN films usually show higher leakage current comparing to HfO₂-based ferroelectrics [99].

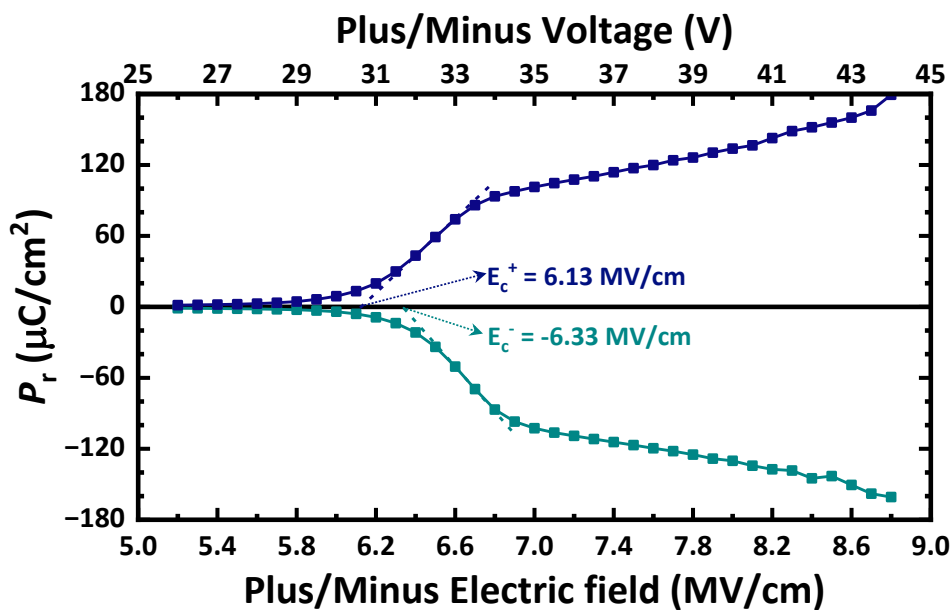


Figure 3.8: P_r with respect to $\pm E$ from a PUND measurement of AlScN capacitor.

Figure 3.8 shows the PUND results of an AlScN capacitor, both in positive and negative polarization side. For this method, E_c can be derived by linear extrapolation of the steepest P_r rising stage. Empirically, this stage is around 20 to 100 $\mu\text{C}/\text{cm}^2$. Besides, for ferroelectric AlScN, $|E_c^+|$ has smaller value than $|E_c^-|$, which is due to favorable N-polar during polarization reversal [97], [162]. This is the so-called

“imprint” effect, and it will be further discussed in sections 3.2.4. and 5.1. Additionally, semi-saturation kinks of the P_r -E relationship can be easily found at 6.7 and -6.8 MV/cm. Although deeper analysis is required, it is observed that when the c -axis orientation is weak or field cycling is applied, the saturation kinks of P_r -E relationship appear at smaller E or even vanish.

In this research, instead of P-E hysteresis, PUND is adopted as the primary method for ferroelectric characterization due to high leakage in AlScN films. Square pulse signals along with 5 μ s of pulse width and 5 μ s of interval are used. For simplicity, P_r -E relationships shown in this research are mainly provided with only the negative polarization part, the lower panel of Figure 3.8. In addition, both P-E hysteresis and PUND measurements are implemented using the same ferroelectric tester (TOYO Corp., FCE-10) in this research.

3.2.3. Endurance cycling

Considering the integration to memory technology, endurance performance is viewed as one of the most crucial factors for ferroelectric thin films. Not only the cycle to breakdown, but also the wake-up and fatigue effects in ferroelectrics can be directly observed, as introduced in section 2.5. Typically, the endurance tests are carried out by applying two alternating schemes, field cycling as electrical stress and P-E/PUND as P_r characterization. The endurance performance is influenced by field cycling conditions such as applied voltage amplitude, pulse waveform, duty cycle, and measurement frequency [163]. The amplitude of the cyclic voltage pulse, which is normally square/rectangle waveform, should be greater than E_c to ensure abundant polarization switching until breakdown. As mentioned in section 2.5., the breakdown incident of dielectric material is governed by defect and conductive filament formation. Naturally, applying larger field during cycling creates more defects, and leads to deteriorated cycles to breakdown. In addition, it has been reported that the endurance strength can be boosted by increasing the cycling frequency [164], [165]. Also, Toprasertpong *et al.* showed that the breakdown strength is related to the overall electrical stressing time for thin HZO capacitors [143].

Figure 3.9 illustrates the operation of endurance cycling test over time in this research. The voltage amplitude is the same in field cycling and PUND measurement.

The frequency of field cycling is set to 500 kHz, i.e., pulse width is 1 μ s.

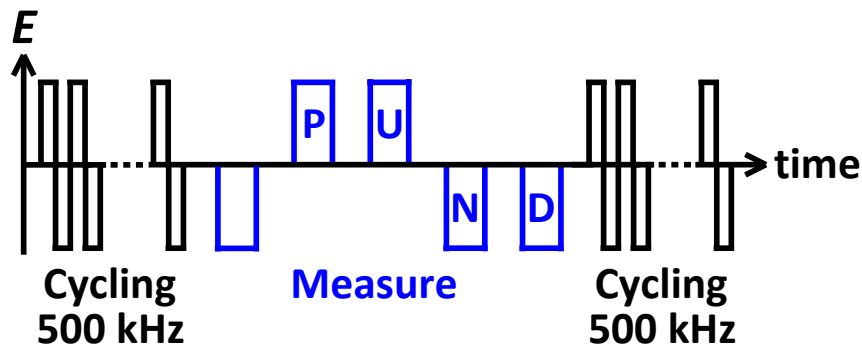


Figure 3.9: Measurement scheme of endurance cycling test in this research.

3.2.4. Capacitance-Voltage

For ferroelectric capacitor, C-V measurement is a useful method to verify and examine the ferroelectric properties inside the film. By superimposing AC small signal voltage on DC voltage input, capacitance and dielectric constant can be determined from the current response, as shown in the following two equations. Note that A and d represents the area and film thickness of the capacitor, respectively.

$$I = \frac{dQ}{dt} = C \frac{dV}{dt}$$

$$C = \frac{\epsilon A}{d} = \frac{\epsilon_0 \epsilon_r A}{d}$$

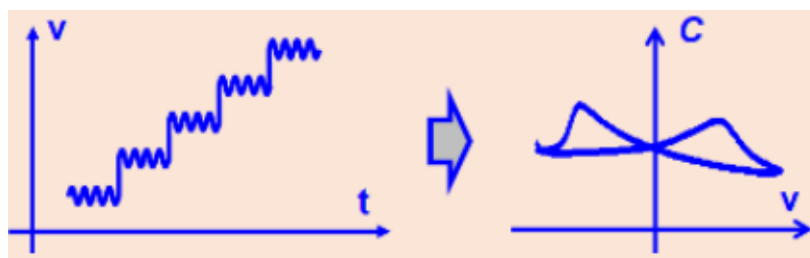


Figure 3.10: Illustration of C-V measurement for ferroelectric capacitors [166].

During C-V measurements, the atoms in the dielectric layer are constantly vibrating due to AC small signal voltage, allowing the detection of capacitance. For non-ferroelectric capacitors, the C-V curves generally show bow-shaped profiles due to charge accumulation or depletion behavior under voltage bias. On the other hand, ferroelectric capacitors demonstrate butterfly-shaped C-V profiles, which will be

explained later. Figure 3.10 illustrates the voltage input and the resulting butterfly curve of C-V measurement for ferroelectric capacitors [166].

C-V measurement is as powerful as P-E and PUND measurement when it comes to revealing the ferroelectricity of thin films. For instance, Figure 3.11 demonstrates the results of P-E and C-V measurements for ferroelectric HZO capacitors with various chemical composition ratios [33]. When Zr composition is lower than 30% or higher than 70%, the P-E hysteresis shows non-ideal ferroelectric response, and butterfly C-V curves are either barely visible or massively distorted. When the Zr composition is 40% and 50%, P-E loops show fine ferroelectric traits, and distinct butterfly C-V curves are presented.

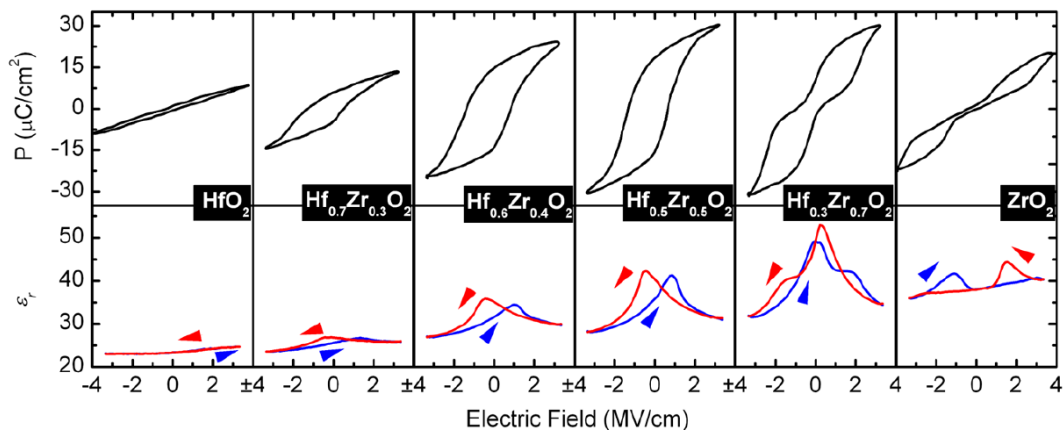


Figure 3.11: P-E and C-V curves for HZO capacitor with various Hf/Zr ratios [33].

Though it seems possible to directly transfer C-V curve and P-E curve via

$$P = \frac{Q}{A} = \frac{\int C dV}{A}$$

, the resulting curves are significantly dispersed from the results of standard P-E measurements [167], [168]. This can be explained by different measurement principles between C-V and P-E. For C-V measurement, instantaneous dielectric response from the film is captured. Providing that superimposed AC signal is small, the induced polarization is reversible. Consequently, the hysteresis loop of “C-V-transferred” P-E curve is hardly observed, and the polarization is considerably smaller than the value from standard P-E. As for P-E, the measurement renders the integrated response of domain reorientation, which differs from C-V. Thus, the interchange between C-V and P-E curves is impracticable.

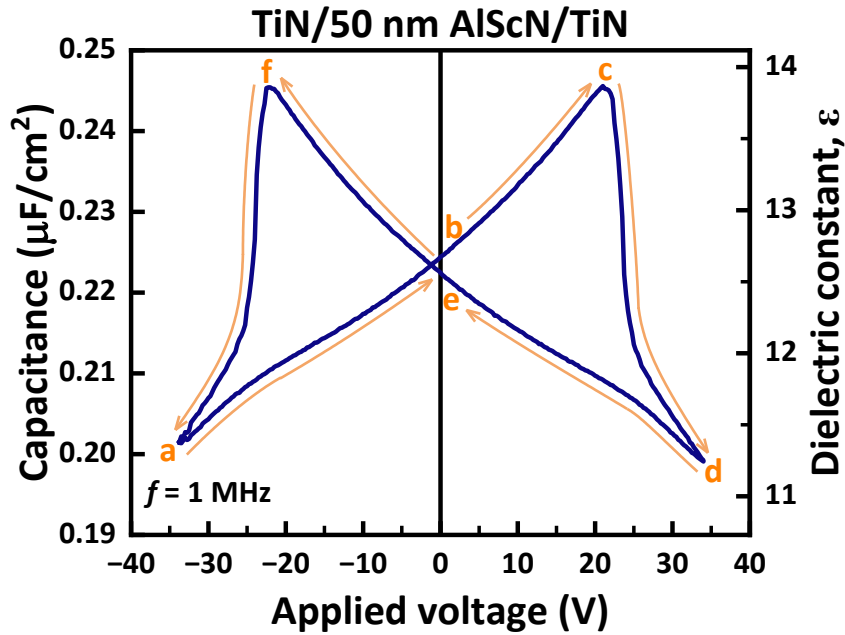


Figure 3.12: An example of C-V measurement for ferroelectric AlScN capacitor.

The voltage sweep is indicated by arrows.

Figure 3.12 delineates an example of C-V measurement for AlScN capacitor in this research. Since AlScN demonstrates poling-free characteristics and natural N-polar right after deposition, applying zero to positive bias will not be able to change the polarization direction [97], as discussed in section 2.3.4. Therefore, the measurement is conducted as this sequence: $a \rightarrow b \rightarrow c \rightarrow d \rightarrow e \rightarrow f \rightarrow a$. For ferroelectric films, polarization inversion is accompanied by crystal structure change, resulting in dielectric constant variation. In Figure 3.12, the sharp and drastic capacitance change from c to d and f to a represent polarization switching in the film. Plus, E_c can be determined by the peaks in C-V curve (points c and f), as those are the spots where the polarization starts to switch. Although other techniques such as P-E and PUND measurements are also available for E_c extraction, as discussed in sections 3.2.1. and 3.2.2., E_c extracted by C-V commonly show lower values than P-E and PUND measurements [169]. Moreover, the ferroelectric films breakdown easily at a lower electric field in C-V than in the other two. This is invoked to the slower voltage sweep rate in C-V than the other two measurements, and the films experience longer voltage stress. More defects are created accordingly, which results in higher leakage and severe local Joule heating in the films. Since the switching barrier is dependent on the specimen temperature, as discussed in section 2.3.4., local Joule heating gives rise to

lower E_c . Furthermore, once the films underwent C-V measurements, the endurance cycle show inferior performance, as more damage is done to the films.

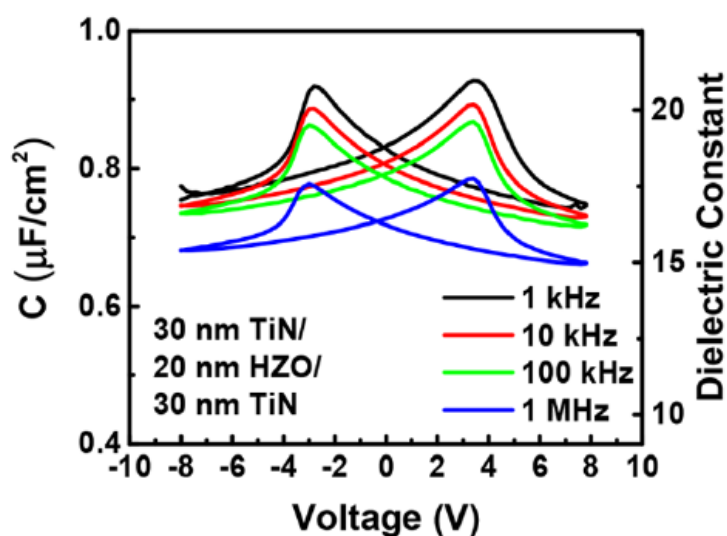


Figure 3.13: C-V measurement for HZO capacitors from 1 kHz to 1 MHz [170].

It is worthwhile to mention that the C-V response is related to measurement frequency under some frequency regime. Figure 3.13 depicts a practical C-V curve for HZO ferroelectric capacitor at different frequencies [170]. Decreasing ϵ_r with increasing frequency is the universal response for dielectrics [171]. At higher frequency, less charges and dipoles in dielectrics are instantaneously induced by the applied electric field, providing weaker contribution to ϵ_r . For PZT, ϵ tends to decline with higher frequency at RT [172]. In the case of HZO capacitor, similar trend is observed up to 1 GHz [173], [174]. Electron trapping at the HZO/electrode interface is responsible for this dependency [174]. Moreover, AlScN also exhibits similar trend [145].

Additionally, imprint effect is a common phenomenon observed in ferroelectric materials, and C-V measurement is one convenient method to monitor it [175]. An apparent sign of ferroelectric films with imprint effect is asymmetric C-V butterfly curves. Note that P-E hysteresis and PFM are other feasible options for identifying the imprint effect [176], [177], [178]. Figure 3.14(a) and (b) illustrate the influence of imprint effect on C-V and P-E curves [101], [179]. The cause of imprint effect is the existence of internal electric field, as discussed in section 2.5. To characterize the imprint effect, the following equation expressed as

$$E_{imp} = \frac{|E_c^+| - |E_c^-|}{2}$$

can be used, where E_c^+ and E_c^- are the peak positions in C-V profile [175]. For AlScN ferroelectrics, the E_{imp} usually demonstrates negative values and slightly shifts toward positive after field cycling [141]. Note that the equation above is also applicable for E_c values extracted from P-E measurements [179], [180].

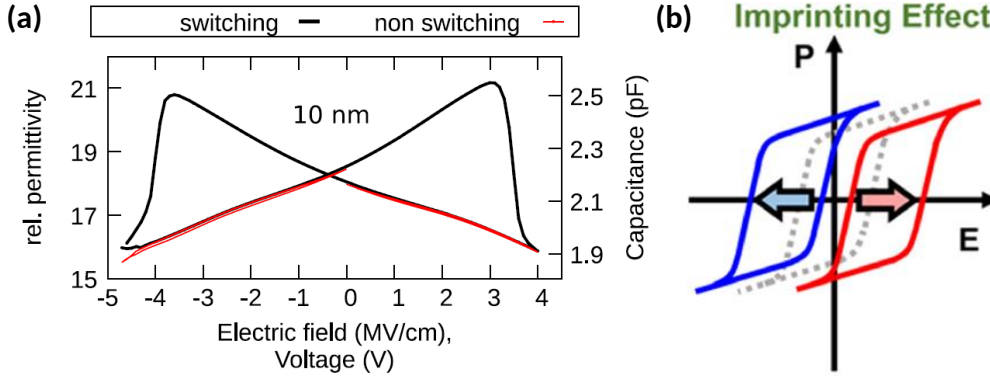


Figure 3.14: (a) Imprint effect indicated by marked difference between $|E_c^+|$ and $|E_c^-|$ values in C-V curve of AlScN capacitor [101]. (b) Imprint effect illustrated by shifting the P-E hysteresis [179].

The C-V measurements in this research are conducted using Keysight/Agilent E4980A Precision LCR Meter [inductance (L), capacitance (C), and resistance (R)]. To avoid the influence of noise, flip measurement is adopted, i.e., TE is grounded while voltage bias is applied to BE. The measurement frequency and the small signal voltage are set to 1 MHz and 25 mV, respectively. Besides, ϵ_i values of AlScN films are extracted from the cross-points of the C-V loops.

3.2.5. Time-Zero Dielectric Breakdown

TZDB is a DC I-V measurement but with monotonical increasing voltage bias until the capacitor breakdown [181]. The information of leakage current and breakdown strength in ferroelectric films can be unveiled. For AlScN, the leakage current level is influenced by switching cycle [133], [134], as introduced in section 2.3.1. Therefore, in this research, fresh AlScN capacitors are used for TZDB measurements. Figure 3.15 delineates the TZDB results of two AlScN capacitors which experienced positive and negative bias to breakdown respectively. The current levels at both sides are almost identical when the bias is under ± 20 V. However, the capacitor with negative bias

sweep show switching behavior due to poling-free and natural N-polar characteristics of AlScN [93], [94], [97], [162], as introduced in section 2.3.4. It is apparent that the breakdown strength is stronger at the positive side.

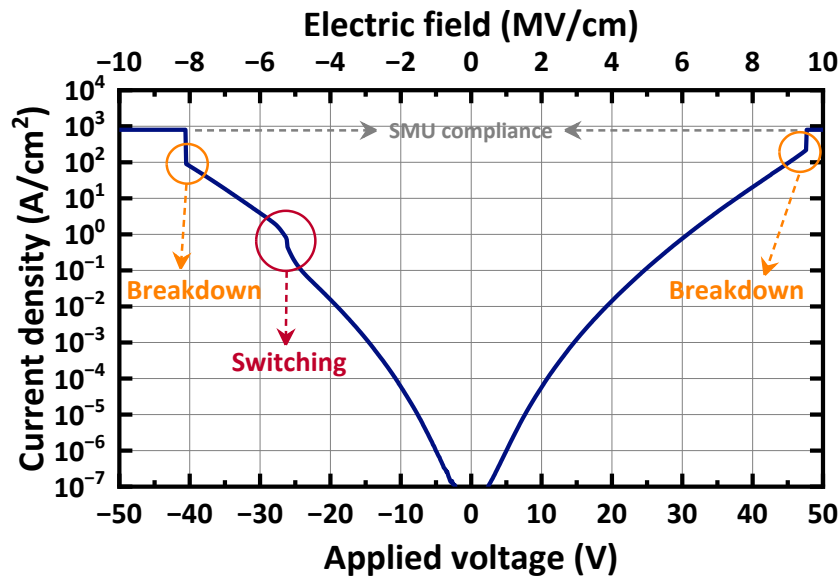


Figure 3.15: TZDB relationships of two as-deposited TiN/AlScN/TiN capacitors underwent positive and negative sweep.

This research utilizes a Keysight/Agilent 4156C Precision Semiconductor Parameter Analyzer to conduct TZDB measurements. The current compliance is set as high as possible to ensure the AlScN ferroelectric capacitors exhibit breakdown event. For simplicity, TZDB results are mainly presented and compared using the positive sweep to avoid switching event.

Chapter 4: Exploration of Reactive Sputtering Conditions for Aluminum Scandium Nitride Thin Films

4.1. Introduction

In this research, reactive sputtering method is adopted to deposit ferroelectric AlScN thin films. This chapter discusses the exploration of deposition conditions that are utterly important for reliable and scalable films. For AlScN thin films, the urgent tasks are enhancing endurance cycle and achieving low-voltage operation, which are related to ferroelectric and dielectric properties such as leakage current, P_r , E_c , E_{BD} , and ϵ_i . As high P_r value is the essence of AlScN, it is desirable to suppress leakage, minimize E_c , boost E_{BD} , and decrease ϵ_i while maintaining sufficient P_r . Herein, the goals are crystal clear.

Based on literatures [117], [182], [183], specific condition parameters for process temperature, DC power and Ar/N₂ gas flow ratio are determined to be 400°C, 300 W and 5/10 sccm/sccm, respectively, to provide the best properties for AlScN thin films. The influence of other sputtering conditions will be discussed as follows.

Section 2.3. elucidated the role of Sc composition in Al_{1-x}Sc_xN films. Various properties could be influenced. Therefore, in section 4.2., the dependence of Sc content in AlSc alloy targets for deposited films is shown. Moreover, the effect of sputtering process pressure and T/S distance are demonstrated in sections 4.3. and 4.4., respectively.

4.2. Dependence of Composition of Aluminum Scandium Target

In this section, the influence of the composition of AlSc alloy sputtering target is discussed.

4.2.1. Experimental Details

The fabrication process of AlScN ferroelectric films mainly followed the description in section 3.1. For the purpose of comparing the influence Sc composition in AlScN thin

films, two samples were fabricated with two different targets. Herein, a high-Sc target ($\text{Al}_{0.53}\text{Sc}_{0.47}$) and a low-Sc target ($\text{Al}_{0.8}\text{Sc}_{0.2}$) were utilized. It should be noted that the process pressure for high-Sc and low-Sc targets were 0.65 Pa and 0.55 Pa, respectively. The reason will be explained in section 4.3. Table 4.1 summarizes the deposition conditions of AlScN films.

TABLE 4.1
SPUTTERING CONDITIONS FOR ALUMINUM SCANDIUM NITRIDE

Deposition parameters		
Sputtering target	$\text{Al}_{0.53}\text{Sc}_{0.47}$ (80 mm dia.)	$\text{Al}_{0.8}\text{Sc}_{0.2}$ (80 mm dia.)
Process temperature (°C)	400	
DC power supply (W)	300	
T/S distance (mm)	100	
Process pressure (Pa)	0.65	0.55
Ar/N ₂ gas flow (sccm)	5/10	

4.2.2. Crystallinity and Composition of Deposited AlScN Thin Films

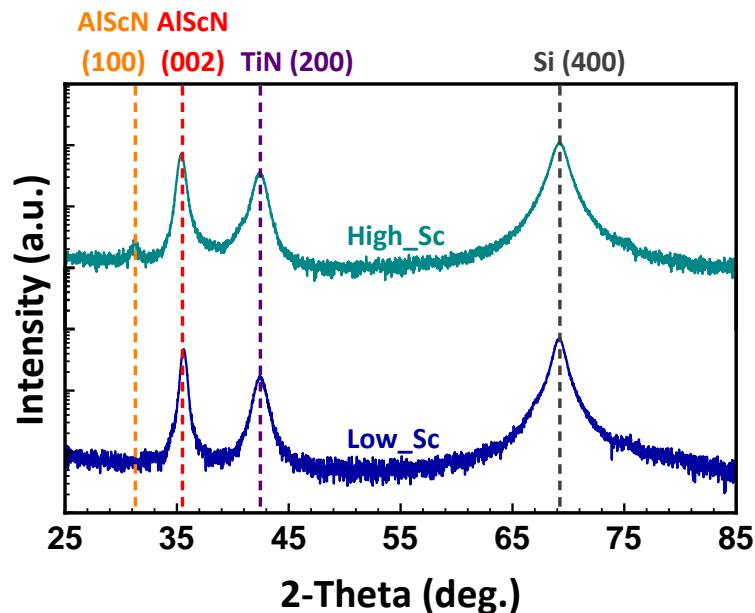


Figure 4.1: XRD analysis for $\text{Al}_{1-x}\text{Sc}_x\text{N}$ films deposited with high-Sc ($\text{Al}_{0.53}\text{Sc}_{0.47}$) and low-Sc ($\text{Al}_{0.8}\text{Sc}_{0.2}$) targets. High c-axis crystallinity is shown in both films.

To prevent surface oxidation and to match the deposition situation during capacitor fabrication, the ferroelectric layer is sandwiched between 10 nm TiN BE and 30 nm TiN TE. Figure 4.1 depicts the results of out-of-plane XRD analysis. Prominent AlScN 002 phase can be spotted in both films, indicating high c-axis orientation crystallinity. Only the film deposited with high-Sc target show a small peak of AlScN 100 phase, which is an *a*-axis oriented phase.

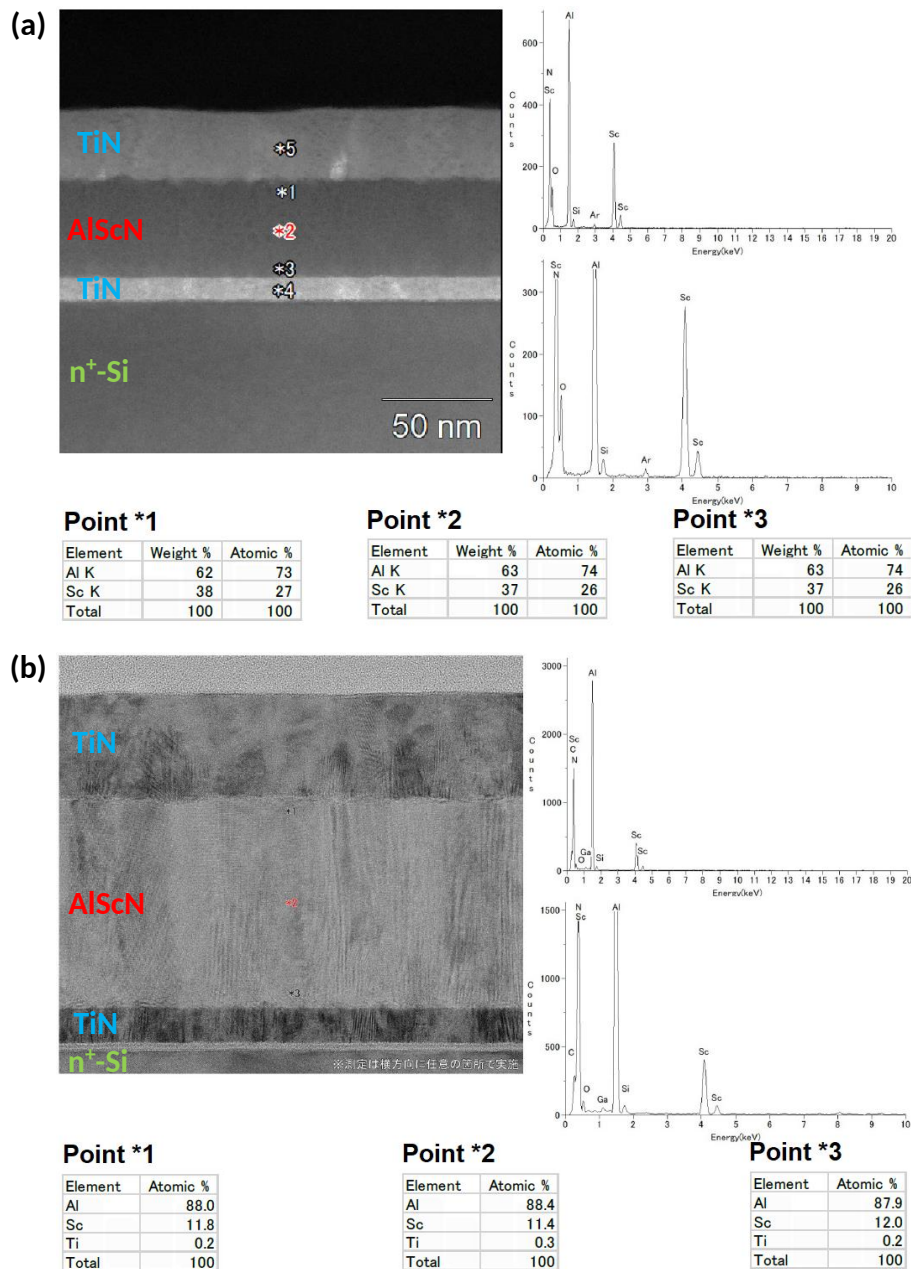


Figure 4.2: TEM and EDX analysis for chemical compositions of AlScN films deposited using (a) high-Sc ($\text{Al}_{0.53}\text{Sc}_{0.47}$) and (b) low-Sc ($\text{Al}_{0.8}\text{Sc}_{0.2}$) targets.

The chemical compositions of deposited films are revealed by TEM and EDX analysis. Figure 4.2(a) and (b) show the results for thin films deposited from high-Sc and low-Sc targets, respectively. The compositions are determined by the average values of Points 1, 2, and 3 in both films, which unveils that the compositions are $\text{Al}_{0.74}\text{Sc}_{0.26}\text{N}$ and $\text{Al}_{0.88}\text{Sc}_{0.12}\text{N}$ when high-Sc and low-Sc targets are used, respectively.

4.2.3. Dielectric and Ferroelectric Properties

Figure 4.3 delineates the butterfly-shaped C-V loops that validate the ferroelectricity in both films. As expected, lower Sc content in the film decreases ϵ [137], [184]. The ϵ_i values are 16.9 and 12.2 for high-Sc and low-Sc content films, respectively, and they are consistent with calculated results [109]. Since E_c can be defined at the peak position of C-V curves, it is apparent that low-Sc content film demonstrates higher $\pm E_c$ values, as described in section 2.3.4. Furthermore, both films exhibit higher E_c values on the negative side, i.e., imprint effect, and the height of positive peaks are higher than the negative ones. These findings suggest asymmetrical charge redistribution in a similar way during polarization switching, in spite the change of Sc content.

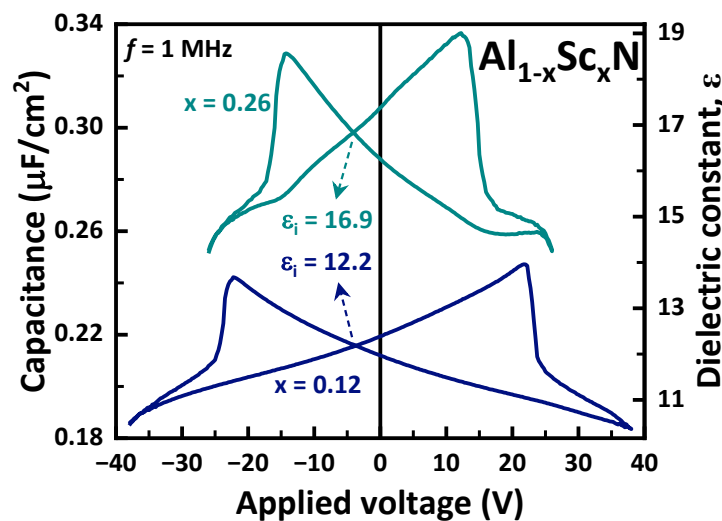


Figure 4.3: Butterfly C-V curves of 50 nm high-Sc and low-Sc content films. The measurement was conducted at 1 MHz. Cross-point of the C-V curves show the information of ϵ_i values.

Figure 4.4 reveals the TZDB results of fabricated capacitors. Note that due to the power limitations of SMU, high-Sc and low-Sc films have different compliance settings. Obviously, the low-Sc film exhibits approximately 1-2 orders of suppressed leakage

along with an enhanced E_{BD} nearly 2 MV/cm. This is attributed to E_g broadening, as mentioned in section 2.3.1. With inhibited leakage, defect generation and filament formation could be mitigated by weaker Joule-heating in low-Sc film, leading to higher E_{BD} .

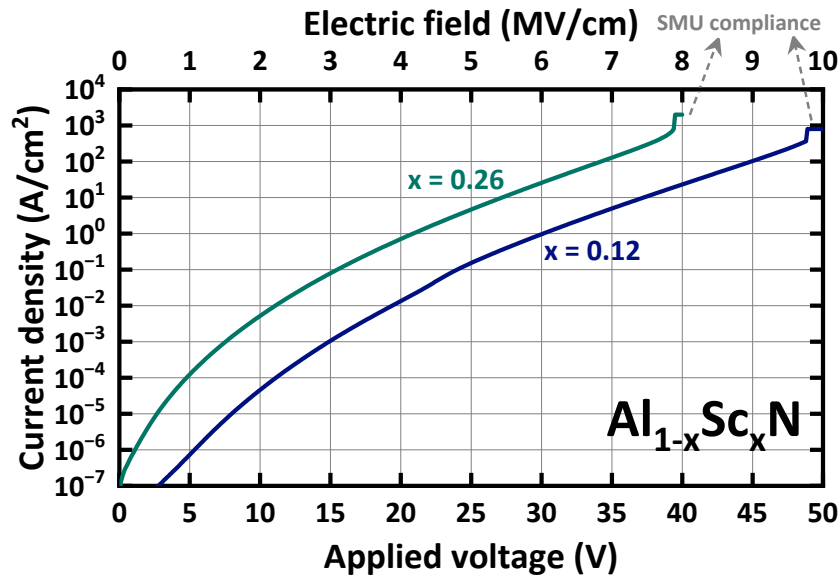


Figure 4.4: Results of TZDB measurements for 50 nm high-Sc and low-Sc content films. Different compliance settings were applied due to SMU limitations.

Figure 4.5 demonstrates the P_r - E relationship from PUND measurement, and low-Sc content film is able to generate higher P_r before breakdown incident occurs. Interestingly, the semi-saturation kink appears at a higher P_r value. Additionally, by linear extrapolating the rising P_r [117], E_c values are extracted as 4.2 MV/cm and 5.8 MV/cm for high-Sc and low-Sc content films, respectively. The above results precisely follow the description in section 2.3.3. and section 2.3.4. Besides, the linear extrapolation slope is higher for low-Sc content film, suggesting lower E_c variability among ferroelectric domains.

Currently, the lowest Sc contents of ferroelectric AlScN films are reported to be 10% by Yasuoka *et al.* [117], and 11% of this research (chapter 5). With Sc content under 10%, the dielectric and ferroelectric properties of low-Sc content film are expected to improve, which are advantageous for future RF electronics and NVM applications, despite the E_c is increased. High E_c is a double-edge sword since the possibility of undesired polarization reversal is lower due to better immunity to noise

from the electrical circuit, but the read-write power consumption is a concern. Therefore, it is suggested that the minimum Sc content should be ~5% to prevent excessively high E_c . Fortunately, the power consumption issue can be compensated with film thickness downscaling as the operation voltage is lowered.

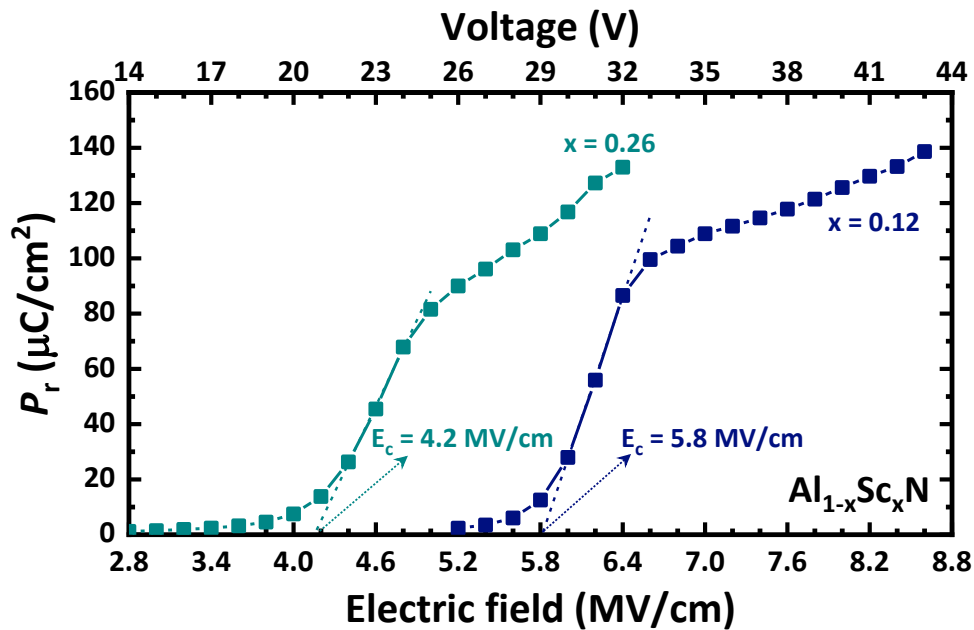


Figure 4.5: P_r -E relationship of PUND measurements for deposited films. E_c values were extracted via linear extrapolation of the rising P_r before reaching semi-saturation kinks [117].

4.3. Dependence of Process Pressure

In this section, the influence of process pressure during AlScN thin film deposition in the chamber is discussed.

4.3.1. Experimental Details

The fabrication process of AlScN ferroelectric capacitors mainly followed the description in section 3.1. As briefly mentioned in section 3.1.2., for reactive sputtering process, there are some factors to limit the minimum chamber pressure for plasma ignition and stable glow discharge [185], [186]. These factors include sputtering power, target material, partial pressure of reactive gas, etc. In this section, sputtering power

and the gas mixture are fixed as 300 W and Ar (5 sccm)/N₂ (10 sccm), respectively, whereas separate comparisons of process pressure for high-Sc target (Al_{0.53}Sc_{0.47}) and low-Sc target (Al_{0.8}Sc_{0.2}) are demonstrated. Table 4.2 summarizes the deposition conditions of AlScN films. It should be clarified that the deposition rate is independent to the process pressure.

TABLE 4.2
SPUTTERING CONDITIONS FOR ALUMINUM SCANDIUM NITRIDE

Deposition parameters		
Sputtering target	Al _{0.53} Sc _{0.47} (80 mm dia.)	Al _{0.8} Sc _{0.2} (80 mm dia.)
Process temperature (°C)	400	
DC power supply (W)	300	
T/S distance (mm)	100	
Process pressure (Pa)	0.65, 0.75, 0.85, and 0.95	0.6, 0.75, and 0.9
Ar/N ₂ gas flow (sccm)	5/10	

4.3.2. Dielectric and Ferroelectric Properties

For AlScN films deposited with high-Sc target (Al_{0.53}Sc_{0.47}), the results of C-V measurements are depicted in Figure 4.6. All high-Sc content films show clear butterfly shape, which suggest the presence of ferroelectricity. As the films are 50 nm thick, ϵ_i values are calculated as 21.1, 21.9, 22.7, and 24.3 for 0.65 Pa, 0.75 Pa, 0.85 Pa, and 0.95 Pa films, respectively. Furthermore, $\pm E_c$ values show monotonically decreasing trends with increasing process pressure. In fact, early studies have shown that tuning the process pressure condition is one straightforward approach to achieve strain engineering in sputtered thin films [187], [188]. For AlScN thin films, it has been verified that in-plane compressive strain exists [189], [190], [191], and the polarization reversal barrier can be lowered by changing the stress/strain level [89], [192]. Rassay *et al.* demonstrated that E_c is lowered when the compressive strain becomes relaxed or even tensile [193]. Herein, the changes in ϵ and E_c can be ascribed to the variation of strain inside the films, which is in correspondence with bond angles, bond lengths and c/a ratio in wurtzite structure [109], [194]. Therefore, the E_c dependence of

process pressure in this case can be understood. Additionally, though further investigation is needed, it should be considered that the c-axis crystallinity of sputtered films, i.e., intensity of AlScN 002 phase, might also be another reason as it is altered at different gas pressure [195], [196], [197], [198].

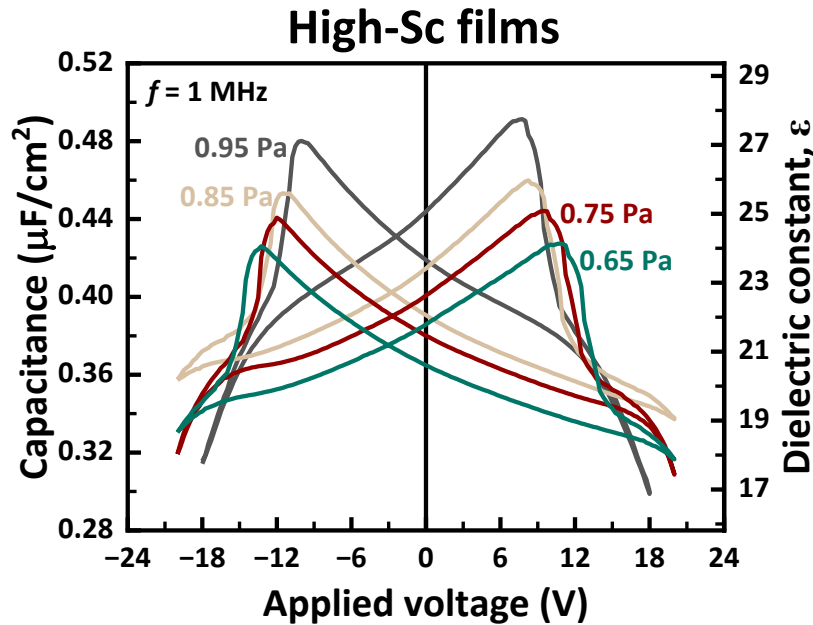


Figure 4.6: Butterfly-shaped C-V curves of 50 nm high-Sc content films. ϵ increases with process pressure.

Figure 4.7 illustrates leakage and E_{BD} properties of all high-Sc content films. Apparently, lower process pressure gives rise to enhanced E_{BD} , which is advantageous. For 0.65 Pa and 0.75 Pa films, the breakdown event happened at higher current level, comparing to 0.85 Pa and 0.95 Pa films. This implies that the films deposited at low pressure are more sustainable under voltage stress. Considering 0.65 Pa, 0.75 Pa, and 0.95 Pa films, the leakage current follows the trend that lower pressure leads to lower leakage. This is invoked to the amount of existing V_N inside the deposited films [134]. Since N_2 possesses triple bond, the dissociation energy is higher than O_2 and H_2 , as shown in Table A1.1. At higher chamber pressure, owing to shorter mean free path to collision, the dissociation is even more difficult, leading to insufficient nitridation of the films. Also, the E_{BD} is decreased due to Joule heating as higher leakage current is passing through. Another explanation to this trend is the number of abnormally oriented grains, pores, and surface roughness of the deposited films [198]. As the process pressure increases, the degree of densification in the films lowers and results

in higher leakage current. In the case of 0.85 Pa film, the slightly suppressed leakage current might be the cause of process variation.

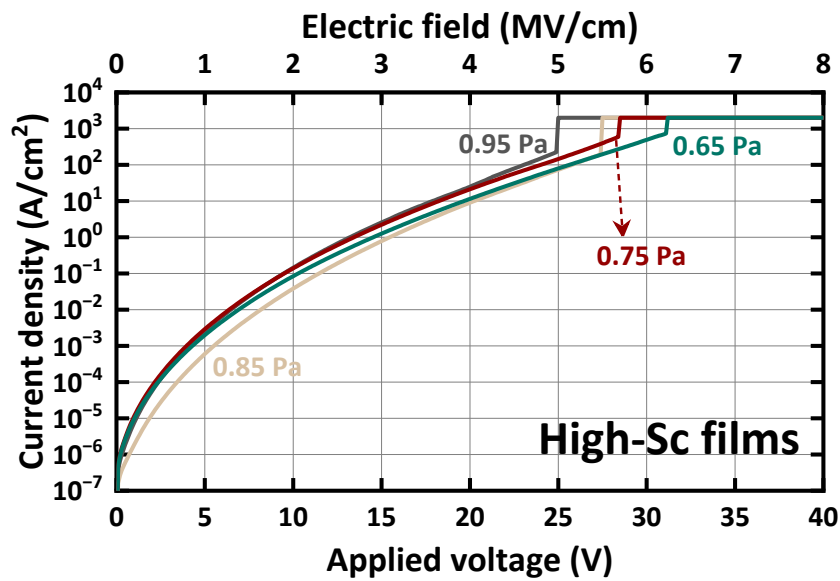


Figure 4.7: Leakage current and breakdown properties of high-Sc content films.

E_{BD} tends to increase with lower process pressure.

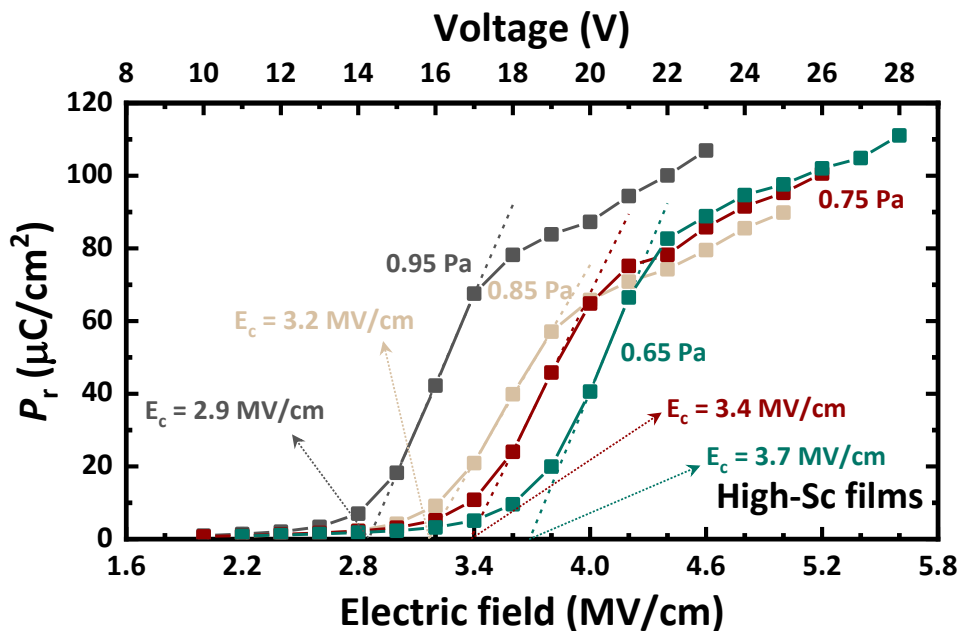


Figure 4.8: P_r -E relationship of PUND measurements for high-Sc content films.

Results of PUND measurements for high-Sc content films is revealed in Figure 4.8. The P_r values are similar and sufficient, as $80 \mu\text{C}/\text{cm}^2$ are achievable in all films. The

semi-saturation kink seems to appear at higher P_r at lower pressure conditions. Plus, as the breakdown strength is enhanced in 0.65 Pa, P_r -E relationship can extend toward higher E regions. It is obvious that as the process pressure decreases, E_c increases from 2.9 to 3.7 MV/cm, which is consistent with Figure 4.6.

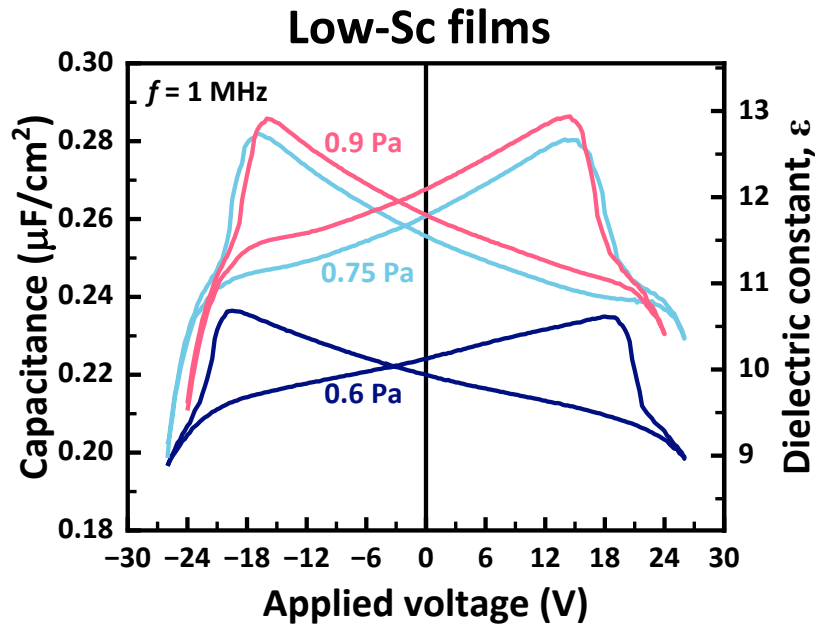


Figure 4.9: C-V loops of 40 nm low-Sc films. ϵ increases with process pressure.

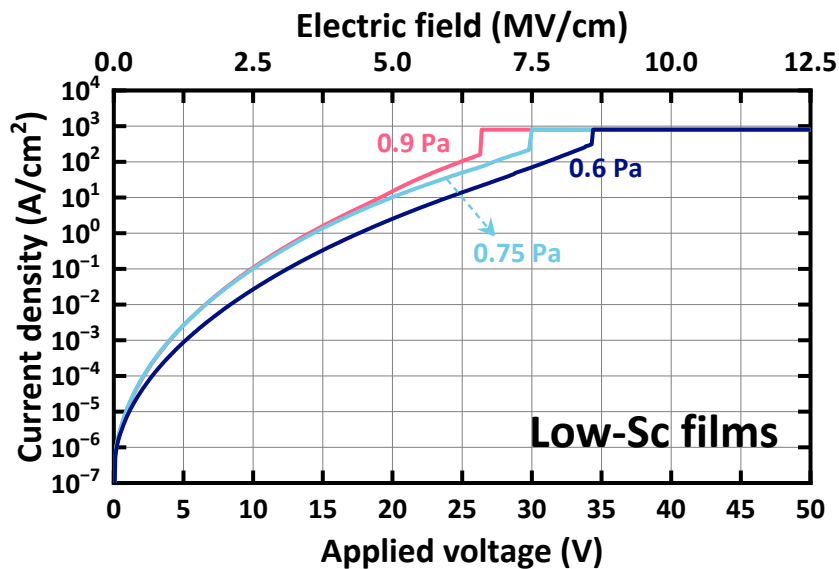


Figure 4.10: Leakage current and breakdown properties of 40 nm low-Sc content films. Suppressed leakage and boosted E_{BD} can be obtained in the films deposited with lower process pressure.

C-V loops in Figure 4.9 presents ferroelectricity in all 40 nm low-Sc content films which were deposited with various process pressure. Similarly, ϵ is found to be increased with higher process pressure, and the derived ϵ_i values are 10, 11.7, and 11.9 for 0.6 Pa, 0.75 Pa, and 0.9 Pa films, respectively. It has been shown that Sc sites are more sensitive to stress/strain than Al sites in wurtzite crystals [110]. Therefore, it is reasonable that ϵ_i variation are not as significant as the high-Sc content case. Again, the $\pm E_c$ values show decremental trend as the process pressure is increased.

Figure 4.10 displays the characteristics of leakage current and E_{BD} for 40 nm low-Sc content films. Similar to high-Sc content films, as the process pressure is lowered, leakage is found to be decreased along with improved E_{BD} .

In summary, all high-Sc and low-Sc content films generally show decreased ϵ , suppressed leakage, and enhanced E_{BD} at lower gas pressure conditions. Although E_c is slightly increased, the discovered results suggest that the improvement of AlScN thin film quality can be assisted with reducing the chamber pressure during sputtering deposition. Consequently, in section 4.2. and section 4.4., the lowest possible pressure values are adopted. In addition, it should be noted that E_c and E_{BD} share the same tendency in both high-Sc and low-Sc cases [117].

4.4. Dependence of Target/Substrate Distance

In this section, the influence of T/S distance during AlScN thin film deposition is discussed.

4.4.1. Experimental Details

The fabrication process of AlScN ferroelectric capacitors mainly followed the description in section 3.1. However, the T/S distance varies among 100, 125, and 150 mm, which are the minimum and maximum achievable values of our sputtering machine. Here, low-Sc target ($Al_{0.8}Sc_{0.2}$) is utilized. Note that since the deposition rate is greatly influenced by T/S distance [199], individual deposition time are determined for all films to meet the goal of 50 nm. Table 4.3 summarizes the deposition conditions of AlScN films.

TABLE 4.3

SPUTTERING CONDITIONS FOR ALUMINUM SCANDIUM NITRIDE

Deposition parameters	
Sputtering target	$\text{Al}_{0.8}\text{Sc}_{0.2}$ (80 mm dia.)
Process temperature ($^{\circ}\text{C}$)	400
DC power supply (W)	300
T/S distance (mm)	100, 125, and 150
Process pressure (Pa)	0.55
Ar/ N_2 gas flow (sccm)	5/10

4.4.2. Dielectric and Ferroelectric Properties

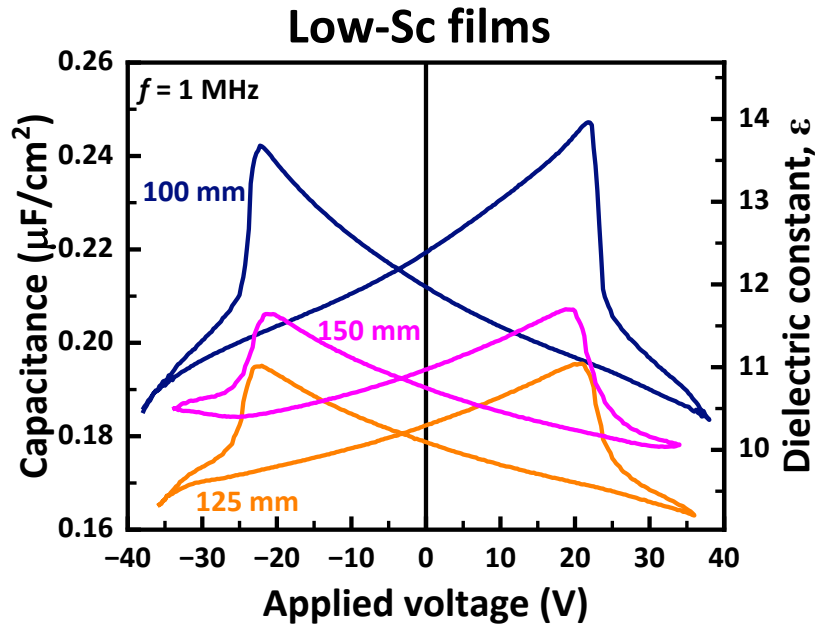


Figure 4.11: Butterfly C-V loops of films deposited with various T/S distance.

Figure 4.11 depicts the C-V curves for 50 nm low-Sc content films. ϵ decreased considerably when the T/S distance is increased from 100 to 125 mm. However, the ϵ regained as the T/S distance increased from 125 to 150 mm. ϵ_i values are calculated as 14.6, 12.2, and 13 for 100 mm, 125 mm, and 150 mm films, respectively. For reactive sputtering, similar to process pressure, T/S distance could impose impact on the crystal orientation and strain status of the film [195], [196], [200]. The ϵ shrinkage between 100 mm and 125 mm can be ascribed to the formation of a -axis oriented grains (AlScN

100 phase), though further XRD analysis is required [201]. For the 150 mm film, the $\pm E_c$ values declined and ϵ_i increased with respect to 100 mm film, indicating that the strain effect took over the influence of a -axis oriented grains.

Figure 4.12 delineates the results obtained from TZDB measurements. All low-Sc content films exhibit almost identical leakage current, whereas E_{BD} is boosted by reducing the T/S distance. The deteriorated breakdown strength in higher T/S distance films can be attributed to the strain effect. Moreover, the E_{BD} trend here roughly follows the dependence of E_c values, which is in consistency with the summary at the end of section 4.3.2.

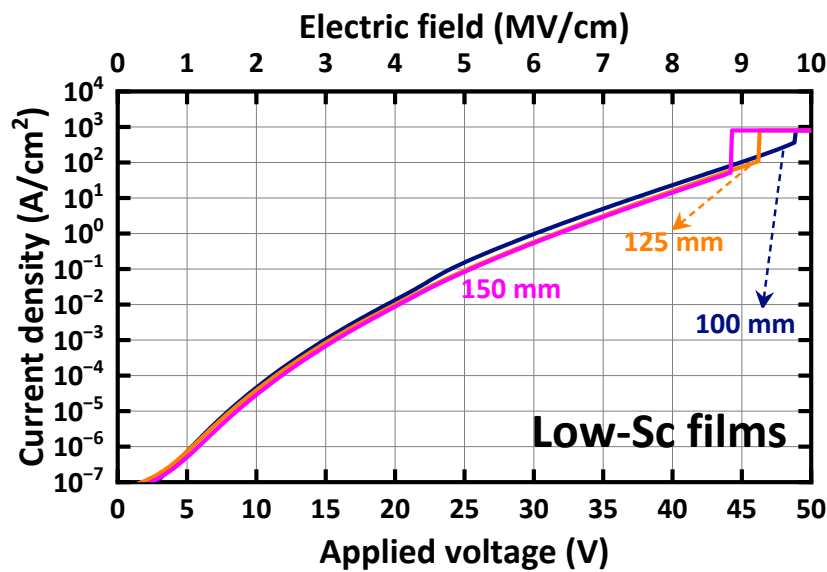


Figure 4.12: TZDB results of 50 nm low-Sc content films.

Measurement results of PUND are illustrated in Figure 4.13. 100 mm generates the highest P_r overall and the semi-saturation kink is obvious. As the T/S distance increases to 125 mm, P_r drastically decreases, implying degraded c -axis orientation in the film. However, the P_r slightly recovers at low E region, which could be related to the strain effect. More ambiguous semi-saturation kinks are found when the T/S distance gains. Moreover, the E_c variation trend from PUND is similar to the trend of E_c of C-V measurement in Figure 4.11. The values are 5.8, 6, and 5.8 MV/cm for 100 mm, 125 mm, and 150 mm films, respectively. Although 100 mm and 150 mm films demonstrate almost the same E_c , the P_r performance of 100 mm film is more advantageous. Considering the overall dielectric and ferroelectric characteristics, 100 mm of T/S distance is the most optimal choice.

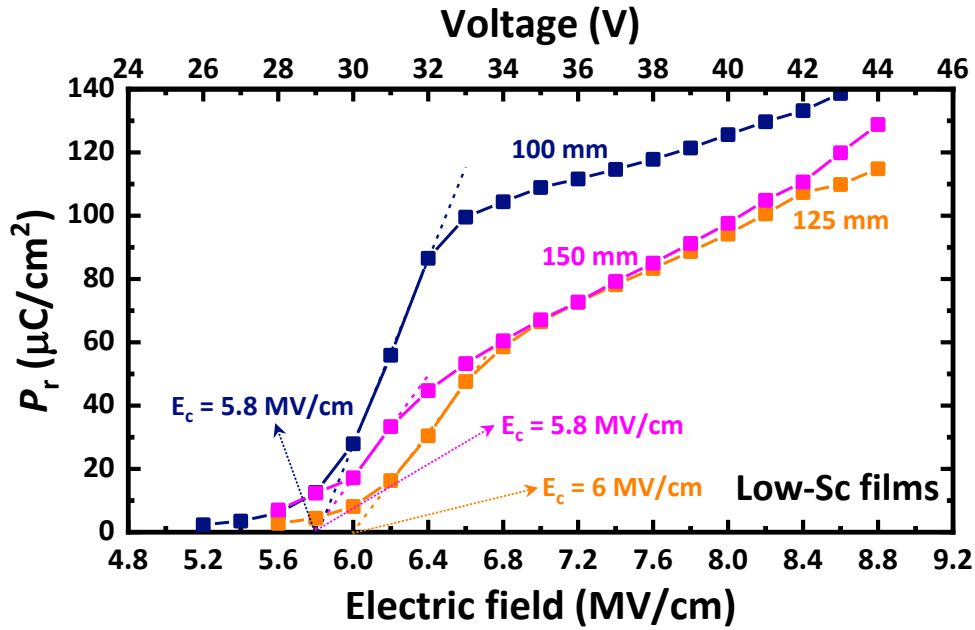


Figure 4.13: P_r -E relationship of PUND measurements for low-Sc content films deposited with various T/S distance.

4.5. Summary of This Chapter

To conquer the challenges that AlScN faces toward advanced memory technology, it is clear that suppressing undesired leakage, improving E_{BD} , lowering ϵ_i , minimizing E_c while sustaining high P_r are urgent tasks. It is intuitive to consider the switching and breakdown mechanisms are governed by the crystal structure of wurtzite AlScN. In this chapter, exploration of sputtering conditions for highly reliable and scalable AlScN thin films is conducted, as detailed in Table 4.4.

It is suggested that the Sc content that falls in the range of 5-15% is advantageous, considering the insulating properties and E_c dependence of the film. By utilizing the lower Sc content ($Al_{0.8}Sc_{0.2}$) alloy target, the unwanted leakage current can be significantly decreased thanks to E_g broadening. E_{BD} is enhanced and ϵ_i is lowered accordingly. Besides, the increased P_r values are consistent with section 2.3.3.

Changing the process pressure is another effective approach to engineer the stress/strain status and the amount of V_N inside thin films. For AlScN, decreasing the sputtering pressure could prevent creation of V_N so that the leakage current can be

inhibited along with boosted breakdown strength. Better surface roughness benefits the insulating properties. The reduced ϵ_i and increased P_r could also be advantageous.

As for T/S distance, it is discovered that when T/S distance is fine tuned, better E_{BD} and P_r can be realized. Orientated grains along c -axis could be greatly influenced in the meantime.

TABLE 4.4
INFLUENCES OF SPUTTERING CONDITIONS

Sputtering conditions	Operation	Influenced properties
Sc content of the target	Low (produce 5-15% of Sc concentration in film)	Suppressed leakage Improved E_{BD} Lower ϵ Increased P_r Increased E_c
Process pressure	Low	Larger compressive strain Less V_N Better surface roughness Better c -axis crystallinity Suppressed leakage Improved E_{BD} Lower ϵ Increased P_r Increased E_c
T/S distance	Suitable	Larger compressive strain Better c -axis crystallinity Suppressed leakage Improved E_{BD} Increased P_r Decreased E_c

In summary, low Sc content target, low process pressure, and suitable T/S distance are favorable for leakage suppression and improved E_{BD} , which are beneficial for endurance performance. However, a trade-off relationship between E_c and E_{BD} is

discovered. Applying the aforementioned approaches could also lead to more in-plane compressive strain that give rise to higher E_c and power consumption concern. Fortunately, this issue can be resolved by thickness downscaling as the operation voltage is lowered.

The following chapters will generally follow the determined deposition conditions in this chapter to achieve better film quality.

Chapter 5: Defect Engineering for Aluminum Scandium Nitride Thin Films by Oxygen Incorporated Sputtering

5.1. Introduction

Literatures have already addressed that defects play a critical role in ferroelectricity of PZT and HfO₂-based ferroelectrics, e.g., wake-up, fatigue, imprint, etc. [202], [203], [204], [205]. Therefore, it can be expected that defects might influence the ferroelectric behavior of III-N ferroelectrics [124], [206]. For AlN films, oxygen has generally been recognized as an aliovalent impurity and the origin of defect centers [207], [208], [209]. As described in section 2.2.2., oxygen contamination is a commonly observed phenomenon in sputter deposited AlN films. Since Al and Sc atoms possess strong affinity toward oxygen, competition occurs between residual oxygen and supplied nitrogen during the reactive sputtering process from AlSc targets, forming partially oxidized Al_{1-x}Sc_xN ferroelectric or Al_{1-x}Sc_xON [123]. Indeed, researchers have experimentally shown that blending slight amount of O₂ into the Ar/N₂ gas mixture can greatly influence the oxygen content [210].

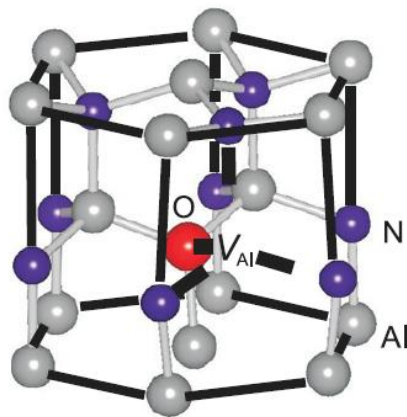


Figure 5.1: AlN wurtzite lattice with complex defect of $(V_{Al}-O_N)^{2-}$ [208]. The cationic sites (Al/Sc) are only coordinated with anionic sites (O/N) in the wurtzite lattice.

Other researches have pointed out that including oxygen atoms to AlN films initially replaces nitrogen atoms in the crystal, and thereby forming O_N [211], [212], similar to the surface oxidation case [149]. At high oxygen concentrations, Al atoms

are reported to be stabilized by bonding octahedrally to the adjacent oxygen atoms [212]. As oxygen concentration becomes higher, the formation of O_N energetically favors the creation of V_{Al} , thereby forming $V_{Al}-O_N$ defect complexes [213]. Figure 5.1 illustrates the $V_{Al}-O_N$ complex defect in AlN wurtzite lattice. In fact, with various spatial and atomic configurations, the defect complexes in the forms of $(V_{Al}-O_N)^{2-}$ and $(V_{Al}-2O_N)^{1-}$ could co-exist in thermal equilibrium [214].

Moreover, introducing oxygen atoms has been shown to reduce the bandgap, lowering both the conduction and valence band offsets to the electrode, raising concerns about leakage current [215]. Crystallinity degradation and incremental domain inversion boundaries are other issues that could be induced with high level oxygen impurities [216]. Moreover, since Sc possesses larger oxygen affinity than Al [123], oxygen-related defects could become particularly invasive while using high-Sc content AlSc targets [217].

In this chapter, in order to characterize the influence of oxygen-induced defects, $Al_{1-x}Sc_xN$ thin films were fabricated with and without intentional O_2 input gas. For the purpose of avoiding excessively high oxygen content in the film, the O_2 flow is limited up to 0.45 sccm in the Ar (5 sccm)/ N_2 (10 sccm) gas ambient, along with a low-Sc content sputtering target. It has been found that oxygen incorporation effectively shrinks E_c and reduces leakage while high P_r is preserved. The presence of $V_{Al}-O_N$ defect complexes also allows for controllable imprint effects. By increasing the oxygen content in the $Al_{1-x}Sc_xN$ films, a nearly linear increase in P_r over E is presented, which is promising for NVM devices in analog circuits for AI applications. In addition, benefiting from these findings, an aggressively scaled AlScON film down to 9 nm was fabricated and characterized.

5.2. Experimental Details

The fabrication process of AlScN ferroelectric capacitors mainly follows the description in section 3.1. In order to include oxygen-atom into 50 nm AlScN thin films, an additional gas inlet is used to blend O_2 (0-0.45 sccm) gas into Ar (5 sccm)/ N_2 (10 sccm) sputtering ambient. Note that the deposition rate remains unchanged with different O_2 flow. Herein, the low-Sc target ($Al_{0.8}Sc_{0.2}$) is utilized along with 0.6 Pa of process

pressure. Table 5.1 summarizes the deposition conditions of AlScON films. Besides, XPS and XRD characterizations are implemented to understand the chemical compositions and crystal orientations in the oxygen-incorporated ferroelectric films, as will be detailed in next section.

TABLE 5.1
SPUTTERING CONDITIONS FOR ALUMINUM SCANDIUM OXYNITRIDE

Deposition parameters	
Sputtering target	Al _{0.8} Sc _{0.2} (80 mm dia.)
Process temperature (°C)	400
DC power supply (W)	300
T/S distance (mm)	100
Process pressure (Pa)	0.6
Ar/N ₂ gas flow (sccm)	5/10
O ₂ gas flow (sccm)	0, 0.15, 0.3, and 0.45

5.3. Material Analysis of Ferroelectric Films Deposited with Oxygen Flux

Figure 5.2 displays information of XPS narrowscan and the calculated compositions of the deposited films. For XPS inspection, the top 30 nm TiN layer is sputter-etched away by Ar in the XPS chamber to reach the AlScON layer. Owing to this sputtering process, C 1s spectra is hardly observed. Therefore, N 1s peak is utilized to calibrate the peak position. The intensity of the spectrum is normalized by the area of the Al 2p spectra. With this inspection, the oxygen atom concentration can be calculated as Figure 5.2 shows. This reveals that the oxygen content (y) ranges from 0.05 to 0.23 with a fixed scandium content (x) of 0.11. Although the base pressure of the sputtering chamber was kept below 10^{-6} Pa before MFM stack deposition, a small amount of oxygen was still incorporated into the film without additional O₂ gas flow ($y = 0.05$), indicating the presence of residual oxygen inside the chamber or the target [118], [122], [124]. Furthermore, it is crucial to understand the status of bonding in AlScON films with various oxygen levels. Since Al serve as an electron donor in Al-O-N system, Al 2p peaks here showed ~ 74.1 eV of binding energy, higher than Al metal

(72.6 eV). As oxygen content increases, the peak shift toward higher binding energy results from larger electronegativity of O atoms and more Al-O bonds. Similar explanation could be applied to Sc 2p peaks. Note that the electronegativity values of Al, Sc, O, and N are 1.61, 1.36, 3.44, and 3.04, respectively. Additionally, for O 1s peaks, shift toward higher energy is observed in higher oxygen concentration films. This shows that when the oxygen concentration is low, O atoms tend to bond with Sc atoms. As the oxygen concentration increases, the amount of Al-O bonds (532.5 eV) increases and become comparable to Sc-O bonds (531.8 eV). Overall, from the observations, more Al-O bonding and Sc-O bonding were replacing Al-N and Sc-N bonding, respectively.

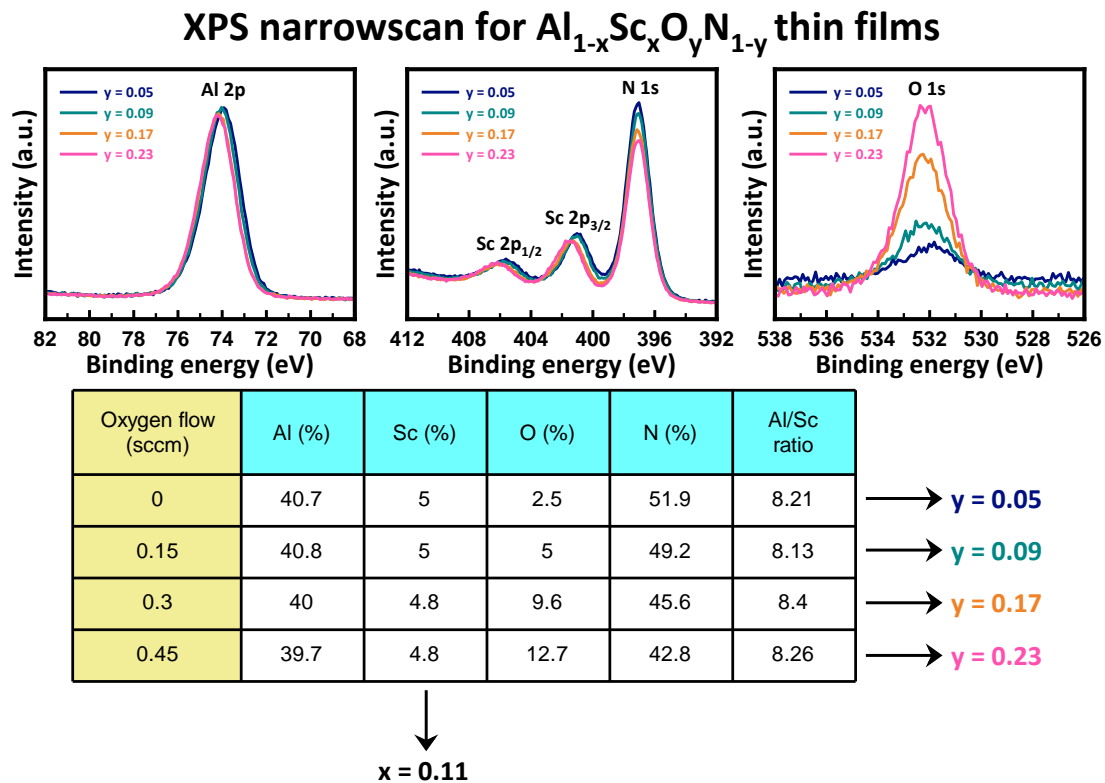


Figure 5.2: XPS spectra and extracted composition of 50 nm AlScON films. The X-ray source is Monochromatic Al K α (1486.6 eV), and the inspection area is 100 μm^2 ($7.854 \times 10^3 \mu\text{m}^2$). The photoelectron TOA is set to 90°, and the inspection depth is 9 nm. The measurement accuracy is within ± 1 at.-%.

The out-of-plane X-ray diffraction (XRD) patterns of the $\text{Al}_{0.89}\text{Sc}_{0.11}\text{O}_y\text{N}_{1-y}$ films are depicted in Figure 5.3(a). For the lowest oxygen content film ($y = 0.05$), a clear $\text{Al}_{0.89}\text{Sc}_{0.11}\text{N}$ 002 phase can be found at 35.6°, suggesting c -axis orientated growth

within the wurtzite crystal structure. When y increases to 0.17, the 002 peak splits into two peaks, with the peak at 36.1° corresponding to a high-oxygen-level phase, i.e., the $\text{Al}_{0.89}\text{Sc}_{0.11}\text{ON}$ 002 phase. This finding suggests that oxygen-atoms are not uniformly distributed within the films, and AlScN grains with different oxygen contents co-exist simultaneously. Other studies have reported that the lattice constant c decreases with increasing oxygen content, as shown in Figure 5.4 [218], [219]. Notably, the 002 rocking curve FWHM of the films shows similar values of approximately 11° , as indicated in Figure 5.3(b). The generally decreasing peak height indicates degraded c -axis crystallinity with more oxygen content. Further increasing the oxygen flow could sabotage the ferroelectricity, as previous research in our group discovers [183].

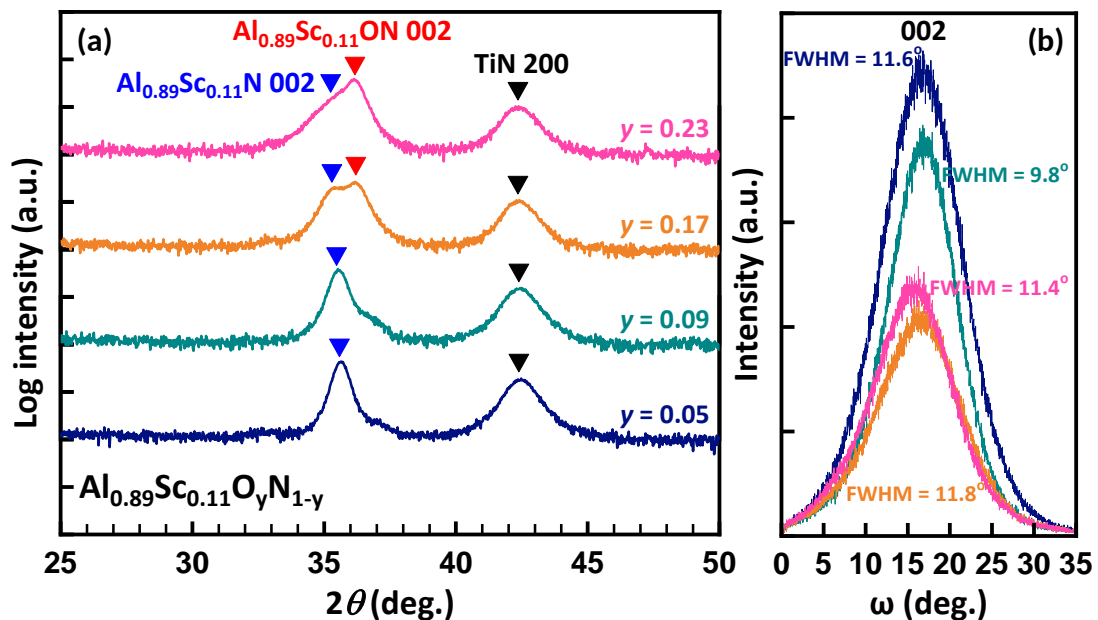


Figure 5.3: (a) Out-of-plane XRD and (b) XRC profiles on 002 plane of 50 nm AlScON films with different oxygen compositions.

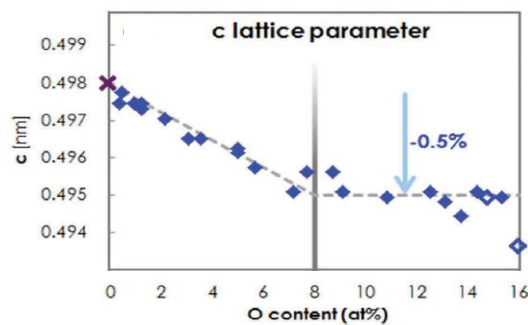


Figure 5.4: Shrinkage in lattice constant c is induced by oxygen content [218].

5.4. Influence on Ferroelectric and Dielectric Properties

5.4.1. Dielectric Constant and Imprint Effect

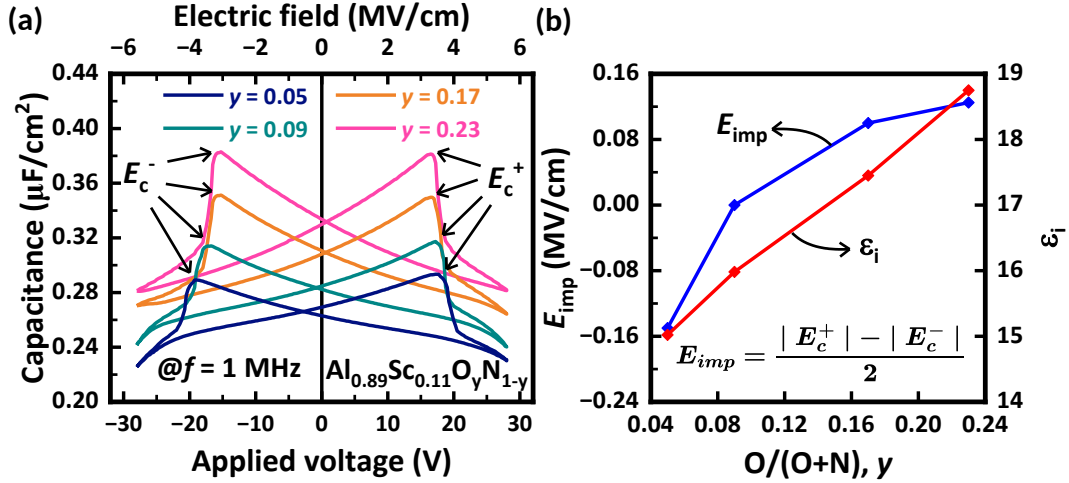


Figure 5.5: (a) Butterfly C-V curves of MFM capacitors with various oxygen contents. (b) E_{imp} and ϵ_i with respect to the oxygen content.

Figure 5.5(a) illustrates distinct butterfly shaped curves from the C-V measurements, confirming the ferroelectric switching behavior of all the deposited films. As described in section 2.5. and section 3.2.4., the imprint effect could be monitored analyzing the peak positions of the curves, i.e., positive and negative coercive field (E_c^+ , E_c^-) shift. Herein, the E_{imp} is calculated using the equation provided in section 3.2.4. and Figure 5.5(b) [175]. With the lowest oxygen content ($y = 0.05$), the E_{imp} is negative owing to favorable N-polar in the $Al_{1-x}Sc_xN$ lattice, as stated in section 2.3.4. [93], [94], [97], [162]. Increasing the oxygen content results in E_{imp} shift toward positive. This implies the switching barrier height for both polarization states can be modified by oxygen content in $Al_{1-x}Sc_xN$ films. Regarding PZT ferroelectrics, interfacial layers, electrical charges, and charged defects could lead to domain wall pinning. Considering HfO_2 -based ferroelectrics, the inhomogeneous distribution of V_O and the stress at the electrode interface due to lattice mismatch are reported as physical sources of the imprint effect [220], [221]. For AlScN, Kim *et al.* proposed that a non-ferroelectric layer and fixed charges reside near or at the AlScN/TiN interface [222]. Therefore, in this case, negatively charged V_{Al-O_N} defect complexes might compensate for the positive

fixed charges, leading to spatial redistribution of the charged defects at the ferroelectric/electrode interfaces and inducing E_{imp} migration. As a result, varying the oxygen content in the $Al_{1-x}Sc_xO_yN_{1-y}$ films offers another opportunity to control E_{imp} besides changing the specimen temperature or conducting additional field cycling [162]. Furthermore, Figure 5.5(b) displays a monotonical increase in the ϵ_i from 15 to 19 with respect to increasing oxygen concentration.

5.4.2. Leakage Current, Breakdown Field and Polarization-Electric Field Hysteresis

TZDB measurements are carried out for all $Al_{1-x}Sc_xO_yN_{1-y}$ capacitors, as disclosed in Figure 5.6(a). The results indicate suppressed leakage and enhanced E_{BD} by 1 MV/cm with increasing y . Some works have proposed that the accumulation of V_N can create leakage paths in $Al_{1-x}Sc_xN$ films, eventually leading to breakdown events [133], [134], [135]. Accordingly, we correlate the better leakage and breakdown results with the increment of O_N , as more V_N are eliminated.

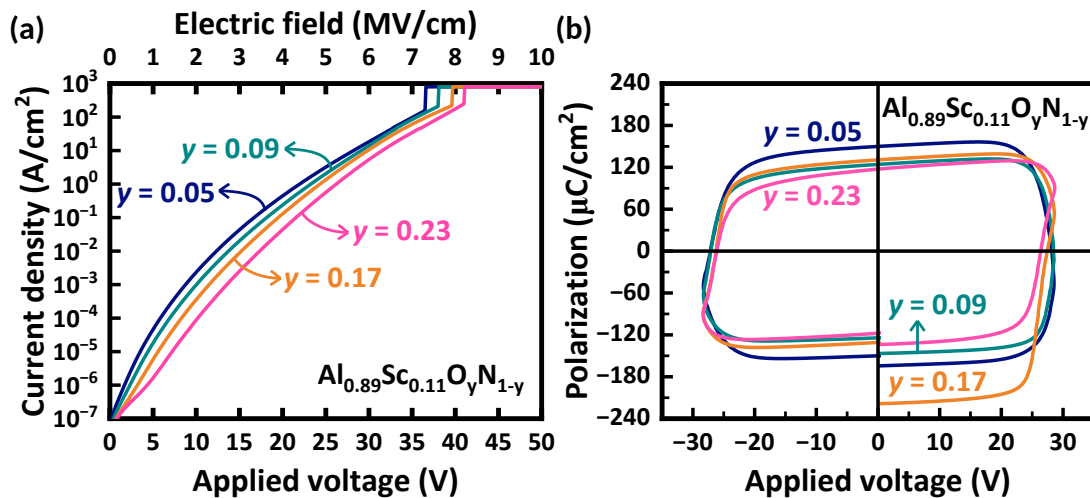


Figure 5.6: (a) TZDB characterization of all the fabricated MFM capacitors. (b) P-V hysteresis loops measured at 10 kHz for the $Al_{0.89}Sc_{0.11}O_yN_{1-y}$ films.

Figure 5.6(b) delineates box-like polarization-voltage (P-V) hysteresis loops at 10 kHz of all fabricated capacitors. Nevertheless, to avoid P_r overestimation due to leakage, PUND measurements are implemented, as detailed in the following section.

5.5. Potential of Multi-Level Operation

Figure 5.7 illustrates the dependence of P_r and E from PUND measurements for all deposited films. Utilizing the method mentioned in section 3.2.2., the negative E_c values are extracted and exhibit a decremental trend with increasing y , as evident from the lower-right inset of Figure 5.7. An E_c reduction of 0.8 MV/cm is observed between the films with lowest and highest oxygen content. This phenomenon is ascribed to the shrinkage at c -axis in wurtzite crystal [218], [223], as V_{Al} has been confirmed to be influential [219]. As a result, it is evident that higher oxygen concentration in the film gives rise to lower E_c and higher ϵ_i values, which is consistent as what Mikolajick *et al.* proposed: E_c highly interrelates to ϵ and show negative correlation [53]. Defect engineering via oxygen incorporation is the only approach discovered to mitigate the high E_c characteristics of AlScN by doping.

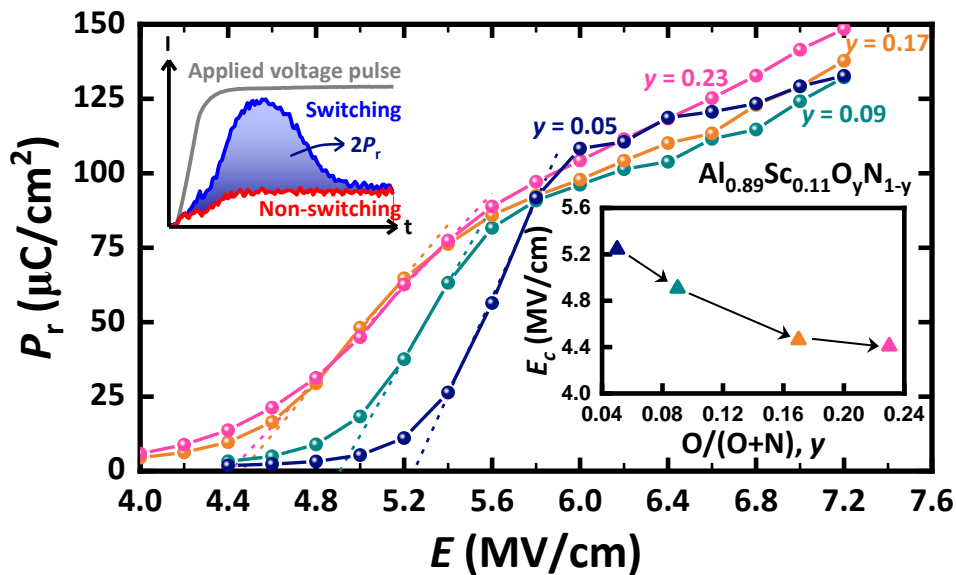


Figure 5.7: Results of PUND measurements for $\text{Al}_{0.89}\text{Sc}_{0.11}\text{O}_y\text{N}_{1-y}$ MFM capacitors with different oxygen concentrations. The upper-left inset depicts a portion of the applied pulse signal and current response during PUND. The lower-right inset shows the dependence between the linearly extrapolated negative E_c and the oxygen content.

In addition, the improved E_c/E_{BD} ratios of the oxygen-containing films are advantageous for thickness downscaling. Plus, the semi-saturation kinks become indistinguishable due to the gradually slanted slope of the extrapolation lines. These

gentler slopes imply greater V_c variability among domains where O atoms are not uniformly distributed, as revealed in the XRD profiles in section 5.3. This allows for partial polarization at lower E with higher oxygen content, resulting in a comparatively linear P_r gain over a wider range of E and potential multi-level operation [224]. Such performance is feasible and can be harnessed in analog circuits for AI applications.

5.6. Endurance Performance and Fatigue Effect

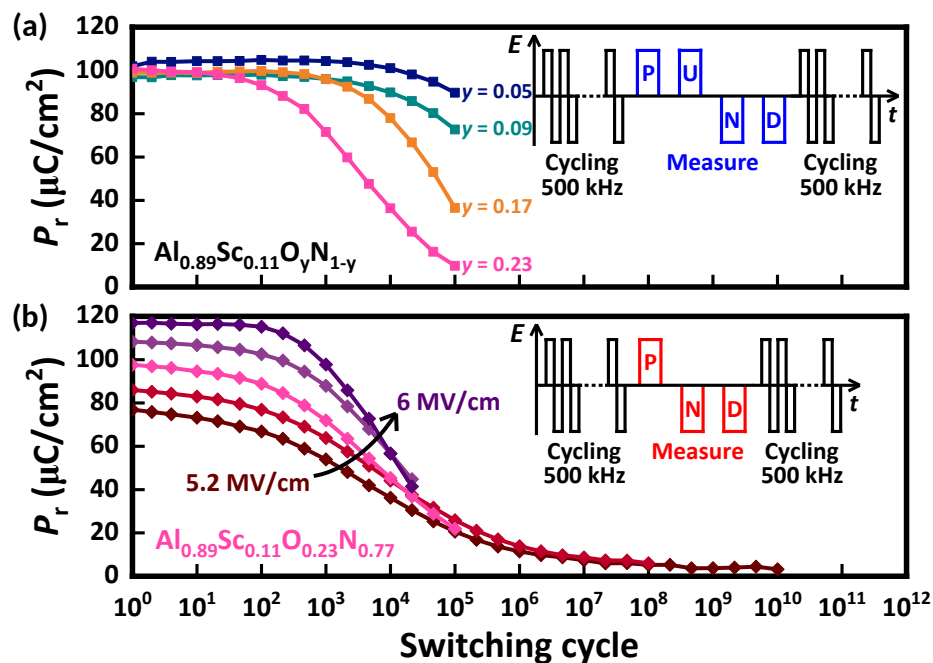


Figure 5.8: (a) Endurance measured by field cycling test of all capacitors with various oxygen content. The target P_r is set to be $100 \mu\text{C}/\text{cm}^2$. (b) A multi-level partial polarization demonstration of $\text{Al}_{0.89}\text{Sc}_{0.11}\text{O}_{0.23}\text{N}_{0.77}$ capacitor from 5.2 to 6 MV/cm.

Endurance cycling is applied to the fabricated MFM capacitors, as shown in Figure 5.8(a). The cycling frequency is set to 500 kHz, and P_r values are measured with PUND operation. To achieve a target P_r of $100 \mu\text{C}/\text{cm}^2$, the applied E during field cycling is chosen for each film with various E_c values. Similar to previous reports in our group, all capacitors exhibit endurance up to 10^5 cycles [133], [183]. Similar tendency is observed in lower oxygen content films ($y = 0.05$ and 0.09), where the P_r values are well maintained before 10^3 cycles of switching. However, fatigue becomes more

pronounced in films with higher oxygen content ($y = 0.17$ and 0.23), presumably due to electron trapping incidents at Sc-O bonding, suggesting a trade-off between reliability and the switching field. Moreover, in the subsequent section 7.1., it will be shown that the oxygen concentration is the highest in the ferroelectric layer at the BE interface. Therefore, defect engineering to this interface could be crucial, as will be shown in chapter 7. Nonetheless, thanks to the gentle slope in the P_r -E relationship, precise control of P_r over 5.2 to 6 MV/cm can be achieved, as illustrated in Figure 5.8(b).

5.7. Potential of Aggressive Scaling

In section 2.4., it is stated that thickness downscaling for AlScN thin films encounters several challenges. The most prominent obstacles are high leakage current that sabotages the ferroelectricity [99], [225], and insufficient P_r due to deteriorated c -axis crystallinity [97], [124], [226]. Consequently, it is advantageous to exploit the benefits from defect engineering, from the results of previous sections in this chapter. Thanks to the features like improved E_{BD} , suppressed leakage, and decreased E_c , aggressive thickness scaling is made possible. This section demonstrates an ultra-thin AlScON ferroelectric capacitor for possible low-voltage operation.

5.7.1. Experimental Details

TABLE 5.2
SPUTTERING CONDITIONS FOR ALUMINUM SCANDIUM OXYNITRIDE

Deposition parameters	
Sputtering target	Al _{0.8} Sc _{0.2} (80 mm dia.)
Process temperature (°C)	400
DC power supply (W)	300
T/S distance (mm)	100
Process pressure (Pa)	0.55
Ar/N ₂ gas flow (sccm)	5/10
O ₂ gas flow (sccm)	0 and 0.45

The fabrication process of AlScON ferroelectric capacitors mainly follows the description in section 3.1. and section 5.2. Likewise, the low-Sc target ($\text{Al}_{0.8}\text{Sc}_{0.2}$) is utilized but with an even lower process pressure of 0.55 Pa to further decrease the leakage at ultra-scaled region. The O_2 gas input is set to 0.45 sccm to extract the maximum benefits from defect engineering. Ellipsometry is used to confirm the deposited film thickness of 9 nm, and TEM analysis is still ongoing. To compare the effectiveness of O_2 gas, another controlling sample is also fabricated without O_2 gas input. Table 5.2 summarizes the deposition conditions of ultra-thin AlScON films.

5.7.2. Influence on Ferroelectric and Dielectric Properties

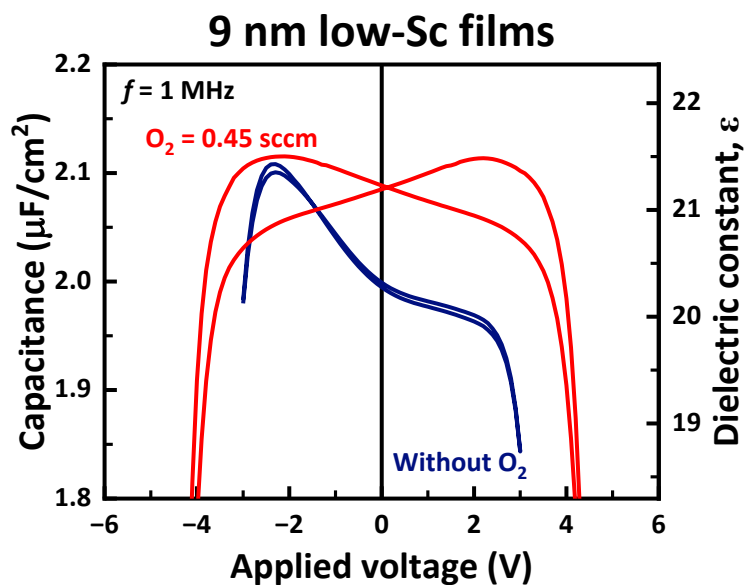


Figure 5.9: C-V curves of 9 nm low-Sc content films. With the incorporation of oxygen, butterfly shape becomes clearer and more symmetrical. The measurement was conducted at 1 MHz.

Figure 5.9 shows the C-V curves of 9 nm AlScN and AlScON films. Owing to the influence of high leakage, the C-V curve of the AlScN film is distorted, and the forward and backward sweep is hardly distinguishable. Plus, the cross-point is ambiguous, making the extraction of ϵ_i impossible. Thankfully, with the assist from oxygen incorporation, a symmetrical and distinct curve is presented by the AlScON film, indicating the existence of ferroelectricity, and ϵ_i is calculated to be 21.2. The divergence of ϵ_i with 50 nm AlSc(O)N films in section 5.4.1. could be attributed to the increased ratio of domain wall area to film volume at scaled thickness, as explained by

Schönweger *et al.* [144]. Additionally, the imprint effect completely disappeared since the E_{imp} is zero for AlScON film in Figure 5.9.

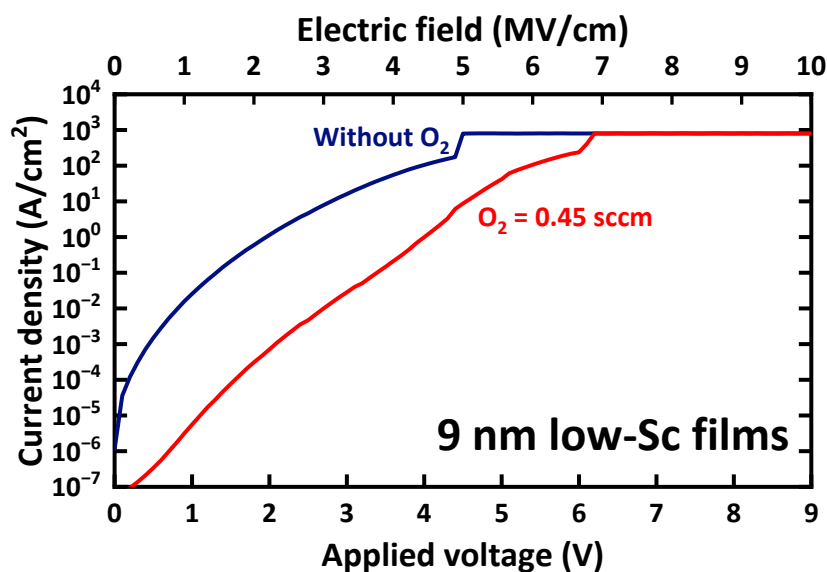


Figure 5.10: TZDB results for 9 nm low-Sc content films. Leakage is suppressed and E_{BD} is improved for AlScON film.

In section 4.2.3., the E_{BD} of 50 nm low-Sc film is about 9.8 MV/cm. However, when the thickness is shrunk to 9 nm, the E_{BD} decreases to 4.9 MV/cm, as Figure 5.10 shows. This indicates that during thickness downscaling, the compromised E_{BD} could hinder the opportunity of device miniaturization. Fortunately, 9 nm AlScON film shows considerable potential since the E_{BD} is enhanced to 6.8 MV/cm, which is consistent with the findings in section 5.4.2. Moreover, the overall leakage current is greatly suppressed before breakdown. At E of 3 MV/cm, the leakage current is suppressed by more than two orders, which helps the demonstration of symmetrical and distinct C-V curve of AlScON film in Figure 5.9.

Due to enlarged leakage current in aggressively downscaled films, the simple P-E measurement could be misleading, and researchers have utilized PUND to characterize the ferroelectric properties of ultra-thin AlScN films [100], [225], [227]. Figure 5.11 delineates the P_r and E relationship from PUND measurements for the deposited AlScON thin film. The P_r values are lower than $5 \mu\text{C}/\text{cm}^2$ owing to the limited thickness down to 9 nm, and the crystallization is expected to be naturally inferior to 50 nm sputtered films. However, the ferroelectricity is revealed. As described in section 2.3.3., E_c should increase with decreased thickness down to 10 nm. In contrast, the E_c

here is extracted as 3.4 MV/cm which is way lower than the values shown in section 5.5. This suggests that the effect of oxygen doping in AlScN is more dominant in thinner films.

It is worth noting that publications of scaled AlScN below 10 nm, though only a few, utilize metal electrodes such as Pt, Al, and Mo [100], [101], [144], [225], [227]. Pt electrodes especially possess great 111 texture, high work function, etc., leading to excellent quality of scaled AlScN films [189], [228]. However, it is not compatible with CMOS technology. Therefore, it should be highlighted that for the first time, this research demonstrates distinct ferroelectricity in scaled film of 9 nm using CMOS-compatible TiN electrodes, showing the feasibility of defect engineering. For films with about 10 nm of thickness, the operation voltage is approximately 4 V [101]. When the thickness is ultra-scaled to 5 nm, the operation voltage is 1-2 V [144]. It is expected that below 1 V operation can be achieved by below 4 nm AlScN thin films with TiN electrodes using defect engineering.

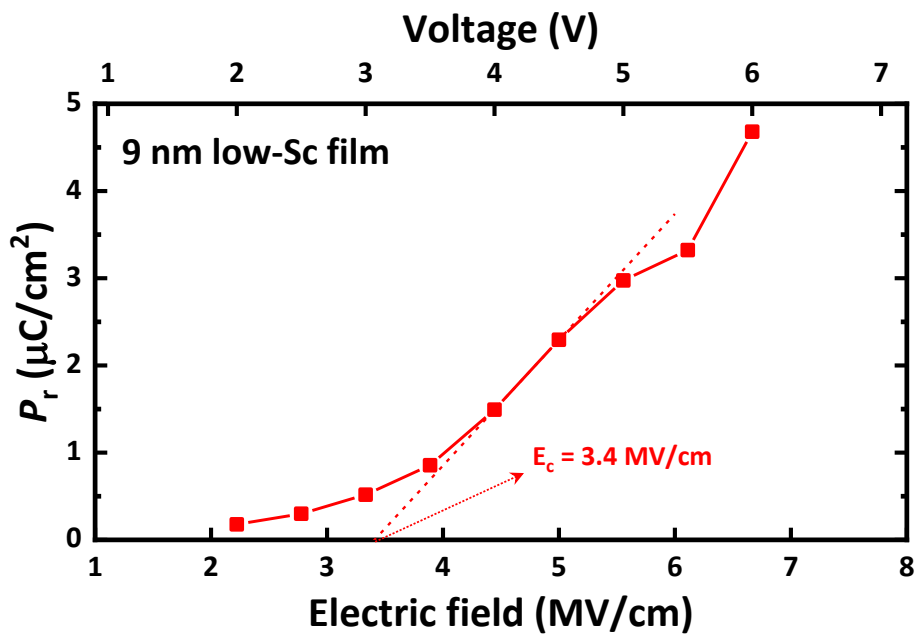


Figure 5.11: PUND results for 9 nm AlScON capacitor. Due to the limited film quality at low thickness, the maximum P_r is $4.7 \mu\text{C}/\text{cm}^2$.

5.8. Summary of This Chapter

In this chapter, the method of defect engineering to AlScN thin films proved to be influential using additional O₂ gas flow. It has been shown that oxygen contamination is unavoidable in reactive sputtering, as 5 at.% of oxygen was incorporated even when additional O₂ gas was not supplied during deposition. Therefore, characterization and analysis are conducted for the influence of oxygen content in Al_{1-x}Sc_xN films in this chapter. Indeed, ferroelectric and dielectric properties of deposited Al_{0.89}Sc_{0.11}O_yN_{1-y} films exhibit visible variations. Intentionally incorporating oxygen into the Al_{0.89}Sc_{0.11}O_yN_{1-y} films creates V_{Al}-O_N complex defects that shift E_{imp}, increase ε_i, suppress leakage, and boost E_{BD}, without apparently diminishing P_r. The proposed defect engineering is one rare approach to effectively shrink E_c by doping for AlScN. Moreover, the gentle slope in the P_r-E relationship at PUND measurements indicates the potential to ease the control of partial polarization switching, which demonstrates the potential of multi-level operation. Notwithstanding the fatigue effect and less-than-ideal endurance cycles, a high P_r with enhanced control over partial polarization is beneficial for analog devices in ANNs applications.

Additionally, ultra-thin AlScON capacitor is fabricated and characterized. For 9 nm AlScN film deposited without O₂ gas flow, the ferroelectricity is destroyed by high leakage current, as evident from C-V measurement. Luckily, the 9 nm AlScON film restores ferroelectricity via defect engineering to massively suppress leakage. Low-voltage operation down to 4 V is made possible. In the meantime, the breakdown strength is improved considerably, and E_c is decreased to an unexpected low value of 3.4 MV/cm. Despite the maximum P_r value is limited to 4.7 μC/cm², the potential of oxygen doping for AlScN films for low-voltage operation is exhibited.

Chapter 6: Oxygen Profiling in Multi-Layer Aluminum Scandium Oxynitride Capacitors

6.1. Introduction

Akiyama *et al.* have shown that including oxygen into sputtered AlN thin films could influence the piezoelectric response in terms of polarity [210]. In chapter 5, it is demonstrated that oxygen incorporation enables control of imprint effect in AlScON ferroelectric. However, the polarity status of pristine AlScON films, i.e., the predominant polarity at the as-deposited state, has yet been discussed. Basically, as introduced in section 2.3.4., AlScN thin films, either deposited by sputtering or MBE, exhibit natural N-polar and poling-free characteristics [93], [94], [97], [162], [229]. Since polarity control of ferroelectrics is desirable for a wide range of applications, it is therefore crucial to understand the influence of oxygen atom inclusion in III-N films. In this chapter, oxygen profiling using AlSc(O)N MFM capacitors with various ferroelectric stack structures are manufactured and examined to unveil the potential of polarity engineering in AlSc(O)N films.

6.2. Experimental Details

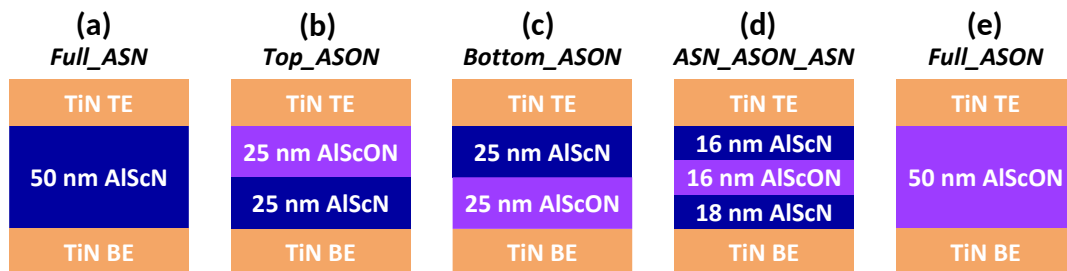


Figure 6.1: Various ferroelectric stacks for multi-layer AlSc(O)N capacitors. The total thickness of ferroelectric layers is 50 nm. The TiN BE and TE are 10 nm and 30 nm, respectively. From (a) to (e), the capacitors are denoted as *Full_ASN*, *Top_ASON*, *Bottom_ASON*, *ASN_ASON_ASN*, and *Full_ASON*, respectively.

The fabrication process of multi-layer AlSc(O)N MFM capacitors mainly follows the description in section 3.1. and section 5.7.1. Figure 6.1 illustrates five ferroelectric stacks that will be analyzed in this chapter. The total thickness of ferroelectric layers is

fixed at 50 nm. For AlScON layers, O₂ gas flow of 0.45 sccm is selected to show the influence to the greatest extent. Table 6.1 summarizes the deposition conditions of stacked AlSc(O)N films. Note that all capacitors are measured at as-deposited state, i.e., before any other electrical characterizations.

TABLE 6.1
SPUTTERING CONDITIONS FOR ALUMINUM SCANDIUM (OXY)NITRIDE

Deposition parameters	
Sputtering target	Al _{0.8} Sc _{0.2} (80 mm dia.)
Process temperature (°C)	400
DC power supply (W)	300
T/S distance (mm)	100
Process pressure (Pa)	0.55
Ar/N ₂ gas flow (sccm)	5/10
O ₂ gas flow (sccm)	0 or 0.45

6.3. Dependence of Polarity at Pristine State

As described in section 3.2.4. and section 3.2.5., switching event in a ferroelectric capacitor can be monitored by C-V or TZDB measurement. In the following section 7.3.1., the as-deposited capacitors are measured to understand the initial polarity in the deposited films. Moreover, TZDB measurement could also bring advantages such as acquiring the information of leakage and breakdown strength, as will be shown in section 6.3.2.

6.3.1. Control of Polarity

In C-V measurement, it is convenient to identify the predominant polarity in pristine films by applying separate C-V sweep operations [97]. The operations start from 0 V, sweeps toward positive or negative direction, and sweeps back to 0 V. The top of Figure 6.2 provides two types of bipolar sweep sequences for all fabricated capacitors. Figure 6.2(a) to (e) display the C-V loops with initial positive sweep, whereas Figure 6.2(f) to

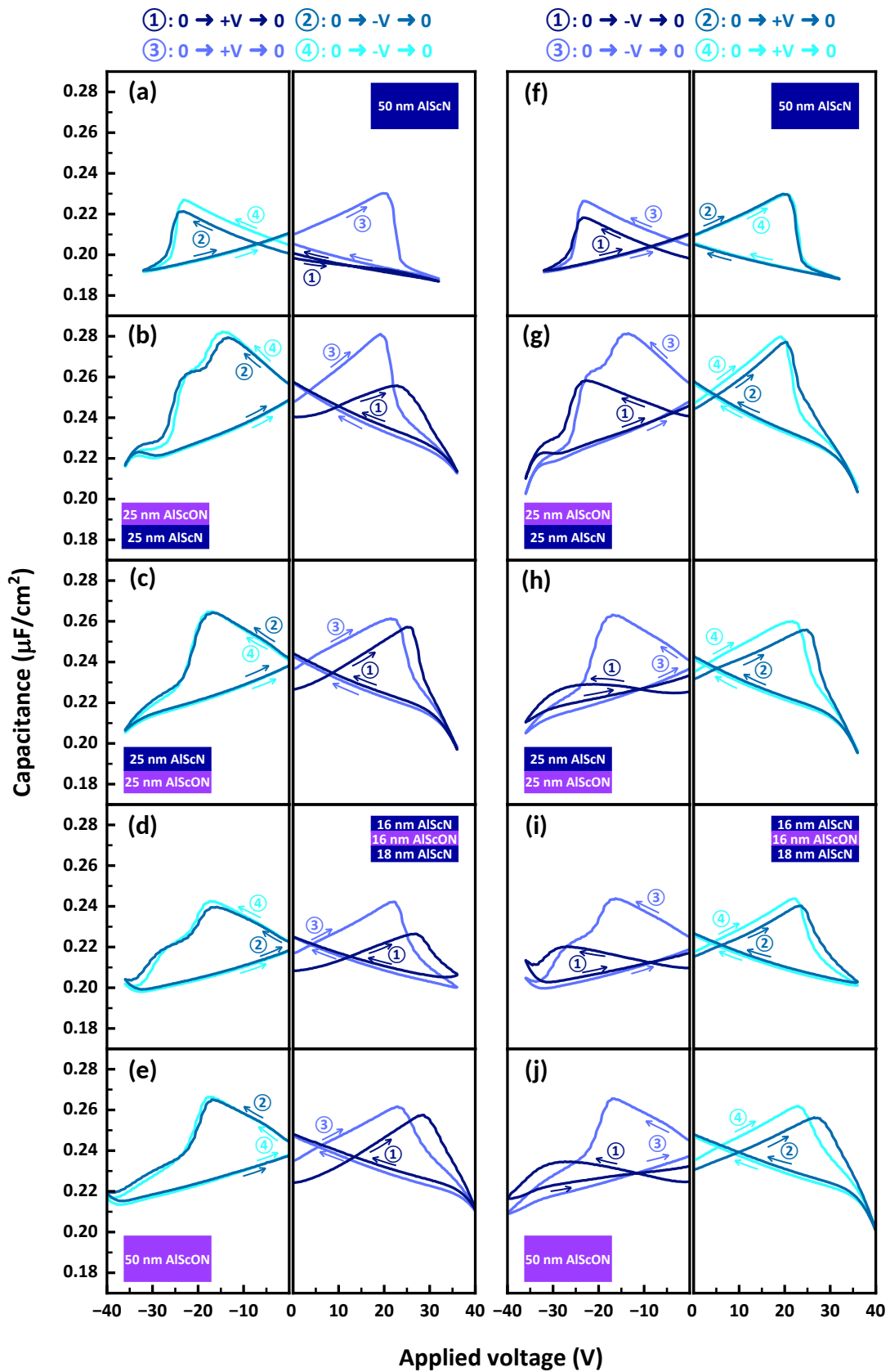


Figure 6.2: Left panels [(a)-(e)] and right panels [(f)-(j)] show the initial positive and negative C-V sweeps for pristine films, respectively.

(j) demonstrate the C-V loops with initial negative sweep. The sweep directions are indicated by small arrows. In section 3.2.4., it is mentioned that the peaks in C-V curves represent the polarization switching incident.

For simplicity, it is clearer to compare *Full_ASN* and *Full_ASON* first. For *Full_ASN*, it is obvious that the film possesses N-polar at pristine state since no switching event is shown at initial positive sweep in Figure 6.2(a), whereas Figure 6.2(f) exhibits polarization reversal at initial negative sweep. This is consistent with the findings in previous research in our group [97]. On the other hand, *Full_ASON* shows prominent switching at initial positive sweep in Figure 6.2(e), whereas the polarization inversion is weak but visible at initial negative sweep in Figure 6.2(j). Apparently, oxygen inclusion in AlScN films changes the predominant polarity from complete N-polar to metal-polar in majority. It is predictable that the percentage of metal-polar grains could be highly related to the oxygen composition in pristine AlScON films.

Further investigating *Top_ASON* and *Bottom_ASON* leads to interesting results. For *Top_ASON*, comparing Figure 6.2(b) and (g), the contribution from N-polar grains seem to be slightly greater than metal-polar grains. This suggests that while oxygen incorporation changes the polarity of some grains in the capping AlScON layer toward metal-polar, the influence of the underlying N-polar AlScN layer should not be neglected. In other words, polarity inheritance could play an important role during sputter deposition [229]. For *Bottom_ASON*, the contribution of metal-polar grains is more dominant, demonstrating similar C-V response to *Full_ASON*, as depicted in Figure 6.2(c) and (h). It is speculated that the residual oxygen could affect the polarity in the capping AlScN layer, since additional O₂ gas was blended during underlying AlScON layer deposition. A further SIMS analysis could be helpful to prove this.

Another intriguing discovery is that in Figure 6.2(b) and (g), two E_c components are spotted at the negative side during most voltage sweeps. From the conclusions in chapter 5, high and low E_c components corresponds to AlScN and AlScON domains, respectively. As delineated in Figure 6.2(g), only high E_c component appears at negative sweep ①, whereas negative sweep ③ shows two E_c components. The phenomenon validates the co-existence of two opposite polarization states in the pristine *Top_ASON* film, i.e., mixed N-polar and metal-polar grains are present at as-deposited state. Due to the aforementioned reason, *Bottom_ASON* does not exhibit

similar phenomenon.

Figure 6.2(d) and (i) plot the C-V results of *ASN_ASON ASN*. In this case, the polarity is 1:1 mixed, as similar peak heights are shown in the initial sweeps ① in both sides. As a result, the polarity is controllable by stacking AlSc(O)N layers. In addition, the two E_c components are also spotted at the negative side, similar to the *Top_ASON* case.

Overviewing the C-V curves in Figure 6.2 (b) to (e), positive E_c tends to show higher values in sweep ① than in sweep ③, regardless of the percentage of metal-polar grains in the films. Same trend can be observed in Figure 6.2 (g) to (j), as sweep ② generates higher E_c , comparing to sweep ④. This can be attributed to the initial traps in oxygen-contained films that hinders the polarization inversion. Indeed, as discussed in section 5.1., oxygen incorporation gives rise to complex defects that influence the ferroelectricity. Fortunately, some of the traps are filled by charges, and stop affecting the switching. Therefore, the positive E_c values shown in the latter sweeps are lowered.

6.3.2. Leakage Current and Breakdown Field

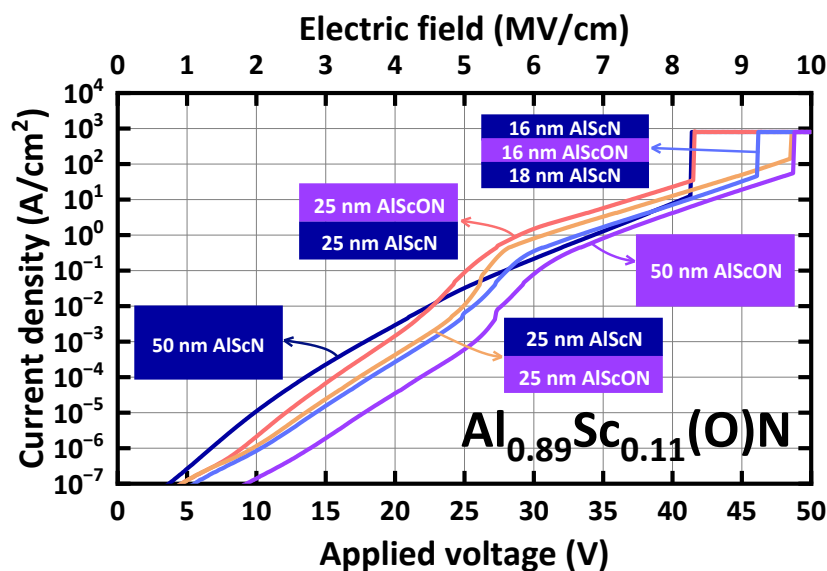


Figure 6.3: TZDB results of fabricated AlSc(O)N capacitors with various ferroelectric stack structures.

Figure 6.3 discloses the TZDB results of all pristine films with various stack structures. Except the *Full ASN* film, all other oxygen-included films exhibit switching event,

which is consistent with the findings in Figure 6.2(a) to (e). Before the switching occurs, the leakage current suppression by oxygen doping is effective and generally related to the degree of oxygen content, which is also consistent with the results in chapter 5. Considering the breakdown fields, *Full_ASN* and *Top_ASON* demonstrate almost the same low values, whereas *Full_ASON* and *Bottom_ASON* share the same high values. Based on the fact that BE is extremely important for the ferroelectric film quality [230], [231], the results here provide an important message that the breakdown strength is highly related to the ferroelectric/BE interface. With higher oxygen concentration at the ferroelectric/BE interface, breakdown strength is enhanced, which is explained by V_N elimination [133]. In the case of *ASN_ASON_ASN*, though oxygen level is low at the ferroelectric/BE interface, leakage and breakdown strength are improved, comparing to *Full_ASN* and *Top_ASON*. This could be attributed to the multi-interfaces in the ferroelectric stack as those might block the leakage path, leading to higher breakdown field [232].

6.4. Summary of This Chapter

In this chapter, the role of oxygen incorporation to multi-layered ferroelectrics with regards to polarity control and insulating properties has been presented. It is found that doping oxygen leads to polarity shifting from N-polar to metal-polar for pristine AlSc(O)N films, depending on the degree of oxygen inclusion, as evident from C-V measurements. For multi-layer structures, *Top_ASON* and *Bottom_ASON* demonstrate dominant N-polar and metal-polar, respectively. Moreover, *Top_ASON* as well as *ASN_ASON_ASN* exhibit one E_c component during the initial negative sweep, and two during the subsequent negative sweep. These results indicate that mixed phases could co-exist in as-deposited state films. Additionally, the current response for multi-layer AlSc(O)N films indeed decreases the leakage level before switching, which is verified by TZDB tests. The breakdown field is found to have high correspondence to the oxygen concentration of ferroelectric/BE interface.

Chapter 7: Interface Oxygen Depletion by Reducing Sputtering Ambient for Endurance Enhancement

7.1. Introduction

In previous chapters, it has been discussed that oxygen concentration plays a key role in terms of defect engineering in AlScN thin films. E_{imp} , E_{BD} , ϵ , leakage current, partial polarization switching, initial polarity, etc., are all considerably influenced. Figure 7.1 illustrates the SIMS analysis of a 50 nm $Al_{0.74}Sc_{0.26}N$ MFM capacitor. Comparing to Al and Ti atoms, Sc atoms possess larger electronegativity difference toward O atoms [123], which means that Sc atoms are more reactive to O atoms during deposition. Overall high oxygen level in AlScN layer could be attributed to the residual oxygen in the chamber which is consumed over sputtering time. Moreover, an oxygen concentration peak is spotted at the ferroelectric/BE interface, which might be influenced by the partially oxidized AlSc target surface.

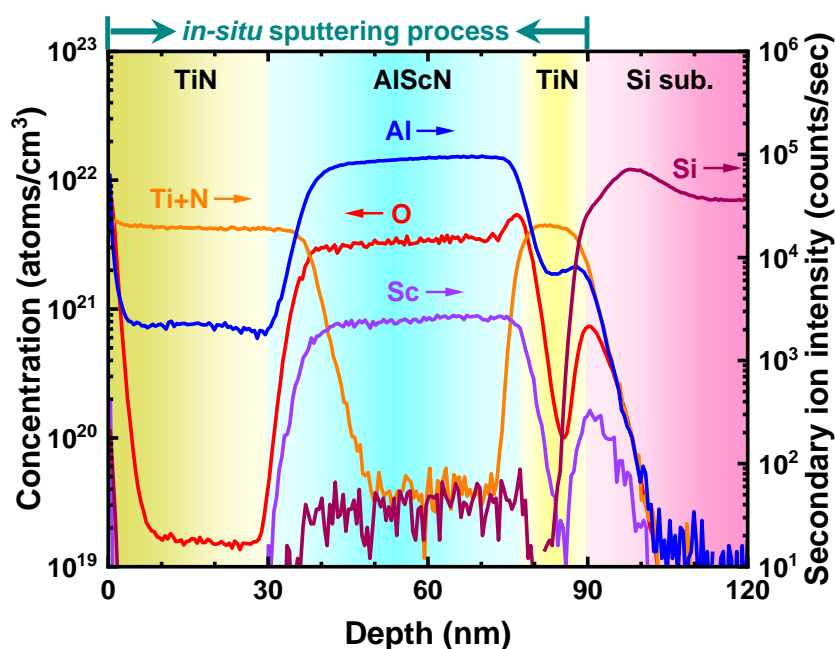


Figure 7.1: SIMS results of a TiN/AlScN/TiN capacitor stack. The oxygen level is typically higher in AlScN layer. Oxidation from the atmosphere after deposition is effectively blocked by the top TiN layer.

In chapter 5, oxygen incorporation has raised concern with regards to endurance

cycle performance. As more oxygen is included in the films, fatigue effect becomes stronger, making the reliability performance non-ideal. High oxygen level at the ferroelectric/BE interface could make the situation more severe. In order to resolve this issue, decreasing the oxygen content could be handy to improve the endurance and mitigate the wake-up or fatigue effects [124]. Therefore, in this chapter, H₂ gas is mixed with the Ar/N₂ ambient during sputtering. With the assist from reducing ambient, O₂ partial pressure can be lowered [233], [234]. Herein, enhanced reliability such as suppressed leakage and increased endurance cycle are demonstrated.

It is worth mentioning that some early studies have revealed that H₂-incorporated annealing could deteriorate the ferroelectricity of PZT due to hydrogen impurities [235], [236], [237], [238]. However, Park *et al.* proved that HZO films possess good resistance to reducing ambient in annealing, as the P_r values are almost unaffected after wake-up procedure [220], [239]. As for AlScN, it is reported that only slight ferroelectricity influence is induced by H₂-incorporated annealing [240]. Nevertheless, for the case here, as H₂ gas is directly included during deposition, a much more considerable impact is expected.

7.2. Experimental Details

TABLE 7.1
SPUTTERING CONDITIONS FOR ALUMINUM SCANDIUM NITRIDE

Deposition parameters		
Sputtering target	Al _{0.53} Sc _{0.47} (80 mm dia.)	Al _{0.8} Sc _{0.2} (80 mm dia.)
Process temperature (°C)	400	
DC power supply (W)	300	
T/S distance (mm)	100	
Process pressure (Pa)	0.7	0.6
(Ar+3%H ₂)/N ₂ gas flow (sccm)	5/10	

The fabrication process of AlScN ferroelectric capacitors mainly follows the description

in section 3.1. In order to decrease the partial pressure of residual oxygen, a noble gas replacement from Ar to (Ar+3%H₂) is implemented. The H₂ flux is as low as 1%. In the meantime, comparisons between high-Sc target (Al_{0.53}Sc_{0.47}) and low-Sc target (Al_{0.8}Sc_{0.2}) are conducted. Note that no deposition rate change is found whether H₂ is included or not, and all films have the same thickness of 60 nm. Table 7.1 summarizes the deposition conditions of AlScN films deposited with and without H₂ gas flow. The deposited films are denoted as *High_Sc*, *High_Sc_H₂*, *Low_Sc*, and *Low_Sc_H₂*.

7.3. Material Analysis of Ferroelectric Films Deposited with Hydrogen Flux

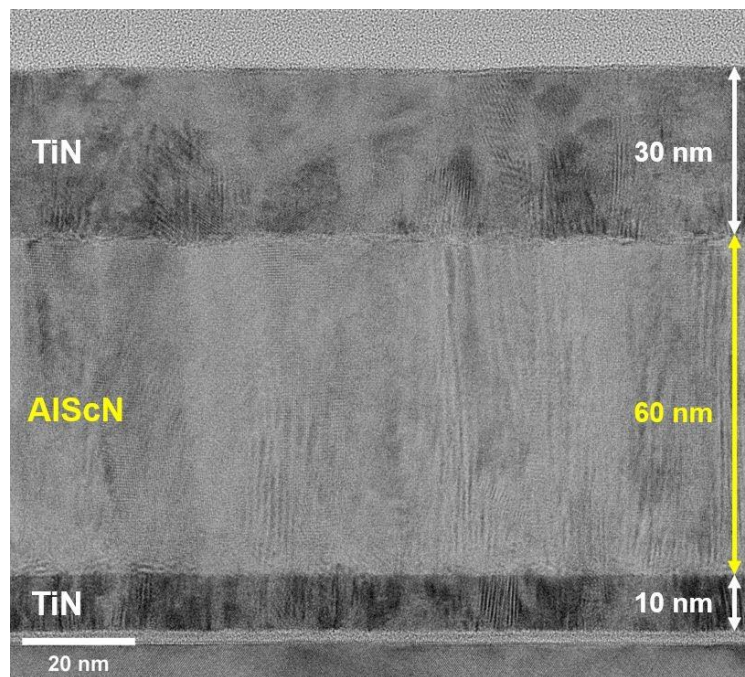


Figure 7.2: Cross-sectional TEM image of TiN/Al_{1-x}Sc_xN/TiN MFM capacitor (*low_Sc*). The deposited ferroelectric layer is 60 nm.

A cross-sectional view of the TiN/Al_{1-x}Sc_xN/TiN film stack is acquired by a high-resolution TEM, as presented in Figure 7.2. The FFT analysis of the sputtered low-Sc film shows *c*-axis oriented texture with a FWHM of 11.4°. Although it is a bright field TEM image, columnar growth is visible. EDX analysis is utilized to confirm the chemical compositions of deposited films. The Sc content are 0.26 and 0.12 for high-Sc and low-Sc films, respectively.

Out-of-plane XRD patterns of AlScN MFM capacitors are illustrated in Figure 7.3(a). XRD peaks spotted at 42.5° are assigned to TiN 200 phase, whereas AlScN 002 phase can be found at around 35.5° . *High_Sc* and *High_Sc_H₂* especially possess extra diffraction peaks of AlScN 100 phase which are observed near 31° [97], [182]. The provided information again indicates that all AlScN films are mostly oriented in the c-axis direction [106], [115], [116], [241], [242]. Compared to the pure AlN 002 XRD peak that resides in 36° , a slight shift in AlScN 002 toward lower angle results from thin films down to 60 nm, as mentioned in other reports [117], [145], [225]. No clear change in the crystal structure is identified with and without the H₂ flow during the sputtering process. Figure 7.3(b) reveals the XRC spectra of deposited films. The peak heights and FWHM values typically decrease with H₂ flow, which suggest the c-axis crystallinity degrades in reducing sputtering ambient [233], [243]. Furthermore, it is possible that the films deposited with H₂ flow have higher degree of compressive strain, since the FWHM values are broaden.

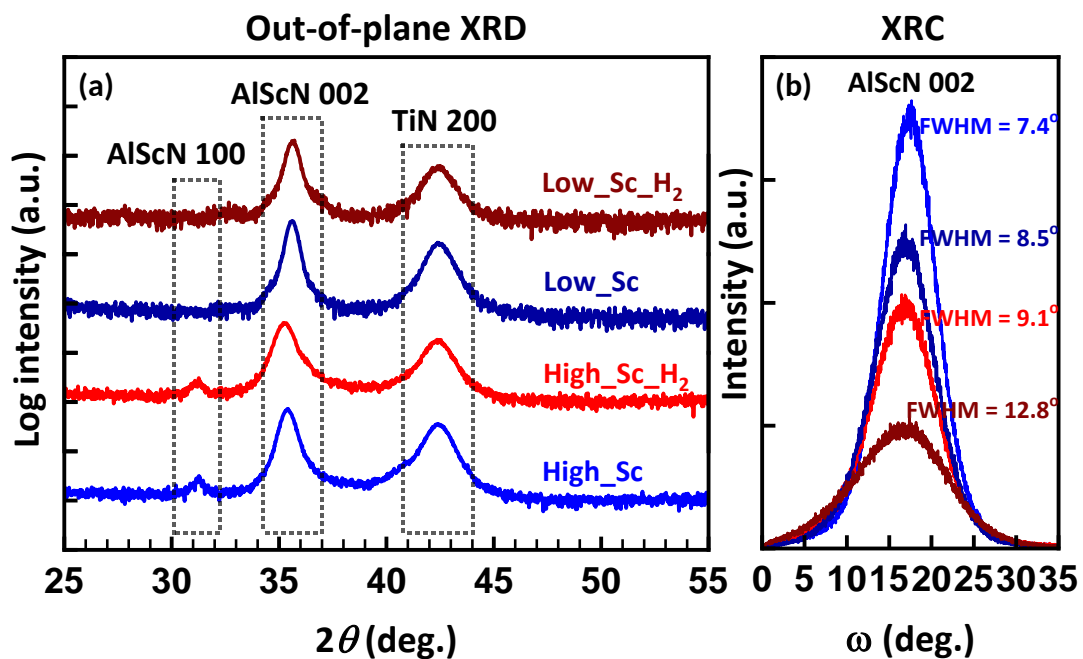


Figure 7.3: (a) Out-of-plane XRD and (b) XRC profiles of deposited 60 nm films sputtered with and without H₂ gas.

7.4. Influence on Ferroelectric and Dielectric Properties

7.4.1. Dielectric constant

Figure 7.4 depicts the butterfly-like C-V switching loops which confirm the ferroelectricity in all films, suggesting the high robustness of ferroelectric $\text{Al}_{1-x}\text{Sc}_x\text{N}$ films against reducing ambient. The extracted ϵ_i of *High_Sc*, *High_Sc_H2*, *Low_Sc*, and *Low_Sc_H2* are calculated to be 22.7, 19.9, 13.9, and 13.3, respectively. For films deposited without H_2 flux, the ϵ_i values are similar to the calculated results, considering the Sc composition in $\text{Al}_{1-x}\text{Sc}_x\text{N}$ ferroelectric [109]. With H_2 gas inclusion, reductions in ϵ_i are observed. According to the observations in chapter 5, lower oxygen concentration in $\text{Al}_{1-x}\text{Sc}_x\text{N}$ layers could contribute to this result, showing the effectiveness of reduced oxygen partial pressure by H_2 gas introduction. Besides, the acquired E_c of *High_Sc* is smaller than *High_Sc_H2*. Again, lower oxygen level and strengthened compressive strain are the origins of this change. For *Low_Sc* and *Low_Sc_H2* films, the E_c dependence will be explained later.

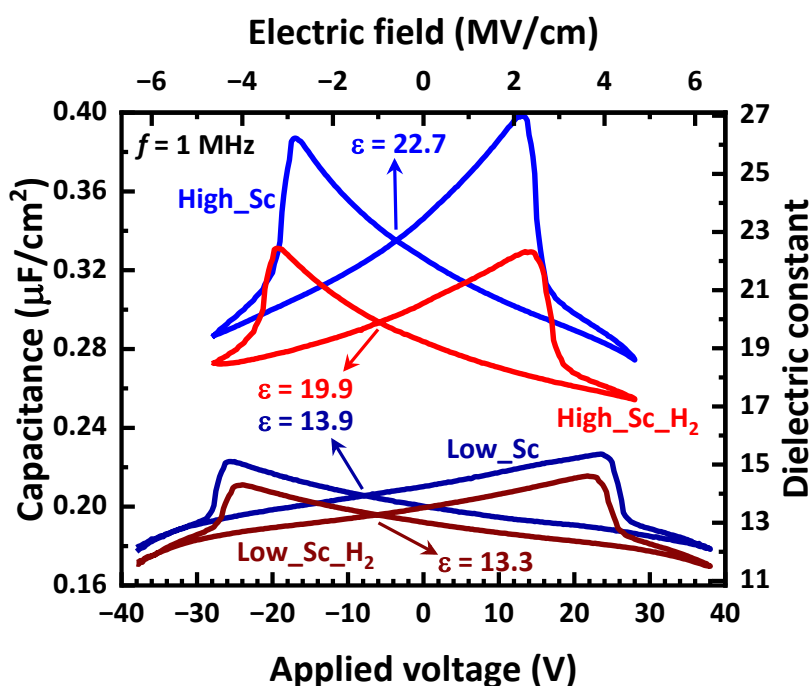


Figure 7.4: C-V characteristics of all deposited films. Dielectric constant decreases with H_2 gas flow.

7.4.2. Leakage Current and Breakdown Field

Figure 7.5 displays the leakage current density obtained from the TZDB measurements. Suppressed leakage current can be found in *Low_Sc* owing to the wider bandgap

compared to that of *High_Sc* sample, which is consistent with section 4.2.3. Also, the E_{BD} is increased by approximately 1 MV/cm. With the addition of H_2 gas to the sputtering environment, not only reduction in leakage current but also E_{BD} enhancement could be realized, as evident from *High_Sc_H2* and *Low_Sc_H2* films in Figure 7.5. This could be explained by the enlarged E_g values with lower oxygen content in the films [215]. However, this is contrary to the conclusion in chapter 5, which shows that higher oxygen incorporation could reduce leakage via V_N elimination. Therefore, the physical mechanism should be different. XPS results in chapter 5 show that about 5 at.% of O atoms exist in the low-Sc content AlScN film without additional O_2 gas flow. It is reasonable to assume that if the oxygen concentration is higher than 5 at%, the leakage suppression is dominated by V_N elimination. On the other hand, when the oxygen level is below 5 at%, the influence of E_g broadening comes into play.

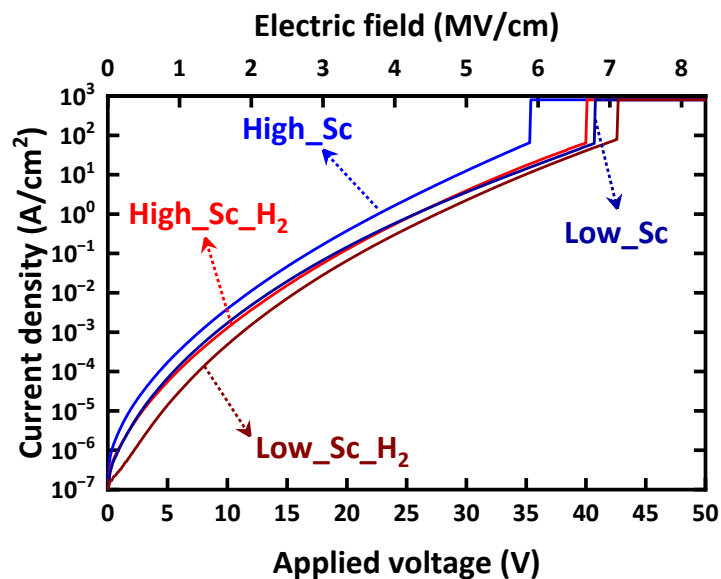


Figure 7.5: TZDB results of all samples. Leakage is suppressed and E_{BD} is improved with H_2 -included sputtering.

7.4.3. Remanent Polarization and Coercive Field

As described in section 3.2.2., PUND characterization is a useful tool to prevent overestimation of P_r in ferroelectrics with high leakage. The obtained P_r values with respect to E are depicted in Figure 7.6. Compared to the *High_Sc* film, higher P_r and E_c are shown in the *Low_Sc* film, which originates from lower Sc content, as discussed previously in section 2.3.4. and section 4.2. Data in Figure 7.6 shows that the films

deposited with H₂ flux generally reach the semi-saturation kinks at a relatively lower P_r value. For *High_Sc* and *High_Sc_H2* films, it is obvious that P_r values become lower in all-electric field regions with H₂ gas flow. This is due to degraded c-axis orientation, as validated from the XRC profiles in Figure 7.3(b). In addition, compared to *Low_Sc*, lower P_r values shown in semi-saturation region for *Low_Sc_H2* can be attributed to the same reason.

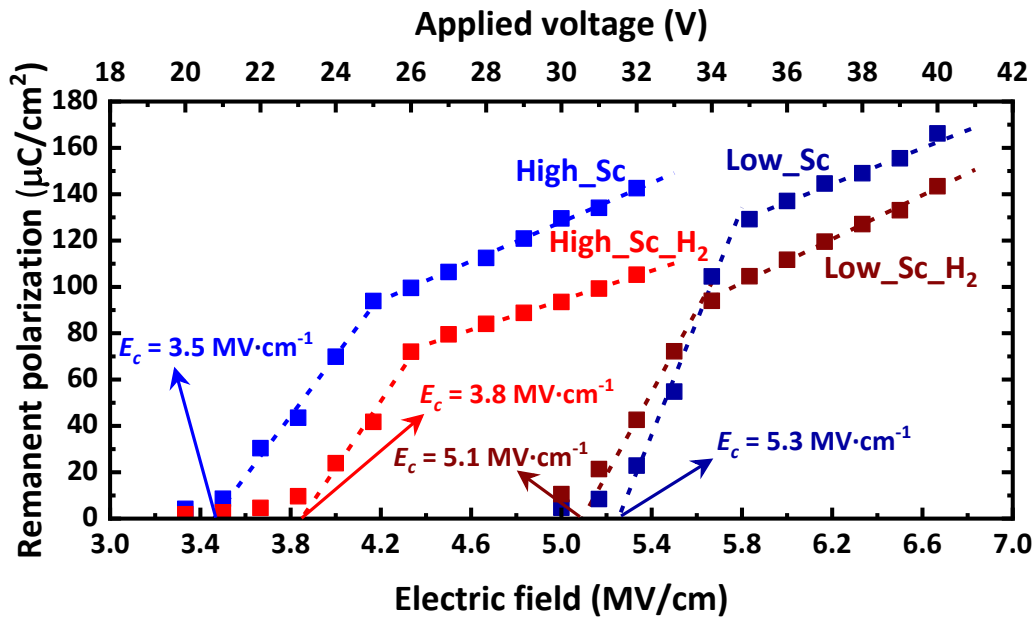


Figure 7.6: P_r-E relationship from PUND measurements for AlScN MFM capacitors deposited with and without H₂ gas flux.

Chapter 5 elucidated that formation of V_{Al} in the Al_{1-x}Sc_xN films could ease the ferroelectric displacement of N atoms, and thereby reduces E_c. [218], [219], [223] The increasing E_c for *High_Sc_H2* can be attributed to the reduction of V_{Al}-O_N complex defects and stronger compressive stress in Al_{0.74}Sc_{0.26}N films. On the contrary, the extracted E_c of *Low_Sc_H2* is slightly lower than *Low_Sc*, which is consistent with the findings in Figure 7.4. This is explained as follows. The Landau-Ginzburg model suggests a linear relationship between E_c and P_r/ε_i [244]. By using the P_r values after the semi-saturation kinks and the ε_i values taken from the C-V measurements, the extracted E_c values show nice agreement with the model. Therefore, the slight reduction in E_c of *Low_Sc_H2* film to that of *Low_Sc* is understandable.

Furthermore, the slope of P_r on E before the semi-saturation kink is identical for *High_Sc* and *High_Sc_H2*, which implies similar E_c variability among ferroelectric

domains. However, the slope is steeper in *Low_Sc* film than that of *Low_Sc_H2*. This phenomenon can be elaborated by FWHM dependence in XRC analysis in Figure 7.3(b). Comparing to high-Sc content films, the FWHM value declines drastically between *Low_Sc* and *Low_Sc_H2* films, indicating deteriorated 002 phase crystallinity. This explains why the P_r -E slopes are the same in *High_Sc* and *High_Sc_H2*, but the slope of *Low_Sc* is much steeper than *Low_Sc_H2*. Nonetheless, a detailed study needs to be conducted to understand the local ferroelectric response.

7.4.4. Ferroelectric Behavior After Field Cycling

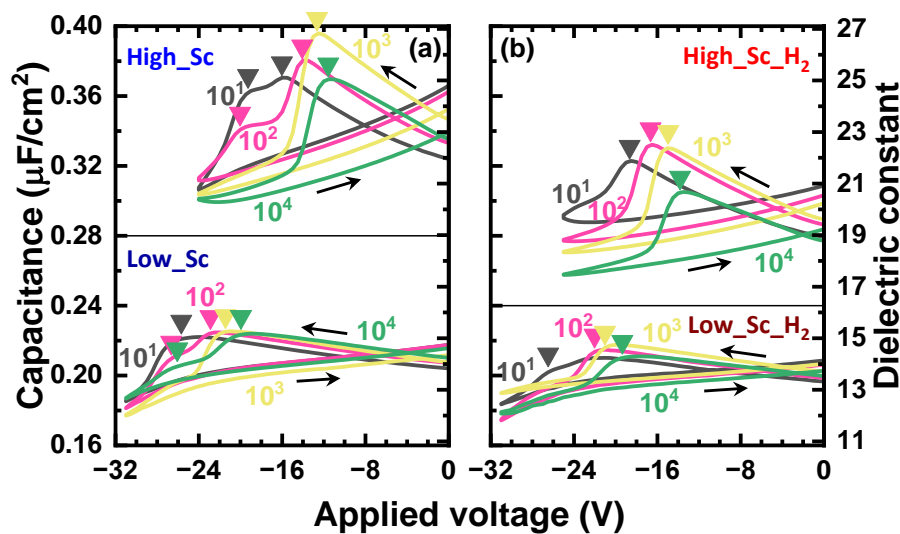


Figure 7.7: C-V measurement sweeping to negative voltage after switching for 10, 10^2 , 10^3 , and 10^4 cycles for (a) *High_Sc* and *Low_Sc* films, and (b) *High_Sc_H2* and *Low_Sc_H2* films.

Figure 7.7(a) and (b) reveal the C-V characteristics measured toward negative voltage direction, after field cycling for 10, 10^2 , 10^3 , and 10^4 cycles. Note that the cycling ends with a positive pulse application, thus polarization reversal can be monitored during the C-V measurements. For *High_Sc*, two peaks at -19 V and -16 V are observed after 10 cycles, inferring a lower E_c appeared after field cycling, in addition to the initial high E_c component. The high E_c component descends and slightly shifts to the negative side after 10^2 cycles. Accompanied by high E_c component vanishment, the low E_c component is enhanced and moves toward the positive side with 10^3 cycles. Peak shift continues with further switching to 10^4 cycles, but the height starts to decrease. Since the peak height or the capacitance value reflects the P_r , the wake-up effect can be

attributed not only to the decrease in E_c but also to the improvement in the P_r . The same trend can be observed for *Low_Sc*, except for little change in the peak height. This indicates that the field cycling induces E_c shrinkage while keeping the same P_r , which suggests that the semi-saturation kinks and regions in P_r - E relationships, displayed in Figure 7.6, is extended to the lower E side by field cycling. The reappeared peak at -26 V after 10^4 cycles may have originated from the switching revive of the pinned ferroelectric domain due to electron trapping. As for the capacitors with H_2 flow, the shift in the peak voltage along with switching cycles exists, as depicted in Figure 7.7(b). Nevertheless, two E_c components are hardly observed. A constant peak height represents a constant P_r , operating in the semi-saturation region. The decrease in the peak height after 10^4 cycles corresponds to the fatigue effect, which is consistent with the following endurance measurements. Although more investigation is needed, analysis of the Sc -content-dependent endurance test with and without H_2 gas flow can give an atomistic understanding of the switching reliability of $Al_{1-x}Sc_xN$ ferroelectric.

7.5. Improved Endurance Performance

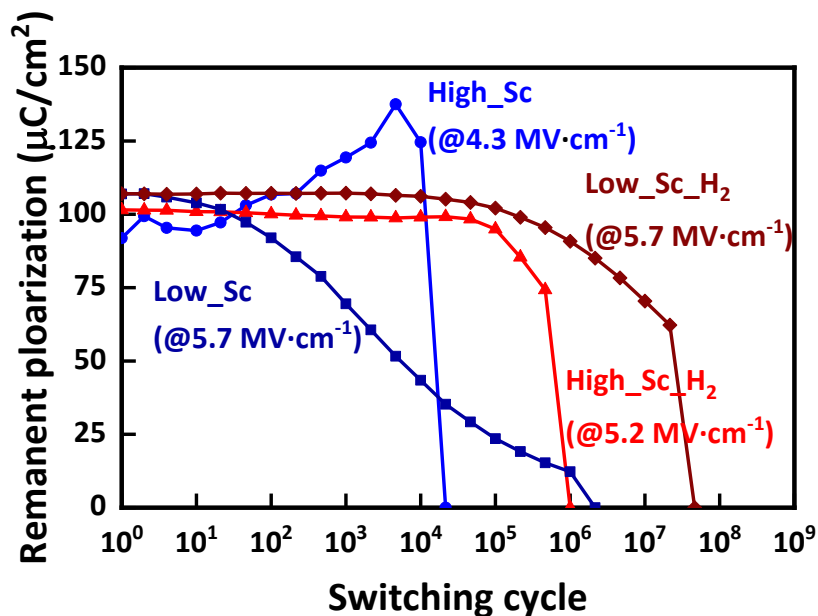


Figure 7.8: Endurance field cycling tests for all deposited films. Different E values are used to meet the target P_r of $100 \mu C/cm^2$ for fair comparison.

Results of field cycling for endurance tests is plotted in Figure 7.8. Since all films

possess various E_c , rectangle cycling pulses with different E are applied for a target P_r of $100 \mu\text{C}/\text{cm}^2$ to make fair comparisons. The wake-up effect is observed in *High_Sc*, showing an increase in P_r from 90 up to $135 \mu\text{C}/\text{cm}^2$. When H_2 gas is introduced, suppressed wake-up effect is shown in *High_Sc_H2*. On the other hand, *Low_Sc* exhibits a much more severe fatigue effect than *Low_Sc_H2* films. These findings imply that oxygen incorporation results in electron trapping incidents at ferroelectric domains [245], [246], [247], which is related to Sc-O bonding, as mentioned in section 5.6.

By comparing *High_Sc* and *High_Sc_H2*, better endurance performance up to nearly 10^6 cycles, two orders of magnitude improvement, is achieved with H_2 gas flow. Likewise, *Low_Sc* and *Low_Sc_H2* follow the same situation, and an extraordinary high switching cycle over of 2×10^7 is achieved. The endurance performance presented here is the record high in the world to date. Moreover, P_r of *Low_Sc* on the switching cycle shows a severe fatigue effect starting from the first 10 time-switching cycles, indicating the high electron trapping nature of the film.

Therefore, the role of oxygen can be derived as follows. Though including oxygen, whether intentionally or unintentionally, could effectively decrease E_c by forming $\text{V}_{\text{Al}}\text{-O}_{\text{N}}$ complex defects, fatigue effect is induced simultaneously due to the presence of Sc-O bonds. Consequently, it is critical to form $\text{V}_{\text{Al}}\text{-O}_{\text{N}}$ complex defects rather than Sc-O bonds when applying defect engineering, and one promising method is to lower the Sc content in the film.

7.6. Potential of Higher Hydrogen Flux

In previous sections, an endurance boost over 10^7 cycles by utilizing reactive sputtering with 1% H_2 flux inclusion is reported, showing the feasibility of reducing ambient for enhanced reliability. Consequently, it is interesting to know what happens if more H_2 flux is blended to Ar/ N_2 gas mixture. In this section, higher percentage of H_2 flux was utilized to form AlScN thin films.

7.6.1. Experimental Details

The fabrication process of AlScN ferroelectric capacitors mainly follows the description

in section 3.1. Different from section 7.2., another gas inlet for H₂ is used to provide higher H₂ flux during ferroelectric deposition. Herein, the high-Sc target (Al_{0.53}Sc_{0.47}) is utilized, and the experiments for low-Sc target (Al_{0.8}Sc_{0.2}) is still ongoing. Note that the deposition rate showed neglectable discrepancy for all sputtered ferroelectric films, as checked by ellipsometry. Table 7.2 summarizes the deposition conditions of AlScN films deposited with various H₂ gas flow. While maintaining 0.7 Pa of process pressure, mixing the H₂ gas flow of 0, 1, 2, and 3 sccm into the sputtering ambient yields 0%, 6.25%, 11.77%, and 16.67% of H₂ flux, respectively.

TABLE 7.2
SPUTTERING CONDITIONS FOR ALUMINUM SCANDIUM NITRIDE

Deposition parameters	
Sputtering target	Al _{0.53} Sc _{0.47} (80 mm dia.)
Process temperature (°C)	400
DC power supply (W)	300
T/S distance (mm)	100
Process pressure (Pa)	0.7
Ar/N ₂ gas flow (sccm)	5/10
H ₂ gas flow/flux (sccm/%)	0, 1, 2, and 3/ 0, 6.25, 11.77, and 16.67

7.6.2. Influence on Ferroelectric and Dielectric Properties

As disclosed in Figure 7.9(a), C-V butterfly loops appear in sputtered Al_{0.74}Sc_{0.26}N films with up to 11.77% of H₂ flux. The disappearance of ferroelectricity in 16.67% H₂ flux film could be attributed to the distinction of *c*-axis orientated grains [233], [243]. Figure 7.9(b) shows that ε_i decreased monotonically with higher H₂ flux, whereas E_c generally exhibits incremental variation on both sides, keeping the same trend shown in section 7.4.1. Moreover, E_{imp} shifts toward zero with more H₂ gas flow.

Figure 7.10 demonstrates the results taken from TZDB measurements. The 0% H₂ flux film exhibits high leakage current due to high-Sc content of the ferroelectric film with lower bandgap value. As H₂ flux increased to 11.77%, suppressed leakage and boosted E_{BD} are prominent, which shows consistency with section 7.4.2. In other

words, under 11.77% H₂ flux, when more H₂ gas is involved in the sputtering, the deposited film tends to have higher E_g, and thus leakage is reduced and E_{BD} is improved. However, when H₂ flux gained to 16.67%, the film not only loses its ferroelectric properties, but also exhibits drastic decline in E_{BD}. This can be ascribed to a total crystal structure variation.

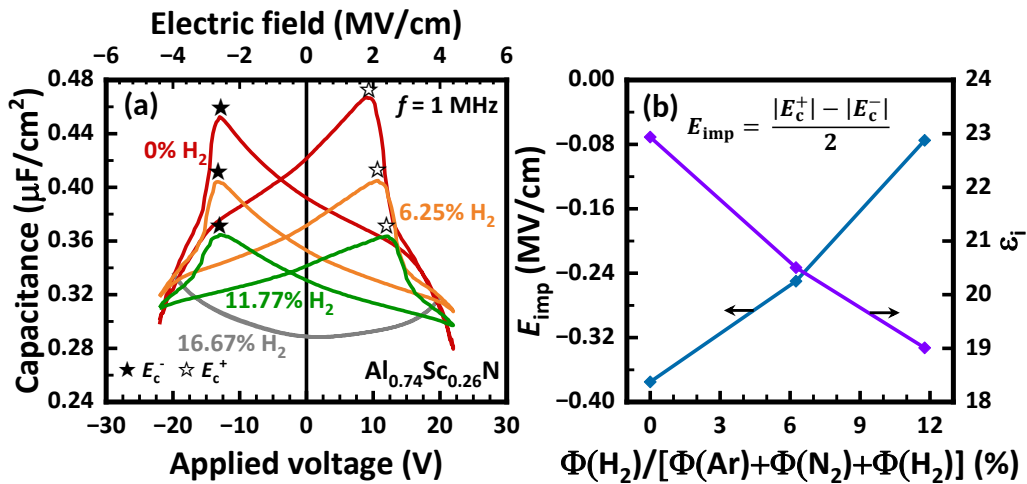


Figure 7.9: (a) C-V curves of fabricated Al_{0.74}Sc_{0.26}N MFM capacitors with high H₂ flux. The ferroelectricity sustains up to 11.77% of H₂ flux. (b) E_{imp} and ε_i in dependence with the H₂ flux percentage.

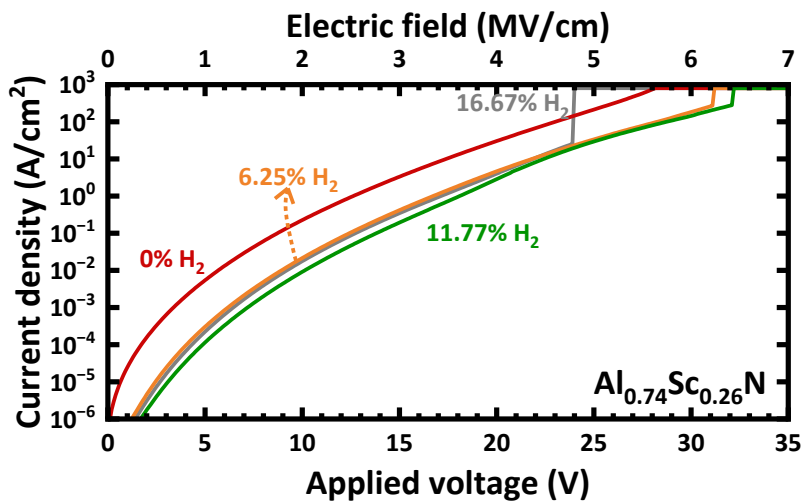


Figure 7.10: TZDB results of all deposited films. Leakage is suppressed and E_{BD} is improved with H₂ included sputtering up to 11.77% H₂ flux.

Figure 7.11 displays the overall P_r-E relationship of PUND measurements. Sputter deposition with higher H₂ flux results in lower P_r at all E region, along with more

ambiguous semi-saturation kinks. The former phenomenon could be explained by deteriorated c-axis orientation growth [233], [243]. E_c values also increased with H_2 flux. These observations are consistent with section 7.4.3. In addition, the linear-like uprising slope of 11.77% H_2 flux film indicates the possibility of multi-level operation for analog accelerators. As oxygen incorporated AlScN capacitors also demonstrate partial polarization reversal and linear P_r - E relationship, high H_2 flux sputtered films possess the disadvantage of higher E_c .

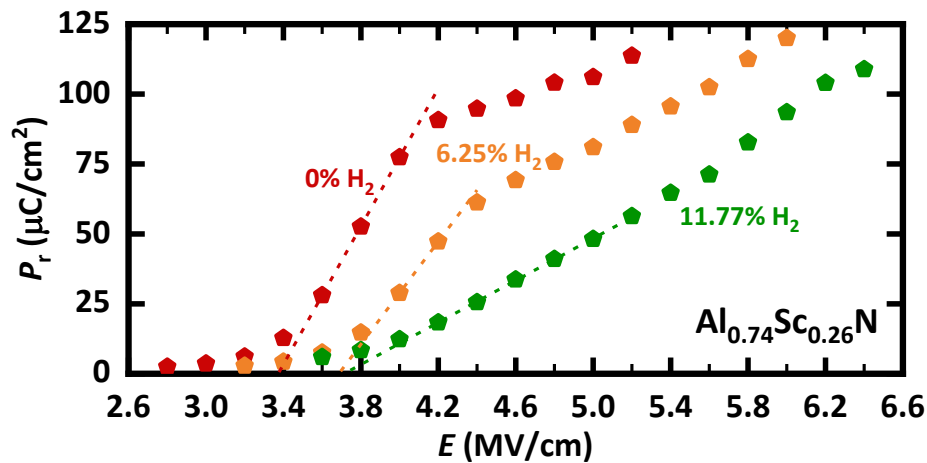


Figure 7.11: P_r - E relationship of fabricated $Al_{0.74}Sc_{0.26}N$ films in PUND measurements.

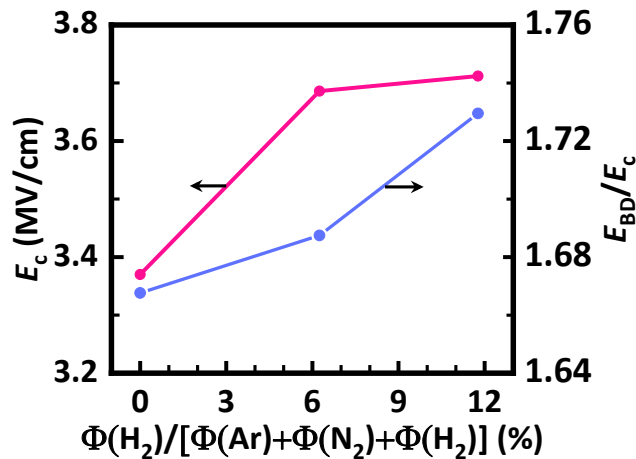


Figure 7.12: Extracted E_c and E_{BD}/E_c ratio with respect to H_2 flux percentage.

Figure 7.12 depicts the tendency of E_c and E_{BD}/E_c ratio obtained from TZDB and PUND tests. The increased E_{BD}/E_c ratio suggests better reliability potential of AlScN thin films prepared by H_2 gas involved sputtering [6]. Nevertheless, the demonstration of

enhanced endurance cycle is unsuccessful due to large leakage passing through the high-Sc content films. Luckily, this issue could be avoided by low-Sc content films, which is one of the topics of future research.

7.7. Summary of This Chapter

From SIMS measurements, a peak oxygen concentration is found at the ferroelectric/BE interface in AlScN MFM capacitors. Oxygen incorporation in sputtered films has been addressed to be influential to fatigue effect and impaired endurance performance, as shown in chapter 5. In this chapter, in order to mitigate fatigue effect and improve endurance cycle, 1% H₂ flux is utilized in reactive sputtering to lower the partial pressure of residual oxygen during ferroelectric layer deposition, resulting in reduced oxygen content in Al_{1-x}Sc_xN thin films. However, the *c*-axis crystallinity is found to be deteriorated due to incorporated H₂ gas, as shown in XRC analysis. Fortunately, all films present prominent ferroelectricity, indicating their robustness to reducing ambient. Although further material analysis is feasible, the effectiveness of oxygen content lowering is validated by declined ϵ_i values. Not only the leakage current is decreased, but also the breakdown strength is enhanced, regardless of the Sc content in Al_{1-x}Sc_xN thin films. These discoveries are contrary to the conclusions in chapter 5. This suggests a different mechanism governing the phenomenon. It is proposed that at low at.% of O atoms, though inputting H₂ gas eliminates O_N in the films, E_g broadening becomes more influential to leakage and breakdown field. In addition, P_r values, related to *c*-axis orientation, are generally decreased due to H₂ gas inclusion in sputtering, which is consistent to the XRC profiles. Wake-up and fatigue effects in the endurance cycling tests disappeared in films with H₂ flow process. Owing to stabilized E_c, a record high endurance cycle of over 10⁷ switching cycles is achieved. The results show that by reducing the oxygen level at AlScN/BE interface, endurance performance can be boosted.

Based on these findings, higher H₂ flux was used during ferroelectric AlScN thin films deposition. Up to 11.77% H₂ flux, ferroelectricity was demonstrated. Moreover, leakage current suppression and E_{BD} enhancement indicates further increased E_g values. However, excessive H₂ flux could give rise to inferior *c*-axis crystallinity, leading

to ferroelectricity distinction. The ferroelectric characterization results of high H₂ flux films show the same tendency with low H₂ flux films, as ϵ_i decreases and E_c increases continuously. Additionally, E_{imp} is shown to be tunable via varying the percentage of H₂ flux, similar to the oxygen incorporated AlScN case. In PUND measurements, linear P_r gain over a broad range of E is observed in 11.77% H₂ flux film. Despite E_c is increased, the possibility of multi-state operation for future analog NVM technology is presented. Additionally, enhanced E_{BD}/E_c ratio is beneficial for endurance improvement. Though more material analysis and further research are required, the potential of utilizing high H₂ flux during sputtering for ferroelectric AlScN thin films is demonstrated. Overall, the influence of H₂ flux included sputtering is demonstrated.

Chapter 8: Guidelines for Aluminum Scandium Nitride Capacitors For High Endurance and Low-Voltage Operation

8.1. Introduction

To improve the scalability and reliability performance of AlScN thin films, sputtering condition exploration, defect engineering, and reducing ambient deposition are proved to be effective in previous chapters. Based on these findings, this chapter elucidates a proposed model for high endurance and low-voltage operation for AlScN MFM capacitors.

8.2. Concept of the Proposed Model and Applicable Experimental Approach

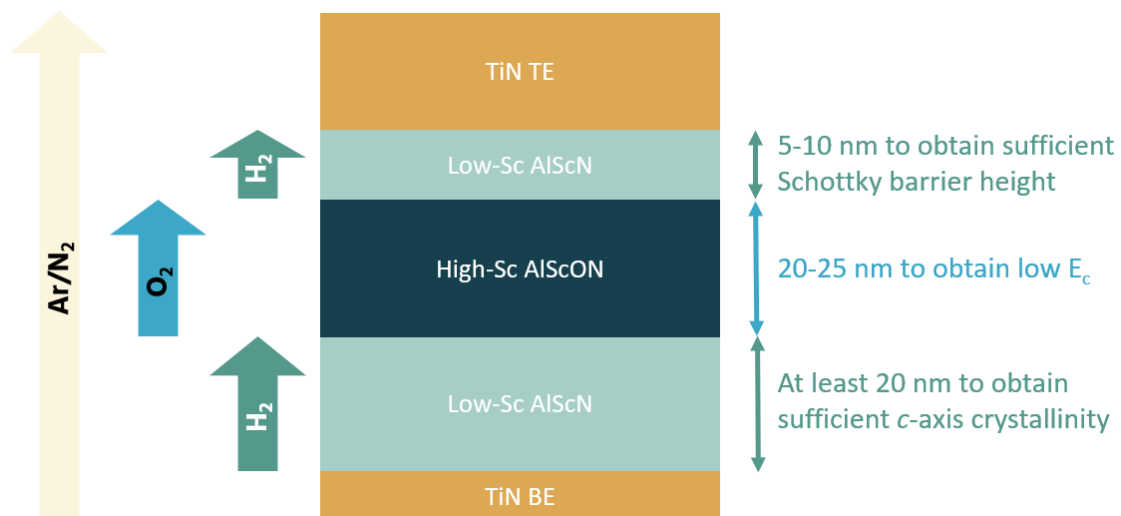


Figure 8.1: Concept of proposed model for AlScN MFM capacitors for high endurance and low-voltage operation.

Figure 8.1 illustrates the proposed model that consists of multi ferroelectric layers with different Sc and O content. For BE and TE, it is still advantageous to choose TiN since it is a CMOS compatible electrode and also offers high effective work function [248]. For the ferroelectric layers, it is proposed that a high-Sc content layer is sandwiched between two low-Sc content layers, as demonstrated in Figure 8.1. Multi-layer

structure could further improve the breakdown strength and inhibit leakage current [232], as mentioned in chapter 6. The thickness ratio should be about 2:2:1 from bottom to top. Moreover, H₂ and O₂ gases are included during sputtering low-Sc and high-Sc content layers, respectively. The reason for this layer arrangement is explained here.

First, the underlying layer utilizes low-Sc layer to suppress leakage current from the interface, and this layer should be deposited with reducing ambient to decrease the oxygen level at the ferroelectric/BE interface. This could help improve endurance and mitigate the fatigue effect. Note that as the underlying layer usually considerably influences the crystallinity of subsequent layers, the low-Sc content layer should be thick enough to obtain better crystallization. This is even more important since sputtering with H₂ inclusion deteriorates c-axis crystallinity, as shown in chapter 7.

Second, high-Sc content is chosen for the sandwiched layer due to its low E_c characteristics. Applying O₂ gas incorporated sputtering could decrease the E_c and increase E_{BD} even more for low-voltage operation, as evident from chapter 5. This layer should also be thick enough to decrease the overall E_c sufficiently. Since this layer is not directly contacted with the electrodes, fatigue effect is expected to be impaired.

Finally, the top layer selects low-Sc content and H₂-included deposition again to block the leakage current flow and prevent fatigue effect. This layer could be thinner by one half than other layers since its purpose is only to secure sufficient Schottky barrier height to the TiN TE.

The description on the right side of Figure 8.1 gives an example of the layer thickness for 50 nm capacitors. However, to achieve low-voltage operation, a thinner multi-layer stack is needed. The proposed model could be effective for total ferroelectric thickness above 5-10 nm since it is still possible to distinguish the interface, border, and bulk regions. However, at ultra-scaled regime under 5 nm, the difference between interface and bulk becomes ambiguous. Therefore, it requires further research and optimization to this model.

8.3. Summary of This Chapter

Based on the results from previous chapters, it is advantageous to combine different techniques to construct guidelines for enhanced endurance performance and better scalability. Several factors such as Sc content and oxygen level are considered and arranged for the multi-layer ferroelectric. The discussed deposition approaches are applicable in experiments. Although the proposed model could be less feasible for its purpose when the thickness is scaled down below 5 nm, it could still be beneficial for further research of ferroelectric layers above 5-10 nm.

Chapter 9: Conclusions and Future Works

9.1. Originality and Key Outcomes

Figure 9.1 illustrates the originality of this research, and the flow can be addressed in five consecutive steps:

- (1) Understanding the material properties of AlScN. Limited endurance and high leakage current are critical issues that should be tackled urgently for the development of AlScN ferroelectrics.
- (2) Exploring the suitable sputtering conditions for AlScN films with enhanced quality. This could help lay the foundation for further technical improvement. A trade-off between E_c and E_{BD} was found.
- (3) Defect engineering by oxygen incorporation was implemented mitigate the high E_c characteristic of AlScN, as $V_{Al}-O_N$ complex defects were formed. The trade-off between E_c and E_{BD} could be overcome. A linear P_r - E relationship unlocked the potential of multi-level operation for analog circuits while preserving high P_r ($> 100 \mu\text{C}/\text{cm}^2$). Besides, aggressive downscaling was made possible with this technique. However, fatigue effect became severe due to the formation of Sc-O bonds. Therefore, it is critical to form $V_{Al}-O_N$ complex defects rather than Sc-O bonds. One feasible approach is to reduce the Sc content in AlScN.
- (4) Oxygen depletion, implemented via reducing sputtering ambient, could lower the oxygen level at AlScN/BE interface where Sc-O bonds induce fatigue effect. Depleting oxygen using H_2 -included sputtering along with less Sc content is effective to boost the switching cycle and avoid wakeup/fatigue effects. Plus, decreased ϵ and suppress leakage are demonstrated. Nevertheless, lower P_r and higher E_c are the drawbacks.
- (5) Guidelines to design highly reliable and scalable ferroelectric AlScN films was proposed using Sc and O content profiling in the multi-layered film enhanced endurance and low-voltage operation.

Detailed key outcomes of each step are elucidated in the following.

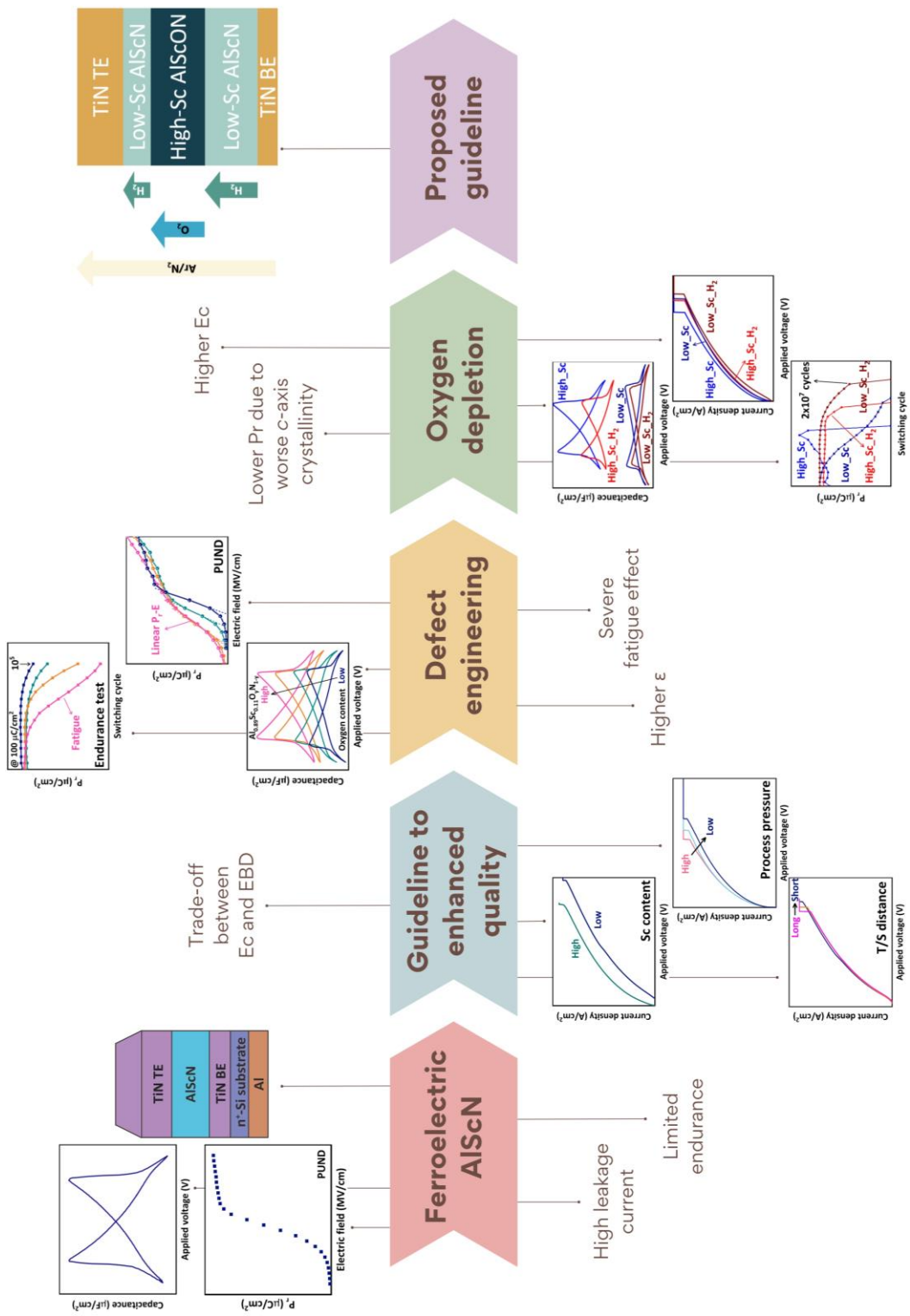


Figure 9.1: Originality of this research illustrated in a flow chart.

Chapter 4 focused on the exploration of suitable deposition conditions for sputtered AlScN thin films. The results are listed as follows:

- (1) Without intentionally doping or defect creation, E_c and E_{BD} share positive correlation.
- (2) Low-Sc content film is favorable over high-Sc due to wider E_g , suppressed leakage, lower ϵ_i , higher P_r , enhanced E_{BD} with the price of higher E_c . Therefore, the usage of AlSc alloy sputtering target with lower Sc content (5-15%) is advantageous.
- (3) Lower process pressure could be beneficial to decrease the leakage current and ϵ_i , while increasing P_r , E_c , and E_{BD} . The surface roughness can also be improved.
- (4) Suitable T/S distance could help inhibit leakage and boost P_r performance by producing better c-axis crystallinity.
- (5) These findings not only pave the way for improved endurance performance but also create the chance for thickness downscaling.

In chapter 5, defect engineering was applied to AlScN films by incorporating O_2 gas during deposition. By increasing the degree of oxygen doping, complex defects that affect the dielectric and ferroelectric properties are generated. The results are demonstrated as follows:

- (1) Oxygen contamination is unavoidable in reactive sputtering.
- (2) XRD profiles show that O atoms are not uniformly distributed inside the film. Plus, O atoms tend to bond with Sc at low oxygen concentration.
- (3) Creating $V_{Al}-O_N$ defect complexes could shift E_{imp} , increase ϵ_i , suppress leakage, and gain partial polarization at low E.
- (4) Defect engineering was found to be one effective way to reduce E_c and boost E_{BD} simultaneously.
- (5) Multi-level operations for analog applications can be realized by defect engineering due to linear P_r -E relationship at PUND measurements.
- (6) However, severe fatigue effects are found when more Sc-O bonds are formed, leading to non-ideal endurance cycles.

- (7) Defect engineering also shows its potential for aggressive thickness downscaling by suppressing large leakage and restoring ferroelectricity. Under 5 V operation is also achievable for AlScN with TiN electrodes.

Chapter 6 discovered that the polarity of pristine films could be controlled by oxygen profiling in stacked AlSc(O)N layers. It was found out that doping oxygen leads to polarity shifting from N-polar to metal-polar, and the magnitude could be tuned by the degree of oxygen inclusion. The details are listed as follows:

- (1) Mixed N-polar and metal-polar phases could co-exist in AlSc(O)N films with various oxygen profiling.
- (2) Two E_c components at the negative side could be discovered when oxygen level difference is large between layers in the stack. However, the positive side only shows one E_c component regardless of the profile of oxygen level.
- (3) The breakdown field is found to have high correspondence to the oxygen concentration at the ferroelectric/BE interface. Besides, multi-interfaces in the ferroelectric stack could also help block the leakage path and increase the breakdown strength.

After understanding the role of oxygen inside AlScN thin films, chapter 7 dedicates to decrease the oxygen content at the AlScN/BE to improve the endurance performance. The results are displayed as follows:

- (1) SIMS measurements proved that an oxygen concentration peak is found at the ferroelectric/BE interface in AlScN MFM capacitors, which could be influential to the fatigue effect in endurance tests.
- (2) The incorporation of H_2 gas in sputtering leads to oxygen depletion with the price of c -axis crystallinity deterioration, regardless of the Sc content in the film.
- (3) AlScN thin films exhibited robustness to reducing ambient during sputtering since prominent ferroelectric properties are demonstrated in various measurements. However, the H_2 flux should be limited to under $\sim 11.77\%$ since the c -axis orientated grains could be distinct.
- (4) H_2 involved sputtering decreases ϵ_i which shows the effectiveness of oxygen

content lowering.

- (5) A different mechanism governing the behavior of leakage and breakdown field is proposed since the results are contrary to the findings in chapter 5. At low at.% of O atoms, films deposited in reducing ambient could possess wider E_g that suppress the leakage and enhance the breakdown field.
- (6) Multi-level operation is also realizable when H_2 flux is high enough, however, E_c increases accordingly.
- (7) Wakeup and fatigue effects are eliminated by reducing sputtering ambient, showing the effectiveness of oxygen level lowering at AlScN/BE interface. A record high endurance cycle of over 10^7 switching cycles is achieved.

Based on all experimental results, guidelines of AlScN MFM capacitors for future high endurance and low-voltage operation are proposed in chapter 8. The details are listed as follows:

- (1) A model of triple ferroelectric layers with different Sc and O content profiling could be feasible.
- (2) The underlying and capping layers should be deposited using reducing ambient and low-Sc target to improve breakdown strength, suppress leakage, and prevent fatigue effect.
- (3) The sandwiched layer should select higher Sc content and take advantage of more complex defects that decreases E_c and gains E_{BD} .
- (4) The proposed model could be effective for total film thickness larger than 5-10 nm.

9.2. Conclusions

Advanced memory technology is attracting massive attention due to the rapid development of AI computing technology. Emerging NVM technology with ferroelectric materials has shown great potential due to their fascinating charge storage nature. III-N ferroelectrics such as AlScN possesses novelty and several

advantages over other popular ferroelectrics like PZT and HZO. However, challenges of AlScN thin films still remained to be conquered. To date, most publications show common characteristics of P_r of over $100 \mu\text{C}/\text{cm}^2$, E_c of 3-7 MV/cm, and ϵ_i of 11-20. Due to the presence of high leakage, the endurance is limited to $\sim 10^5$ cycles, and aggressive thickness downscaling is difficult to realize. Consequently, this research aims for improving scalability and reliability of AlScN thin films. In order to achieve high endurance and low-voltage operation, several properties of AlScN must be engineered. As high P_r value is the essence of AlScN, it is desirable to suppress leakage, minimize E_c , boost E_{BD} , and decrease ϵ_i while maintaining sufficient P_r . As mentioned in the previous section 9.1., this research adopts step-by-step technical improvements to reach the goals.

This research focused on *in-situ* reactive sputtering of TiN/AlScN/TiN metal-ferroelectric-metal (MFM) capacitors in principle and dedicates to exploring the suitable deposition conditions. By tuning the Sc content of the AlSc alloy target, process pressure, and T/S distance, improved film quality was achieved. It is shown that low Sc content film ($\text{Al}_{0.88}\text{Sc}_{0.12}\text{N}$) is preferred over high Sc films ($\text{Al}_{0.74}\text{Sc}_{0.26}\text{N}$) due to its advantageous properties, including a wider bandgap E_g , reduced leakage current, lower dielectric constant ϵ , higher remnant polarization P_r , and improved breakdown field strength E_{BD} . These features are further enhanced by lower process pressures during sputtering, which reduce V_N and improve surface roughness, leading to decreased leakage current and higher E_{BD} . Additionally, searching for the suitable T/S distance during deposition was shown to be advantageous for enhanced ferroelectricity and breakdown strength. Moreover, it was validated that E_c and E_{BD} share the same trend during these experiments, indicating a trade-off relationship. These findings not only paved the way for improved endurance performance but also created the chance for thickness downscaling.

When the oxygen level in AlScN is intentionally increased, defect complexes are created and thereby influence the ferroelectricity. Increased $V_{\text{Al-O-N}}$ defect complexes could ease the N-atom displacement and decrease E_c , which is beneficial for low voltage operation. As evident from PUND measurements, partial polarization is achieved at low E regions along with linear P_r -E relationship, indicating the potential of multi-level operation. Including oxygen into the ferroelectric also changes the polar

states in pristine films from N-polar to metal-polar. Moreover, the leakage is suppressed due to V_N elimination, which helps the demonstration of below 5 V operation in this research. However, prominent fatigue effects are induced due to trapping/de-trapping incidents at Sc-O bonds.

To resolve this issue, a method of sputtering with reducing ambient was implemented to deplete the oxygen level at the ferroelectric/BE interface. H_2 gas inclusion could decrease the partial pressure of residual O_2 in the chamber and form AlScN thin films with low oxygen level. Note that ferroelectric AlScN thin films exhibited great robustness against reducing ambient at deposition. As the amount of defect complexes declined, E_c increased accordingly. Fortunately, due to E_g enlargement, leakage suppression and E_{BD} enhancement were presented. Similar to the high oxygen level case, the P_r -E relationship showed linear-like behavior, but the overall P_r was lowered owing to worse *c*-axis crystallinity. Most importantly, since the Sc-O bondings at the ferroelectric/BE interface were removed by oxygen depletion, the endurance performance was boosted to over 10^7 cycles.

In addition, the role of oxygen was understood as follows. Despite defect engineering via oxygen incorporation could effectively reduce E_c , the accompanied fatigue is severe. Therefore, it is critical to form $V_{Al}-O_N$ complex defects rather than Sc-O bonds, and one promising method is to lower the Sc content in the film

Guidelines that extract the benefits from defect engineering and oxygen depletion were proposed. By applying combinations of Sc and O content profiling to the multi-layered ferroelectric stack, further improvement in endurance and scalability was expected. In summation, this research enhances the reliability and scalability features of AlScN thin films, and hopefully contributes to the development of ferroelectric AlScN for future advanced NVM technology.

9.3. Outlook and Future Works

In this research, low-Sc content down to 11% of $Al_{1-x}Sc_xN$ films are fabricated and characterized. As mentioned in section 4.5., an even lower Sc content approaching 5% could be feasible for further leakage suppression and breakdown enhancement.

Excessively low Sc content could lead to extremely high E_c which is not beneficial for low-voltage operation. Research regarding this is still ongoing by our team.

Moreover, TiN is used as electrodes for ferroelectric AlScN owing to its refractory properties and compatibility to CMOS technology. However, since the BE and TE engineering are shown to be influential for ferroelectrics like perovskites and fluorites [41], [230], [231], [249], it is worth researching the material selection of electrodes. This could involve properties such as crystal structure, texture, lattice constant, stress/strain status, grain size, surface roughness, (effective) work function, chemical reactivity to AlScN, etc.

Nowadays, as discussed in section 2.2., the deposition of ferroelectric AlScN thin films is accomplished by PVD sputtering or epitaxial growth methods. ALD growth of conformal AlScN films could be advantageous for capacitors in 3D architecture, e.g. NAND flash [250], [251]. Nonetheless, forming preferential AlN 002 orientation could be challenging in ALD chambers [252]. Besides, the crystallization in ultra-thin AlScN films might be another obstacle. Fortunately, ternary ALD process with supercycle approach could be feasible for AlScN [253].

Finally, the integration of AlScN thin films into FeRAM and FeFET technology is promising. Some recent works have demonstrated large memory window using AlScN as ferroelectric and oxide semiconductors as channel materials [254], [255]. Our team has already obtained some preliminary results of AlScN-based FeRAM and In_2O_3 FeFET with ferroelectric AlScN.

Reference

- [1] Nobel Foundation. *The Nobel Prize in Physics 1956*. Accessed: Jan. 5th, 2025. [Online]. Available: <https://www.nobelprize.org/prizes/physics/1956/summary/>
- [2] S. M. Sze, Y. Li, and K. K. Ng, *Physics of Semiconductor Devices*, 4th ed., USA: John Wiley and Sons, Inc., 2021.
- [3] Y. Taur and T. K. Ning, *Fundamentals of Modern VLSI Devices*, 3rd ed., Cambridge, UK: Cambridge University Press, 2022.
- [4] H. Iwai, "NMOS LSI Development from 1970's to the beginning of 1980's," *2021 IEEE 14th International Conference on ASIC (ASICON)*, pp. 1-4, 2021.
- [5] Redgate Blog. *What's the real story behind the explosive growth of data?* Accessed: Jan. 5th, 2025. [Online]. Available: <https://explodingtopics.com/blog/data-generated-per-day>
- [6] K. H. Kim, I. Karpov, R. H. Olsson III, and D. Jariwala, "Wurtzite and fluorite ferroelectric materials for electronic memory," *Nature Nanotechnology*, vol. 18, no. 5, pp. 422-441, 2023.
- [7] J. von Neumann, *The Computer and the Brain*, 3rd ed., USA: Yale University Press, 2012.
- [8] A. Sebastian, M. Le Gallo, R. Khaddam-Aljameh, and E. Eleftheriou, "Memory devices and applications for in-memory computing," *Nature Nanotechnology*, vol. 15, no. 7, pp. 529-544, 2020.
- [9] D. Kuzum, R. G. Jeyasingh, B. Lee, and H.-S. P. Wong, "Nanoelectronic programmable synapses based on phase change materials for brain-inspired computing," *Nano Letters*, vol. 12, no. 5, pp. 2179-2186, 2012.
- [10] H.-S. P. Wong and S. Salahuddin, "Memory leads the way to better computing," *Nature Nanotechnology*, vol. 10, no. 3, pp. 191-4, 2015.
- [11] P. Mannocci, M. Farronato, N. Lepri, L. Cattaneo, A. Glukhov, Z. Sun, and D. Ielmini, "In-memory computing with emerging memory devices: Status and outlook," *APL Machine Learning*, vol. 1, no. 1, 2023.
- [12] J. Wang, X. Wang, C. Eckert, A. Subramaniyan, R. Das, D. Blaauw, and D. Sylvester, "A 28-nm Compute SRAM With Bit-Serial Logic/Arithmetic Operations for Programmable In-Memory Vector Computing," *IEEE Journal of Solid-State Circuits*, vol. 55, no. 1, pp. 76-86, 2020.
- [13] S. Mittal, G. Verma, B. Kaushik, and F. A. Khanday, "A survey of SRAM-based in-memory computing techniques and applications," *Journal of Systems Architecture*, vol. 119, 2021.
- [14] A. Moitra, A. Bhattacharjee, Y. Li, Y. Kim, and P. Panda, "When in-memory computing meets spiking neural networks—A perspective on device-circuit-

- system-and-algorithm co-design,” *Applied Physics Reviews*, vol. 11, no. 3, 2024.
- [15] T. P. Xiao, C. H. Bennett, B. Feinberg, S. Agarwal, and M. J. Marinella, “Analog architectures for neural network acceleration based on non-volatile memory,” *Applied Physics Reviews*, vol. 7, no. 3, 2020.
- [16] D. Ielmini and H. S.-P. Wong, “In-memory computing with resistive switching devices,” *Nature Electronics*, vol. 1, no. 6, pp. 333-343, 2018.
- [17] A. I. Khan, A. Keshavarzi, and S. Datta, “The future of ferroelectric field-effect transistor technology,” *Nature Electronics*, vol. 3, no. 10, pp. 588-597, 2020.
- [18] T. Mikolajick, U. Schroeder, and S. Slesazeck, “The Past, the Present, and the Future of Ferroelectric Memories,” *IEEE Transactions on Electron Devices*, vol. 67, no. 4, pp. 1434-1443, 2020.
- [19] “A century of ferroelectricity,” *Nature Materials*, vol. 19, no. 2, pp. 129, 2020.
- [20] J. Valasek, “Piezo-Electric and Allied Phenomena in Rochelle Salt,” *Physical Review*, vol. 17, no. 4, pp. 475-481, 1921.
- [21] G. Busch and P. Scherrer, “Eine neue seignette-elektrische Substanz,” *Die Naturwissenschaften*, vol. 23, no. 43, pp. 737-737, 1935.
- [22] A. von Hippel, R. G. Breckenridge, F. G. Chesley, and L. Tisza, “High dielectric constant ceramics,” *Industrial & Engineering Chemistry*, vol. 38, no. 11, pp. 1097-1109, 1946.
- [23] G. Shirane and A. Takeda, “Phase Transitions in Solid Solutions of PbZrO_3 and PbTiO_3 (I) Small Concentrations of PbTiO_3 ,” *Journal of the Physical Society of Japan*, vol. 7, no. 1, pp. 5-11, 1952.
- [24] G. Shirane, K. Suzuki, and A. Takeda, “Phase Transitions in Solid Solutions of PbZrO_3 and PbTiO_3 (II) X-ray Study,” *Journal of the Physical Society of Japan*, vol. 7, no. 1, pp. 12-18, 1952.
- [25] I. Ross, “Semiconductive translating device,” patent no: 2791760A, 1957.
- [26] D. Bondurant, “Ferroelectronic ram memory family for critical data storage,” *Ferroelectrics*, vol. 112, no. 1, pp. 273-282, 1990.
- [27] T. P. Ma and J.-P. Han, “Why is nonvolatile ferroelectric memory field-effect transistor still elusive?,” *IEEE Electron Device Letters*, vol. 23, no. 7, pp. 386-388, 2002.
- [28] S. Khanna, S. C. Bartling, M. Clinton, S. Summerfelt, J. A. Rodriguez, and H. P. McAdams, “An FRAM-Based Nonvolatile Logic MCU SoC Exhibiting 100% Digital State Retention at $V_{DD} = 0$ V Achieving Zero Leakage With <400-ns Wakeup Time for ULP Applications,” *IEEE Journal of Solid-State Circuits*, vol. 49, no. 1, pp. 95-106, 2014.
- [29] A. S. Bhalla and A. Saxena, “Ferroelectricity: 100 years on,” *Physics World*, vol. 33, no. 11, pp. 38-41, 2021.

- [30] A. R. Jayakrishnan, J. S. Kim, M. Hellenbrand, L. S. Marques, J. L. MacManus-Driscoll, and J. P. B. Silva, "Growth of emergent simple pseudo-binary ferroelectrics and their potential in neuromorphic computing devices," *Materials Horizons*, vol. 11, no. 10, pp. 2355-2371, 2024.
- [31] T. S. Böscke, J. Müller, D. Bräuhäus, U. Schröder, and U. Böttger, "Ferroelectricity in hafnium oxide thin films," *Applied Physics Letters*, vol. 99, no. 10, 2011.
- [32] S. Fichtner, N. Wolff, F. Lofink, L. Kienle, and B. Wagner, "AlScN: A III-V semiconductor based ferroelectric," *Journal of Applied Physics*, vol. 125, no. 11, 2019.
- [33] J. Muller, T. S. Boscke, U. Schroder, S. Mueller, D. Brauhaus, U. Bottger, L. Frey, and T. Mikolajick, "Ferroelectricity in Simple Binary ZrO_2 and HfO_2 ," *Nano Letters*, vol. 12, no. 8, pp. 4318-4323, 2012.
- [34] M. Uehara, R. Mizutani, S. Yasuoka, T. Shiraishi, T. Shimizu, H. Yamada, M. Akiyama, and H. Funakubo, "Demonstration of ferroelectricity in ScGaN thin film using sputtering method," *Applied Physics Letters*, vol. 119, no. 17, 2021.
- [35] A. A. Balaraman and S. Dutta, "Inorganic dielectric materials for energy storage applications: a review," *Journal of Physics D: Applied Physics*, vol. 55, no. 18, 2022.
- [36] X. Yuan, J. Shi, Y. Kang, J. Dong, Z. Pei, and X. Ji, "Piezoelectricity, Pyroelectricity, and Ferroelectricity in Biomaterials and Biomedical Applications," *Advanced Materials*, vol. 36, no. 3, pp. e2308726, 2024.
- [37] A. K. Saha and S. K. Gupta, "Negative capacitance effects in ferroelectric heterostructures: A theoretical perspective," *Journal of Applied Physics*, vol. 129, no. 8, 2021.
- [38] L. W. Martin and A. M. Rappe, "Thin-film ferroelectric materials and their applications," *Nature Reviews Materials*, vol. 2, no. 2, 2016.
- [39] D. H. Lee, Y. Lee, Y. H. Cho, H. Choi, S. H. Kim, and M. H. Park, "Unveiled Ferroelectricity in Well-Known Non-Ferroelectric Materials and Their Semiconductor Applications," *Advanced Functional Materials*, vol. 33, no. 42, 2023.
- [40] I. J. Kim and J. S. Lee, "Ferroelectric Transistors for Memory and Neuromorphic Device Applications," *Advanced Materials*, vol. 35, no. 22, 2023.
- [41] C. A. P. de Araujo, J. D. Cuchiaro, L. D. McMillan, M. C. Scott, and J. F. Scott, "Fatigue-free ferroelectric capacitors with platinum electrodes," *Nature*, vol. 374, no. 6523, pp. 627-629, 1995.
- [42] T. Schenk, M. Petic, S. Slesazek, U. Schroeder, and T. Mikolajick, "Memory technology-a primer for material scientists," *Reports on Progress in Physics*, vol. 83, no. 8, pp. 086501, 2020.

- [43] M. Bohr, R. Chau, T. Ghani, and K. Mistry, "The High-k Solution," *IEEE Spectrum*, vol. 44, no. 10, pp. 29-35, 2007.
- [44] J. Müller, U. Schröder, T. S. Böske, I. Müller, U. Böttger, L. Wilde, J. Sundqvist, M. Lemberger, P. Kücher, T. Mikolajick, and L. Frey, "Ferroelectricity in yttrium-doped hafnium oxide," *Journal of Applied Physics*, vol. 110, no. 11, 2011.
- [45] S. Mueller, J. Mueller, A. Singh, S. Riedel, J. Sundqvist, U. Schroeder, and T. Mikolajick, "Incipient Ferroelectricity in Al-Doped HfO₂ Thin Films," *Advanced Functional Materials*, vol. 22, no. 11, pp. 2412-2417, 2012.
- [46] U. Schroeder, C. Richter, M. H. Park, T. Schenk, M. Pesic, M. Hoffmann, F. P. G. Fengler, D. Pohl, B. Rellinghaus, C. Zhou, C. C. Chung, J. L. Jones, and T. Mikolajick, "Lanthanum-Doped Hafnium Oxide: A Robust Ferroelectric Material," *Inorganic Chemistry*, vol. 57, no. 5, pp. 2752-2765, 2018.
- [47] S. Mueller, C. Adelman, A. Singh, S. Van Elshocht, U. Schroeder, and T. Mikolajick, "Ferroelectricity in Gd-Doped HfO₂ Thin Films," *ECS Journal of Solid State Science and Technology*, vol. 1, no. 6, pp. N123-N126, 2012.
- [48] K. Xu, T. Wang, J. Yu, Y. Liu, Z. Li, C. Lu, J. Song, J. Meng, H. Zhu, Q. Sun, D. W. Zhang, and L. Chen, "Fluorite-structured antiferroelectric hafnium-zirconium oxide for emerging nonvolatile memory and neuromorphic-computing applications," *Applied Physics Reviews*, vol. 11, no. 2, 2024.
- [49] M. Dogan, N. Gong, T. P. Ma, and S. Ismail-Beigi, "Causes of ferroelectricity in HfO₂-based thin films: an ab initio perspective," *Physical Chemistry Chemical Physics*, vol. 21, no. 23, pp. 12150-12162, 2019.
- [50] S. J. Kim, D. Narayan, J.-G. Lee, J. Mohan, J. S. Lee, J. Lee, H. S. Kim, Y.-C. Byun, A. T. Lucero, C. D. Young, S. R. Summerfelt, T. San, L. Colombo, and J. Kim, "Large ferroelectric polarization of TiN/Hf_{0.5}Zr_{0.5}O₂/TiN capacitors due to stress-induced crystallization at low thermal budget," *Applied Physics Letters*, vol. 111, no. 24, 2017.
- [51] H. J. Kim, M. H. Park, Y. J. Kim, Y. H. Lee, W. Jeon, T. Gwon, T. Moon, K. D. Kim, and C. S. Hwang, "Grain size engineering for ferroelectric Hf_{0.5}Zr_{0.5}O₂ films by an insertion of Al₂O₃ interlayer," *Applied Physics Letters*, vol. 105, no. 19, 2014.
- [52] U. Schroeder, M. H. Park, T. Mikolajick, and C. S. Hwang, "The fundamentals and applications of ferroelectric HfO₂," *Nature Reviews Materials*, vol. 7, no. 8, pp. 653-669, 2022.
- [53] T. Mikolajick, S. Slesazek, H. Mulaosmanovic, M. H. Park, S. Fichtner, P. D. Lomenzo, M. Hoffmann, and U. Schroeder, "Next generation ferroelectric materials for semiconductor process integration and their applications," *Journal of Applied Physics*, vol. 129, no. 10, 2021.
- [54] J. Okuno, T. Kunihiro, K. Konishi, M. Materano, T. Ali, K. Kuehnel, K. Seidel, T.

- Mikolajick, U. Schroeder, M. Tsukamoto, and T. Umebayashi, "1T1C FeRAM Memory Array Based on Ferroelectric HZO With Capacitor Under Bitline," *IEEE Journal of the Electron Devices Society*, vol. 10, pp. 29-34, 2022.
- [55] A. Sheikholeslami and P. G. Gulak, "A survey of circuit innovations in ferroelectric random-access memories," *Proceedings of the IEEE*, vol. 88, no. 5, pp. 667-689, 2000.
- [56] International Roadmap for Devices and Systems (IRDS) 2023 update.
- [57] W. Wang, T. Eshita, K. Takai, S. Amari, K. Nakamura, M. Oikawa, N. Sato, S. Ozawa, M. Nakabayashi, S. Mihara, Y. Hikosaka, H. Saito, K. Inoue, and K. Nagai, "Highly Reliable 4 Mb FeRAM Using a Newly Developed PLZT Capacitor With a Bi-Doped SRO Interlayer," *IEEE Electron Device Letters*, vol. 45, no. 11, pp. 2126-2129, 2024.
- [58] H. Jiao, X. Wang, S. Wu, Y. Chen, J. Chu, and J. Wang, "Ferroelectric field effect transistors for electronics and optoelectronics," *Applied Physics Reviews*, vol. 10, no. 1, 2023.
- [59] J. Robertson, "High dielectric constant gate oxides for metal oxide Si transistors," *Reports on Progress in Physics*, vol. 69, no. 2, pp. 327-396, 2006.
- [60] A. Molle, S. Baldovino, S. Spiga, and M. Fanciulli, "High permittivity materials for oxide gate stack in Ge-based metal oxide semiconductor capacitors," *Thin Solid Films*, vol. 518, no. 6, pp. S96-S103, 2010.
- [61] P. Laukkanen, M. P. J. Punkkinen, M. Kuzmin, K. Kokko, J. Lång, and R. M. Wallace, "Passivation of III-V surfaces with crystalline oxidation," *Applied Physics Reviews*, vol. 8, no. 1, 2021.
- [62] E. Yurchuk, J. Muller, S. Muller, J. Paul, M. Pesic, R. van Bentum, U. Schroeder, and T. Mikolajick, "Charge-Trapping Phenomena in HfO₂-Based FeFET-Type Nonvolatile Memories," *IEEE Transactions on Electron Devices*, vol. 63, no. 9, pp. 3501-3507, 2016.
- [63] K. Ni, P. Sharma, J. Zhang, M. Jerry, J. A. Smith, K. Tapily, R. Clark, S. Mahapatra, and S. Datta, "Critical Role of Interlayer in Hf_{0.5}Zr_{0.5}O₂ Ferroelectric FET Nonvolatile Memory Performance," *IEEE Transactions on Electron Devices*, vol. 65, no. 6, pp. 2461-2469, 2018.
- [64] S. Beyer, S. Dunkel, M. Trentzsch, J. Muller, A. Hellmich, D. Utess, J. Paul, D. Kleimaier, J. Pellerin, S. Muller, J. Ocker, A. Benoist, H. Zhou, M. Mennenga, M. Schuster, F. Tassan, M. Noack, A. Pourkeramati, F. Muller, M. Lederer, T. Ali, R. Hoffmann, T. Kampfe, K. Seidel, H. Mulaosmanovic, E. T. Breyer, T. Mikolajick, and S. Slesazek, "FeFET: A versatile CMOS compatible device with game-changing potential," *2020 IEEE International Memory Workshop (IMW)*, pp. 1-4, 2020.

- [65] A. J. Tan, Y.-H. Liao, L.-C. Wang, N. Shanker, J.-H. Bae, C. Hu, and S. Salahuddin, "Ferroelectric HfO₂ Memory Transistors With High- κ Interfacial Layer and Write Endurance Exceeding 10¹⁰ Cycles," *IEEE Electron Device Letters*, vol. 42, no. 7, pp. 994-997, 2021.
- [66] J. Hwang, Y. Goh, and S. Jeon, "Effect of Insertion of Dielectric Layer on the Performance of Hafnia Ferroelectric Devices," *IEEE Transactions on Electron Devices*, vol. 68, no. 2, pp. 841-845, 2021.
- [67] Z. Luo, Z. Wang, Z. Guan, C. Ma, L. Zhao, C. Liu, H. Sun, H. Wang, Y. Lin, X. Jin, Y. Yin, and X. Li, "High-precision and linear weight updates by subnanosecond pulses in ferroelectric tunnel junction for neuro-inspired computing," *Nature Communications*, vol. 13, no. 1, pp. 699, 2022.
- [68] D. Jena, R. Page, J. Casamento, P. Dang, J. Singhal, Z. Zhang, J. Wright, G. Khalsa, Y. Cho, and H. G. Xing, "The new nitrides: layered, ferroelectric, magnetic, metallic and superconducting nitrides to boost the GaN photonics and electronics eco-system," *Japanese Journal of Applied Physics*, vol. 58, no. SC, 2019.
- [69] Nobel Foundation. *The Nobel Prize in Physics 2014*. Accessed: Jan. 5th, 2025. [Online]. Available: <https://www.nobelprize.org/prizes/physics/2014/summary/>
- [70] B. G. Levi, "Nobel Prize in Physics recognizes research leading to high-brightness blue LEDs," *Physics Today*, vol. 67, no. 12, pp. 14-17, 2014.
- [71] H. Riechert, "Lighting the 21st century," *physica status solidi (a) - applications and materials science*, vol. 212, no. 5, pp. 893-896, 2015.
- [72] S.-i. Inoue, N. Tamari, and M. Taniguchi, "150 mW deep-ultraviolet light-emitting diodes with large-area AlN nanophotonic light-extraction structure emitting at 265 nm," *Applied Physics Letters*, vol. 110, no. 14, 2017.
- [73] J. Li, Z. Y. Fan, R. Dahal, M. L. Nakarmi, J. Y. Lin, and H. X. Jiang, "200 nm deep ultraviolet photodetectors based on AlN," *Applied Physics Letters*, vol. 89, no. 21, 2006.
- [74] Z. Zhang, M. Kushimoto, T. Sakai, N. Sugiyama, L. J. Schowalter, C. Sasaoka, and H. Amano, "A 271.8 nm deep-ultraviolet laser diode for room temperature operation," *Applied Physics Express*, vol. 12, no. 12, 2019.
- [75] R. Dingle, H. L. Störmer, A. C. Gossard, and W. Wiegmann, "Electron mobilities in modulation-doped semiconductor heterojunction superlattices," *Applied Physics Letters*, vol. 33, no. 7, pp. 665-667, 1978.
- [76] T. Mimura, S. Hiyamizu, T. Fujii, and K. Nanbu, "A New Field-Effect Transistor with Selectively Doped GaAs/n-Al_xGa_{1-x}As Heterojunctions," *Japanese Journal of Applied Physics*, vol. 19, no. 5, 1980.

- [77] M. Asif Khan, A. Bhattarai, J. N. Kuznia, and D. T. Olson, "High electron mobility transistor based on a GaN-Al_xGa_{1-x}N heterojunction," *Applied Physics Letters*, vol. 63, no. 9, pp. 1214-1215, 1993.
- [78] L. F. Eastman and U. K. Mishra, "The toughest transistor yet [GaN transistors]," *IEEE Spectrum*, vol. 39, no. 5, pp. 28-33, 2002.
- [79] U. K. Mishra, P. Parikh, and W. Yi-Feng, "AlGaN/GaN HEMTs-an overview of device operation and applications," *Proceedings of the IEEE*, vol. 90, no. 6, pp. 1022-1031, 2002.
- [80] K. J. Chen, O. Haberlen, A. Lidow, C. I. Tsai, T. Ueda, Y. Uemoto, and Y. Wu, "GaN-on-Si Power Technology: Devices and Applications," *IEEE Transactions on Electron Devices*, vol. 64, no. 3, pp. 779-795, 2017.
- [81] M. Akita, S. Kishimoto, and T. Mizutani, "High-frequency measurements of AlGa_xGaN HEMTs at high temperatures," *IEEE Electron Device Letters*, vol. 22, no. 8, pp. 376-377, 2001.
- [82] Y. Murase, K. Asano, I. Takenaka, Y. Ando, H. Takahashi, and C. Sasaoka, "T-Shaped Gate GaN HFETs on Si With Improved Breakdown Voltage and f_{MAX} ," *IEEE Electron Device Letters*, vol. 35, no. 5, pp. 524-526, 2014.
- [83] P. Daoust, P. Desjardins, R. A. Masut, V. Gosselin, and M. Côté, "Ab initio piezoelectric properties of Al_{0.5}Sc_{0.5}N: Impact of alloy configuration on the $d_{33,f}$ piezoelectric strain coefficient," *Physical Review Materials*, vol. 1, no. 5, 2017.
- [84] C. Fei, X. Liu, B. Zhu, D. Li, X. Yang, Y. Yang, and Q. Zhou, "AlN piezoelectric thin films for energy harvesting and acoustic devices," *Nano Energy*, vol. 51, pp. 146-161, 2018.
- [85] F. Tasnadi, B. Alling, C. Hoglund, G. Wingqvist, J. Birch, L. Hultman, and I. A. Abrikosov, "Origin of the anomalous piezoelectric response in wurtzite Sc_xAl_{1-x}N alloys," *Physical Review Letters*, vol. 104, no. 13, pp. 137601, 2010.
- [86] S. Zhang, D. Holec, W. Y. Fu, C. J. Humphreys, and M. A. Moram, "Tunable optoelectronic and ferroelectric properties in Sc-based III-nitrides," *Journal of Applied Physics*, vol. 114, no. 13, 2013.
- [87] O. Ambacher, J. Smart, J. R. Shealy, N. G. Weimann, K. Chu, M. Murphy, W. J. Schaff, L. F. Eastman, R. Dimitrov, L. Wittmer, M. Stutzmann, W. Rieger, and J. Hilsenbeck, "Two-dimensional electron gases induced by spontaneous and piezoelectric polarization charges in N- and Ga-face AlGa_xGaN heterostructures," *Journal of Applied Physics*, vol. 85, no. 6, pp. 3222-3233, 1999.
- [88] H. Wang, N. Adamski, S. Mu, and C. G. Van de Walle, "Piezoelectric effect and polarization switching in Al_{1-x}Sc_xN," *Journal of Applied Physics*, vol. 130, no. 10, 2021.

- [89] B. Bhattarai, X. Zhang, W. Xu, Y. Gu, W. J. Meng, and A. C. Meng, "Effect of Sc spatial distribution on the electronic and ferroelectric properties of AlScN," *Materials Horizons*, vol. 11, no. 21, pp. 5402-5408, 2024.
- [90] J. Hayden, M. D. Hossain, Y. Xiong, K. Ferri, W. Zhu, M. V. Imperatore, N. Giebink, S. Troler-McKinstry, I. Dabo, and J.-P. Maria, "Ferroelectricity in boron-substituted aluminum nitride thin films," *Physical Review Materials*, vol. 5, no. 4, 2021.
- [91] D. Wang, S. Mondal, J. Liu, M. Hu, P. Wang, S. Yang, D. Wang, Y. Xiao, Y. Wu, T. Ma, and Z. Mi, "Ferroelectric YAlN grown by molecular beam epitaxy," *Applied Physics Letters*, vol. 123, no. 3, 2023.
- [92] S. Yang, D. Wang, M. M. H. Tanim, D. Wang, and Z. Mi, "Molecular beam epitaxy and characterization of ferroelectric quaternary alloy $\text{Sc}_{0.2}\text{Al}_{0.45}\text{Ga}_{0.35}\text{N}$," *Applied Physics Letters*, vol. 124, no. 19, 2024.
- [93] S. Calderon V, J. Hayden, S. M. Baksa, W. Tzou, S. Troler-McKinstry, I. Dabo, J. P. Maria, and E. C. Dickey, "Atomic-scale polarization switching in wurtzite ferroelectrics," *Science*, vol. 380, no. 6649, pp. 1034-1038, 2023.
- [94] N. Wolff, S. Fichtner, B. Haas, M. R. Islam, F. Niekiel, M. Kessel, O. Ambacher, C. Koch, B. Wagner, F. Lofink, and L. Kienle, "Atomic scale confirmation of ferroelectric polarization inversion in wurtzite-type AlScN," *Journal of Applied Physics*, vol. 129, no. 3, 2021.
- [95] A. Krishnamoorthy, S. C. Tiwari, A. Nakano, R. K. Kalia, and P. Vashishta, "Electric-field-induced crossover of polarization reversal mechanisms in $\text{Al}_{1-x}\text{Sc}_x\text{N}$ ferroelectrics," *Nanotechnology*, vol. 32, no. 49, 2021.
- [96] R. Guido, P. D. Lomenzo, M. R. Islam, N. Wolff, M. Gremmel, G. Schonweger, H. Kohlstedt, L. Kienle, T. Mikolajick, S. Fichtner, and U. Schroeder, "Thermal Stability of the Ferroelectric Properties in 100 nm-Thick $\text{Al}_{0.72}\text{Sc}_{0.28}\text{N}$," *ACS Applied Materials & Interfaces*, vol. 15, no. 5, pp. 7030-7043, 2023.
- [97] S.-L. Tsai, T. Hoshii, H. Wakabayashi, K. Tsutsui, T.-K. Chung, E. Y. Chang, and K. Kakushima, "Room-temperature deposition of a poling-free ferroelectric AlScN film by reactive sputtering," *Applied Physics Letters*, vol. 118, no. 8, 2021.
- [98] S. Yasuoka, T. Shimizu, A. Tateyama, M. Uehara, H. Yamada, M. Akiyama, and H. Funakubo, "Impact of Deposition Temperature on Crystal Structure and Ferroelectric Properties of $(\text{Al}_{1-x}\text{Sc}_x)\text{N}$ Films Prepared by Sputtering Method," *physica status solidi (a) – applications and materials science*, vol. 218, no. 17, 2021.
- [99] D. Wang, J. Zheng, P. Musavigharavi, W. Zhu, A. C. Foucher, S. E. Troler-McKinstry, E. A. Stach, and R. H. Olsson, "Ferroelectric Switching in Sub-20 nm Aluminum Scandium Nitride Thin Films," *IEEE Electron Device Letters*, vol. 41,

- no. 12, pp. 1774-1777, 2020.
- [100] R. Mizutani, S. Yasuoka, T. Shiraishi, T. Shimizu, M. Uehara, H. Yamada, M. Akiyama, O. Sakata, and H. Funakubo, "Thickness scaling of $(\text{Al}_{0.8}\text{Sc}_{0.2})\text{N}$ films with remanent polarization beyond $100 \mu\text{C cm}^{-2}$ around 10 nm in thickness," *Applied Physics Express*, vol. 14, no. 10, 2021.
- [101] G. Schönweger, M. R. Islam, N. Wolff, A. Petraru, L. Kienle, H. Kohlstedt, and S. Fichtner, "Ultrathin $\text{Al}_{1-x}\text{Sc}_x\text{N}$ for Low-Voltage-Driven Ferroelectric-Based Devices," *physica status solidi (RRL) – Rapid Research Letters*, vol. 17, no. 1, 2022.
- [102] P. Wang, D. Wang, N. M. Vu, T. Chiang, J. T. Heron, and Z. Mi, "Fully epitaxial ferroelectric ScAlN grown by molecular beam epitaxy," *Applied Physics Letters*, vol. 118, no. 22, 2021.
- [103] N. Wolff, G. Schönweger, I. Streicher, M. R. Islam, N. Braun, P. Straňák, L. Kirste, M. Prescher, A. Lotnyk, H. Kohlstedt, S. Leone, L. Kienle, and S. Fichtner, "Demonstration and STEM Analysis of Ferroelectric Switching in MOCVD-Grown Single Crystalline $\text{Al}_{0.85}\text{Sc}_{0.15}\text{N}$," *Advanced Physics Research*, vol. 3, no. 5, 2024.
- [104] Z. Liu, X. Wang, X. Ma, Y. Yang, and D. Wu, "Doping effects on the ferroelectric properties of wurtzite nitrides," *Applied Physics Letters*, vol. 122, no. 12, 2023.
- [105] D. Drury, K. Yazawa, A. Mis, K. Talley, A. Zakutayev, and G. L. Brennecke, "Understanding Reproducibility of Sputter-Deposited Metastable Ferroelectric Wurtzite $\text{Al}_{0.6}\text{Sc}_{0.4}\text{N}$ Films Using In Situ Optical Emission Spectrometry," *physica status solidi (RRL) – Rapid Research Letters*, vol. 15, no. 5, 2021.
- [106] S. Satoh, K. Ohtaka, T. Shimatsu, and S. Tanaka, "Crystal structure deformation and phase transition of AlScN thin films in whole Sc concentration range," *Journal of Applied Physics*, vol. 132, no. 2, 2022.
- [107] Y. Xue, D. Cui, M. Kang, Y. Wang, H. Zhang, H. Yuan, X. Gao, J. Su, Z. Lin, J. Miao, J. Zhang, Y. Hao, and J. Chang, "Reversal barrier and ferroelectric polarization of strained wurtzite $\text{Al}_{1-x}\text{Sc}_x\text{N}$ ferroelectric alloys," *Applied Physics Letters*, vol. 125, no. 15, 2024.
- [108] O. Ambacher, S. Mihalic, E. Wade, M. Yassine, A. Yassine, N. Feil, and B. Christian, "Influence of alloying and structural transition on the directional elastic and isotropic thermodynamic properties of wurtzite and layered hexagonal $\text{Sc}_x\text{Al}_{1-x}\text{N}$ crystals," *Journal of Applied Physics*, vol. 132, no. 17, 2022.
- [109] O. Ambacher, B. Christian, N. Feil, D. F. Urban, C. Elsässer, M. Prescher, and L. Kirste, "Wurtzite ScAlN , InAlN , and GaAlN crystals, a comparison of structural, elastic, dielectric, and piezoelectric properties," *Journal of Applied Physics*, vol. 130, no. 4, 2021.

- [110] F. Yang, "Physics of Ferroelectric Wurtzite $\text{Al}_{1-x}\text{Sc}_x\text{N}$ Thin Films," *Advanced Electronic Materials*, 2024.
- [111] D. Wang, S. Yang, J. Liu, D. Wang, and Z. Mi, "Perspectives on nitride ferroelectric semiconductors: Challenges and opportunities," *Applied Physics Letters*, vol. 124, no. 15, 2024.
- [112] S. Fichtner, M. Yassine, C. G. Van de Walle, and O. Ambacher, "Clarification of the spontaneous polarization direction in crystals with wurtzite structure," *Applied Physics Letters*, vol. 125, no. 4, 2024.
- [113] T. Kumada, M. Ohtsuka, K. Takada, and H. Fukuyama, "Influence of sputter power and N_2 gas flow ratio on crystalline quality of AlN layers deposited at 823 K by RF reactive sputtering," *physica status solidi (c) - current topics in solid state physics*, vol. 9, no. 3-4, pp. 515-518, 2011.
- [114] H. Takeuchi, M. Ohtsuka, and H. Fukuyama, "Effect of sputtering power on surface characteristics and crystal quality of AlN films deposited by pulsed DC reactive sputtering," *physica status solidi (b) - basic solid state physics*, vol. 252, no. 5, pp. 1163-1171, 2015.
- [115] M. Akiyama, T. Kamohara, K. Kano, A. Teshigahara, Y. Takeuchi, and N. Kawahara, "Enhancement of piezoelectric response in scandium aluminum nitride alloy thin films prepared by dual reactive cosputtering," *Advanced Materials*, vol. 21, no. 5, pp. 593-6, 2009.
- [116] M. Akiyama, K. Umeda, A. Honda, and T. Nagase, "Influence of scandium concentration on power generation figure of merit of scandium aluminum nitride thin films," *Applied Physics Letters*, vol. 102, no. 2, 2013.
- [117] S. Yasuoka, T. Shimizu, A. Tateyama, M. Uehara, H. Yamada, M. Akiyama, Y. Hiranaga, Y. Cho, and H. Funakubo, "Effects of deposition conditions on the ferroelectric properties of $(\text{Al}_{1-x}\text{Sc}_x)\text{N}$ thin films," *Journal of Applied Physics*, vol. 128, no. 11, 2020.
- [118] M. A. Signore, A. Taurino, D. Valerini, A. Rizzo, I. Farella, M. Catalano, F. Quaranta, and P. Siciliano, "Role of oxygen contaminant on the physical properties of sputtered AlN thin films," *Journal of Alloys and Compounds*, vol. 649, pp. 1267-1272, 2015.
- [119] Y.-C. Yang, C.-T. Chang, Y.-C. Hsiao, J.-W. Lee, and B.-S. Lou, "Influence of high power impulse magnetron sputtering pulse parameters on the properties of aluminum nitride coatings," *Surface and Coatings Technology*, vol. 259, pp. 219-231, 2014.
- [120] M. A. Moram, Z. H. Barber, and C. J. Humphreys, "The effect of oxygen incorporation in sputtered scandium nitride films," *Thin Solid Films*, vol. 516, no. 23, pp. 8569-8572, 2008.

- [121] S. Berg, N. Eguchi, V. Grajewski, S. W. Kim, and E. Fromm, "Effect of contamination reactions on the composition and mechanical properties of magnetron sputtered TiN coatings," *Surface and Coatings Technology*, vol. 49, no. 1-3, pp. 336-341, 1991.
- [122] Y. Morri and Y. Koido, "Sputtering target and manufacturing method therefor," patent no: 11236416B2, 2017.
- [123] W. M. Haynes, D. R. Lide, and T. J. Bruno, *CRC Handbook of Chemistry and Physics*, 97th ed., Boca Raton: CRC Press, 2016.
- [124] S. K. Ryoo, K. D. Kim, H. W. Park, Y. B. Lee, S. H. Lee, I. S. Lee, S. Byun, D. Shim, J. H. Lee, H. Kim, Y. H. Jang, M. H. Park, and C. S. Hwang, "Investigation of Optimum Deposition Conditions of Radio Frequency Reactive Magnetron Sputtering of Al_{0.7}Sc_{0.3}N Film with Thickness down to 20 nm," *Advanced Electronic Materials*, vol. 8, no. 11, 2022.
- [125] B. Sundarapandian, A. Yassine, L. Kirste, M. Baeumler, P. Straňák, E. Fisslthaler, M. Prescher, M. Yassine, A. Nair, M. Raghuvanshi, and O. Ambacher, "Influence of growth temperature on the properties of aluminum nitride thin films prepared by magnetron sputter epitaxy," *Journal of Applied Physics*, vol. 134, no. 18, 2023.
- [126] M. Uehara, K. Hirata, Y. Nakamura, S. A. Anggraini, K. Okamoto, H. Yamada, H. Funakubo, and M. Akiyama, "Excellent piezoelectric and ferroelectric properties of Sc_xGa_{1-x}N alloy with high Sc concentration," *APL Materials*, vol. 12, no. 12, 2024.
- [127] S. Calderon V, J. Hayden, M. Delower, J.-P. Maria, and E. C. Dickey, "Effect of boron concentration on local structure and spontaneous polarization in AlBN thin films," *APL Materials*, vol. 12, no. 2, 2024.
- [128] R. Deng, S. R. Evans, and D. Gall, "Bandgap in Al_{1-x}Sc_xN," *Applied Physics Letters*, vol. 102, no. 11, 2013.
- [129] M. Baeumler, Y. Lu, N. Kurz, L. Kirste, M. Prescher, T. Christoph, J. Wagner, A. Žukauskaitė, and O. Ambacher, "Optical constants and band gap of wurtzite Al_{1-x}Sc_xN/Al₂O₃ prepared by magnetron sputter epitaxy for scandium concentrations up to x = 0.41," *Journal of Applied Physics*, vol. 126, no. 4, 2019.
- [130] B. M. Melnick, J. F. Scott, C. A. Paz De Araujo, and L. D. McMillan, "Thickness dependence of D.C. leakage current in lead zirconate-titanate (PZT) memories," *Ferroelectrics*, vol. 135, no. 1, pp. 163-168, 1992.
- [131] G. Teowee, E. L. Quackenbush, C. D. Baertlein, J. M. Boulton, and D. R. Uhlmann, "Fatigue and retention behaviors of Pt-PZT-metal capacitors with various top metallizations," *Proceedings of 1994 IEEE International Symposium on Applications of Ferroelectrics*, pp. 523-526, 1994.

- [132] N. Liu, C. Luo, H. Wu, Y. Ding, X. Lu, Z. Yan, J.-M. Liu, and G. Yuan, "Precise control of fatigue, wake-up, charge injection, and break-down in $\text{Hf}_{0.5}\text{Zr}_{0.5}\text{O}_2$ -based ferroelectric memories," *Applied Physics Letters*, vol. 124, no. 19, 2024.
- [133] S.-L. Tsai, T. Hoshii, H. Wakabayashi, K. Tsutsui, T.-K. Chung, E. Y. Chang, and K. Kakushima, "Field cycling behavior and breakdown mechanism of ferroelectric $\text{Al}_{0.78}\text{Sc}_{0.22}\text{N}$ films," *Japanese Journal of Applied Physics*, vol. 61, no. SJ, 2022.
- [134] J. Kataoka, S.-L. Tsai, T. Hoshii, H. Wakabayashi, K. Tsutsui, and K. Kakushima, "A possible origin of the large leakage current in ferroelectric $\text{Al}_{1-x}\text{Sc}_x\text{N}$ films," *Japanese Journal of Applied Physics*, vol. 60, no. 3, 2021.
- [135] C. Liu, Q. Wang, W. Yang, T. Cao, L. Chen, M. Li, F. Liu, D. K. Loke, J. Kang, and Y. Zhu, "Multiscale Modeling of $\text{Al}_{0.7}\text{Sc}_{0.3}\text{N}$ -based FeRAM: the Steep Switching, Leakage and Selector-free Array," *2021 IEEE International Electron Devices Meeting (IEDM)*, pp. 8.1.1-8.1.4, 2021.
- [136] D. Wang, P. Wang, S. Mondal, Y. Xiao, M. Hu, and Z. Mi, "Impact of dislocation density on the ferroelectric properties of ScAlN grown by molecular beam epitaxy," *Applied Physics Letters*, vol. 121, no. 4, 2022.
- [137] T. Yanagitani and M. Suzuki, "Electromechanical coupling and gigahertz elastic properties of ScAlN films near phase boundary," *Applied Physics Letters*, vol. 105, no. 12, 2014.
- [138] J. Casamento, S. M. Baksa, D. Behrendt, S. Calderon, D. Goodling, J. Hayden, F. He, L. Jacques, S. H. Lee, W. Smith, A. Suceava, Q. Tran, X. Zheng, R. Zu, T. Beechem, I. Dabo, E. C. Dickey, G. Esteves, V. Gopalan, M. D. Henry, J. F. Ihlefeld, T. N. Jackson, S. V. Kalinin, K. P. Kelley, Y. Liu, A. M. Rappe, J. Redwing, S. Trolier-McKinstry, and J.-P. Maria, "Perspectives and progress on wurtzite ferroelectrics: Synthesis, characterization, theory, and device applications," *Applied Physics Letters*, vol. 124, no. 8, 2024.
- [139] C. E. Dreyer, A. Janotti, C. G. Van de Walle, and D. Vanderbilt, "Correct Implementation of Polarization Constants in Wurtzite Materials and Impact on III-Nitrides," *Physical Review X*, vol. 6, no. 2, 2016.
- [140] M. Uehara, R. Mizutani, S. Yasuoka, T. Shimizu, H. Yamada, M. Akiyama, and H. Funakubo, "Lower ferroelectric coercive field of ScGaN with equivalent remanent polarization as ScAlN," *Applied Physics Express*, vol. 15, no. 8, 2022.
- [141] M. Gremmel and S. Fichtner, "The interplay between imprint, wake-up, and domains in ferroelectric $\text{Al}_{0.70}\text{Sc}_{0.30}\text{N}$," *Journal of Applied Physics*, vol. 135, no. 20, 2024.
- [142] S. S. Cheema, D. Kwon, N. Shanker, R. Dos Reis, S. L. Hsu, J. Xiao, H. Zhang, R. Wagner, A. Datar, M. R. McCarter, C. R. Serrao, A. K. Yadav, G. Karbasian, C. H. Hsu, A. J. Tan, L. C. Wang, V. Thakare, X. Zhang, A. Mehta, E. Karapetrova, R. V.

- Chopdekar, P. Shafer, E. Arenholz, C. Hu, R. Proksch, R. Ramesh, J. Ciston, and S. Salahuddin, "Enhanced ferroelectricity in ultrathin films grown directly on silicon," *Nature*, vol. 580, no. 7804, pp. 478-482, 2020.
- [143] K. Toprasertpong, K. Tahara, Y. Hikosaka, K. Nakamura, H. Saito, M. Takenaka, and S. Takagi, "Low Operating Voltage, Improved Breakdown Tolerance, and High Endurance in $\text{Hf}_{0.5}\text{Zr}_{0.5}\text{O}_2$ Ferroelectric Capacitors Achieved by Thickness Scaling Down to 4 nm for Embedded Ferroelectric Memory," *ACS Applied Materials & Interfaces*, vol. 14, no. 45, pp. 51137-51148, 2022.
- [144] G. Schonweger, N. Wolff, M. R. Islam, M. Gremmel, A. Petraru, L. Kienle, H. Kohlstedt, and S. Fichtner, "In-Grain Ferroelectric Switching in Sub-5 nm Thin $\text{Al}_{0.74}\text{Sc}_{0.26}\text{N}$ Films at 1 V," *Advanced Science*, vol. 10, no. 25, 2023.
- [145] S. Yasuoka, R. Mizutani, R. Ota, T. Shiraishi, T. Shimizu, S. Yasui, Y. Ehara, K. Nishida, M. Uehara, H. Yamada, M. Akiyama, Y. Imai, O. Sakata, and H. Funakubo, "Enhancement of crystal anisotropy and ferroelectricity by decreasing thickness in (Al,Sc)N films," *Journal of the Ceramic Society of Japan*, vol. 130, no. 7, pp. 436-441, 2022.
- [146] K. D. Kim, Y. B. Lee, S. H. Lee, I. S. Lee, S. K. Ryoo, S. Y. Byun, J. H. Lee, and C. S. Hwang, "Impact of operation voltage and NH_3 annealing on the fatigue characteristics of ferroelectric AlScN thin films grown by sputtering," *Nanoscale*, vol. 15, no. 40, pp. 16390-16402, 2023.
- [147] R. Guido, T. Mikolajick, U. Schroeder, and P. D. Lomenzo, "Role of Defects in the Breakdown Phenomenon of $\text{Al}_{1-x}\text{Sc}_x\text{N}$: From Ferroelectric to Filamentary Resistive Switching," *Nano Letters*, vol. 23, no. 15, pp. 7213-7220, 2023.
- [148] M. Li, H. Lin, K. Hu, and Y. Zhu, "Oxide overlayer formation on sputtered ScAlN film exposed to air," *Applied Physics Letters*, vol. 121, no. 11, 2022.
- [149] Z. Fang, E. Wang, Y. Chen, X. Hou, K. C. Chou, W. Yang, J. Chen, and M. Shang, "Wurtzite AlN(0001) Surface Oxidation: Hints from Ab Initio Calculations," *ACS Applied Materials & Interfaces*, vol. 10, no. 36, pp. 30811-30818, 2018.
- [150] T. Schenk, E. Yurchuk, S. Mueller, U. Schroeder, S. Starschich, U. Böttger, and T. Mikolajick, "About the deformation of ferroelectric hystereses," *Applied Physics Reviews*, vol. 1, no. 4, 2014.
- [151] M. Lederer, T. Kampfe, T. Ali, F. Muller, R. Olivo, R. Hoffmann, N. Laleni, and K. Seidel, "Ferroelectric Field Effect Transistors as a Synapse for Neuromorphic Application," *IEEE Transactions on Electron Devices*, vol. 68, no. 5, pp. 2295-2300, 2021.
- [152] J. F. Scott, "Ferroelectrics go bananas," *Journal of Physics: Condensed Matter*, vol. 20, no. 2, 2008.
- [153] T. Schenk, U. Schroeder, and T. Mikolajick, "Dynamic leakage current

- compensation revisited," *IEEE Transactions on Ultrasonics, Ferroelectrics, and Frequency Control*, vol. 62, no. 3, pp. 596-9, 2015.
- [154] R. Meyer, R. Waser, K. Prume, T. Schmitz, and S. Tiedke, "Dynamic leakage current compensation in ferroelectric thin-film capacitor structures," *Applied Physics Letters*, vol. 86, no. 14, 2005.
- [155] J. F. Scott, L. Kammerdiner, M. Parris, S. Traynor, V. Ottenbacher, A. Shawabkeh, and W. F. Oliver, "Switching kinetics of lead zirconate titanate submicron thin-film memories," *Journal of Applied Physics*, vol. 64, no. 2, pp. 787-792, 1988.
- [156] A. Gomez and U. Celano, "Nano-positive up negative down in binary oxide ferroelectrics," *APL Materials*, vol. 12, no. 2, 2024.
- [157] P. Wang, D. Wang, S. Mondal, and Z. Mi, "Ferroelectric N-polar ScAlN/GaN heterostructures grown by molecular beam epitaxy," *Applied Physics Letters*, vol. 121, no. 2, 2022.
- [158] B.-T. Lin, Y.-W. Lu, J. Shieh, and M.-J. Chen, "Induction of ferroelectricity in nanoscale ZrO₂ thin films on Pt electrode without post-annealing," *Journal of the European Ceramic Society*, vol. 37, no. 3, pp. 1135-1139, 2017.
- [159] Z. Gao, Y. Luo, S. Lyu, Y. Cheng, Y. Zheng, Q. Zhong, W. Zhang, and H. Lyu, "Identification of Ferroelectricity in a Capacitor With Ultra-Thin (1.5-nm) Hf_{0.5}Zr_{0.5}O₂ Film," *IEEE Electron Device Letters*, vol. 42, no. 9, pp. 1303-1306, 2021.
- [160] H. Naganuma, Y. Inoue, and S. Okamura, "Evaluation of Electrical Properties of Leaky BiFeO₃ Films in High Electric Field Region by High-Speed Positive-Up-Negative-Down Measurement," *Applied Physics Express*, vol. 1, 2008.
- [161] S. Lancaster, S. Slesazeck, and T. Mikolajick, "On the Thickness Scaling of Ferroelectric Hafnia," *IEEE Transactions on Materials for Electron Devices*, vol. 1, pp. 36-48, 2024.
- [162] S. Fichtner, F. Lofink, B. Wagner, G. Schonweger, T.-N. Kreuzer, A. Petraru, and H. Kohlstedt, "Ferroelectricity in AlScN: Switching, Imprint and sub-150 nm Films," *2020 Joint Conference of the IEEE International Frequency Control Symposium and International Symposium on Applications of Ferroelectrics (IFCS-ISAF)*, pp. 1-4, 2020.
- [163] M. K. Lenox, S. T. Jaszewski, S. S. Fields, N. Shukla, and J. F. Ihlefeld, "Impact of Electric Field Pulse Duration on Ferroelectric Hafnium Zirconium Oxide Thin Film Capacitor Endurance," *physica status solidi (a) - applications and materials science*, vol. 221, no. 2, 2023.
- [164] M. Grossmann, D. Bolten, O. Lohse, U. Boettger, R. Waser, and S. Tiedke, "Correlation between switching and fatigue in PbZr_{0.3}Ti_{0.7}O₃ thin films," *Applied Physics Letters*, vol. 77, no. 12, pp. 1894-1896, 2000.

- [165] S. Starschich, S. Menzel, and U. Böttger, "Pulse wake-up and breakdown investigation of ferroelectric yttrium doped HfO₂," *Journal of Applied Physics*, vol. 121, no. 15, 2017.
- [166] J. Li, Y. Qu, M. Si, X. Lyu, and P. D. Ye, "Multi-Probe Characterization of Ferroelectric/Dielectric Interface by C-V, P-V and Conductance Methods," *2020 IEEE Symposium on VLSI Technology*, pp. 1-2, 2020.
- [167] D. Bolten, O. Lohse, M. Grossmann, and R. Waser, "Reversible and irreversible domain wall contributions to the polarization in ferroelectric thin films," *Ferroelectrics*, vol. 221, no. 1, pp. 251-257, 1999.
- [168] S. Deng, Z. Jiang, S. Dutta, H. Ye, W. Chakraborty, S. Kurinec, S. Datta, and K. Ni, "Examination of the Interplay Between Polarization Switching and Charge Trapping in Ferroelectric FET," *2020 IEEE International Electron Devices Meeting (IEDM)*, pp. 4.4.1-4.4.4, 2020.
- [169] S. Mukherjee, J. Bizindavyi, S. Clima, M. I. Popovici, V. V. Afanas'ev, and J. Van Houdt, "Resolving the discrepancy between coercive voltages extracted from C-V and P-V measurements in a ferroelectric capacitor," *Solid-State Electronics*, vol. 212, 2024.
- [170] M. Si, X. Lyu, and P. D. Ye, "Ferroelectric Polarization Switching of Hafnium Zirconium Oxide in a Ferroelectric/Dielectric Stack," *ACS Applied Electronic Materials*, vol. 1, no. 5, pp. 745-751, 2019.
- [171] A. K. Jonscher, "The 'universal' dielectric response," *Nature*, vol. 267, no. 5613, pp. 673-679, 1977.
- [172] S. Kamba, V. Bovtun, J. Petzelt, I. Rychetsky, R. Mizaras, A. Brilingas, J. Banys, J. Grigas, and M. Kosec, "Dielectric dispersion of the relaxor PLZT ceramics in the frequency range 20 Hz-100 THz," *Journal of Physics: Condensed Matter*, vol. 12, no. 4, pp. 497-519, 2000.
- [173] K. Takada, S. Takarae, K. Shimamoto, N. Fujimura, and T. Yoshimura, "Time-Dependent Imprint in Hf_{0.5}Zr_{0.5}O₂ Ferroelectric Thin Films," *Advanced Electronic Materials*, vol. 7, no. 8, 2021.
- [174] T. Kim, E. R. Borujeny, I. Sardinero-Meirás, J. Grajal, K. C. Cadien, D. A. Antoniadis, and J. A. Del Alamo, "AC Impedance Characteristics of Ferroelectric Hf_{0.5}Zr_{0.5}O₂: from 1 kHz to 10 GHz," *2023 International Electron Devices Meeting (IEDM)*, pp. 1-4, 2023.
- [175] Y. Hiranaga, T. Mimura, T. Shimizu, H. Funakubo, and Y. Cho, "Local C-V mapping for ferroelectrics using scanning nonlinear dielectric microscopy," *Journal of Applied Physics*, vol. 128, no. 24, 2020.
- [176] F. P. G. Fengler, M. Hoffmann, S. Slesazek, T. Mikolajick, and U. Schroeder, "On the relationship between field cycling and imprint in ferroelectric Hf_{0.5}Zr_{0.5}O₂,"

- Journal of Applied Physics*, vol. 123, no. 20, 2018.
- [177] Z. Liu, K. Toprasertpong, Z. Cai, M. Takenaka, and S. Takagi, "Role of charge injection/de-trapping in imprint behavior of ferroelectric Hf_{0.5}Zr_{0.5}O₂ thin film," *Applied Physics Letters*, vol. 125, no. 7, 2024.
- [178] A. Gruverman, B. J. Rodriguez, A. I. Kingon, R. J. Nemanich, A. K. Tagantsev, J. S. Cross, and M. Tsukada, "Mechanical stress effect on imprint behavior of integrated ferroelectric capacitors," *Applied Physics Letters*, vol. 83, no. 4, pp. 728-730, 2003.
- [179] H. Shin, V. Gaddam, Y. Goh, Y. Jeong, G. Kim, Y. Qin, and S. Jeon, "A method of controlling the imprint effect in hafnia ferroelectric device," *Applied Physics Letters*, vol. 122, no. 2, 2023.
- [180] Y. Goh, J. Hwang, M. Kim, Y. Lee, M. Jung, and S. Jeon, "Selector-less Ferroelectric Tunnel Junctions by Stress Engineering and an Imprinting Effect for High-Density Cross-Point Synapse Arrays," *ACS Applied Materials & Interfaces*, vol. 13, no. 49, pp. 59422-59430, 2021.
- [181] D. K. Schroder, *Semiconductor Material and Device Characterization*, 3rd ed., USA: John Wiley and Sons, Inc., 2005.
- [182] R. Shibukawa, S.-L. Tsai, T. Hoshii, H. Wakabayashi, K. Tsutsui, and K. Kakushima, "Influence of sputtering power on the switching and reliability of ferroelectric Al_{0.7}Sc_{0.3}N films," *Japanese Journal of Applied Physics*, vol. 61, no. SH, 2022.
- [183] S.-L. Tsai, "A Study on Reliability and Scalability of Ferroelectric AlScN Films," PhD Thesis, Department of Electrical and Electronic Engineering, Tokyo Institute of Technology, 2023.
- [184] G. Wingqvist, F. Tasnádi, A. Zukauskaitė, J. Birch, H. Arwin, and L. Hultman, "Increased electromechanical coupling in w-Sc_xAl_{1-x}N," *Applied Physics Letters*, vol. 97, no. 11, 2010.
- [185] S. M. Rossnagel, D. Mikalsen, H. Kinoshita, and J. J. Cuomo, "Collimated magnetron sputter deposition," *Journal of Vacuum Science & Technology A: Vacuum, Surfaces, and Films*, vol. 9, no. 2, pp. 261-265, 1991.
- [186] S. Kadlec and J. Musil, "Low pressure magnetron sputtering and selfsputtering discharges," *Vacuum*, vol. 47, no. 3, pp. 307-311, 1996.
- [187] H. Windischmann, "Intrinsic stress in sputter-deposited thin films," *Critical Reviews in Solid State and Materials Sciences*, vol. 17, no. 6, pp. 547-596, 1992.
- [188] G. F. Iriarte, J. G. Rodriguez, and F. Calle, "Effect of substrate-target distance and sputtering pressure in the synthesis of AlN thin films," *Microsystem Technologies*, vol. 17, no. 3, pp. 381-386, 2011.
- [189] P. Musavigharavi, A. C. Meng, D. Wang, J. Zheng, A. C. Foucher, R. H. Olsson, and E. A. Stach, "Nanoscale Structural and Chemical Properties of Ferroelectric

- Aluminum Scandium Nitride Thin Films,” *The Journal of Physical Chemistry C*, vol. 125, no. 26, pp. 14394-14400, 2021.
- [190] S. R. C. McMitchell, A. M. Walke, K. Banerjee, S. Mertens, X. Piao, M. Mao, K. Katcko, G. Vellianitis, M. Van Dal, Y.-M. Lin, G. Van den Bosch, R. Delhougne, and G. S. Kar, “Engineering Strain and Texture in Ferroelectric Scandium-Doped Aluminium Nitride,” *ACS Applied Electronic Materials*, vol. 5, no. 2, pp. 858-864, 2023.
- [191] Y. Tokita, T. Hoshii, H. Wakabayashi, K. Tsutsui, and K. Kakushima, “Identification of compressive strain in thin ferroelectric $Al_{1-x}Sc_xN$ films by Raman spectroscopy,” *Japanese Journal of Applied Physics*, vol. 63, no. 4, 2024.
- [192] H. Moriwake, R. Yokoi, A. Taguchi, T. Ogawa, C. A. J. Fisher, A. Kuwabara, Y. Sato, T. Shimizu, Y. Hamasaki, H. Takashima, and M. Itoh, “A computational search for wurtzite-structured ferroelectrics with low coercive voltages,” *APL Materials*, vol. 8, no. 12, 2020.
- [193] S. Rassay, F. Hakim, C. Li, C. Forgey, N. Choudhary, and R. Tabrizian, “A Segmented-Target Sputtering Process for Growth of Sub-50 nm Ferroelectric Scandium–Aluminum–Nitride Films with Composition and Stress Tuning,” *physica status solidi (RRL) – Rapid Research Letters*, vol. 15, no. 5, 2021.
- [194] M. Noor-A-Alam, Z. O. Olszewski, and M. Nolan, “Ferroelectricity and Large Piezoelectric Response of AlN/ScN Superlattice,” *ACS Applied Materials & Interfaces*, vol. 11, no. 22, pp. 20482-20490, 2019.
- [195] M. Ishihara, S. J. Li, H. Yumoto, K. Akashi, and Y. Ide, “Control of preferential orientation of AlN films prepared by the reactive sputtering method,” *Thin Solid Films*, vol. 316, no. 1-2, pp. 152-157, 1998.
- [196] X.-H. Xu, H.-S. Wu, C.-J. Zhang, and Z.-H. Jin, “Morphological properties of AlN piezoelectric thin films deposited by DC reactive magnetron sputtering,” *Thin Solid Films*, vol. 388, no. 1-2, pp. 62-67, 2001.
- [197] H. Y. Liu, G. S. Tang, F. Zeng, and F. Pan, “Influence of sputtering parameters on structures and residual stress of AlN films deposited by DC reactive magnetron sputtering at room temperature,” *Journal of Crystal Growth*, vol. 363, pp. 80-85, 2013.
- [198] J. Xi, D. Zhou, Y. Tong, Y. Zhao, and T. Lv, “Effect of abnormally oriented grains on the ferroelectric properties of $Al_{0.65}Sc_{0.35}N$ thin films,” *Materials Today Communications*, vol. 41, 2024.
- [199] M. Ozimek, W. Wilczyński, and B. Szubzda, “Magnetic thin film deposition with pulsed magnetron sputtering: deposition rate and film thickness distribution,” *IOP Conference Series: Materials Science and Engineering*, vol. 113, 2016.
- [200] A. Neidhardt, U. Reinhold, E. Schroeter, and W. Wuttke, “Position dependences

- in planar magnetron sputtering of TiN films," *Thin Solid Films*, vol. 173, no. 1, pp. 109-127, 1989.
- [201] T. Kim, J. Kim, R. Dalmau, R. Schlessler, E. Preble, and X. Jiang, "High-Temperature Electromechanical Characterization of AlN Single Crystals," *IEEE Transactions on Ultrasonics, Ferroelectrics, and Frequency Control*, vol. 62, no. 10, pp. 1880-7, 2015.
- [202] N. Setter, D. Damjanovic, L. Eng, G. Fox, S. Gevorgian, S. Hong, A. Kingon, H. Kohlstedt, N. Y. Park, G. B. Stephenson, I. Stolitchnov, A. K. TagansteV, D. V. Taylor, T. Yamada, and S. Streiffer, "Ferroelectric thin films: Review of materials, properties, and applications," *Journal of Applied Physics*, vol. 100, no. 5, 2006.
- [203] Y. Zhou, H. K. Chan, C. H. Lam, and F. G. Shin, "Mechanisms of imprint effect on ferroelectric thin films," *Journal of Applied Physics*, vol. 98, no. 2, 2005.
- [204] H. Chen, X. Zhou, L. Tang, Y. Chen, H. Luo, X. Yuan, C. R. Bowen, and D. Zhang, "HfO₂-based ferroelectrics: From enhancing performance, material design, to applications," *Applied Physics Reviews*, vol. 9, no. 1, 2022.
- [205] A. Chouprik, D. Negrov, E. Y. Tsybal, and A. Zenkevich, "Defects in ferroelectric HfO₂," *Nanoscale*, vol. 13, no. 27, pp. 11635-11678, 2021.
- [206] P. Wang, B. Wang, D. A. Laleyan, A. Pandey, Y. Wu, Y. Sun, X. Liu, Z. Deng, E. Kioupakis, and Z. Mi, "Oxygen defect dominated photoluminescence emission of Sc_xAl_{1-x}N grown by molecular beam epitaxy," *Applied Physics Letters*, vol. 118, no. 3, 2021.
- [207] M. Kazan, B. Rufflé, C. Zgheib, and P. Masri, "Oxygen behavior in aluminum nitride," *Journal of Applied Physics*, vol. 98, no. 10, 2005.
- [208] Q. Yan, A. Janotti, M. Scheffler, and C. G. Van de Walle, "Origins of optical absorption and emission lines in AlN," *Applied Physics Letters*, vol. 105, no. 11, 2014.
- [209] K. Genji and T. Uchino, "Time-resolved photoluminescence characterization of oxygen-related defect centers in AlN," *Applied Physics Letters*, vol. 109, no. 2, 2016.
- [210] M. Akiyama, T. Kamohara, K. Kano, A. Teshigahara, and N. Kawahara, "Influence of oxygen concentration in sputtering gas on piezoelectric response of aluminum nitride thin films," *Applied Physics Letters*, vol. 93, no. 2, 2008.
- [211] G. A. Slack, R. A. Tanzilli, R. O. Pohl, and J. W. Vandersande, "The intrinsic thermal conductivity of AlN," *Journal of Physics and Chemistry of Solids*, vol. 48, no. 7, pp. 641-647, 1987.
- [212] R. A. Youngman and J. H. Harris, "Luminescence Studies of Oxygen-Related Defects In Aluminum Nitride," *Journal of the American Ceramic Society*, vol. 73, no. 11, pp. 3238-3246, 1990.

- [213] J. M. Mäki, I. Makkonen, F. Tuomisto, A. Karjalainen, S. Suihkonen, J. Räisänen, T. Y. Chemekova, and Y. N. Makarov, "Identification of the $V_{Al}-O_N$ defect complex in AlN single crystals," *Physical Review B*, vol. 84, no. 8, 2011.
- [214] Q. Zhou, Z. Zhang, H. Li, S. Golovynskyi, X. Tang, H. Wu, J. Wang, and B. Li, "Below bandgap photoluminescence of an AlN crystal: Co-existence of two different charging states of a defect center," *APL Materials*, vol. 8, no. 8, 2020.
- [215] G. Nakada, Y. Kirihara, A. Yasui, K. Kakushima, and H. Nohira, "Estimation of the band alignment of metal/AlScN interfaces by hard X-ray photoelectron spectroscopy," *Japanese Journal of Applied Physics*, vol. 63, no. 5, 2024.
- [216] S. Acharya, X. Wang, Q. Xu, M. Zhang, J. Chai, P. Luo, P. C. Lim, P. Yang, L. Shen, C. Sun, and K. Yao, "Role of oxygen on structure and piezoelectric properties of $Al_{0.65}Sc_{0.35}N$ thin films," *Physical Review Applied*, vol. 22, no. 4, 2024.
- [217] J. Casamento, H. G. Xing, and D. Jena, "Oxygen Incorporation in the Molecular Beam Epitaxy Growth of $Sc_xGa_{1-x}N$ and $Sc_xAl_{1-x}N$," *physica status solidi (b) - basic solid state physics*, vol. 257, no. 4, 2020.
- [218] M. Fischer, M. Trant, K. Thorwarth, R. Crockett, J. Patscheider, and H. J. Hug, "Understanding the microstructural evolution and mechanical properties of transparent Al-O-N and Al-Si-O-N films," *Science and Technology of Advanced Materials*, vol. 20, no. 1, pp. 1031-1042, 2019.
- [219] P. Gasparotto, M. Fischer, D. Scopece, M. O. Liedke, M. Butterling, A. Wagner, O. Yildirim, M. Trant, D. Passerone, H. J. Hug, and C. A. Pignedoli, "Mapping the Structure of Oxygen-Doped Wurtzite Aluminum Nitride Coatings from Ab Initio Random Structure Search and Experiments," *ACS Applied Materials & Interfaces*, vol. 13, no. 4, pp. 5762-5771, 2021.
- [220] M. H. Park, H. J. Kim, Y. J. Kim, T. Moon, K. D. Kim, Y. H. Lee, S. D. Hyun, and C. S. Hwang, "Study on the internal field and conduction mechanism of atomic layer deposited ferroelectric $Hf_{0.5}Zr_{0.5}O_2$ thin films," *Journal of Materials Chemistry C*, vol. 3, no. 24, pp. 6291-6300, 2015.
- [221] F. Mehmood, M. Hoffmann, P. D. Lomenzo, C. Richter, M. Materano, T. Mikolajick, and U. Schroeder, "Bulk Depolarization Fields as a Major Contributor to the Ferroelectric Reliability Performance in Lanthanum Doped $Hf_{0.5}Zr_{0.5}O_2$ Capacitors," *Advanced Materials Interfaces*, vol. 6, no. 21, 2019.
- [222] K. D. Kim, Y. B. Lee, S. H. Lee, I. S. Lee, S. K. Ryoo, S. Byun, J. H. Lee, H. Kim, H. W. Park, and C. S. Hwang, "Evolution of the Ferroelectric Properties of AlScN Film by Electrical Cycling with an Inhomogeneous Field Distribution," *Advanced Electronic Materials*, vol. 9, no. 5, 2023.
- [223] G. Schönweger, A. Petraru, M. R. Islam, N. Wolff, B. Haas, A. Hammud, C. Koch, L. Kienle, H. Kohlstedt, and S. Fichtner, "From Fully Strained to Relaxed:

- Epitaxial Ferroelectric $\text{Al}_{1-x}\text{Sc}_x\text{N}$ for III-N Technology,” *Advanced Functional Materials*, vol. 32, no. 21, 2022.
- [224] K. H. Kim, Z. Han, Y. Zhang, P. Musavigharavi, J. Zheng, D. K. Pradhan, E. A. Stach, R. H. Olsson, 3rd, and D. Jariwala, “Multistate, Ultrathin, Back-End-of-Line-Compatible AlScN Ferroelectric Diodes,” *ACS Nano*, vol. 18, no. 24, pp. 15925-15934, 2024.
- [225] J. X. Zheng, M. M. A. Fiagbenu, G. Esteves, P. Musavigharavi, A. Gunda, D. Jariwala, E. A. Stach, and R. H. Olsson, “Ferroelectric behavior of sputter deposited $\text{Al}_{0.72}\text{Sc}_{0.28}\text{N}$ approaching 5 nm thickness,” *Applied Physics Letters*, vol. 122, no. 22, 2023.
- [226] S. K. Ryoo, K. D. Kim, W. Choi, P. Sriboriboon, S. Heo, H. Seo, Y. H. Jang, J. W. Jeon, M. K. Yeom, S. H. Lee, H. S. Park, Y. Kim, and C. S. Hwang, “Fabrication of Ultrathin Ferroelectric $\text{Al}_{0.7}\text{Sc}_{0.3}\text{N}$ Films under Complementary-Metal-Oxide-Semiconductor Compatible Conditions by using $\text{HfN}_{0.4}$ Electrode,” *Advanced Materials*, vol. 37, no. 1, 2025.
- [227] D. Wang, P. Wang, S. Mondal, M. Hu, D. Wang, Y. Wu, T. Ma, and Z. Mi, “Thickness scaling down to 5 nm of ferroelectric ScAlN on CMOS compatible molybdenum grown by molecular beam epitaxy,” *Applied Physics Letters*, vol. 122, no. 5, 2023.
- [228] M. R. Islam, G. Schonweger, N. Wolff, A. Petraru, H. Kohlstedt, S. Fichtner, and L. Kienle, “A Comparative Study of Pt/ $\text{Al}_{0.72}\text{Sc}_{0.28}\text{N}$ /Pt-Based Thin-Film Metal-Ferroelectric-Metal Capacitors on GaN and Si Substrates,” *ACS Applied Materials & Interfaces*, vol. 15, no. 35, pp. 41606-41613, 2023.
- [229] S. Mondal, E. Hershkovitz, G. Baucom, M. M. Hasan Tanim, S. Dabas, B. Chatterjee, H. Kim, R. Tabrizian, and Z. Mi, “Polarity controlled ScAlN multilayer transduction structures grown by molecular beam epitaxy,” *APL Materials*, vol. 12, no. 11, 2024.
- [230] A. Huang and S. R. Shannigrahi, “Effect of bottom electrode and resistive layer on the dielectric and ferroelectric properties of sol-gel derived BiFeO_3 thin films,” *Journal of Alloys and Compounds*, vol. 509, no. 5, pp. 2054-2059, 2011.
- [231] Y. Lee, Y. Goh, J. Hwang, D. Das, and S. Jeon, “The Influence of Top and Bottom Metal Electrodes on Ferroelectricity of Hafnia,” *IEEE Transactions on Electron Devices*, vol. 68, no. 2, pp. 523-528, 2021.
- [232] J. X. Zheng, D. Wang, P. Musavigharavi, M. M. A. Fiagbenu, D. Jariwala, E. A. Stach, and R. H. Olsson, “Electrical breakdown strength enhancement in aluminum scandium nitride through a compositionally modulated periodic multilayer structure,” *Journal of Applied Physics*, vol. 130, no. 14, 2021.
- [233] Y.-J. Yong and J.-Y. Lee, “Characteristics of hydrogenated aluminum nitride films

- prepared by radio frequency reactive sputtering and their application to surface acoustic wave devices," *Journal of Vacuum Science & Technology A: Vacuum, Surfaces, and Films*, vol. 15, no. 2, pp. 390-393, 1997.
- [234] Y.-S. Kang, Y.-J. Yong, P. S. Lee, and J.-Y. Lee, "Roles of Hydrogen on the Composition and Bonding of Atoms in Hydrogenated Aluminum Nitride Films Prepared by RF Reactive Sputtering," *Journal of The Electrochemical Society*, vol. 149, no. 1, 2002.
- [235] K. Kushida-Abdelghafar, H. Miki, K. Torii, and Y. Fujisaki, "Electrode-induced degradation of $\text{Pb}(\text{Zr}_x\text{Ti}_{1-x})\text{O}_3$ (PZT) polarization hysteresis characteristics in Pt/PZT/Pt ferroelectric thin-film capacitors," *Applied Physics Letters*, vol. 69, no. 21, pp. 3188-3190, 1996.
- [236] Y. Fujisaki, K. Kushida-Abdelghafar, Y. Shimamoto, and H. Miki, "The effects of the catalytic nature of capacitor electrodes on the degradation of ferroelectric $\text{Pb}(\text{Zr,Ti})\text{O}_3$ thin films during reductive ambient annealing," *Journal of Applied Physics*, vol. 82, no. 1, pp. 341-344, 1997.
- [237] J.-P. Han and T. P. Ma, "Electrode dependence of hydrogen-induced degradation in ferroelectric $\text{Pb}(\text{Zr,Ti})\text{O}_3$ and $\text{SrBi}_2\text{Ta}_2\text{O}_9$ thin films," *Applied Physics Letters*, vol. 71, no. 9, pp. 1267-1269, 1997.
- [238] S. Aggarwal, S. R. Perusse, C. W. Tipton, R. Ramesh, H. D. Drew, T. Venkatesan, D. B. Romero, V. B. Podobedov, and A. Weber, "Effect of hydrogen on $\text{Pb}(\text{Zr,Ti})\text{O}_3$ -based ferroelectric capacitors," *Applied Physics Letters*, vol. 73, no. 14, pp. 1973-1975, 1998.
- [239] M. H. Park, J. H. Kim, J. Y. Kim, W. Lee, K. H. Kim, and S. C. Hwang, "Effect of forming gas annealing on the ferroelectric properties of $\text{Hf}_{0.5}\text{Zr}_{0.5}\text{O}_2$ thin films with and without Pt electrodes," *Applied Physics Letters*, vol. 102, no. 11, 2013.
- [240] N. Sun, K. Okamoto, S. Yasuoka, S. Doko, N. Matsui, T. Irisawa, K. Tsunekawa, T. Katase, T. Koganezawa, T. Nakatani, R. Kumara, O. Sakata, and H. Funakubo, "High stability of the ferroelectricity against hydrogen gas in $(\text{Al,Sc})\text{N}$ thin films," *Applied Physics Letters*, vol. 125, no. 3, 2024.
- [241] A. Zukauskaitė, G. Wingqvist, J. Palisaitis, J. Jensen, P. O. Å. Persson, R. Matloub, P. Murali, Y. Kim, J. Birch, and L. Hultman, "Microstructure and dielectric properties of piezoelectric magnetron sputtered $w\text{-Sc}_x\text{Al}_{1-x}\text{N}$ thin films," *Journal of Applied Physics*, vol. 111, no. 9, 2012.
- [242] Y. Lu, M. Reusch, N. Kurz, A. Ding, T. Christoph, L. Kirste, V. Lebedev, and A. Žukauskaitė, "Surface Morphology and Microstructure of Pulsed DC Magnetron Sputtered Piezoelectric AlN and AlScN Thin Films," *physica status solidi (a) – applications and materials science*, vol. 215, no. 9, 2017.
- [243] H. Lee, K.-Y. Lee, Y. Yong, J.-Y. Lee, and G. Kim, "Effect of hydrogen addition on

- the preferred orientation of AlN films prepared by reactive sputtering,” *Thin Solid Films*, vol. 271, no. 1-2, pp. 50-55, 1995.
- [244] V. M. Fridkin and S. Ducharme, “General features of the intrinsic ferroelectric coercive field,” *Physics of the Solid State*, vol. 43, no. 7, pp. 1320-1324, 2001.
- [245] W. L. Warren, D. Dimos, B. A. Tuttle, R. D. Nasby, and G. E. Pike, “Electronic domain pinning in Pb(Zr,Ti)O₃ thin films and its role in fatigue,” *Applied Physics Letters*, vol. 65, no. 8, pp. 1018-1020, 1994.
- [246] D. Dimos, H. N. Al-Shareef, W. L. Warren, and B. A. Tuttle, “Photoinduced changes in the fatigue behavior of SrBi₂Ta₂O₉ and Pb(Zr,Ti)O₃ thin films,” *Journal of Applied Physics*, vol. 80, no. 3, pp. 1682-1687, 1996.
- [247] M. Pešić, F. P. G. Fengler, L. Larcher, A. Padovani, T. Schenk, E. D. Grimley, X. Sang, J. M. LeBeau, S. Slesazek, U. Schroeder, and T. Mikolajick, “Physical Mechanisms behind the Field-Cycling Behavior of HfO₂-Based Ferroelectric Capacitors,” *Advanced Functional Materials*, vol. 26, no. 25, pp. 4601-4612, 2016.
- [248] R. Ota, S. Yasuoka, R. Mizutani, T. Shiraishi, K. Okamoto, K. Kakushima, T. Koganezawa, O. Sakata, and H. Funakubo, “Scalable ferroelectricity of 20 nm-thick (Al_{0.8}Sc_{0.2})N thin films sandwiched between TiN electrodes,” *Journal of Applied Physics*, vol. 134, no. 21, 2023.
- [249] F. Huang, B. Saini, L. Wan, H. Lu, X. He, S. Qin, W. Tsai, A. Gruverman, A. C. Meng, H. P. Wong, P. C. McIntyre, and S. Wong, “Dimensional Scaling of Ferroelectric Properties of Hafnia-Zirconia Thin Films: Electrode Interface Effects,” *ACS Nano*, vol. 18, no. 27, pp. 17600-17610, 2024.
- [250] J. Li, G. Chai, and X. Wang, “Atomic layer deposition of thin films: from a chemistry perspective,” *International Journal of Extreme Manufacturing*, vol. 5, no. 3, 2023.
- [251] T. Jussila, A. Philip, T. Tripathi, K. Nielsch, and M. Karppinen, “Atomic layer deposition of magnetic thin films: Basic processes, engineering efforts, and road forward,” *Applied Physics Reviews*, vol. 10, no. 4, 2023.
- [252] E. Österlund, H. Seppänen, K. Běspalova, V. Miikkulainen, and M. Paulasto-Kröckel, “Atomic layer deposition of AlN using atomic layer annealing—Towards high-quality AlN on vertical sidewalls,” *Journal of Vacuum Science & Technology A: Vacuum, Surfaces, and Films*, vol. 39, no. 3, 2021.
- [253] A. J. M. Mackus, J. R. Schneider, C. Maclsaac, J. G. Baker, and S. F. Bent, “Synthesis of Doped, Ternary, and Quaternary Materials by Atomic Layer Deposition: A Review,” *Chemistry of Materials*, vol. 31, no. 4, pp. 1142-1183, 2018.
- [254] S. Y. Oh, S. Kim, G. Lee, J.-H. Park, D. Jeon, S. Kim, and G. Yoo, “Wide-Range

Threshold Voltage Tunable β -Ga₂O₃FETs With a Sputtered AlScN Ferroelectric Gate Dielectric," *IEEE Electron Device Letters*, vol. 45, no. 9, pp. 1558-1561, 2024.

- [255] S. Oh, S. Yoon, Y. Lim, G. Lee, and G. Yoo, "Improved lateral figure-of-merit of heteroepitaxial α -Ga₂O₃ power MOSFET using ferroelectric AlScN gate stack," *Applied Physics Letters*, vol. 125, no. 19, 2024.
- [256] Y.-R. Luo, *Comprehensive Handbook of Chemical Bond Energies*, 1st ed., Boca Raton: CRC Press, 2007.

Appendix

TABLE A1.1
LIST OF BOND DISSOCIATION ENERGY [123], [256]

Bond dissociation energy (kJ/mol)	
H-H	435.7799 ± 0.0001
O=O	498.36 ± 0.17
N \equiv N	944.84 ± 0.10
Al-N	$\leq 368 \pm 15$
Al-O	501.9 ± 10.6
Sc-N	464 ± 84
Sc-O	671.4 ± 1.0

Curriculum Vitae

SI-MENG CHEN PhD student

✉ chen.s.ap@m.titech.ac.jp ☎ 080-7416-5077 📍 Kawasaki-shi, Kanagawa 213-0013

Dedicated and passionate PhD candidate in Electrical and Electronic Engineering with a strong commitment to expanding the frontiers of knowledge in the field. Possesses six years of hands-on experimentation with semiconductor processing within cleanroom environments. Specialized in precision experimental design, comprehensive data analysis, and strategic multi-disciplinary research integration. Boasts a distinguished publication record of six peer-reviewed articles in scientific journals. Eager to contribute cutting-edge research capabilities to a dynamic research institute, driving innovation in device technologies while upholding scientific excellence.

🎓 EDUCATION

2015/09 – 2019/06
Taiwan

Bachelor of Science, National Chiao Tung University

- Major in material science and engineering
- Undergraduate research on the ferroelectricity of Al-doped HfZrO₂
- Trained with semiconductor process experiments in a cleanroom environment
- Extraneous coursework in electronics, circuit theory, electromagnetics, semiconductor physics and semiconductor processing
- Leader of the animal conservation club at university

2020/04 – 2022/03
Japan

Master of Engineering, Tokyo Institute of Technology

- Graduate major in electrical and electronic engineering (Dual-master degree program)
- Master's research on self-polarised AlScN gate dielectrics in GaN-HEMT for power applications
- Focused on suitable gate dielectrics with large spontaneous polarization for threshold voltage tuning
- Engaged with HEMT fabrication and characterization
- Demonstrated the potential of polarization engineering in GaN-HEMT for normally-off operation

2019/09 – 2023/02
Taiwan

Master of Science, National Yang Ming Chiao Tung University

- Graduate major in semiconductor technology (Dual-master degree program)
- Master's research on InGaAs gate-all-around (GAA) nanowire MOSFETs for low-power logic applications
- Extensive exploration of nanowire channel formation and in-situ ALD gate stack process
- Contributed to GAA MOSFET fabrication and characterization
- Experimental demonstration of suppressed short channel effects in aggressively scaled transistors

2022/04 – present
Japan

Doctor of Philosophy, Institute of Science Tokyo

- Graduate major in electrical and electronic engineering
- Doctoral research on reliable and scalable ferroelectric AlScN thin films for advanced memory technology
- Advanced understanding of novel wurtzite ferroelectric materials
- Collaborated closely with colleagues to overcome technical challenges
- Developed PVD (sputtering) process guidelines for optimized ferroelectricity in AlScN thin films
- Focused on defect engineering in AlScN to realize multi-level operation for analog applications
- Achieved a world record (2024) endurance cycle of 2×10^7 by reactive sputtering

TECHNICAL SKILLS

Semiconductor device manufacturing

Device electrical characterization

Thin film growth

Data curation & analysis

Paper writing & editing

LANGUAGES

Chinese (Mandarin)
Native



English
IELTS 7.0 (Academic module)



Japanese
JLPT N2



DIGITAL SKILLS

Microsoft PowerPoint | Microsoft Excel | Microsoft Word | OriginPro

PUBLICATIONS

Google Scholar
link to page. [↗](#)

ORCID
<https://orcid.org/0000-0001-7714-6129> [↗](#)

Journal Paper:

- **Si-Meng Chen**, Sung-Lin Tsai, Kazuto Mizutani, Takuya Hoshii, Hitoshi Wakabayashi, Kazuo Tsutsui, Edward Yi Chang, and Kuniyuki Kakushima, " GaN high electron mobility transistors (HEMTs) with self-upward-polarized AlScN gate dielectrics toward enhancement-mode operation," Japanese Journal of Applied Physics, vol. 61, no. SH, 2022. [↗](#)
- **Si-Meng Chen**, Takuya Hoshii, Hitoshi Wakabayashi, Kazuo Tsutsui, Edward Yi Chang, and Kuniyuki Kakushima, "Reactive sputtering of ferroelectric AlScN films with H₂ gas flow for endurance improvement," Japanese Journal of Applied Physics, vol. 63, no. 3, 2024. [↗](#)
- **Si-Meng Chen**, Hirofumi Nishida, Sung-Lin Tsai, Takuya Hoshii, Kazuo Tsutsui, Hitoshi Wakabayashi, Edward Yi Chang, and Kuniyuki Kakushima, "Oxygen-Atom Incorporated Ferroelectric AlScN Capacitors for Multi-Level Operation," IEEE Electron Device Letters, vol. 45, no. 11, pp. 2090-2093, 2024. [↗](#)
- Hua-Lun Ko, Quang Ho Luc, Ping Huang, **Si-Meng Chen**, Jing-Yuan Wu, Che-Wei Hsu, Nhan-Ai Tran, and Edward Yi Chang, "Nitrogen-Passivated (010) In_{0.53}Ga_{0.47}As FinFETs With High Peak gm and Reduced Leakage Current," IEEE Transactions on Electron Devices, vol. 69, no. 2, pp. 495-499, 2022. [↗](#)
- Hua-Lun Ko, Quang Ho Luc, Ping Huang, **Si-Meng Chen**, Jing-Yuan Wu, Nhan-Ai Tran, Heng-Tung Hsu, and Edward Yi Chang, "Sub-10 nm Top Width Nanowire InGaAs Gate-All-Around MOSFETs with Improved Subthreshold Characteristics and Device Reliability," IEEE Journal of Electron Devices Society, vol. 10, pp. 188-191, 2022. [↗](#)
- Hua-Lun Ko, Quang Ho Luc, Ping Huang, **Si-Meng Chen**, Jing-Yuan Wu, Che-Wei Hsu, Nhan-Ai Tran, and Edward Yi Chang, "Electrical Characteristics of In_{0.53}Ga_{0.47}As Gate-All-Around MOSFETs with Different Nanowire Shapes," IEEE Transactions on Electron Devices, vol. 69, no. 8, pp. 4183-4187, 2022. [↗](#)

Publication List

Journal Paper:

Paper I: Si-Meng Chen, Takuya Hoshii, Hitoshi Wakabayashi, Kazuo Tsutsui, Edward Yi Chang, and Kuniyuki Kakushima, "Reactive sputtering of ferroelectric AlScN films with H₂ gas flow for endurance improvement," *Japanese Journal of Applied Physics*, vol. 63, no. 3, 2024.

Paper II: Si-Meng Chen, Hirofumi Nishida, Sung-Lin Tsai, Takuya Hoshii, Kazuo Tsutsui, Hitoshi Wakabayashi, Edward Yi Chang, and Kuniyuki Kakushima, "Oxygen-Atom Incorporated Ferroelectric AlScN Capacitors for Multi-Level Operation," *IEEE Electron Device Letters*, vol. 45, no. 11, pp. 2090-2093, 2024.

Conference Paper:

Paper III: Si-Meng Chen, Sung-Lin Tsai, Takuya Hoshii, Hitoshi Wakabayashi, Kazuo Tsutsui, and Kuniyuki Kakushima, "Influence of H₂ in Reactive Sputtering of Ferroelectric AlScN Films," *International Conference on Solid State Devices and Materials (SSDM)*, pp. 675-676, 2023.

Paper IV: Si-Meng Chen, Hirofumi Nishida, Takuya Hoshii, Kazuo Tsutsui, Hitoshi Wakabayashi, Edward Yi Chang, and Kuniyuki Kakushima, "Ferroelectricity Engineered AlScN Thin Films Prepared by Hydrogen Included Reactive Sputtering for Analog Applications," *IEEE Silicon Nanoelectronics Workshop (SNW)*, pp. 29-30, 2024.

Extraneous Journal and Conference Papers

The following are the papers that I have contributed to, but the content is not included in this thesis. Some papers are related to this research.

Paper V: Si-Meng Chen, Sung-Lin Tsai, Kazuto Mizutani, Takuya Hoshii, Hitoshi Wakabayashi, Kazuo Tsutsui, Edward Yi Chang, and Kuniyuki Kakushima, " GaN high electron mobility transistors (HEMTs) with self-upward-polarized AlScN gate dielectrics toward enhancement-mode operation," *Japanese Journal of Applied Physics*, vol. 61, no. SH, 2022.

- Paper VI:** Si-Meng Chen, Sung-Lin Tsai, Kazuto Mizutani, Takuya Hoshii, Hitoshi Wakabayashi, Kazuo Tsutsui, and Kuniyuki Kakushima, "GaN HEMTs with self-upward-polarized AlScN gate dielectrics toward enhancement-mode operation," *2021 International Workshop on Dielectric Thin Films for Future Electron Devices (IWDTF)*, pp.83-84, 2021.
- Paper VII:** Hitomi Hasegawa, Si-Meng Chen, Takuya Hoshii, Kazuo Tsutsui, Hitoshi Wakabayashi, Edward Yi Chang, and Kuniyuki Kakushima, "Bottom Electrode Material Selection for Ferroelectric AlScN Films," *International Workshop on Nanodevice Technologies (IWNT)*, Nov. 15th, 2024.
- Paper VIII:** Jia-Hong Lin, Ting-Tzu Kuo, Si-Meng Chen, Hirofumi Nishida, An Li, Takuya Hoshii, Hitoshi Wakabayashi, Ting-Chang Chang, and Kuniyuki Kakushima, "Fabrication of FeFET with ferroelectric AlScN film and In₂O₃ channel," The 72nd JSAP Spring Meeting 2025, Mar. 14th-17th, 2025.
- Paper IX:** Hua-Lun Ko, Quang Ho Luc, Ping Huang, Si-Meng Chen, Jing-Yuan Wu, Che-Wei Hsu, Nhan-Ai Tran, and Edward Yi Chang, "Nitrogen-Passivated (010) In_{0.53}Ga_{0.47}As FinFETs With High Peak g_m and Reduced Leakage Current," *IEEE Transactions on Electron Devices*, vol. 69, no. 2, pp. 495-499, 2022.
- Paper X:** Hua-Lun Ko, Quang Ho Luc, Ping Huang, Jing-Yuan Wu, Si-Meng Chen, Nhan-Ai Tran, Heng-Tung Hsu, and Edward Yi Chang, "Sub-10 nm Top Width Nanowire InGaAs Gate-All-Around MOSFETs with Improved Subthreshold Characteristics and Device Reliability," *IEEE Journal of Electron Devices Society*, vol. 10, pp. 188-191, 2022.
- Paper XI:** Hua-Lun Ko, Quang Ho Luc, Ping Huang, Si-Meng Chen, Jing-Yuan Wu, Che-Wei Hsu, Nhan-Ai Tran, and Edward Yi Chang, "Electrical Characteristics of In_{0.53}Ga_{0.47}As Gate-All-Around MOSFETs with Different Nanowire Shapes," *IEEE Transactions on Electron Devices*, vol. 69, no. 8, pp. 4183-4187, 2022.
- Paper XII:** Hua-Lun Ko, Quang Ho Luc, Ping Huang, Jing-Yuan Wu, Che-Wei Hsu, Si-Meng Chen, Nhan-Ai Tran, and Edward Yi Chang, "Nitrogen-Passivated InGaAs Gate-All-Around MOSFETs with Lowest Off-Current," *International Electron Devices & Materials Symposium (IEDMs)*, Oct. 15th-16th, 2020.

Paper XIII: Hua-Lun Ko, Quang Ho Luc, Si-Meng Chen, Ping Huang, Jing-Yuan Wu, Che-Wei Hsu, Nhan-Ai Tran, and Edward Yi Chang, “Effectively Suppressed Short Channel Effects Use Nitrogen-Passivated of InGaAs Gate-All-Around MOSFETs for High Switching Speed Logic Application,” *ECS Meeting Abstracts*, vol. MA2020-02, no. 51, p. 3836, 2020.